NANOROBOTIC END-EFFECTORS: DESIGN, FABRICATION, AND IN SITU CHARACTERIZATION

By

Zheng Fan

A DISSERTATION

Submitted to
Michigan State University
in partial fulfillment of the requirements
for the degree of

Electrical Engineering - Doctor of Philosophy

2015

ABSTRACT

NANOROBOTIC END-EFFECTORS: DESIGN, FABRICATION, AND IN SITU CHARACTERIZATION

By

Zheng Fan

Nano-robotic end-effectors have promising applications for nano-fabrication, nano-manufacturing, nano-optics, nano-medical, and nano-sensing; however, low performances of the conventional end-effectors have prevented the widespread utilization of them in various fields. There are two major difficulties in developing the end-effectors: their nano-fabrication and their advanced characterization in the nanoscale. Here we introduce six types of end-effectors: the nanotube fountain pen (NFP), the super-fine nanoprobe, the metal-filled carbon nanotube (m@CNT)-based sphere-on-pillar (SOP) nanoantennas, the tunneling nanosensor, and the nanowire-based memristor. The investigations on the NFP are focused on nano-fluidics and nano-fabrications. The NFP could direct write metallic “inks” and fabricating complex metal nanostructures from 0D to 3D with a position servo control, which is critically important to future large-scale, high-throughput nanodevice production. With the help of NFP, we could fabricate the end-effectors such as super-fine nanoprobe and m@CNT-based SOP nanoantennas. Those end-effectors are able to detect local flaws or characterize the electrical/mechanical properties of the nanostructure. Moreover, using electron-energy-loss-spectroscopy (EELS) technique during the operation of the SOP optical antenna opens a new basis for the application of nano-robotic end-effectors. The technique allows advanced characterization of the physical changes, such as carrier diffusion, that are directly responsible for the device’s properties. As the device was coupled with characterization techniques of scanning-trasmission-electron-microscopy (STEM), the development of tunneling nanosensor advances this field of science

into quantum world. Furthermore, the combined STEM-EELS technique plays an important role in our understanding of the memristive switching performance in the nanowire-based memristor. The developments of those nano-robotic end-effectors expend the study abilities in investigating the *in situ* nanotechnology, providing efficient ways in *in situ* nanostructure fabrication and the advanced characterization of the nanomaterials.

ACKNOWLEDGEMENTS

First of all, I sincerely appreciate my advisor, Dr. Lixin Dong, who offered me the opportunity to carry out my research in the United States. He was always willing to discuss the research with me and provide guidance to my study.

I would also like to thank my committee members: Drs. Ning Xi, Tim Hogan, Wen Li, Xudong Fan, and Wei Lai. They provided instructive suggestion and technical support in the completion and the presentation of this dissertation.

Next, I would like to express my gratitude to my colleagues, Dr. Fubo Rao, Gautham Dharuman, Miao Yu, and Chinwe Nyenke. They were very helpful in carrying out the experiment and provided lively discussion and fruitful advises.

Finally, I thank my parents, who always supported me during these years' study. I dedicate this dissertation to them.

TABLE OF CONTENTS

LIST OF TABLES vii

LIST OF FIGURES viii

CHAPTER 1 INTRODUCTION 1
1.1 Overview 1
1.2 Work Performed 6
1.3 Research Objectives 9

CHAPTER 2 NANOTUBE FOUNTAIN PEN 11
2.1 Introduction and Design of the Nanotube Fountain Pen (NFP) 11
2.2 Continuous Mass Feeding 15
2.3 Mechanism Analysis of the Inter/Intra Nanotube Mass Flow 20
2.4 The Application of the NFP 26
2.4.1 NFP Writing Capillary 26
2.4.2 NFP Ink Reloading Process 30
2.5 Chapter Summary 32

CHAPTER 3 SLIDING PROBE METHOD 33
3.1 Introduction of the Sliding Probe Method 33
3.2 Two-Point and Multi-Point Sliding Probe Method 36
3.3 Differential Sliding Probe Method 46
3.4 Chapter Summary 52

CHAPTER 4 SPHERE-ON-PILLAR OPTICAL NANO-ANTENNA 54
4.1 Introduction of the Metal-Filled Carbon Nanotube-Based Sphere-on-Pillar Optical Nano-Antenna 55
4.2 EBIB 57
4.2 EMBB 60
4.2.1 EMBB on a Conductive Surface 60
4.2.2 EMBB on a Non-Conductive Surface 68
4.3 Shaping the Deposit using the Heat Sink Effect 72
4.4 In situ Optical Antenna Experiment 78
4.5 Chapter Summary 81

CHAPTER 5 TUNNELING NANOSENSOR 83
5.1 Introduction of the Nanowire-Based Tunneling Nanosensor 83
5.2 Modeling 84
5.3 Simulation 90
5.4 B_4C Peapod Nanowire-Based Tunneling Nanosensor 92
5.4.1 Introduction of the B_4C Peapod Nanowire 92
5.4.2 Elemental Detection of the B_4C Peapod Nanowire 93
5.4.3 *In situ* Buckling of the B_4C Peapod Nanowire 97
5.4.4 Force/Displacement Sensing using B_4C Peapod Nanowire 102

5.4.5 Summary 109
5.5 Chapter Summary 110

CHAPTER 6 COPPER-OXIDE NANOWIRE-BASED MEMRISTOR 111
6.1 Introduction of the Memristor 112
6.2 Fabrication and Characterization of the Copper-Oxide Nanowire-Based Memristor 114
6.3 Mechanism Analysis of the Memristive Switch 120
6.4 Memsensor 126
6.5 Chapter Summary 128

CHAPTER 7 SUMMARY AND FUTURE WORK 129
7.1 Summary 129
7.2 Future Works 131

BIBLIOGRAPHY 133

LIST OF TABLES

Table 1.1: The end-effector devices and applied techniques 3
Table 2.1: Comparison of power threshold of NFP with different diameters 25

LIST OF FIGURES

Figure 1.1: Nanorobots work on a pipeline and fabricate nanodevices atom by atom. 1

Figure 1.2: Nanorobotic end-effectors: (a) Nanotube fountain pen, (b) Super-fine nanoprobe, (c) m@CNTs-based SOP optical nanoantennas, (d) Nanowire-based tunneling nanosensor, (e) CuO NW-based memristor. 5

Figure 2.1: The schematic of NFP. By applying a bias, the encapsulated metal can be continuously flowed out for nanostructure fabrication. 12

Figure 2.2: *I-t* characterization during the NFP "writing" process. The initial state (0~300) is defined as "OFF" (external bias: 1.0 V) and the state after the mass migration starts as "ON" (external bias: 1.5 V). Insets show the initial mass inside the nanotube injector is 1.9 fg, while the deposited mass is 29.0 fg (about 15 times more than the original mass). 13

Figure 2.3: Mass accumulation process. The mass is accumulated from the neighbor CNTs. 15

Figure 2.4: The model for NFP "writing". The initial *I-V* curve of NFP in the "OFF" state shows a non-ohmic/charging characteristic. Inset shows the two junctions exist at the two ends of tube. 16

Figure 2.5: The *I-V* curves for the combination of different junctions (C-C and C-S). 17

Figure 2.6: The generation of super fine nanowire by using a Cu@CNT with a hole on the tip. Inset shows a pre-fabricated hole on the tip of CNT will help in the wire size control; providing a geometry pattern to the nanowire. 18

Figure 2.7: The generation of super fine nanowire by using a Cu@CNT with a hole on the tip. Inset shows a pre-fabricated hole on the tip of CNT will help in the wire size control; providing a geometry pattern to the nanowire. 19

Figure 2.8: The process shows the competition between electromigration force and thermal gradient force during the mass transportation process. When the bias reached 2.2 V, the inner mass was separated in the center and transferred to the two ends, formed a "gap". As the center of the nanotube was presumed to be the high-resistance point, or "hottest spot," the thermal gradient force in turn diverted from the center towards the two ends; therefore, the inner mass split process is obviously attributed to the actuation of temperature gradient force. By further adding the voltage at 0.1 V intervals until the external bias reached 2.5 V, it can be noted that with the reinforcement of electromigration effect, the mass is transferred from the upper part to the lower part in an average rate of 2.2 ag/s. 20

Figure 2.9: The mass flow rate study on a Cu@CNT combined with a network reservoir. The relation between the transferred mass and time inside the tube was given as: $m = 0.0168t^2 - 0.0681t + 1.9971$. Thus, the flow rate was expressed as: $dm/dt = 0.0336t - 0.0681$, indicate a linearly accessed mass flow. 21

Figure 2.10: The modeling of the mass transport. 22

Figure 2.11: The process analysis of NFP "writing". During the "writing", the mass flow rate changes along the acceleration current. Insets show the representative TEM images at different acceleration current and the current curve shows a remarkable regular staircase with step sizes of

about 1.2 μA as the driven bias increased on the step of 0.2 V. The size of the generated nanowire is comparable to the diameter of tube. 23

Figure 2.12: The simulation of the mass flowing out process. 24

Figure 2.13: The simulation of the thermal distribution along different sized NFP. It shows that the nanotube with small diameter has higher temperature than the one with large diameter. 25

Figure 2.14: Correlation of the NFP diameter *D* with the external electric energy. 26

Figure 2.15: The crystalline phase analysis of as-generated nanowire. Due to the molten state at the connection between the deposit and the injector, it provides possible to shape the deposited structures. 27

Figure 2.16: The applications of NFP on (a) The writing process of the Letter "N". By manually positioning the molten copper onto the probe can freeze it immediately, and thereby construct the nanostructure as depicted a stick figure, (b) The writing process of the Letter "L". 28

Figure 2.17: The demonstration of using different sized CNTs to generate nanostructures. 29

Figure 2.18: The demonstration of the modulating of deposits by adjusting the position of injector. The original diameter of nanotube is about 47.2 nm; however, the diameter of deposited nanowire is 85.3nm, which is much larger than the size of nanotube. 29

Figure 2.19: The NFP reloading. (a) The reloading in a NFP with a lower inputted energy, the process lasts for 74 s. (b) Current-time characterization about reload process with different inputted energy. (c) The reloading process with higher electrical energy, the reload process lasts for 6 s. 31

Figure 2.20: The simulation of the thermal distribution along a CNT as the external bias increased. 32

Figure 3.1: (a) Conventional two-terminal measurement, (b) Conventional four-terminal measurement. 34

Figure 3.2: (a) Sliding probe methods for *in situ* electric property characterization. By contacting a probe to different points (P_0 (tip), P_1, …, P_n (root)) on an individual nanostructure, the resistance of the nanostructure is measured. (b) The equivalent circuit of the measurement loop, where R_H, $R_{H\text{-}S}$, R_S, and $R_{S\text{-}P}$ represents the resistance of the sample holder, the contact resistance of the sample holder to the sample (a nanostructure), the resistance of the sample and the contact resistance of the probe to the sample, respectively. The method can be used to investigate a variety of nanostructures, particularly suitable for local transport measurement for a hetero-structure. 35

Figure 3.3: (a) A hetero-structure, (b) A structure with local defects/doping, (c) A non-uniformed nanostructure. 37

Figure 3.4: Multipoint continuous sliding or differential ($n \rightarrow \infty$) sliding, together with flexible probes. 38

Figure 3.5: Multipoint continuous sliding or differential ($n \rightarrow \infty$) sliding, together with specimen shape-adapting. 39

Figure 3.6: The corresponding TEM image for the TaC nanowire sliding probe characterization. A STM probe contacts to the tip (a) and the root (b) of the nanowire in two measurements, respectively. 40

Figure 3.7: (a) *I-V* characterization and the resistance curve of a TaC nanowire using the sliding probe method. A bias is applied between the sample holder and the probe and swept from -500 mV to 500 mV. The resistance is found from the slope of the linear *I-V* curves. The resistance here is calculated to be 93.9 Ω (bias: -500mV to -100 mV and 100 mV to 500 mV) in average, (b) characterization and the resistivity curve of a TaC nanowire using the sliding probe method. As the diameter of the nanowire is 290.2 nm and the length of it is 9.8 μm, the *I-V* resistivity of it is calculated to be 63.6 ± 0.8 μΩ·cm (bias: -500 mV to -100 mV and 100 mV to 500mV) in average. 42

Figure 3.8: The corresponding TEM image for the sliding probe characterization of carbon microfiber. A STM probe contacts to the tip (left), center (mid) and the root (right) of the microfiber with three measurements taken, respectively. 43

Figure 3.9: (a) *I-V* characterization and the resistance curve of the carbon fiber. A bias is applied between the sample holder and the probe and swept from -500 mV to 500 mV. The resistance is found from the slope of the linear *I-V* curves. The resistance here is calculated to be 32.3 kΩ from tip to mid and 11.1 kΩ from mid to root (bias: -500 mV to -100 mV and 100 mV to 500 mV) in average, (b) *I-V* characterization and the resistivity curve of the carbon fiber. The diameter of the carbon fiber from tip to mid is 297.6 nm and the length of it is 29.7 μm.The diameter from mid to root is 297.6 nm and the length is 23.8 μm. The resistivity of it is calculated to be 0.2-0.7 Ω·cm and 0.1-0.2 Ω·cm (bias: -500mV to -100 mV and 100 mV to 500 mV) respectively. 45

Figure 3.10: (a) The copper-filled CNT and the probe, (b) Soft probe fabrication. By using the EMBD, a copper stick is deposited on the tip of probe, and the stick is served as a new probe to acquire more accuracy. 46

Figure 3.11: The differential sliding to a single CNT, the probe sliding on a copper filled carbon nanotube in a uniformed speed (about 10 nm/s) under the bias of 500 mV, the resistance of it along the moving direction is found during the sliding process. 47

Figure 3.12: The *I-t* curve recorded by differential sliding method. During the sliding, the current value steadily decreased along the length of CNT, described precisely about the increasing of resistance. 48

Figure 3.13: The impacting test of a CNT. The blue line is a reference line to the CNT, and the red line shows the top position of it. The distance between the tip of the CNT and the reference line before the impact is 5.14 nm. After the impact, the distance increased to 8.82 nm. Therefore, the deformation here is 3.68 nm, and the correspondent impact force is 187.8 pN. According to the change of resistance during this approach is 0.95 kΩ, then the parameter δ is calculated as 5.07 Ω/pN. 49

Figure 3.14: The resistance versus length curve during the sliding process. The *R-L* curve represents the resistance before the elimination of the impact force influence versus the length of CNT, which can be fitted by a one-order curve with the appropriateness of 0.8211. After the elimination of the impact force influence, the correspondent R_{ei}-*L* curve has an improved fitted appropriateness of 0.9376. 50

Figure 3.15: Shape adapted probe fabrication. By repeatedly attaching the CNT to the copper stick, the deposited copper tip would be reheated and reshaped to a perfectly adapted shape of the tip to the specimen. 51

Figure 3.16: The shape adapted sliding process, which may improve the accuracy by keeping a constant contact resistance. 52

Figure 4.1: (a) The setup of EBIB, (b) Time-resolved EBIB processes. 57

Figure 4.2: Time sequences of bubbling differed at different current densities and tube sizes.... 58

Figure 4.3: As the e-beam exposure suddenly stopped during EBIB, the squeezed-out metal recrystallized and resulted in a facet shape. 59

Figure 4.4: The schematic of the electromigration-based bubbling. 61

Figure 4.5: A sphere on the tip formed by EMBB (a) Before the EMBB process, (b) As-formed bubble. 62

Figure 4.6: EMBB processes. The tip of Cu@CNT was physically contacted with the probe. Applying a voltage between the probe and the sample holder establishes an electrical circuit through a CNT and injects thermal energy into the system via Joule heating. By increasing the applied voltage, the local temperature can be increased past the melting point of the copper encapsulated in a tube. Then, the encapsulated materials may deliver from the carbon shells, and nanospheres are bubbled over the CNT tips in a short time (16.87 s). 63

Figure 4.7: (a) I-V characterization before and after the flowing. (b) I-t characterization during EMBB. 64

Figure 4.8: The sphere on a nanotube induced by a small probe. The small size of the probe makes it possible to keep thermal energy on the particle, which makes it remain in molten state and shape the particle into a perfect sphere. By separating the molten sphere from the probe, the spherical shape was kept. 65

Figure 4.9: (a) The EMBB with a large probe serving as a large heat sink; (b) The EMBB with a probe serving as a small heat sink. 66

Figure 4.10: (a) The copper sphere on a nanotube induced by a CNT which served as a small heat sink. Inset illustrates that the cooledsphere shows a single crystal diffraction pattern, (b) Reheating/remelting can be achieved by placing the sphere on the tip of CNTs. Insets show the transformation of the sphere from single crystal to poly crystal, which represents the gradual melting process. 67

Figure 4.11: (a) A metal layer on the object surface is necessary to form the electrical circuit for EMBB. (b) By using a probe attached to the side wall of the m@CNT, the surface of the object can made either conductive or insulating. 69

Figure 4.12: (a) TEM images recorded the EMBB using the configuration shown in Figure 2.2.11(b). The initial mass inside the CNT is estimated to be 5.7 fg at 0 s. At 663 s, 4.4 fg (77.2%) has deposited while the rest mass evaporated and/or diffused onto the surface of the probe. It can be seen that at 0 s, there was an empty section close to the tip of the CNT, which was filled up at 420 s; showing that the flow started inside the CNT. The extra sphere at the CNT tip was a result of that. The fact that the transport direction was pointing to the CNT tip confirmed that the electromigration is responsible for this flow. Then, at 480 s, the volume of the sphere at the CNT

tip decreased as a result of evaporation. There was no obvious change occurred till the moment at 650 s. At 660 s, within 3 seconds, the CNT was drained off and a large sphere formed on the CNT tip. Because the distance between the deposit and the probe is small and the contact between the probe and the CNT was not firm, the CNT slide back and the deposit dropped onto the probe, (b) The current-time curve recorded during the whole process. The peak at 360 s represent that the contact resistance between the probe and the CNT improved, which was caused by relative slipping of the probe and the CNT. Before and after that moment, no obvious changes of the current have been observed. During the same period, no remarkable mass flow has occurred according to the video. When the flow started at 660 s, an abrupt inflation of the current has been monitored, in the meantime, the CNT was drained off and a large spherical deposit (diameter: 37.5 nm) appeared at the CNT tip..... 70

Figure 4.13: (a) The experiment setup for the EMBB on the surface with excellent electric and thermal conductivity, (b) The experiment setup for the EMBB on the surface with resistive surface, (c) The processes for the EMBB against a conductive surface (an Au-coated W-tip), (d) The processes for the EMBB against a resistive surface (an empty CNT)..... 71

Figure 4.14: (a) TEM images (frames of a video) of EMBB against a thermal conductive surface; (b) Current density vs. time curve of the EMBB process. 73

Figure 4.15: EMBB processes on a thermally/electrically resistive object. (a) Metal flows out from a copper-filled CNT, (b) A spherical deposit on the tip of a CNT by EMBB, (c) EMBB shape control process, (d) Modified nanostructure on the tip..... 75

Figure 4.16: (a) EMBB process recorded by video, (b) Current density vs. time curves for EMBB. 76

Figure 4.17: (a) Shape control process recorded by video, (b) Current density vs. time curves for shape control. 77

Figure 4.18: A model of a sphere-on-pillar optical nano-antenna. 78

Figure 4.19: Electric field strength in the center of the gap as a function of the wavelength for various CNT lengths. Some of the resonant wavelengths for the paired structures are indicated with corresponding arrows..... 79

Figure 4.20: A pair of sphere-on-tip nanostructures fabricated by EBIB. Inset shows a pair of m@CNTs positioned together before EBIB is performed..... 80

Figure 4.21: EELS excitation on the volume center and the surface of a sphere (Refer to Figure 2.1.20 for the positions that the electron beam focused on). The inset shows the eV peak at a magnification of 10x at 10 eV. 81

Figure 5.1: Proposed structure and the decrease in separation as the nanowire subjected to external buckling force. E_1 and E_2 are the Young's modulus of the insulating and metallic regions respectively; δ_0 is the initial separation between the metallic regions; δ is the separation between the lower edges, θ is the angle of rotation of the plane of the metallic region and α is the terminal deflection angle under the action of force; D and d are the outer and inner diameters of the core-shell structure..... 84

Figure 5.2: An expanded schematic for the geometric analysis to obtain relation between separation and angle of rotation..... 85

Figure 5.3: Normalized deformed axes of the nanowire corresponding to terminal angles of α = 20, 40, and 60°. 87

Figure 5.4: Strain-gap separation characterization obtained from nanowire with different initial width of 0.8 nm. 89

Figure 5.5: Potential profile of the metal-insulator-metal junction under the application of a low bias V. Φ_B is the average barrier height. E_F and W_F are the Fermi energy and the work function of the conductive material respectively. 90

Figure 5.6: (a) Influence of nanorod diameter d on tunneling current density. D = 20 nm and d ranges from 1 to 19 nm. (b), Influence of initial separation δ_0 on tunneling current density. δ_0 ranges from 0.7 to 0.8 nm. (c), Influence of nanowire length l on tunneling current density. l ranges from 200 to 600 nm. (d), Influence of work function W_F on tunneling current density. W_F ranges from 4 to 5 eV..... 92

Figure 5.7: SEM image of the as-synthesized sample. 93

Figure 5.8: TEM image of the nanowires. Discrete nanorods with the unique cavity structures can be seen in the nanowire, as shown in the close-up view in the inset..... 94

Figure 5.9: (a) TEM image of a single nanowire with a catalyst particle on the tip. (b) The corresponding scanning transmission electron microscope (STEM) image of (a). (c)-(f) Respective element distribution maps of B, C, Ni and Si. 95

Figure 5.10: XRD pattern of the B_4C peapod nanostructures. The inset is a representative EELS spectrum taken from the nanostructure. 96

Figure 5.11: (a) A representative HRTEM image of the B_4C peapod nanostructure. (b) The close-up view and the corresponding FFT pattern (the inset) of (a). The electron beam irradiation direction is along [010] of B_4C. (c), The close-up view and the corresponding FFT pattern (the inset) of (a), showing that the embedded nanorods are Ni_6Si_2B. 96

Figure 5.12: In situ buckling and electromechanical characterization of a B_4C peapod nanostructure inside a TEM. (a) An STM built in a TEM holder serves as a nanomanipulator. (b) Experimental setup. A conductive AFM cantilever was installed on the specimen holder using a 0.35 mm thick Au wire and was used to characterize the nanowires and measure the force applied on the nanowire. 97

Figure 5.13: The buckling process recorded by TEM images: stressing (a)-(f), releasing (g)-(l). 98

Figure 5.14: Schematic drawing of the nanowire before and after buckling. 99

Figure 5.15: Relation between strain and the change of the inter-nanorod separation. 100

Figure 5.16: Relation between the strain and the inter-nanorod separation. 100

Figure 5.17: Schematic drawing of a position/force sensor based on an encapsulated B_4C peapod nanostructure. 101

Figure 5.18: *I-V* properties show the positive piezoresistivity of the nanowire, i.e., as the nanowire undergoes stress, current increases under a constant bias (140 V). 102

Figure 5.19: $\Delta L/L$-$\Delta R/R$ curves show that the average nominal gauge factor is 8.0..... 103

Figure 5.20: Position sensing using a nanowire. The end of the nanowire on the STM probe was moved toward the AFM cantilever, whereas the position was determined from the STM controller. The curves show the variations in the current and resistance with changes in position. 104

Figure 5.21: Force sensing using a nanowire. The force is calibrated using an AFM cantilever by monitoring its deflection and can be determined through either the current or the resistance. The curves show the first eight points for the process of "Stressing 2". 106

Figure 5.22: Force/displacement sensing with inter-nanorod tunneling effect in a B_4C peapod nanostructure. The stressing process recorded with TEM images..... 106

Figure 5.23: A HRTEM image shows that the inter-nanorod separation δ under the external stress can be smaller than 1 nm, which is appropriate for tunneling. 107

Figure 5.24: The relation between the current and the strain of the nanowire. The inter-nanorod current increases with the increase of external force at different rates under an external bias voltage of 25 V. At the low-stress stage, the current increases approximately linearly to the external force, and the strain-current curve is fitted by $I = 0.0741\varepsilon - 0.8626$. However, starting from the point h on, the current jumps abruptly and increases with a quasi-exponential trend to the external force. This abrupt increase and the quasi-exponential trend strongly suggest that inter-nanorod tunneling occurred. In this case, the current force curve in the high strain region (point h-j) fits well with an exponential curve well: $I = 1E\text{-}04e^{0.121\varepsilon}$. 108

Figure 5.25: Relations between the strain and the natural logarithm value of current in the B_4C nanostructures with different inter-nanorod gap distances. All curves fit with the linear trends, thus show the quasi-exponential relations. 109

Figure 6.1: The fabrication of CuO NW (a) The non-flaking nanowire arrays were grown on the surface of the copper substrate after 2-hour incubation in a box oven at 500℃. Inset I shows the detailed image of a single nanowire. Inset II shows that as-fabricated nanowires are distributed in the substrate at a high density of about 4~6 wires per 100 square nanometer. (b) HRTEM image indicates an inter-planar spacing of 2.53 Å of the nanowire. 113

Figure 6.2: (a) A single wire was picked up by a probe using a nanorobotic manipulator installed inside a scanning electron microscope (SEM), (b) The selected nanowire was fixed on the probe by using focused-ion-beam chemical vapor deposition (FIB-CVD), (c) The setup for the electrical characterization of a single CuO NW. 115

Figure 6.3: E-beam-based forming. The schematic of the e-beam-based and the insulator behavior of the original CuO NW was changed to memristive switching character during forming process..... 116

Figure 6.4: The gradual forming process of the CuO NW demonstrated by using TEM..... 117

Figure 6.5: The resistive switching behavior as δ= 13.5 nm. 118

Figure 6.6: The resistive switching behavior as δ= 200 nm. 118

Figure 6.7: The resistive switching behavior as δ= 375 nm. 119

Figure 6.8: The relation between the switching intensity ε and the forming length δ is: $\varepsilon = 0.0008\delta^2 + 0.0082\delta + 1.0036$. 119

Figure 6.9: The characterization of the deoxidized segment. The Cu $L_{2,3}$ edge spectra of the nanowire at point B before and after the electron irradiation, with standard Cu^{2+} and Cu^{1+} spectra superimposed as references. Before the irradiation, the Cu spectrum is coincided with Cu^{2+} very well, proving its 100% CuO composition. The spectrum after the e-beam irradiation shows an intermediate state between the Cu^{2+} and the Cu^{1+}. We termed the state as CuO_{1-x} (a mixture of Cu_2O and CuO). 121

Figure 6.10: The Cu $L_{2,3}$ edge spectra of an unirradiated area at point A before and after the electron "set" process. The higher L_2 peak intensity after the "set" process indicates the presence of more Cu^{1+}, which corresponds to the increase of oxygen vacancies..... 122

Figure 6.11: (a) The model of the nanowire that after the forming process. After the forming of a part of CuO NW to CuO_{1-x}, the oxygen cations are excessive in this segment due to the loss of oxygen atoms. The spectrum at B shows an oxygen vacancies rich performance than the spectrum at point A. (b) The STEM-EEL spectra of the CuO NW after the forming process. The spectra topology represents the distinguish oxygen vacancy density difference along the nanowire..... 123

Figure 6.12: (a) The model of the nanowire after the set procedure (from HRS to LRS). Set procedure: the anode is placed on the part of CuO_{1-x} and the cathode is in the CuO side. As sweeping the bias between two electrodes, the vacancies in CuO_{1-x} part are transport all through the nanowire that drives by the electric force. Meanwhile, the electrons pass through the conductive paths that explored by the cations. Therefore, the conductivity decreased. The gap between the spectrum at point A and point B is narrowed, which indicates the migration of oxygen vacancies from B to A. (b) The STEM-EEL spectra of the CuO NW after the set procedure. The spectra topology clearly indicates the migration of the oxygen vacancies from rich area (B) to the poor area (A)..... 124

Figure 6.13: (a) The model of the nanowire after the reset procedure (from LRS to HRS). To switch from LRS to HRS (reset procedure), the electric force direction was switched according to the alternate of external polar, which in turn broke the conductive path along the nanowire and makes the resistance back to the original high status. The gap between the two spectra opened again, which indicates the reversal migration of the oxygen vacancies from A to B. (b) The correspondent STEM-EEL spectra for the CuO NW after the reset switching process. The reversal of O^{2-} migration is clearly indicated..... 125

Figure 6.14: The application of CuO NW-based memristor as a displacement transducer. (a) The switching threshold voltage V_{th} was decreased according to the increasing of the deformation ratio σ. The displacement of the attached probe is measured by the deformation of the bending wire. 127

CHAPTER 1

INTRODUCTION

1.1 Overview

The pipeline factory that assembles nano-electromechanical systems (NEMS) is no longer a science fiction fantasy. Scientists are now attempting to molecularly manufacture nanodevices in a high-throughput mode. Richard Feynman predicted 50 years ago that one day people would manipulate matter atom by atom by using some sophisticated techniques; today, the nanorobotic manipulator enables the positioning and manipulation of nanomaterials down to nano or even atomic scale, which greatly extends our abilities to explore the "room at the bottom" [1]. With the help of nanorobotic manipulators, researchers have made great progress in several areas such

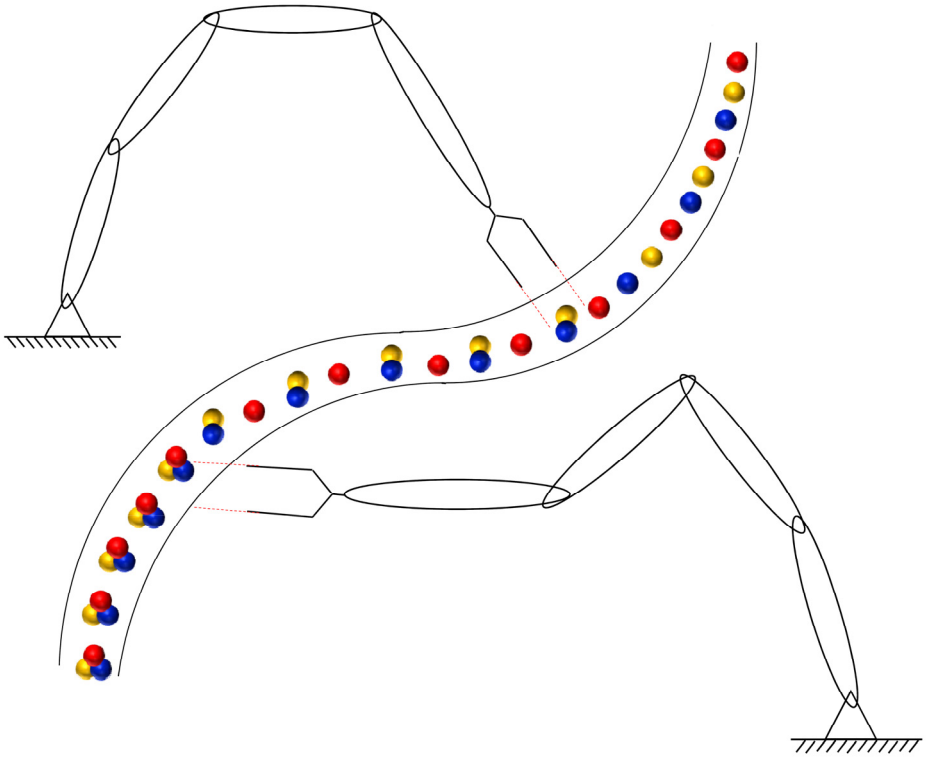

Figure 1.1: Nanorobots work on a pipeline and fabricate nanodevices atom by atom.

as nanomedicine [2, 3], nano-optics [4], nanophotonics [5], and nanofluidics [6, 7]. Researchers have fabricated and assembled sample prototype NEMS devices individually by using manipulators prior to large-scale production [8-10]. Analog to the Fordism production mode, this process resembles the movement from manual production of individual items to a large-scale fabrication mode. We can imagine that an automated nanomanufacturing pipeline will one day fabricate nanodevices atom by atom, as shown in Figure 1.1, like robots making cars in assembly-lines. Because of its advantages of precise position/movement control, the nanorobotic manipulator is a perfect "worker" candidate for future nanomanufacturing pipelines. To date, no suitable nanotools or nanosensors can be used currently for reliable nanorobotic batch fabrication. The conventionally end-effectors we currently uses, such as nanoprobes and nanogrippers are not sophisticate enough to fulfill the requirements of nanomanipulation. In order to build a reliable bridge between the nanorobotic manipulator and the nanoworld, the qualified intelligent end-effectors must come first.

Table 1.1: The end-effector devices and applied techniques

Devices \ Techniques	Manipulation	Deposition	Sliding	EELS	STEM	STEM-EELS	Chemical workstation
NFP	*	*					
Sliding probe	*	*	*				
Optical nanoantenna	*	*	*	*			
B_4C NW-based tunneling	*			*	*		
CuO NW-based tunneling	*			*	*	*	
Memristor	*			*	*	*	
Open-cell *in situ* nanobatteries	*			*	*	*	*

In this report, six types of prototype devices are introduced, including the nanotube fountain pen in Figure 1.2(a); a super-fine nanoprobe for electro/mechanical characterization of nanomaterial in Figure 1.2(b); the metal filled carbon nanotube (m@CNTs)-based sphere-on-pillar (SOP) optical nanoantennas in Figure 1.2(c); the nanowire-based tunneling nanosensor in Figure 1.2(d), the copper oxide nanowire (CuO NW)-based memristor in Figure 1.2(e); and the lithium ion *in situ* nano-battery in Figure 1.2(f). During the research on the end-effectors, several *in situ* techniques are involved, such as nano-manipulation, nanofluidic control, the sliding probe method, electron energy loss spectroscopy (EELS), scanning transmission electron microscopy (STEM), STEM-EELS, and ion migration detecting. In coupling the nano-robotic end-effectors and the *in situ* techniques, the scope of the research area was extended from mechanical testing to composition evolution, and eventually reached chemical reaction analysis. As shown in Table

1.1, the major interests of the investigations of first three end-effectors were nano-manipulation and nanofabrication. In the study of the nanowire-based nanosensor, in which the advanced characterization techniques, such as EELS and STEM were involved in the study of memsensor used as end-effector showed great potentials for detecting the physical changes such as carrier diffusion, that are directly responsible for the device's properties change. Finally, the STEM-EELS characterization technique, which is technique combination of STEM and EELS, played an important role in understanding the tunneling performance of the peapod nanosensor.

In the following section, my progress in the studies of several end-effectors coupled with nanofabrication, nanomanipulation, and advanced characterization method is reviewed in the following section. The potential applications of these end-effectors and associated *in situ* nanotechniques in several disciplines are discussed.

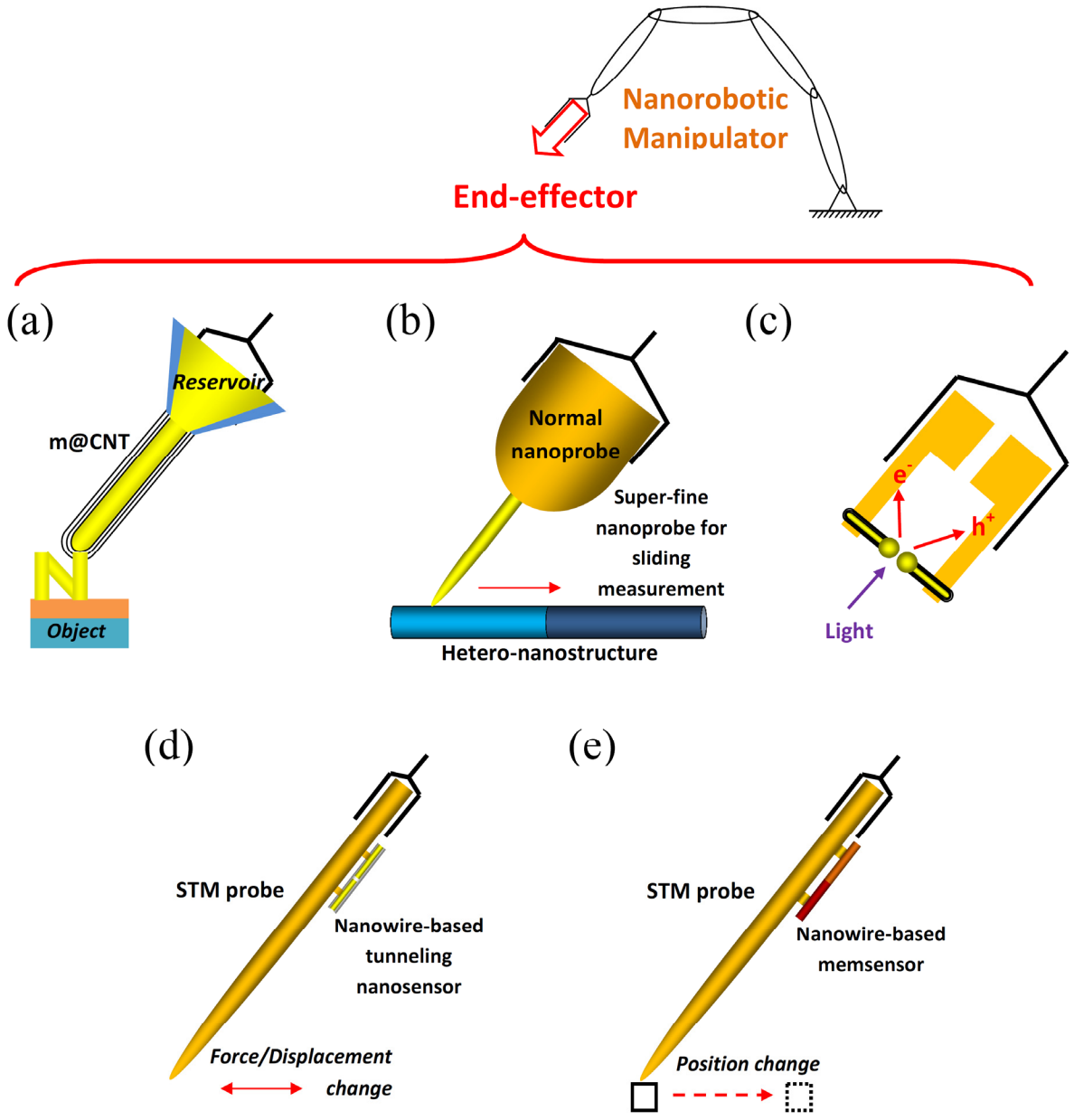

Figure 1.2: Nanorobotic end-effectors: (a) Nanotube fountain pen, (b) Super-fine nanoprobe, (c) m@CNTs-based SOP optical nanoantennas, (d) Nanowire-based tunneling nanosensor, (e) CuO NW-based memristor.

1.2 Work Performed

This section provides a brief introduction to the research described in this dissertation. Chapter 2 through 6 are each devoted to a specific end-effectors. Research on the first three devices focused mainly on nanomanipulation and nanofabrication. In chapter 2, the NFP was developed into a novel additive nanofabrication method that features continuous mass feeding. This technique resolved the mass-shortage problem in the m@CNTs during the mass deposition and allowed the fabrication of three-dimensional (3D) complex nanostructures. The prototype used an m@CNT as a pen-tip injector and a reservoir for continuous mass feeding. The deposition of the metal was based on nanofluidic mass flow from the pen-tip nanotube and the continuous mass feeding was implemented by inter-nanotube mass transport of the encapsulated metals. Experimental evidence showed that the electromigration effect, rather than the thermal gradient force, was the main mechanism of the mass transportation. The switching states ("ON" or "OFF") of the NFP "writing" was realized by drifting of the copper atoms that was induced by external electric energy to overcome the energy barrier and collapse the blocked junction (ON). Additionally, investigation of the "writing" mechanism enabled us to fabricate desired 3D nanostructures in a continuous mode. As a general-purpose nanofabrication tool, the NFP will be the key to improving 3D nanoscale devices, which are of critical importance in the semiconductor industry.

In chapter 3, with the help of NFP, a super-fine nanoprobe with a diameter of several nanometers was fabricated. By using this nanoprobe, a sliding probe method for the *in situ* characterization of electrical property of individual one-dimensional (1D) nanostructures was designed by eliminating the contact resistance between the fixed-end support and the specimen. The key to achieving a high resolution was to keep resistance constant between the end of the

specimen and the sliding probe. To achieve this goal, several techniques were developed: multipoint continuous sliding, flexible probes, and specimen-shape adapting using nanorobotic manipulation inside a TEM. Compared with conventional two- and four-terminal methods, these sliding probe methods allowed *in situ* characterization because of their higher resolution and their greater simplicity in setup. Furthermore, they were superior to local property characterization, which is of particular interest for heterostructured nanomaterials and defect detection.

For the m@CNTs-based SOP optical nanoantennas in the third part, controlled fabrication of metal nanospheres on nanotube tips for optical antennas was investigated experimentally. Resembling soap bubble blowing using a straw, the fabrication process was based on nanofluidic mass delivery at the attogram scale using m@CNTs. Two methods were investigated including electron-beam-induced bubbling (EBIB) and electromigration-based bubbling/deposition (EMBB/EMBD). EBIB involved the bombardment of an m@CNT with a high energy electron beam of a transmission electron microscope (TEM), by which the encapsulated metal is melted and forced out from the nanotube tip, generating a metallic particle on a nanotube tip. If the case that the encapsulated materials inside the CNT have a higher melting point than what the beam energy can reach, EMBB is an optional process to apply. Experiments showed that, under a low bias (2.0 - 2.5 V), nanoparticles can be formed on the nanotube tips. The final shape and the crystalline type of the nanoparticles were determined by the cooling rate. Instant cooling occurred with a relatively large heat sink and caused the instant shaping of the solid deposit, which was typically similar to the shape of the molten state. With a smaller heat sink as a probe, it was possible to keep the deposit in a molten state. Instant cooling by separating the deposit from the probe can result in a perfect sphere. Surface and volume plasmons characterized by

electron energy loss spectroscopy (EELS) indicated that resonance occurred between a pair of the as-fabricated sphere on the tip structures. Such spheres on pillars can serve as nano-optical antennas and will enable devices such as scanning near-field optical microscope (SNOM) probes, scanning anodes for field emitters, and single molecule detectors, which can find applications in bio-sensing, molecular detection, and high-resolution optical microscopy.

In chapter 5, an alignment-free electron tunneling device was modeled. It was characterized by a series of concentric nanowire segments structured as metal-vacuum-metal (MVM) or metal-insulator-metal (MIM) tunneling junctions. The shrink of the nanogap, which occurred when the nanowire buckled, facilitated the electron tunneling current and implied an empirical relation between the gap width and the current strength. This device was implemented by using boron carbide (B_4C) nanowires in which conductive cylindrical nano-segments were covered with an insulating shell and the distance between neighboring segments was limited to sub-nanometer range. Using nanorobotic manipulation, it was discovered that the prototyped device demonstrated the feasibility of the proposed model, and thus introduce a new ground in the investigation of tunneling current.

Chapter 6 describes the *in situ* formation and the characterization of nanowire-based memristors and their potential applications as sensors with memory (memristic sensors or "memsensors" in short). An electro-beam-based forming (EBBF) technique was developed for the actuation of the memristive characters from an individual CuO NW. Meanwhile, in order to correlate transport properties with the carrier's distribution along the nanowire, several *in situ* characterization techniques were applied in this end-effector, such as EELS, STEM, and element energy spectroscopy. All experimental investigations were performed inside a TEM. The initial CuO NW memristors were formed by focusing electron-beam irradiation on nanowire to

generate oxygen vacancies as charge carriers. Current-voltage properties showed distinctive hysteresis characteristics of memristors. The mechanism of such memristic behaviors could be explained by an oxygen vacancy migration model. The presence and migration of the oxygen vacancies were observed with EELS. Investigations also revealed that the memristic behavior can be influenced by the deformation of the nanowire, showing that the nanowire memristor can serve as a sensor capable of memorizing deformation and force. The CuO NW-based memristors would enrich the binary transition oxide family but are simpler and more compact design than the conventional thin-film versions. With these advantages, the CuO NW-based memristors will not only facilitate their applications in nanoelectronics but also play a unique role in micro-/nanoelectromechanical systems (MEMS/NEMS) as well.

1.3 Research Objectives

The overall objective of this research was to advance the characterization of electromechanical properties of several nanomaterials and investigate their future application as nanorobotic end-effectors or nanosensors. As shown in the overview section, the nano-robots are viable candidates for the future pipelines that molecularly reproduce the nano-devices. Nano-robots equipped with high performance end-effectors, could become key to future high-throughput nanodevice fabrication.

The specific objectives of this research were to:

- design an NFP and realize 3D metal printing at the nanoscale or even atomic level.
- fabricate a super-fine nanoprobe using NFP and carry out *in situ* electro/mechanical characterization of the hetero-nanostructure with a higher resolution and in a fast mode than the conventional characterization method.

● develope a SOP optical-nanoantenna from m@CNTs by using EBIB or EMBB (NFP without reservoir).

● develop an alignment-free tunneling nanosensor by using B_4C peapod nanowire or gap-embedded CuO-Cu concentric nanostructure and characterize its tunneling behavior.

● characterize the ion migration along the $CuO\text{-}CuO_{1-x}$ nanostructure by using the STEM-EELS technology.

CHAPTER 2

NANOTUBE FOUNTAIN PEN

The introduction of additive manufacturing (*aka* 3D printing) by Chuck Hull of 3D Systems Corp in the industry marked the advantage of building from bottom up and distributed manufacturing. The printing with metals, treated as final frontier in 3D printing, has achieved remarkable advancement in recent years [11-16]. Compared with conventional metal component manufacturing process that usually lasts from weeks to months and lacks dynamics in product design, 3D printers allow the lean manufacturing of the machine parts, indicating a new revolution in the manufacturing industry. The recent progress in the miniaturization of the electromechanical system raises the question that whether the 3D metal printing can be realized at the nanoscale or even atomic level, which is also the core of bottom-up nanotechnology defined as molecular manufacturing [17].

2.1 Introduction and Design of the Nanotube Fountain Pen (NFP)

At the nanometer scale, different from conventional nanolithographic technologies [18-20], additive nanolithography is a bottom up approach for the fabrication of nanostructures and devices, especially three-dimensional ones, by depositing materials onto a substrate [21-25]. Additive nanolithography typically involves a high energy beam or a scanning probe. Among the beam-based methods, the direct laser writing (DLW) [21] has the advantage of fast prototyping speed, but this technique cannot be used to deposit metal materials. Electron-beam-induced deposition (EBID) [23] and the focused-ion-beam chemical vapor deposition (FIB-CVD) [24] have higher resolution and allow multi-material and high resolution deposition including metals,

but their large energy and longtime consumption limited their applications in the 3D nanodevice batch fabrication. On the other hand, the probe-based additive nanolithographic methods, such as dip-pen nanolithography (DPN) [22] and polymer pen lithography (PPL) [26], are developed with advantages of high throughput and lower energy consumption than the beam-based methods, however, no metallic deposits can be obtainable.

In fact, the 3D metal nanostructure fast prototyping is still a technical challenge for the existing additive nanolithographic methods. Here we propose a NFP for direct writing with metallic "inks". The NFP consists of a reservoir and a nanotube injector to transport metal atoms onto a conductive substrate, forming an arbitrary nanostructure. As a pen-type lithography method technique besides of the availability of metallic structures, a NFP has

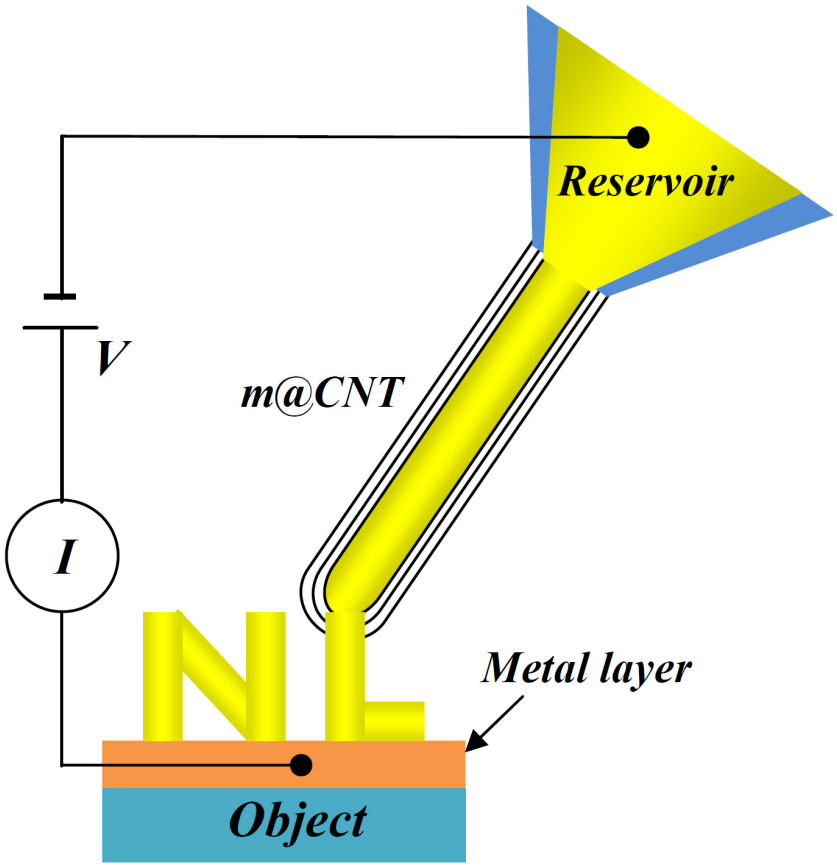

Figure 2.1: The schematic of NFP. By applying a bias, the encapsulated metal can be continuously flowed out for nanostructure fabrication.

the advantage of continuous writing ability as compared with a nanotube pencil [20] and the DPN. This resenbling the development of their macroscale counterparts, from pencils, to dip pens, and fountain pens. In history, dip pens were developed from using inks for leaving permanent records, and fountain pens were invented for continuous writing.

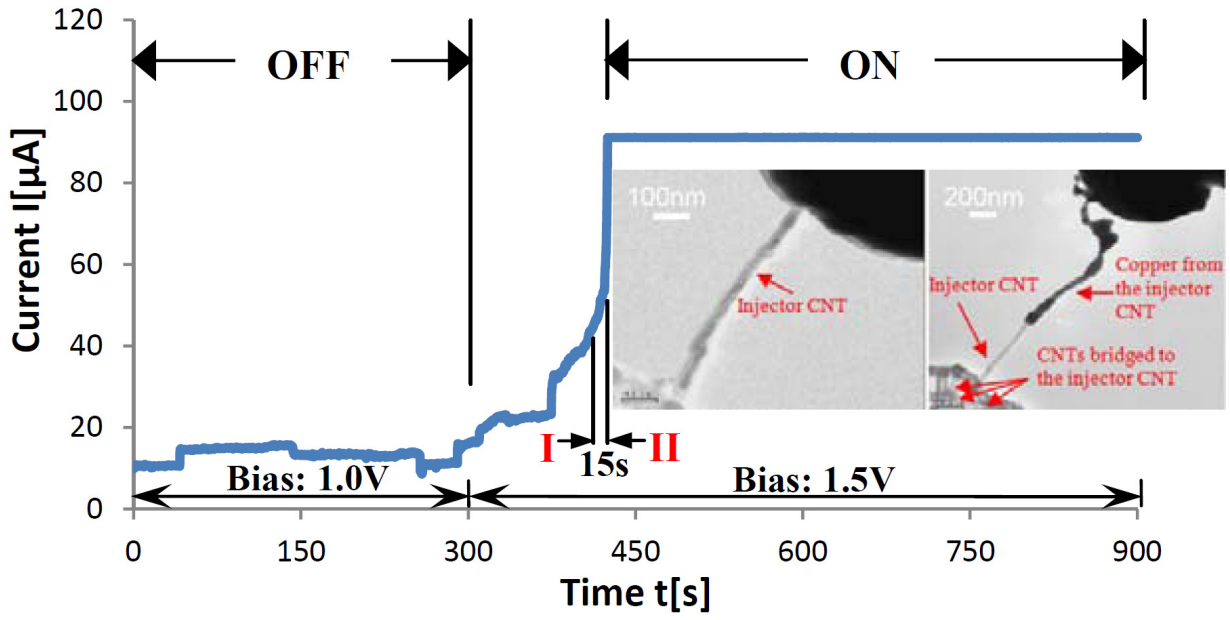

Figure 2.2: *I-t* characterization during the NFP "writing" process. The initial state (0~300) is defined as "OFF" (external bias: 1.0 V) and the state after the mass migration starts as "ON" (external bias: 1.5 V). Insets show the initial mass inside the nanotube injector is 1.9 fg, while the deposited mass is 29.0 fg (about 15 times more than the original mass).

We have experimentally investigated the feasibility of NFP in fabricating complex metal nanostructures from 0D to 3D with a position servo control. Figure 2.1 shows the schematic of NFP, where a single copper-filled carbon nanotube (Cu@CNT) is used as the pen tip, and nanotube networks as a reservoir. The experiments have been performed with a scanning tunneling microscope (STM) built inside a transmission electron microscope (TEM) holder (FM2000E STM-TEM holder (Nanofactory Instruments AB)). The STM is used as a manipulator to manually realize the position servo control. By positioning the tip on a conductive substrate, a circuit can be established between the two ends of the NFP to achieve mass delivery.

Figure 2.2 shows that the copper inside the neighboring CNTs can be sucked into the CNT injector under a stable bias. It has been estimated from the geometry and the density of copper that the initial mass inside the nanotube injector is 1.9 fg, while the deposited mass is 29.0 fg (about 15 times more than the original mass). The extra mass is attributed to those inside the nanotubes attached to the CNT injector.

2.2 Continuous Mass Feeding

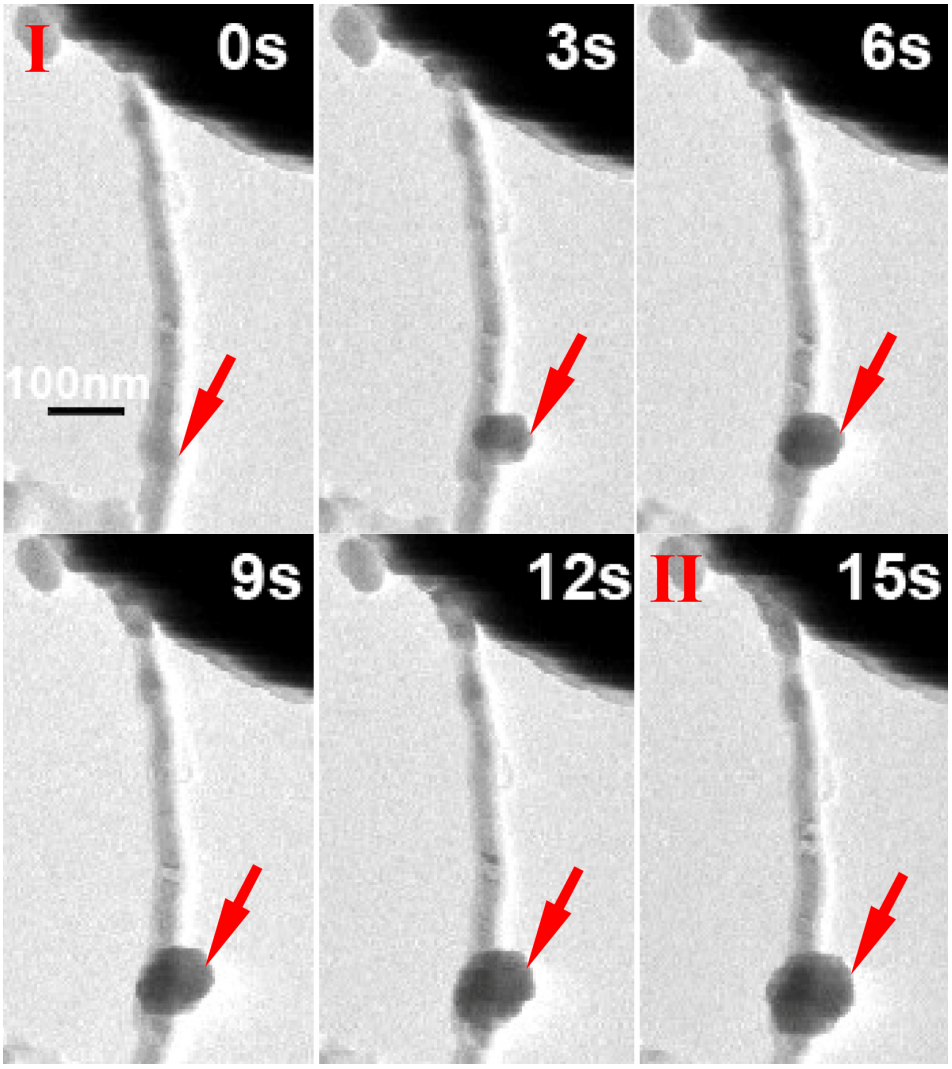

Figure 2.3: Mass accumulation process. The mass is accumulated from the neighbor CNTs.

The current-time (*I-t*) curve during the continuous mass delivery is shown in Figure 2.2. As the bias increases from zero in increments of 0.1 V, the delivery begins after the external bias reaches 1.0 V. The initial state (0~300 s) exhibits a normal CNT electrical property, with a conductivity of 30 μS. The degradation process (starting at 300 s) of the resistance occurs as an external bias of 1.5 V is applied. The sudden increase of the current at 410 s is attributed to the healing of the carbon shells under higher voltage bias [27]. In order to prevent the electric

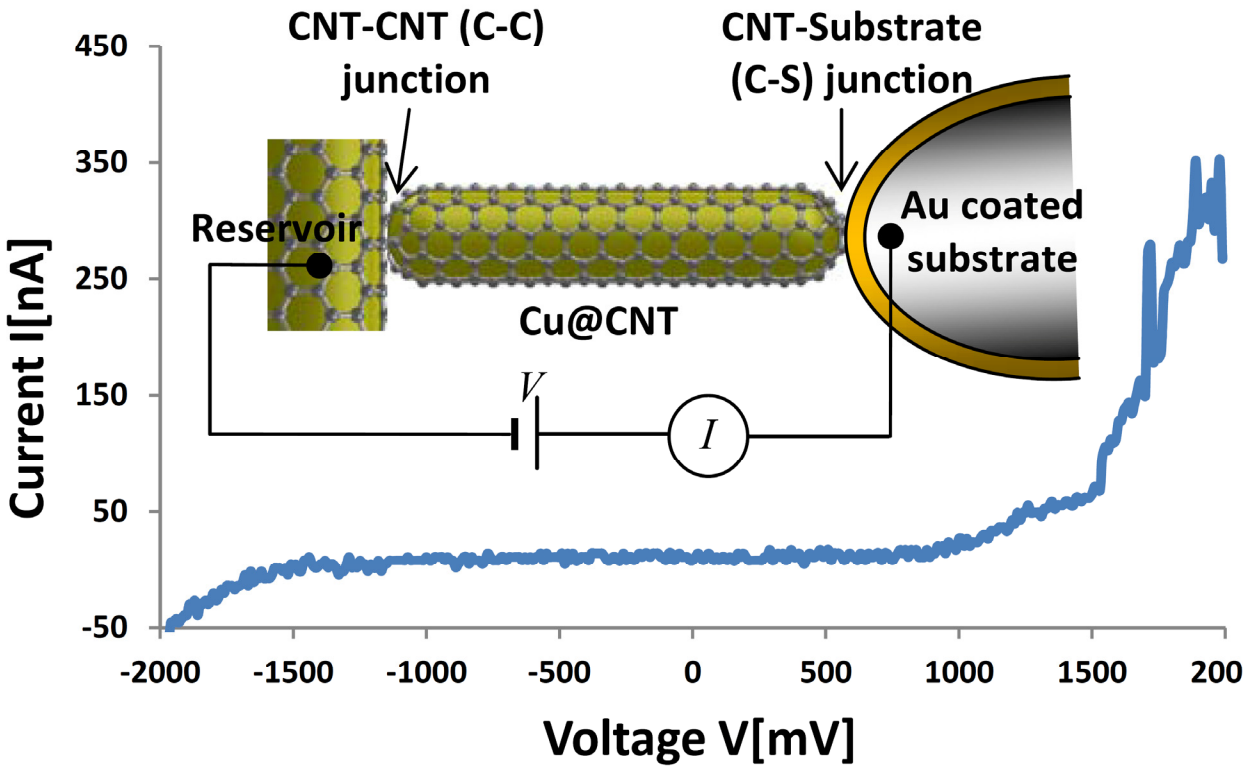

Figure 2.4: The model for NFP "writing". The initial *I-V* curve of NFP in the "OFF" state shows a non-ohmic/charging characteristic. Inset shows the two junctions exist at the two ends of tube.

breakdown of the nanotube [28, 29], the current is restricted to 90 μA. The accumulation of mass from the reservoir takes place while the current sharply increases. The nanotubes serve as bridges to transfer the mass from the neighboring CNTs to the injector and deposit onto the object [7, 30]. Figure 2.3 contains a series of video frames illustrating that the migration begins when the mass is accumulated on the side wall of the tube close to the junction site between the nanotube injector and the network. A mass of 14 fg is transferred from the external reservoir.

To analyze the NFP writing process, we defined the initial state (0~300 s) as "OFF" (external bias: 1.0 V) and the state after the writing begins as "ON" (external bias: 1.5 V). The current-voltage (*I-V)* curves at ON and OFF contain important information for deciphering the nature of mass accumulation and migration. It shows in Figure 2.4 that a non-ohmic/rectifying

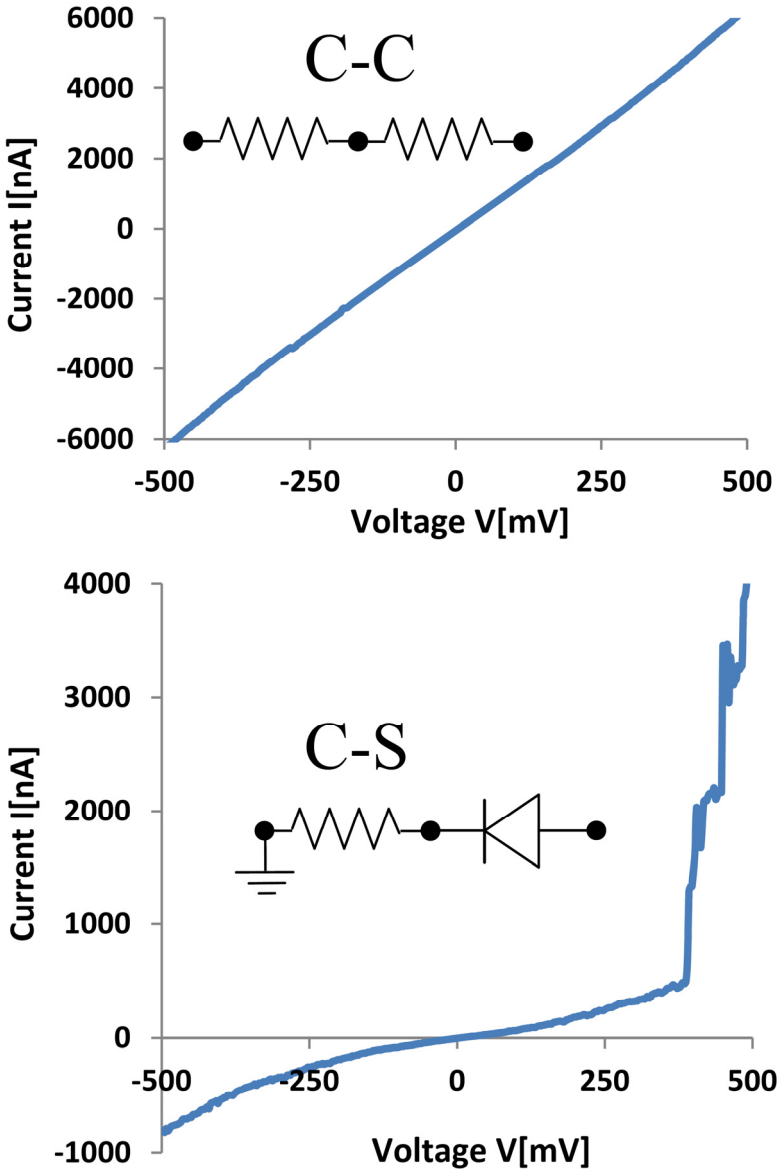

Figure 2.5: The *I-V* curves for the combination of different junctions (C-C and C-S).

contact exists at the CNT injector - Substrate (C-S) interface or the CNT injector - CNT network (C-C) interface. However, it is difficult to identify the specific roles of each interface, as well as the contributions of them to the mass accumulation. In order to distinguish one from each other, we have carried out an experiment to verify the performance of each interface. We used different CNTs to make contact with CNT and Au surfaces, and then obtained the *I-V* curves for each of them. In Figure 2.5, the linear *I-V* curve demonstrates that both the interfaces (CNT network -

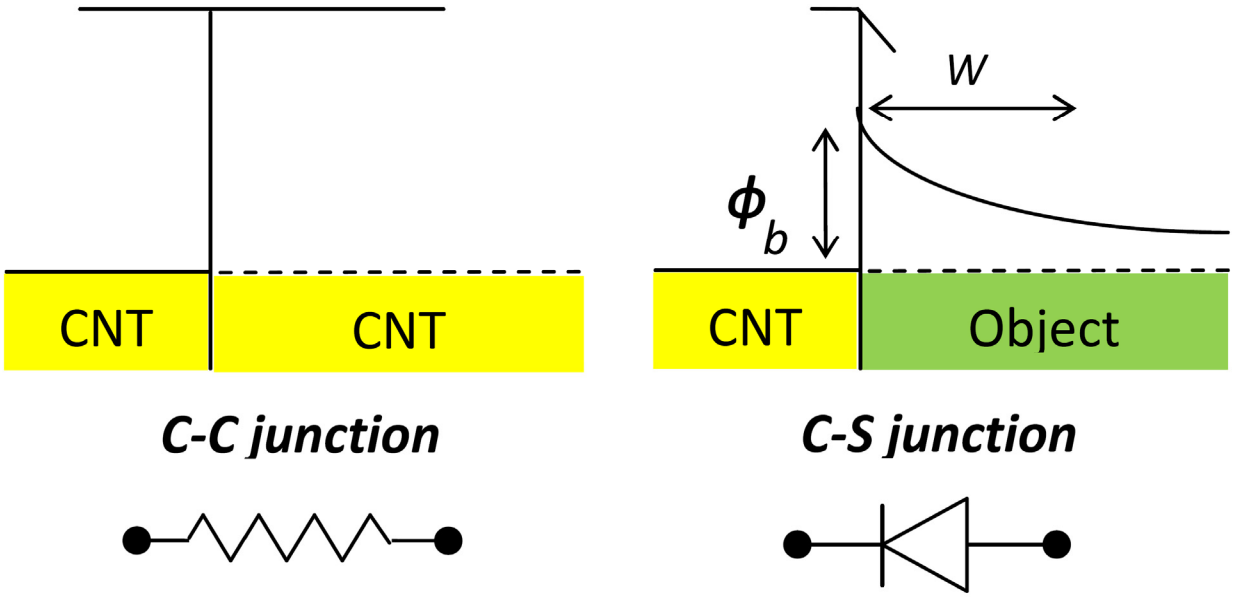

Figure 2.6: The generation of super fine nanowire by using a Cu@CNT with a hole on the tip. Inset shows a pre-fabricated hole on the tip of CNT will help in the wire size control; providing a geometry pattern to the nanowire.

CNT injector, CNT injector - CNT) are ohmic. In contrast, the measurements by using the same injector to make contact with an Au object reveal a non-ohmic characteristic, which suggests there are at least one interface is limited by the non-ohmic transport. Due to the oxidation of the metal (Au) probe as well as the defects that may exist on the CNT surface, there will be an energy barrier between the CNT injector and the Au object surface as illustrated in the energy diagram of Figure 2.6. These defects produce a barrier height and maintain a non-ohmic *I-V* property at lower external energy (OFF) state, which is similar to the *I-V* curve in Figure 2.4. When the bias voltage is increased and the system is turned ON, the non-ohmic junction (C-S) will collapse and shift to an ohmic contact. The previously mentioned metal accumulation process in Figure 2.3 further confirms the junction model: as the current is sharply increased at the transition state between OFF and ON, the electromigration-driven force is increased accordingly (the driving mechanism will be introduced in the next paragraph). As illustrated in

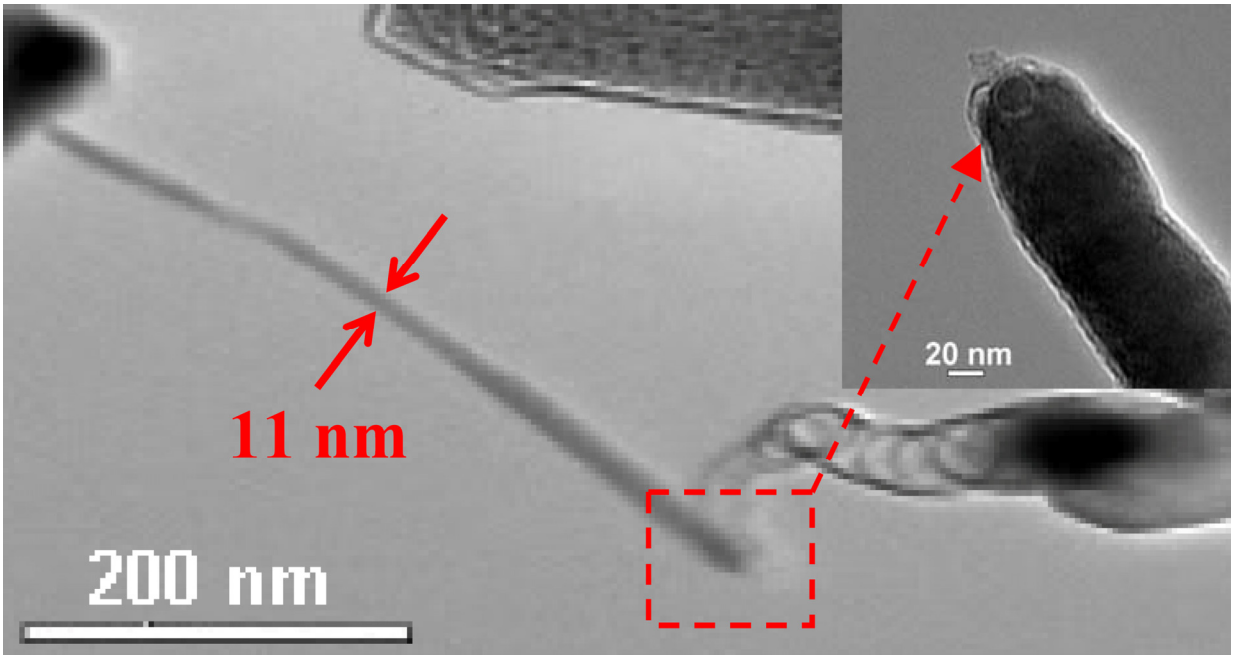

Figure 2.7: The generation of super fine nanowire by using a Cu@CNT with a hole on the tip. Inset shows a pre-fabricated hole on the tip of CNT will help in the wire size control; providing a geometry pattern to the nanowire.

Figure 2.4, due to the equal energy barrier at the C-C junction and the electromigration effect from cathode to anode [31, 32], the mass from the reservoir is continuously migrating into the injector. However, the energy barrier between the C-S junction has not collapsed enough at this time (Figure 2.5(b)); therefore, the C-S junction still not open to mass flow. Moreover, the sealed condition and the increasing pressure caused by the streaming material, the carbon shell is broken at the highest pressure position. Comparing the *I-V* curves at ON and OFF states, we conclude that in the OFF state, the C-C junction is ohmic and C-S junction is rectified. In the ON state, the blocked junction collapsed and enables the transport. Here, a question may arise about the junction model: What is the sequence of an initially opened C-S junction? We have carried out an experiment to obtain the answer. In Figure 2.7, a Cu@CNT with a hole was selected as starting material for the "writing" test. Due to the direct contact between the inner metal and the probe surface, the blocked junction is released at the beginning. During the "writing" test, there

is no transition between the OFF and ON state and the writing begins instantaneously when the contact is made, producing a superfine metal nanowire. Additionally, the generated nanowire has the diameter of 11 nm, which is comparable to the hole diameter of 19 nm, as shown in the inset of Figure 2.7. The writing tests demonstrate the possibility of fabricating a superfine metal nanowire with the diameter controlled by a pre-fabricated hole, which promises the potentials to reduce the diameter of nanowire down to a few nanometers, or even a single atom chain.

2.3 Mechanism Analysis of the Inter/Intra Nanotube Mass Flow

The question that remains is which effect drives the mass flow. Several former researchers have investigated the fundamental mechanism of the mass migration and have showed that the electromigration effect and the thermal gradient effect are the main driven forces of the mass

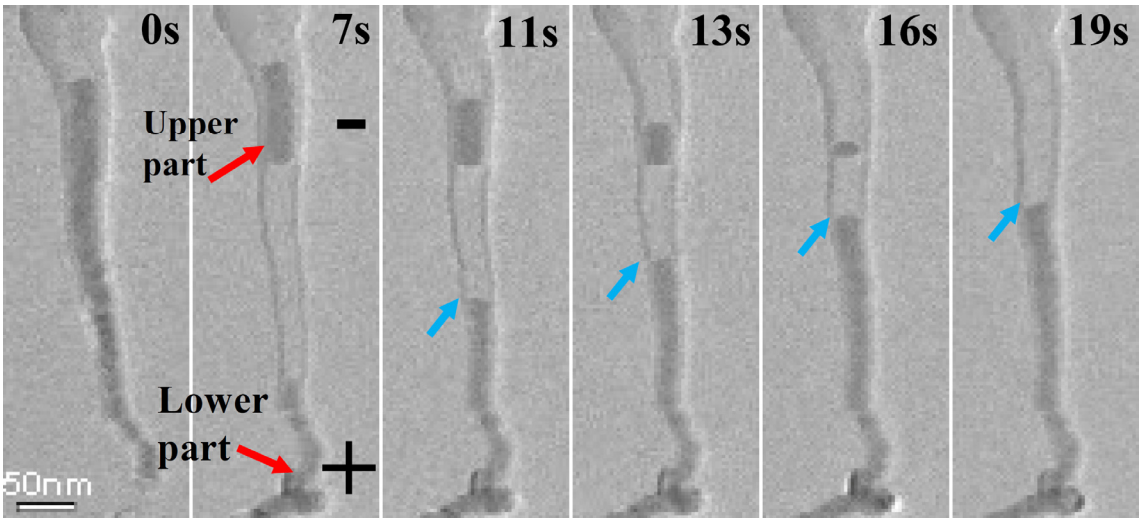

Figure 2.8: The process shows the competition between electromigration force and thermal gradient force during the mass transportation process. When the bias reached 2.2 V, the inner mass was separated in the center and transferred to the two ends, formed a "gap". As the center of the nanotube was presumed to be the high-resistance point, or "hottest spot," the thermal gradient force in turn diverted from the center towards the two ends; therefore, the inner mass split process is obviously attributed to the actuation of temperature gradient force. By further adding the voltage at 0.1 V intervals until the external bias reached 2.5 V, it can be noted that with the reinforcement of electromigration effect, the mass is transferred from the upper part to the lower part in an average rate of 2.2 ag/s.

flow [6, 33-37]. These two effects were also observed in the NFP writing process. Figure 2.8 shows the mass delivery inside a NFP without the reservoir. When the external bias reaches 2.0 V (0 s), the dark contrast and the boiling sign indicate the molten state of the copper wire. As the voltage is increased to 2.2 V (7 s), the mass in the center suddenly evaporates, clearly revealing the thermal effect [27]. Nevertheless, by further increasing the voltage in 0.1 V increments until the external bias reaches a higher value (2.5 V, 11s), the mass begins to migrate from the upper part to the lower portion of the tube, following the direction of the electromigration force. As we carried out the same experiment using a nanotube attached with a reservoir, the process is similar to the previous experiments; initially, the mass in the center evaporates and then flows from the anode to the cathode. When the reservoir is added on the bottom, the mass from the reservoir could continuously migrate into the nanotube and finally fill the gap between the upper and lower portion. Figure 2.9 illustrates that the relation between the transferred mass and time

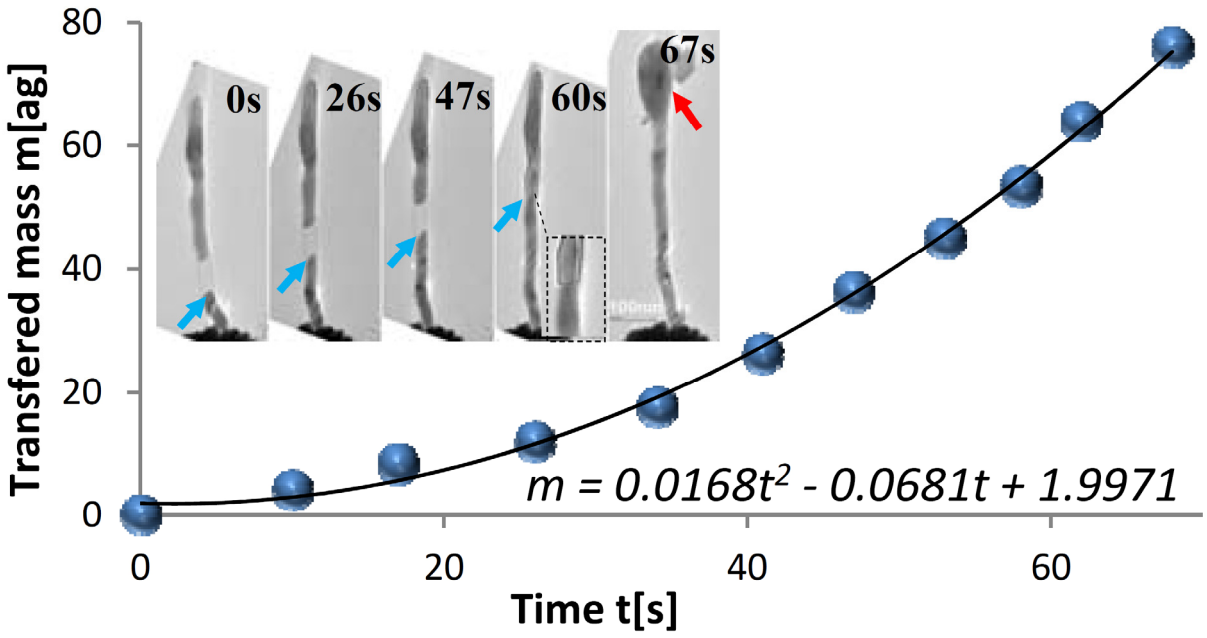

Figure 2.9: The mass flow rate study on a Cu@CNT combined with a network reservoir. The relation between the transferred mass and time inside the tube was given as: $m = 0.0168t^2 - 0.0681t + 1.9971$. Thus, the flow rate was expressed as: $dm/dt = 0.0336t - 0.0681$, indicate a linearly accessed mass flow.

inside the tube is given as: $m = 0.0168t^2 - 0.0681t + 1.9971$. Thus, the flow rate is expressed as: $dm/dt = 0.0336t - 0.0681$, indicating a linear mass flow.

Based on the experimental observations, we propose a general model in Figure 2.10 to elucidate the dynamics during the mass flow. At the beginning of the mass evaporation process,

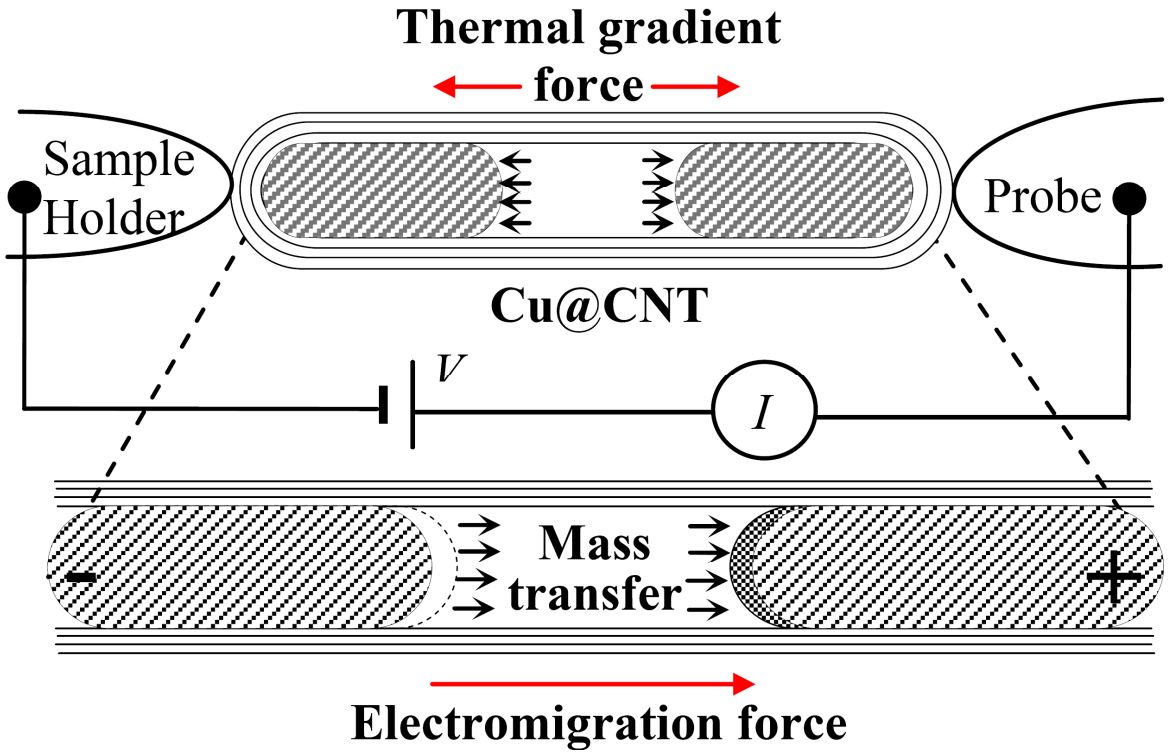

Figure 2.10: The modeling of the mass transport.

the NFP is in the OFF state. Thus the low profile current in turn produces a lower electromigration force. If we assume the mass migration is driven by this effect, the mass in Figure 2.8 and 2.9 should consistently move from cathode to anode; however, the mass evaporates in the center is not moving in the single direction. Because the center of the nanotube is always the hottest spot [27, 29, 38], part of the mass was evaporated and diverted from hot part to the cold part by thermal gradient force. At the transition between the OFF and ON state, the

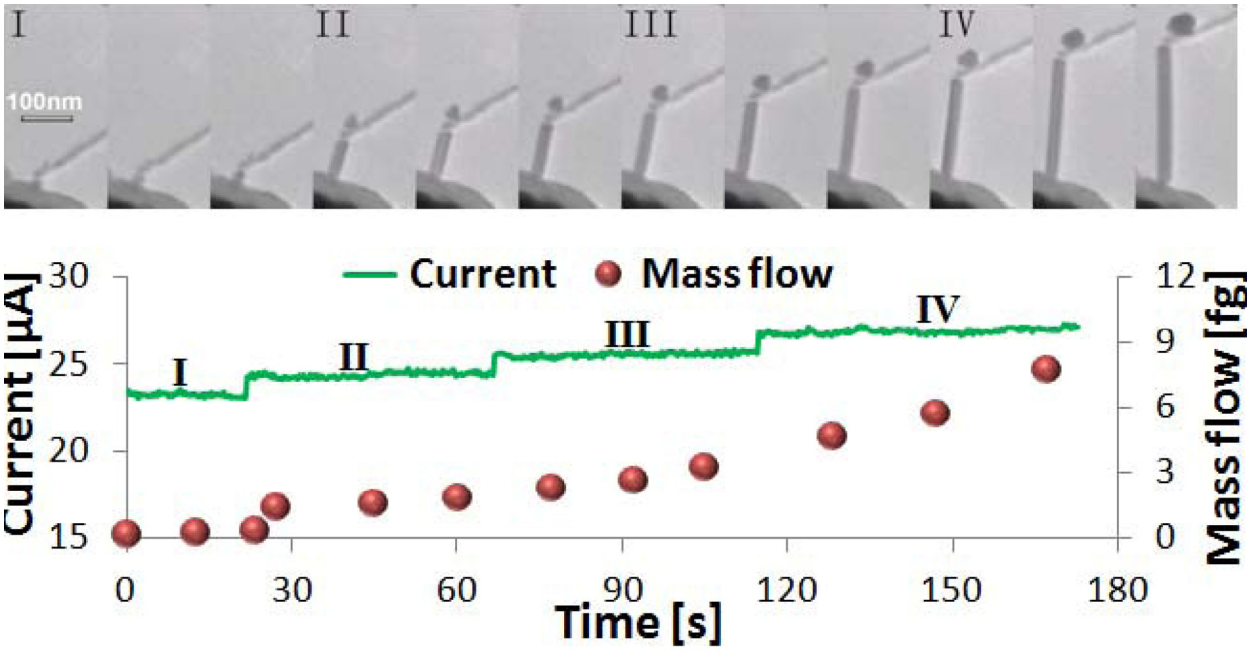

Figure 2.11: The process analysis of NFP "writing". During the "writing", the mass flow rate changes along the acceleration current. Insets show the representative TEM images at different acceleration current and the current curve shows a remarkable regular staircase with step sizes of about 1.2 μA as the driven bias increased on the step of 0.2 V. The size of the generated nanowire is comparable to the diameter of tube.

current sharply increases, and the electromigration force is reinforced and overcomes the thermal force, which plays a dominant role in migration. As a result, the mass ultimately flow from cathode to anode. Finally, as the blocked junction at the C-S interface collapses during the ON state, the mass is able to leave the tube.

The NFP mass flow rate also shows a linear correspondence to the applied current after the system reaches the ON state and begins writing. Figure 2.11 shows that when the driven bias increases at increments of 0.2 V, the current curve shows a remarkable regular staircase with step sizes of about 1.2 μA, and the mass flow rate is also accelerated. In addition, inset demonstrates that the diameter of a deposited nanowire (17 nm) is comparable to the diameter of the tube (18 nm) in Figure 2.11. Indeed, all the nanowire we have produced has a similar size to the original tube. We assumed that, as the block at the C-S junction is released, the copper atoms would pass

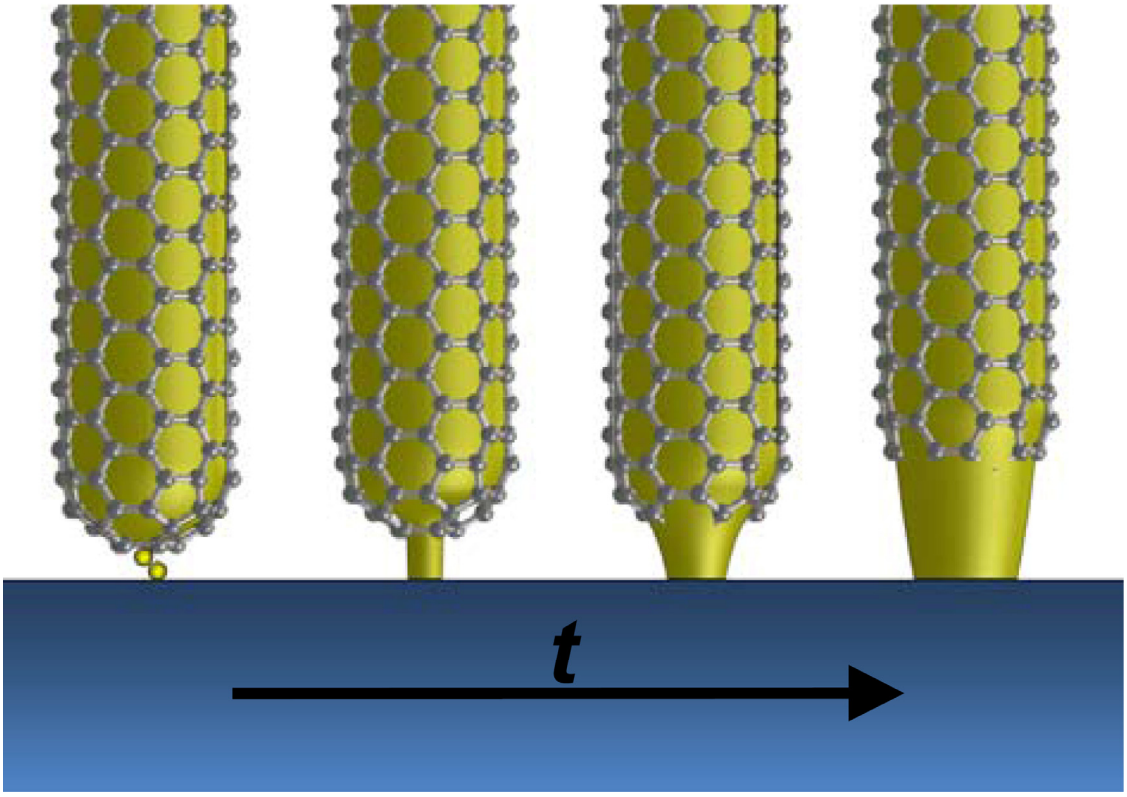

Figure 2.12: The simulation of the mass flowing out process.

through the junction and form the conductive filament channel between the inner copper atoms and the probe surface. As shown in Figure 2.12, due to the mesh structure of the nanotube tip, once one or more copper atoms penetrate the carbon hole and overcome the energy barrier, the C-S junction would collapse. Then, the conductivity of neighbor holes would also be affected. The copper would flow out and generate a nanowire with a size similar to that of the tube. It is crucial to note that the electric energy (applied voltage and current) required to break the junction is mainly related to the tube size. As illustrated in Figure 2.13, we modeled the NFP system as a single Cu@CNT. With a bias (2 V) added on the two ends of tubes with diameters of 12 nm and 20 nm respectively, the current and thermal distributions along the tube can be plotted. Because the current density in the small tube is intensified, the temperature profile along the nanotube with a smaller diameter is higher than that along the thick tube. Additionally, the

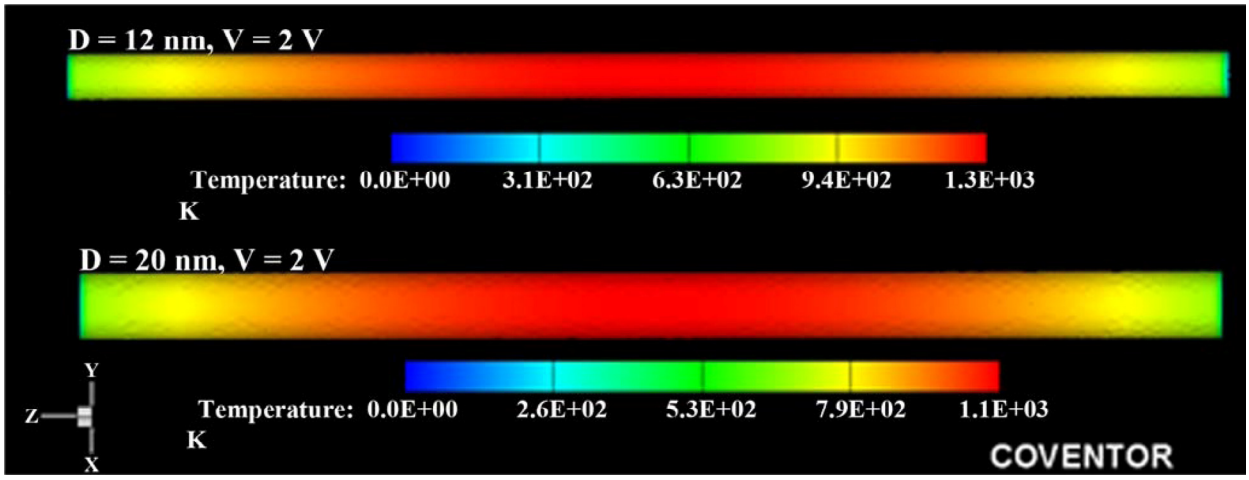

Figure 2.13: The simulation of the thermal distribution along different sized NFP. It shows that the nanotube with small diameter has higher temperature than the one with large diameter.

more intensified current induces a greater electromigration force, which helps the copper atoms pass through the energy barrier and the blocked junction collapsed. However, for the CNTs with a large diameter, higher power will be needed to make copper flow. Table 2.1 shows the injected electrical power P ($P=IV$) for the tubes of different sizes to make the mass flowing out. Figure 2. 14 shows the diameter-power (DP) curve which can be fitted by: $D = -8E\text{-}05P^2 + 0.1366P + 11.595$.

Table 2.1: Comparison of power threshold of NFP with different diameters

D (nm)	I (μA)	V (V)	P (μW)
26.9	44.3	1.2	53.2
37.5	91.1	1.5	136.7
47.2	193.8	2.0	387.6
56.0	205.5	2.3	472.7
69.9	331.5	2.5	828.8

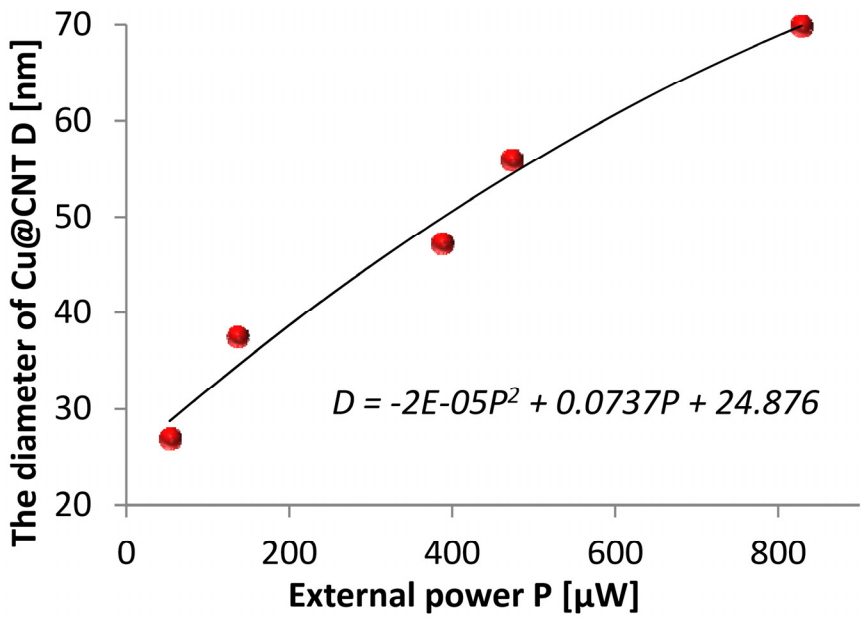

Figure 2.14: Correlation of the NFP diameter *D* with the external electric energy.

2.4 The Application of the NFP

2.4.1 NFP Writing Capillary

As the nanowires were written on the object, their shape was formed immediately due to the excellent thermal conductivity of the probe that cools down the deposit [39]. Reheating of the cooled-down deposit was not achieved because the volume of the probe (tip radius: 120 nm, root radius: 10 µm) was much larger than that of the copper deposit. The probe served as a heat sink with essentially infinite capacity compared with the copper deposit. A detailed examination of the crystalline structure of the generated nanowire can further explain their shaping process. Figure 2.15 illustrates the crystalline analysis of the generated nanowire. At the contact area between the probe and nanotube (area I), the crystalline phase of the deposited copper shows a poly-crystalline phase. This is attributable to the instant cool-down at the heat sink [39]; the molten mass is not crystallized enough before it forms the solid state. In contrast, area II reveals

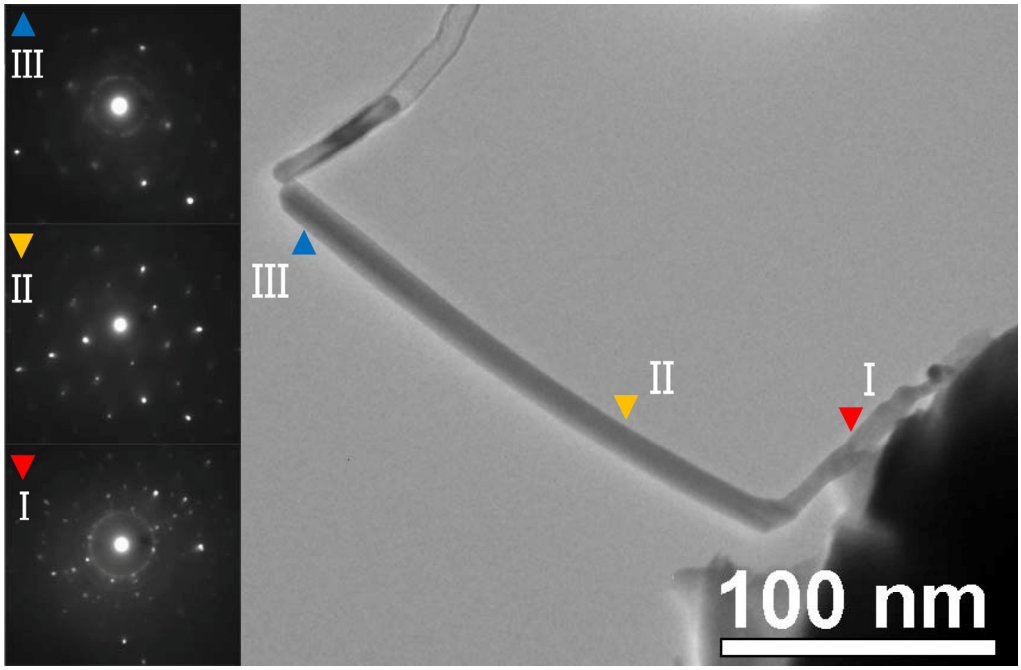

Figure 2.15: The crystalline phase analysis of as-generated nanowire. Due to the molten state at the connection between the deposit and the injector, it provides possible to shape the deposited structures.

single-crystalline phases since it is far from the heat sink. Moreover, according to the dark contrast and the amorphous phase seem in area III. We can confirm the molten state at this position. Therefore, the molten state in area III provides opportunity to shape the final structure by manually positioning of injector.

Our results allow the Cu@CNTs to be used as a NFP, quantitatively address the contribution of the electromigration driving force to the mass transportation, and attempting to model the "writing" process. Furthermore, the potential practical applications of NFP are also important. In the following, we will first describe representative experiments with multi-NFP, and then compare the drawing with a single NFP.

Two 3D capital letters, "N" and "L"; were fabricated. As shown in Figure 2.16(a), by attaching the tip of the injector to the probe during the mass flow, the shape of the molten nanowire deposit can be adjusted, and the letter "N" will be produced eventually. For the capital

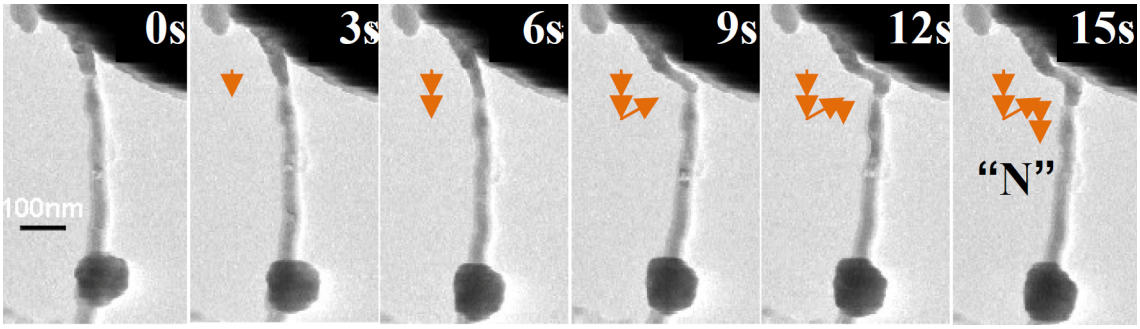

(a)

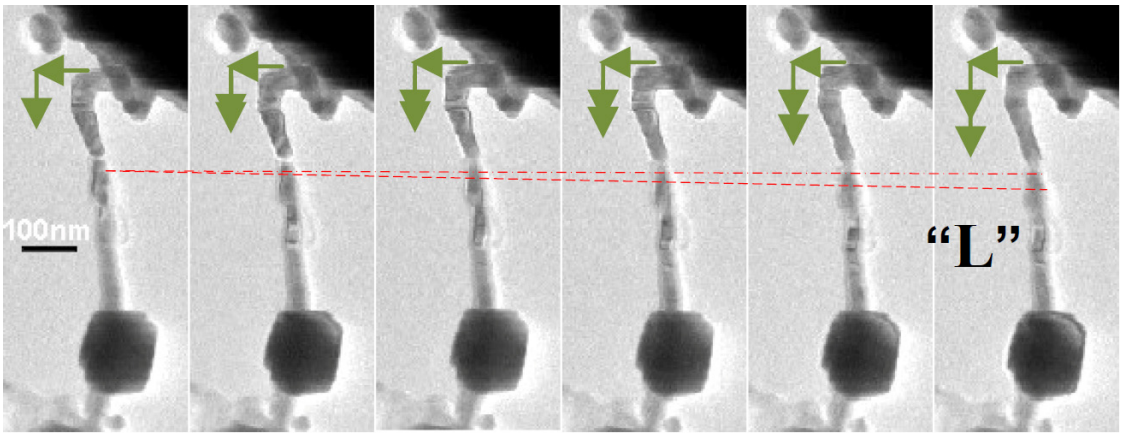

(b)

Figure 2.16: The applications of NFP on (a) The writing process of the Letter “N”. By manually positioning the molten copper onto the probe can freeze it immediately, and thereby construct the nanostructure as depicted a stick figure, (b) The writing process of the Letter “L”.

letter “L”, in Figure 2.16(b), the injector was moved during the mass flow to form the letter. Moreover, Figure 2.17 shows it is possible to construct a nanoscale composition with components of different diameters. Due to the complexity of using nanotubes with different diameters for fabrication, we have also investigated using a single nanotube to fabricate components of different sizes. The representative demonstration in Figure 2.18 shows that the injector moved back and forth in a small range, trying to deposit the mass at the same height as much as possible. Hence, those deposits would melt together and form a component that is much larger than the original size of the copper core inside the tube.

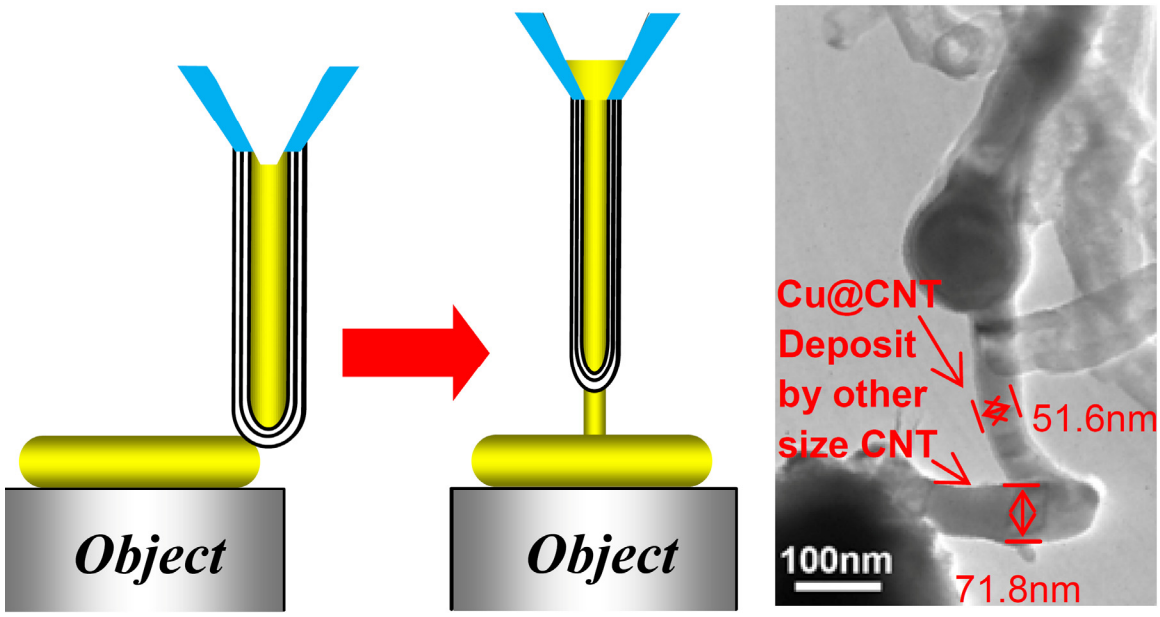

Figure 2.17: The demonstration of using different sized CNTs to generate nanostructures.

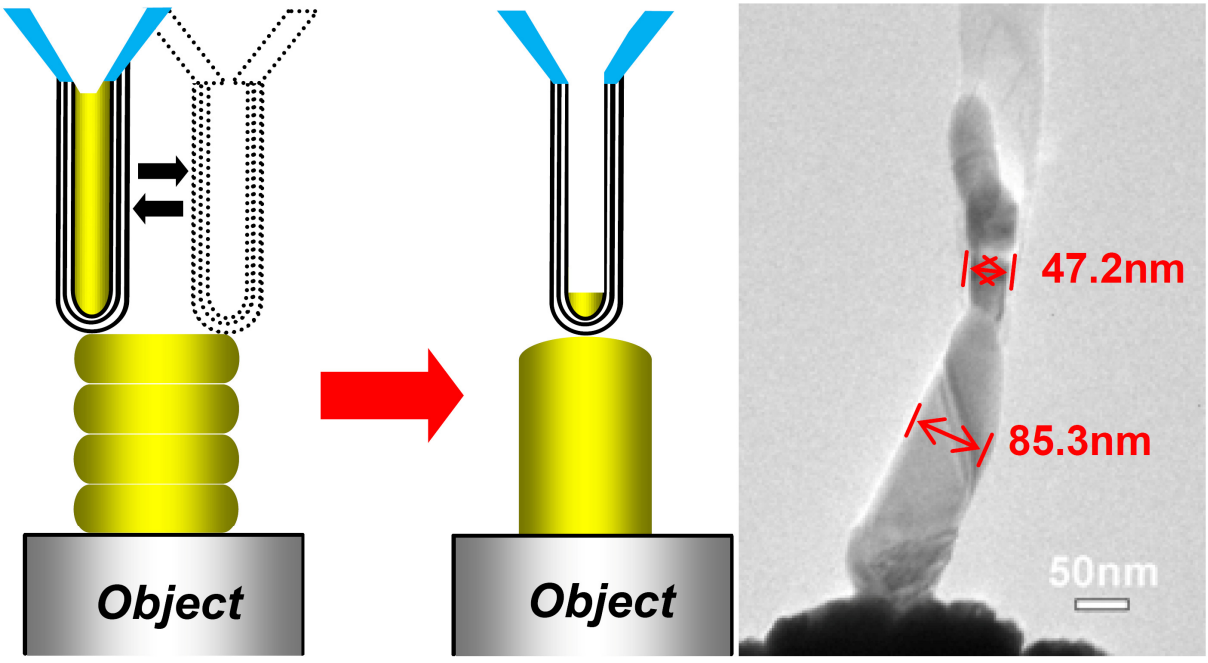

Figure 2.18: The demonstration of the modulating of deposits by adjusting the position of injector. The original diameter of nanotube is about 47.2 nm; however, the diameter of deposited nanowire is 85.3nm, which is much larger than the size of nanotube.

2.4.2 NFP Ink Reloading Process

The single tube construction consumes a lot of mass. Although we can accumulate a mass that is ten times more than the original in CNT, it is still not enough to construct complex devices, such as large scale integrated circuits. As a result, the mass "reloading" process after the mass in reservoir is used up was investigated. We selected a Cu@CNT half filled with mass to curry on the mass reloading experiment. Because the blocked junction between the probe and the tube was blocked, the inner mass could not flow out at the beginning. Figure 2.19(a) shows that the "reloading" process (frames 1-2) occurred as the external bias reached 1 V; however, due to the lower input driving energy, only a small amount of mass was melted and transported, and the mass accumulation speed during 63 s was only 0.52 nm/s (Figure 2.19(b)). In contrast, Figure 2.19(c) demonstrates that as we increased the bias voltage to 1.5 V, a huge mass reloading suddenly occurred. During this process (frames 3-4, 6 s), and the mass transport speed reached 96.2 nm/s. We simulate the NFP under these two external voltages to understand the nature of mass reloading. In Figure 2.20, as the NFP was simulated as a single Cu@CNT with the diameter of 12 nm, the current-induced thermal distribution illustrate that the high temperature portion along the tube (red portion) enlarged due to the increasing bias from 1.0 V to 1.5 V. This allowed more mass to melt, and with the increase of the electromigration force, the transport of this mass was readily realized. Therefore, we concluded that the increased input of electrical energy induced the melting and migration of a large amount of mass, which provided the potential for reloading the mass.

Additional research is necessary to develop the NFP methodology into a batch fabrication routine tool similar to polymer pen lithography (PPL) [26], and we believe there are already clear advantages: First, the batch assembly of the CNT injector is relatively simple [40, 41]; Second,

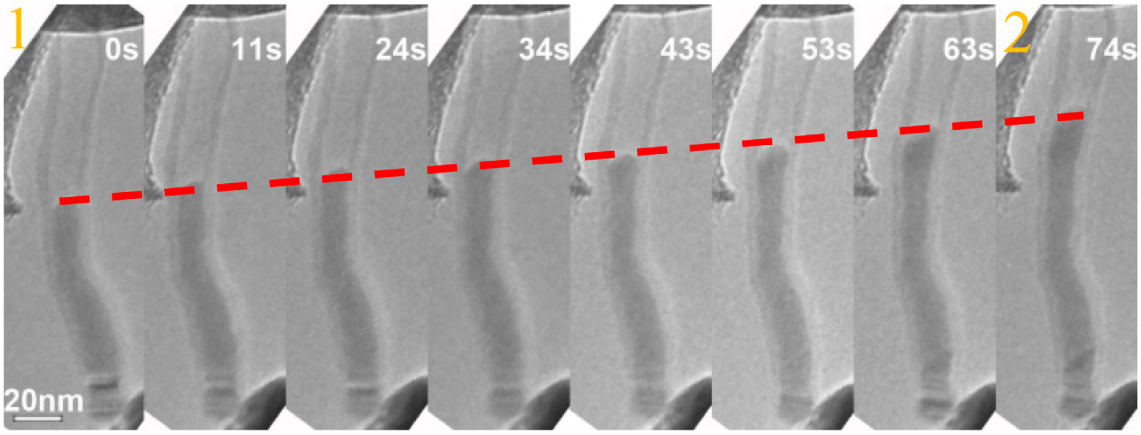

(a)

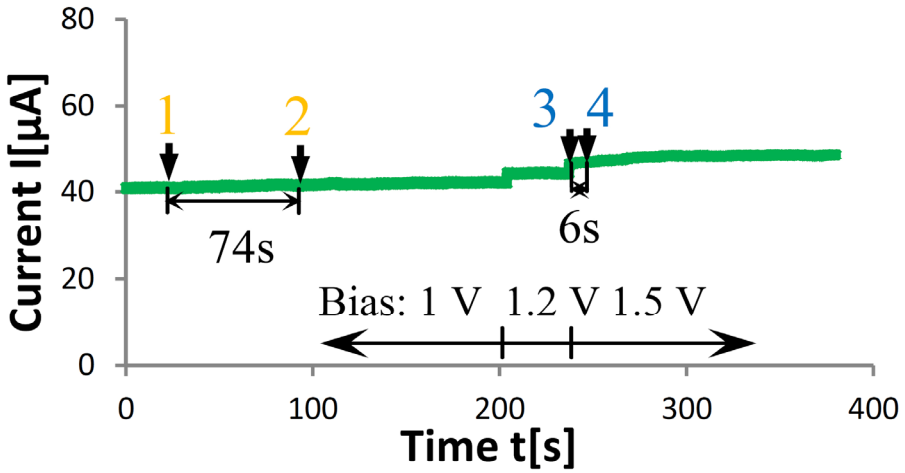

(b)

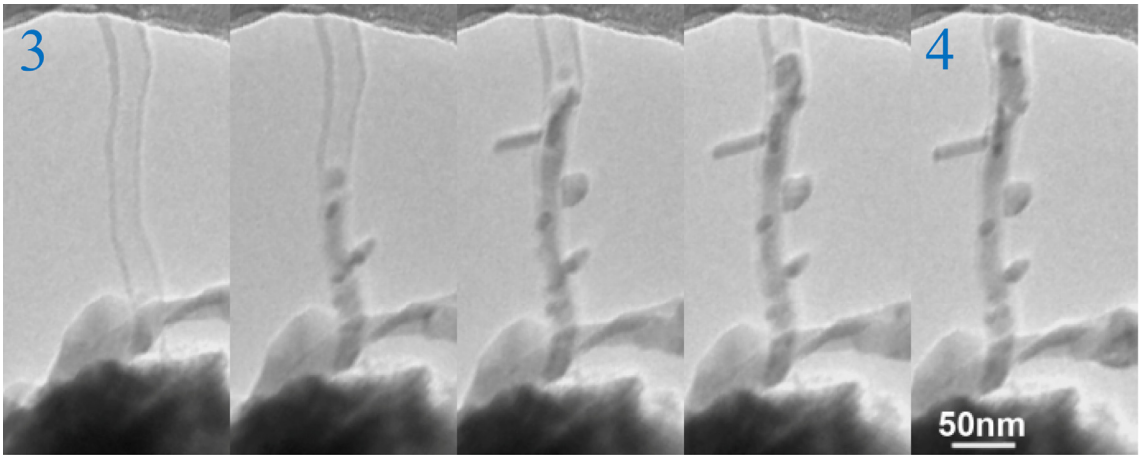

(c)

Figure 2.19: The NFP reloading. (a) The reloading in a NFP with a lower inputted energy, the process lasts for 74 s. (b) Current-time characterization about reload process with different inputted energy. (c) The reloading process with higher electrical energy, the reload process lasts for 6 s.

the NFP is more durable than the dip-pen probe, as there is no need to dip into ink for further writing (a reservoir would be added on each CNT injector); Finally, the mass delivery control demonstrated in this paper can be used in further investigation of NFP batch "writing".

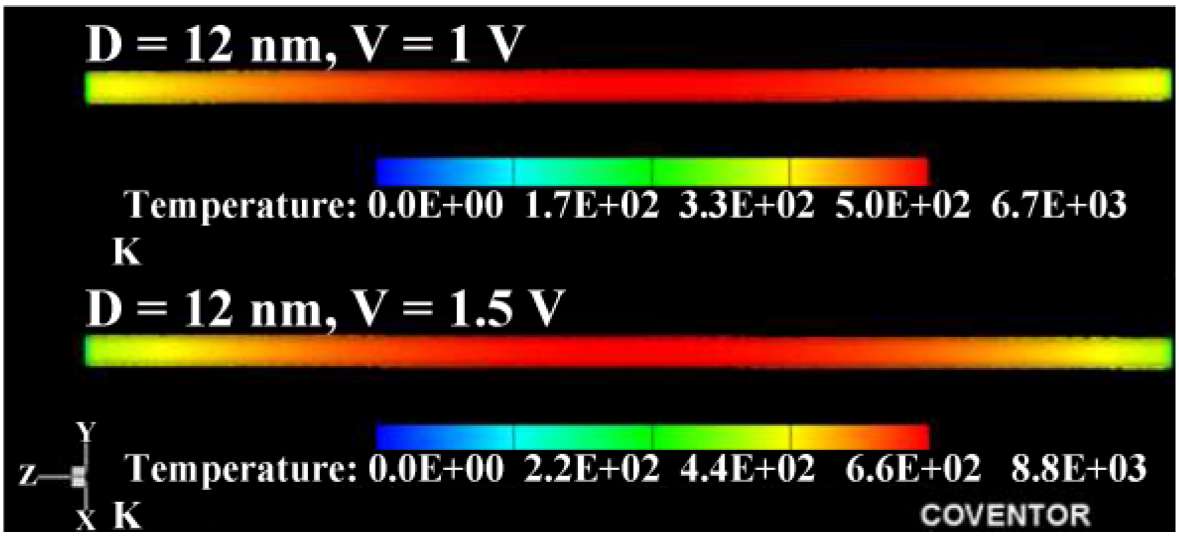

Figure 2.20: The simulation of the thermal distribution along a CNT as the external bias increased.

2.5 Chapter Summary

In summary, we have demonstrated the application of a CNT injector and network as a NFP for manufacturing nanostructures. The experimental results establish that the switching states ("ON" or "OFF") of the NFP writing are realized by means of the drifting of the copper atoms that induce by external electric energy to overcome the energy barrier and collapse the blocked junction (ON). The external injected energy, the bias voltage, and the current control the writing speed of the NFP. With the understanding of the forming process of the as-deposited nanostructures, it is possible to shape the deposit during the "writing" process. We have also studied the practical applications of this technique; several 3D structures and "writing" methods were demonstrated.

CHAPTER 3

SLIDING PROBE METHOD

In situ fast characterization of electrical properties of individual one-dimensional (1D) nanostructures are developed by using the super-fine nanoprobe that fabricated by NFP. The key to achieve a high resolution of the electrical/mechanical properties of the nanostructure during the sliding probe characterization is to keep the contact resistance constant by controlling the contact force and area between the specimen and the sliding probe. We have developed several techniques and tools including differential sliding, flexible probes, and specimen-shape adaptable probes using nanorobotic manipulation. Compared with conventional methods, these sliding probe methods allow *in situ* characterization with a higher resolution and in a fast mode. Furthermore, they are superior for local property characterization, which is of particular interest for the nanomaterials in heterostructure and the defects detection of the nanostructure.

3.1 Introduction of the Sliding Probe Method

In situ characterization of electrical transport property of individual nanostructures is of growing interest for accelerating the development of novel nanomaterials, correlating their transport properties to their atomic structures, and selecting suitable building blocks for electronic, sensing, actuation, electromechanical, or electrochemical systems [42-44]. Conventionally, two-terminal method [43, 45] shown in Figure 3.1(a) and four-terminal method [42, 46-48] shown in Figure 3.1(b), using either fixed electrodes or movable probes, have been applied in such measurements.

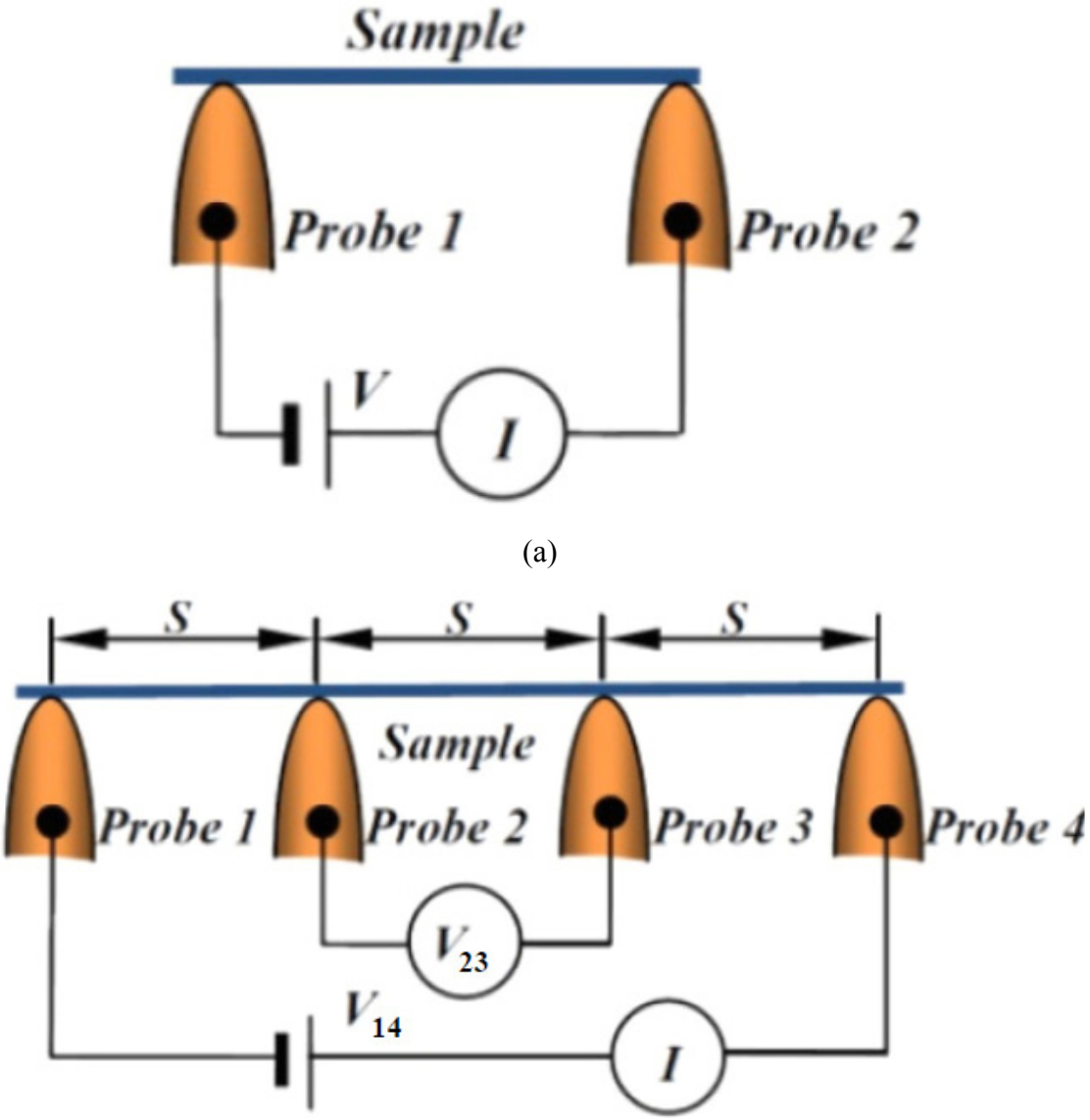

Figure 3.1: (a) Conventional two-terminal measurement, (b) Conventional four-terminal measurement.

Theoretically, as shown in Figure 3.1(a), two-terminal methods do not allow determination of the intrinsic electrical transport properties due to the contact resistance between the probes and the sample that lies inside the measurement loop. The measurement accuracy is determined by the ratio of $(R_{P1\text{-}S} + R_{S\text{-}P2})/R_S$, where $R_{P1\text{-}S}$, $R_{S\text{-}P2}$, and R_S represent the contact resistance between probes 1 and 2 and the nanostructure, and the intrinsic resistance of the

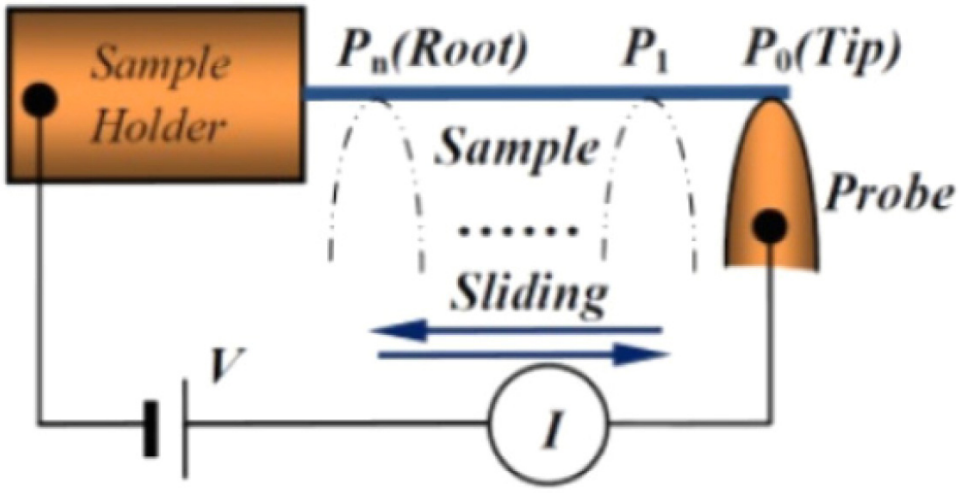

(a)

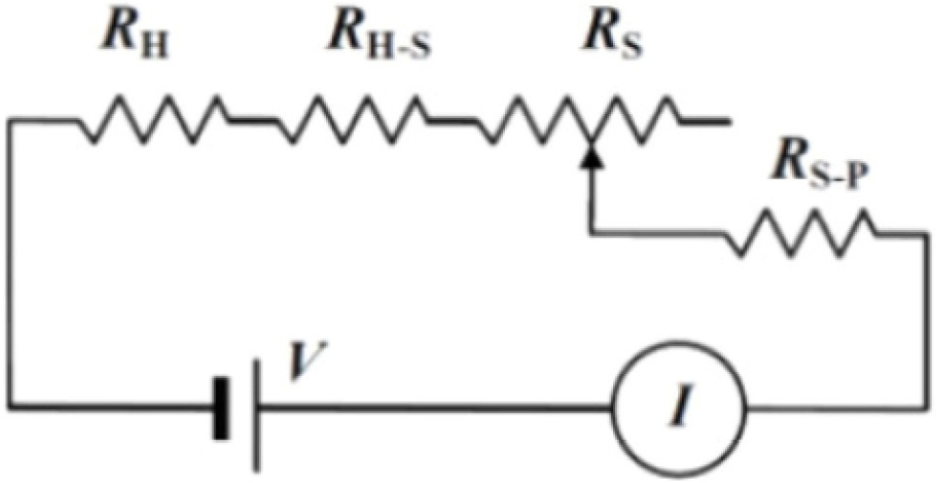

(b)

Figure 3.2: (a) Sliding probe methods for *in situ* electric property characterization. By contacting a probe to different points (P_0 (tip), P_1, …, P_n (root)) on an individual nanostructure, the resistance of the nanostructure is measured. (b) The equivalent circuit of the measurement loop, where R_H, R_{H-S}, R_S, and R_{S-P} represents the resistance of the sample holder, the contact resistance of the sample holder to the sample (a nanostructure), the resistance of the sample and the contact resistance of the probe to the sample, respectively. The method can be used to investigate a variety of nanostructures, particularly suitable for local transport measurement for a hetero-structure.

nanostructure, respectively. Technically, it is possible to improve the contact by coating the probes with low-resistance materials, soldering the nanostructure onto the probes, or compressing the nanostructure using the probes. Two-terminal methods were applied to *in situ*

characterization, especially for the electromechanical coupling property, due to their simplicity and flexibility when a manipulation probe is used. However, when the resistance of the nanostructure is close to the magnitude of the contact resistance, the conventional two-terminal method fails. A standard method that eliminates the contribution of contact is the four-terminal measurement, but it is a challenge to apply this technique to an individual nanostructure. First, it is difficult to fabricate nanoelectrode or probe arrays with a nanoscale separation S (see Figure 3.1(b)). Second, additional degrees of freedom are needed for orienting the holder of the array so that the four probes make contacts to an individual nanostructure, which is difficult to be achieved by using up-to-date nanorobotic manipulators. Third, it is particularly difficult to simultaneously make contact to a low-dimensional structure such as nanotubes (NTs) or nanowires (NWs) in four points, especially when they are free-standing. Finally, using four manipulators to position four separate probes onto a nanostructure would be ideal, but is very costly. In addition, this solution is not attainable due to the limitation of the space inside a TEM.

With these insights, we proposed a sliding probe method [49], in which a manipulation probe is used together with a fixed electrode or probe, as shown in Figure 3.2(a). By sliding a probe along an individual nanostructure, its electrical transport properties can be characterized at different positions (e.g, the tip or the root). The resistance of the sample (nanostructure) can be measured by finding the difference between any two measurements.

3.2 Two-Point and Multi-Point Sliding Probe Method

In Figure 3.2(b), where R_H, $R_{H\text{-}S}$, R_S, and $R_{S\text{-}P}$ represent the resistance of the sample holder, the contact resistance of the sample holder to the sample, the resistance of the sample, and the contact resistance between the probe and the sample, respectively shows the circuit of the

measurement loop represents the experiments setup in Figure 3.2(a). The overall resistance when the probe make contacts with any two points P_i and P_j (i, j = 0, 1, …, n and i < j) are expressed as $R_i = R_H + R_{H\text{-}S} + R_{S,\,i} + R_{S\text{-}P,\,i}$ and $R_j = R_H + R_{H\text{-}S} + R_{S,\,j} + R_{S\text{-}P,\,j}$, respectively. Therefore, the resistance of the sample between points P_i and P_j is $R_{ij} = R_i - R_j = R_{S,\,i} - R_{S,\,j} + R_{S\text{-}P,\,i} - R_{S\text{-}P,\,j}$. It can be seen that the resistance of the sample holder and the contact resistance at the fixed end between the sample holder R_H and $R_{H\text{-}S}$ are eliminated. Hence, the difference between the two measurements when the probe contacts to any two points P_i and P_j of the nanostructure ($R_{ij} = R_i - R_j$) reflects the intrinsic resistance of the nanostructure between them ($R_{S,\,i} - R_{S,\,j}$), assuming that the contact resistance between the probe and the nanostructure is the same for the two cases ($R_{S\text{-}P,\,i} = R_{S\text{-}P,\,j}$). Compared with the conventional two-terminal methods in Figure 3.1(a), only one side of the contact resistance is involved in the measurements, it is more feasible to keep the contact resistance between the two contact positions ($R_{S\text{-}P,\,i} \approx R_{S\text{-}P,\,j}$) and then eliminate them by subtracting. Hence, this sliding probe method yields higher accuracy for *in*

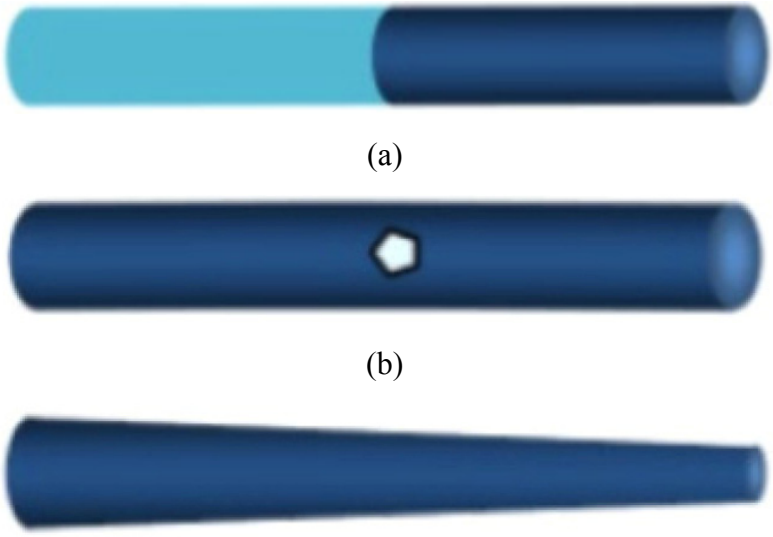

(a)

(b)

(c)

Figure 3.3: (a) A hetero-structure, (b) A structure with local defects/doping, (c) A non-uniformed nanostructure.

situ characterization of electric property than the two-terminal methods and holds simplicity when it compares to four-terminal methods.

Basic sliding probe methods including two and three discrete contacting points which shown effective elsewhere using nanorobotic manipulation inside a TEM [49]. The methods can be used to investigate a variety of nanostructures, particularly suitable for local electrical transport property measurements of a hetero-structure as illustrated in Figure 3.3(a), a structure with local defects/doping sites as shown in Figure 3.3(b), or a non-uniformly shaped structure as illustrated in Figure 3.3(c). In this report, we propose several enhanced techniques for improving the uniformity of the contact resistance between the probe and the sample at different positions ($R_{S\text{-}P,\,i} \approx R_{S\text{-}P,\,j}$). These include (1) multipoint continuous sliding or differential ($n \to \infty$) sliding, (2) flexible probes as shown in Figure 3.4, and (3) specimen-shape adapting of probe tips

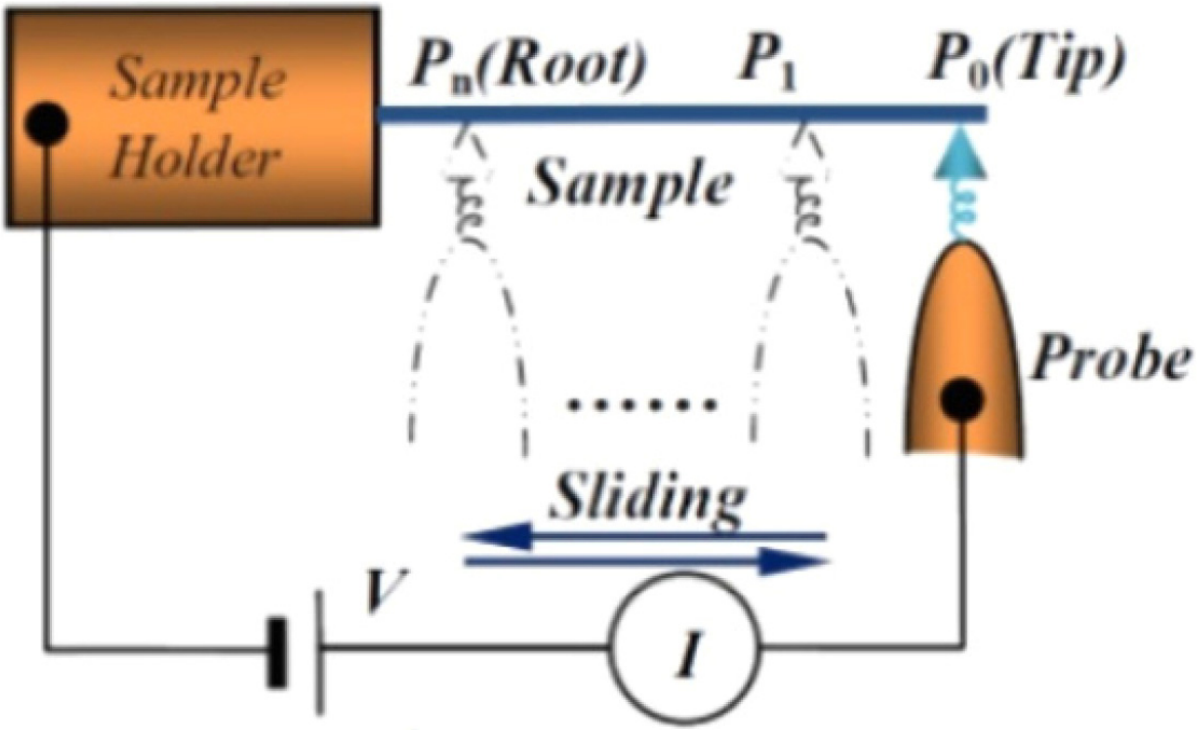

Figure 3.4: Multipoint continuous sliding or differential ($n \to \infty$) sliding, together with flexible probes.

as shown in Figure 3.5. These techniques enable the electrical measurements in a feasible way and broadening the applications of the sliding methods.

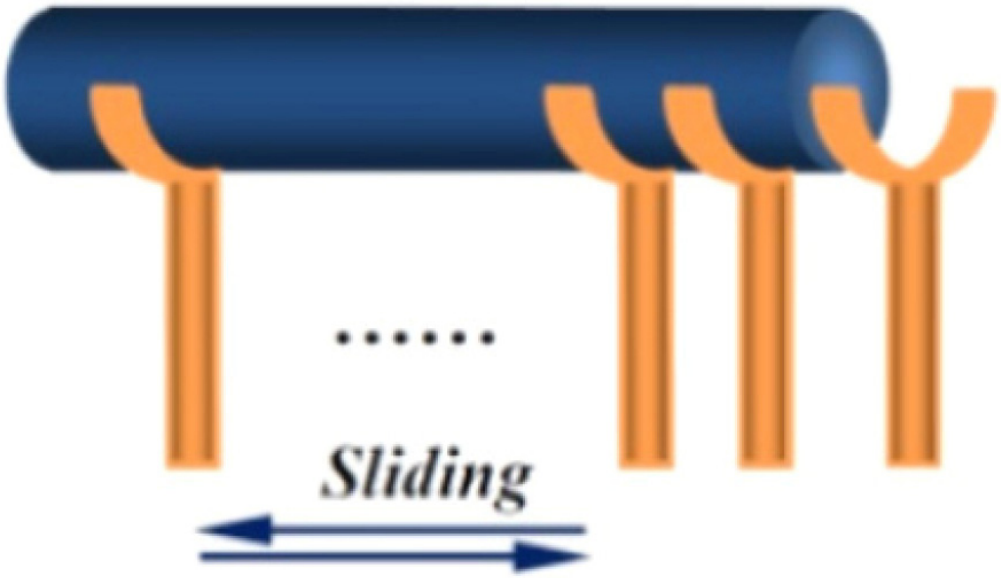

Figure 3.5: Multipoint continuous sliding or differential ($n \rightarrow \infty$) sliding, together with specimen shape-adapting.

The experiments were performed in a TEM (JEOL 2200FS) equipped with a field emission gun. The raw materials were attached with silver paint to a 0.35 mm thick Au wire, which was positioned in the specimen holder. The probe was an etched 10 μm thick tungsten wire with a tip radius of approximately 100 nm (Picoprobe, T-4-10-1 mm). To improve conductivity, the probes were coated with a thin Au film (thickness ca. 21 nm). The motion of the probe was controlled by a STM (scanning tunneling microscope) - TEM holder (FM2000E, Nanofactory Instruments AB). The probe can be positioned inside a millimeter-scale workspace with a sub-nanometer resolution, with the STM unit actuated by a three-degree-of-freedom piezotube, making it

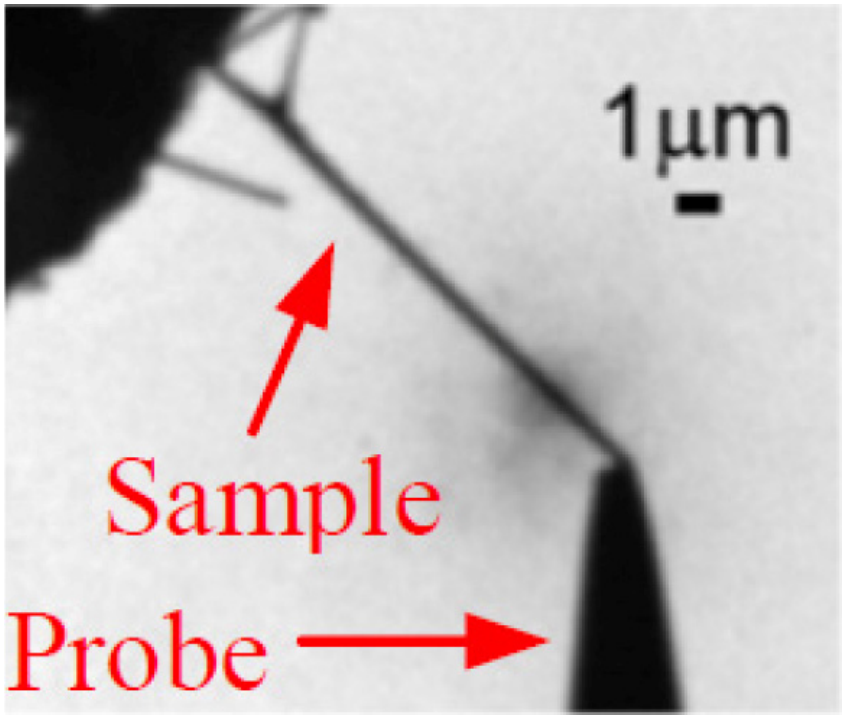

(a)

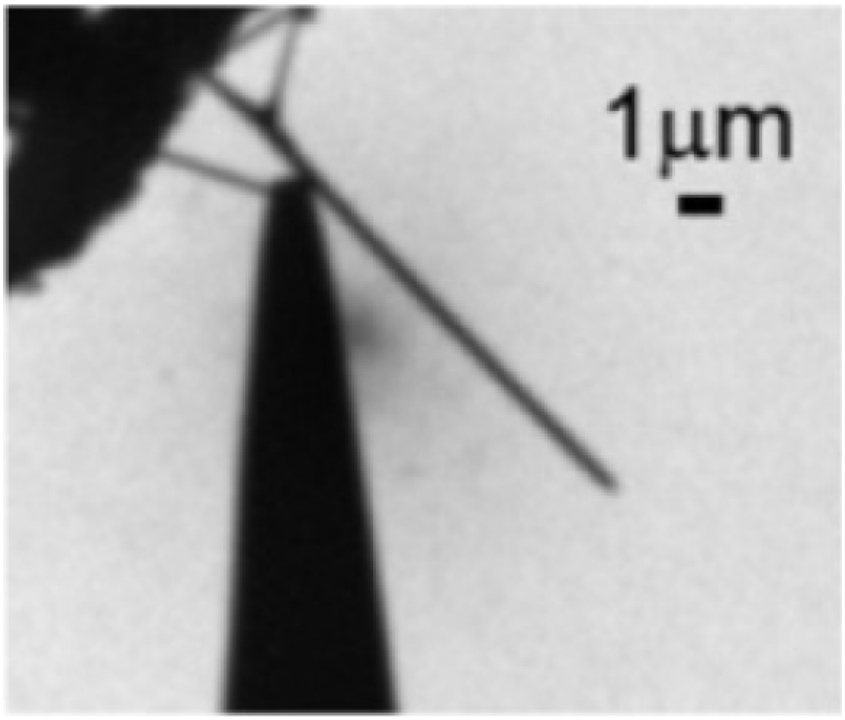

(b)

Figure 3.6: The corresponding TEM image for the TaC nanowire sliding probe characterization. A STM probe contacts to the tip (a) and the root (b) of the nanowire in two measurements, respectively.

possible to select a specific object and take the multi-point sliding probe measurement of different nanostructures.

Experiments are performed to demonstrate the electrical property measurement by applying the multipoint sliding probe method (Figure 3.2(a)) to a variety of nano- and microstructures. The first demonstration is the IV characterization of an individual TaC nanowire. The second demonstration is the similar measurement applied to the carbon microfiber (CMF) where nanowires grow. The process of these measurements are as follows: To the individual nanowire, the STM probe respectively makes contact with two positions on the sample, including the tip in Figure 3.6(a) and the root in Figure 3.6(b) of the nanowire in two measurements. A bias was applied between the sample holder and the probe that swept from -500 mV to 500 mV. The current-voltage (*I-V*) curves were taken simultaneously during this process. In regard to the carbon microfiber, the contacts were made on three positions on the sample by using the STM probe, including the tip (Inset: left), the middle (Inset: middle), and the root (Inset: right) of the nanowire in three measurements.

According to the *I-V* properties, the resistance of carbide nanowires and carbon microfibers was changing in accordance with the current value. Therefore, a mathematical method was proposed to understand the resistance between the two contact areas. Firstly, to the measurement of TaC nanowire, we assume that the IV curves of TaC nanowire in tip and root (see Figure 3.7(a)) are linearly fitted by:

$$I_C = aV_C + b \tag{1}$$

where, I_C is the current under the bias of V_C when the probe is on the contact area. Therefore, the resistance from the sample holder to the contact area is easy to be obtained. As we got the

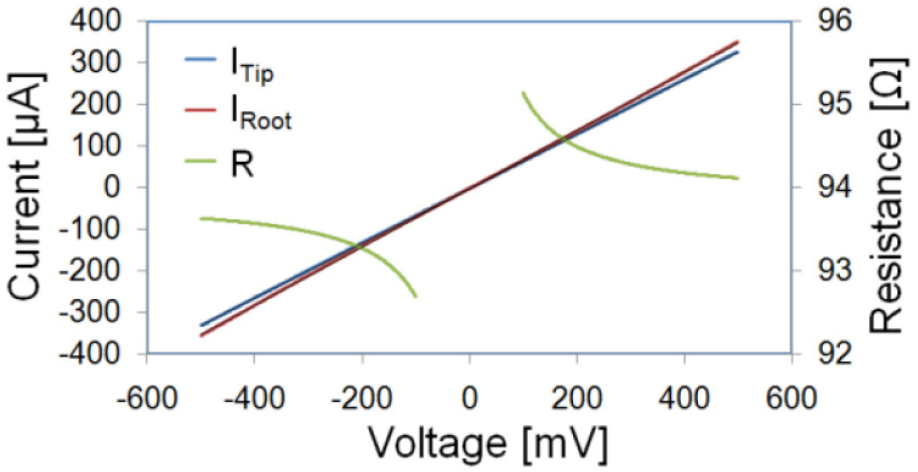

(a)

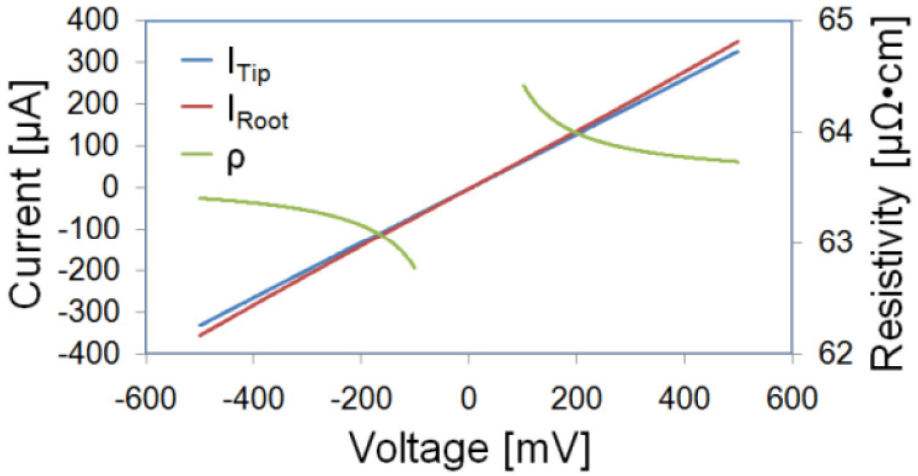

(b)

Figure 3.7: (a) *I-V* characterization and the resistance curve of a TaC nanowire using the sliding probe method. A bias is applied between the sample holder and the probe and swept from -500 mV to 500 mV. The resistance is found from the slope of the linear *I-V* curves. The resistance here is calculated to be 93.9 Ω (bias: -500mV to -100 mV and 100 mV to 500 mV) in average, (b) characterization and the resistivity curve of a TaC nanowire using the sliding probe method. As the diameter of the nanowire is 290.2 nm and the length of it is 9.8 μm, the *I-V* resistivity of it is calculated to be 63.6 ± 0.8 μΩ·cm (bias: -500 mV to -100 mV and 100 mV to 500mV) in average.

relation between the resistance and the current, the resistant between two contact areas can be derived as:

$$R_{ij} = R_i - R_j = R_{S,\,i} - R_{S,\,j} + R_{S\text{-}P,\,i} - R_{S\text{-}P,\,j}$$

$$= \frac{1 - d/I_i}{c} - \frac{1 - b/I_i}{a} + R_{S\text{-}P,\,i} - R_{S\text{-}P,\,j} \qquad (2)$$

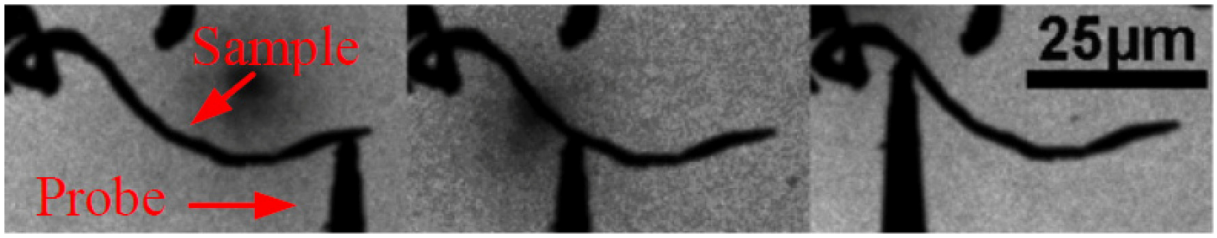

Figure 3.8: The corresponding TEM image for the sliding probe characterization of carbon microfiber. A STM probe contacts to the tip (left), center (mid) and the root (right) of the microfiber with three measurements taken, respectively.

Assuming that the contact resistances between the probe and the nanostructure are the same in the two contact areas ($R_{S\text{-}P,\ i} = R_{S\text{-}P,\ j}$). Therefore, the influence of contact resistance between the two areas was eliminated in equation (2). The fitted curve on the tip and root is: $I_{Root} = 0.6995V_{Root} - 2.6529$, the appropriateness of fitting here is $X^2 = 0.9999$; and $I_{Tip} = 0.6564V_{Tip} - 2.5418$, $X^2 = 1.000$, where I and V are in μA and mV, respectively, as shown in Figure 3.7(a) and (b). According to equation (2), as the influence of the contact resistance was erased, the resistance between the tip and root is 93.9 Ω (bias: -500 mV to -100 mV and 100 mV to 500 mV) in average. The diameter and the length of the nanowire are 292.0 nm and 10.0 μm, respectively, so the resistivity of the nanowire is calculated to be 63.6 μΩ·cm (bias: -500 mV to -100 mV and 100 mV to 500 mV) in average, which is comparable to the resistivity of bulk TaC materials [50] (137 μm thick and 4.6 cm long: 32.7-117.4 μΩ·cm for a variety of compositions). The measured value is closer to the average of two limits. The result reveals the accuracy of the measurement.

Secondly, to the measurement of CMFs illustrated in Figure 3.8, where the measured IV curves in these three positions can be perfectly fitted into a three degree polynomial as shown in in Figure 3.9(a):

$$I_c = aV_c^3 + bV_c^2 + cV_c + d \tag{3}$$

To find an analytical solution to the above equation, we transform the equation into:

$$(aI_c^2)R_c^3 + (bI_c)R_c^2 + cR_c + (d/I_c - 1) = 0 \tag{4}$$

The resistance R_c from the sample holder to different contact areas can be solved from equation (4). Then, the resistance between these contact areas can be calculated using equation (2). The fitting curves on tip, middle and root are shown as follows:

$$I_{Tip} = 5.0\times10^{-5}V_{Tip}^{3} - 5\times10^{-4}\,V_{Tip}^{2} + 24.541V_{Tip} - 190.96 \qquad X^2 = 0.9997 \qquad (5)$$

$$I_{Mid} = 4.0\times10^{-5}V_{Mid}^{3} - 1.8\times10^{-3}\,V_{Mid}^{2} + 33.111V_{Mid} - 127.46 \qquad X^2 = 0.9999 \qquad (6)$$

$$I_{Root} = 2.0\times10^{-5}V_{Root}^{3} - 1.0\times10^{-4}\,V_{Root}^{2} + 41.76V_{Root} - 193.3 \qquad X^2 = 1.0000, \qquad (7)$$

where I_{Tip} is the current under the bias of V_{Tip} when the probe contacts on the tip; I_{Mid} is the current under the bias of V_{Mid} when the probe contacts on the middle; I_{Root} is the current under the bias of V_{Root} when the probe contacts on the root. V_{Root}, V_{Mid} and V_{Tip} here are the biases which swept from -500 mV to 500 mV when the probe contacts the carbon microfiber in three positions.

According to equation (2), the resistance of it was calculated to be 32.3 kΩ from tip to mid and 11.1 kΩ from mid to root (bias: -500 mV to -100 mV and 100 mV to 500 mV) in average. The average diameter and the length of the carbon fiber from tip to mid are 2.2 μm and 29.7 μm, and from mid to root are 2.2 μm and 23.8 μm, respectively. As a result, its resistivity was calculated to be 0.2-0.7 Ω·cm and 0.1-0.2 Ω·cm as shown in Figure 3.9(b). The fact that the resistivity of these two parts is very close indicates the accuracy of the sliding method.

The result of multipoint sliding probe method precisely reveals the electrical properties of nanostructures. The results show the high conductivity of the carbide NWs. To the TaC NWs, the resistivity is 63.6 ± 0.8 μΩ·cm. According to our sliding probe measurements of the CMF from which NbC NWs growed, the resistivity is within the range of 0.1-0.7 Ω·cm.

Using multipoint sliding, the transport properties can be accurately characterized by fully removing the contact resistance on the fixed end and partially erasing resistance on the sliding

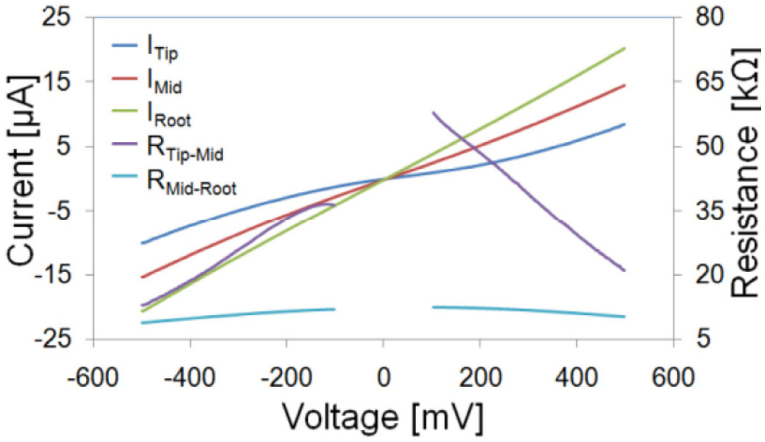

(a)

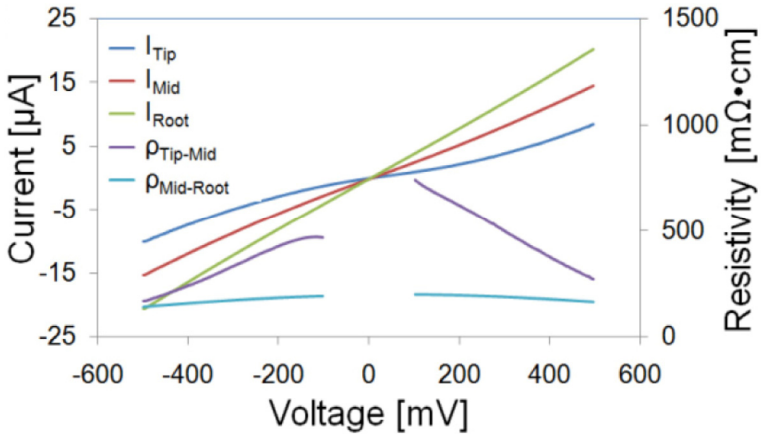

(b)

Figure 3.9: (a) *I-V* characterization and the resistance curve of the carbon fiber. A bias is applied between the sample holder and the probe and swept from -500 mV to 500 mV. The resistance is found from the slope of the linear *I-V* curves. The resistance here is calculated to be 32.3 kΩ from tip to mid and 11.1 kΩ from mid to root (bias: -500 mV to -100 mV and 100 mV to 500 mV) in average, (b) *I-V* characterization and the resistivity curve of the carbon fiber. The diameter of the carbon fiber from tip to mid is 297.6 nm and the length of it is 29.7 μm.The diameter from mid to root is 297.6 nm and the length is 23.8 μm. The resistivity of it is calculated to be 0.2-0.7 Ω·cm and 0.1-0.2 Ω·cm (bias: -500mV to -100 mV and 100 mV to 500 mV) respectively.

side [49], which is suitable for measuring the hetero-nanostructure as shown in Figure 3.3(a). To further improve the measurement resolution, the contact force and area between the probe and the sample has to be controlled to keep the contact resistance constant. To keep the force constant, an elastic contact is preferred over a stiff one. To keep the area constant, shape-

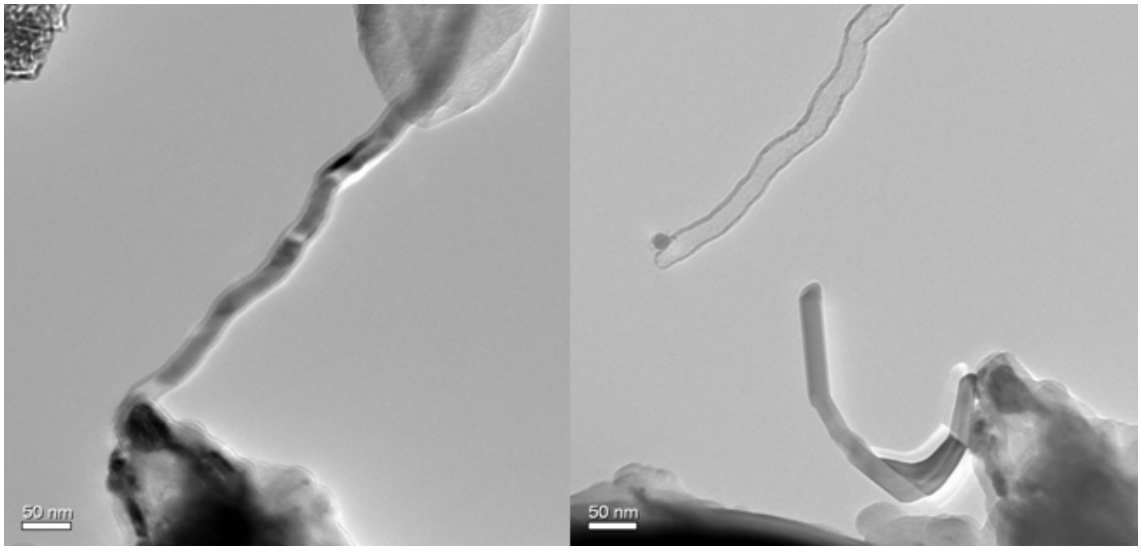

(a) (b)

Figure 3.10: (a) The copper-filled CNT and the probe, (b) Soft probe fabrication. By using the EMBD, a copper stick is deposited on the tip of probe, and the stick is served as a new probe to acquire more accuracy.

adaptable probe tip is superior to a pointed due to its ability to maintain the contact and its higher average effect over the contact area.

3.3 Differential Sliding Probe Method

A novel flexible sliding probe method is proposed in this section for keeping the contact force constant during the measurement. This method is particularly suitable to the measurement of non-uniform nanostructures, such as an irregularly shaped CNT. A copper nanowire is fixed on the probe tip by using electromigration-based deposition (EMBD) [39], as shown in Figure 3.10(a) and (b). The encapsulated metal can be delivered out of the carbon shells, creating a nanoscale soft probe attached on the tip of the probe. Since the volume of the nanoscale flexible probe is much smaller than the STM probe (tip radius: 100 nm, root radius: 10 μm), the surface-force–induced-binding between the sample and the probe during sliding will be increased accordingly (the attractive surface force is largely depends on the volume of the contact objects).

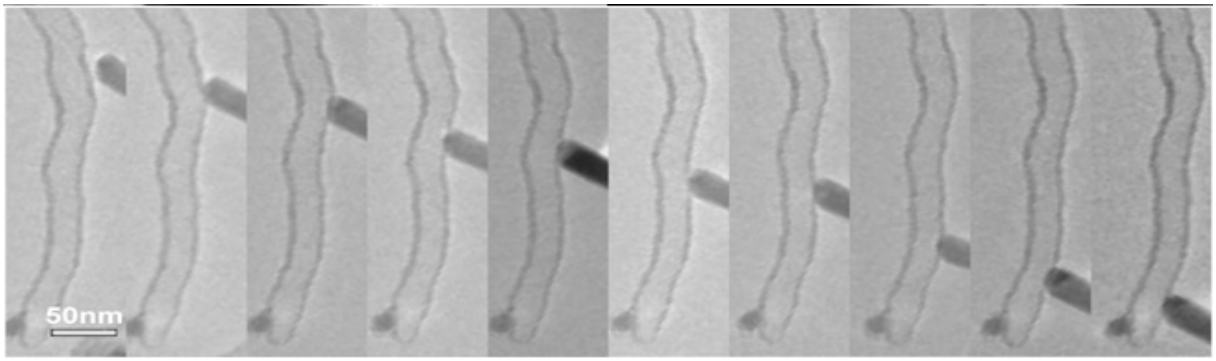

Figure 3.11: The differential sliding to a single CNT, the probe sliding on a copper filled carbon nanotube in a uniformed speed (about 10 nm/s) under the bias of 500 mV, the resistance of it along the moving direction is found during the sliding process.

Thus, it is easier to keep a constant contact force by using the nanoscale flexible probe. Furthermore, in previous investigations, using either a fixed electrode or a movable probe, contact has been made only on several positions on a sample. The limited number of contact points can provide data to describe the general characteristics of the nanostructure but not local properties; therefore, a differential sliding technique is proposed for using the soft probe. Figure 3.11 shows that when the soft probe continuously slides on a copper-filled carbon nanotube (Cu@CNT) at a uniform speed (about 10 nm/s) under a bias of 500 mV, the resistance along the direction of movement was measured continuously. The current value steadily decreased along the length of the CNT, while the resistance increased accordingly, which is illustrated in Figure 3.12.

This differential sliding method using a soft probe has the advantage that changes in the contact resistance R_c was neglected during the measurement and the stick-slip effect is also largely eliminated (avoided) with soft probe sliding. Using the current-time (*I*-*t*) curve and a real-time video generated by the TEM during the sliding process, the sliding speed, the bias between the probe and the CNT, and the resistance versus length curves can be obtained. In the experiment, the original data fit a straight line with $R^2 = 0.8211$. If the resistivity of the CNT is

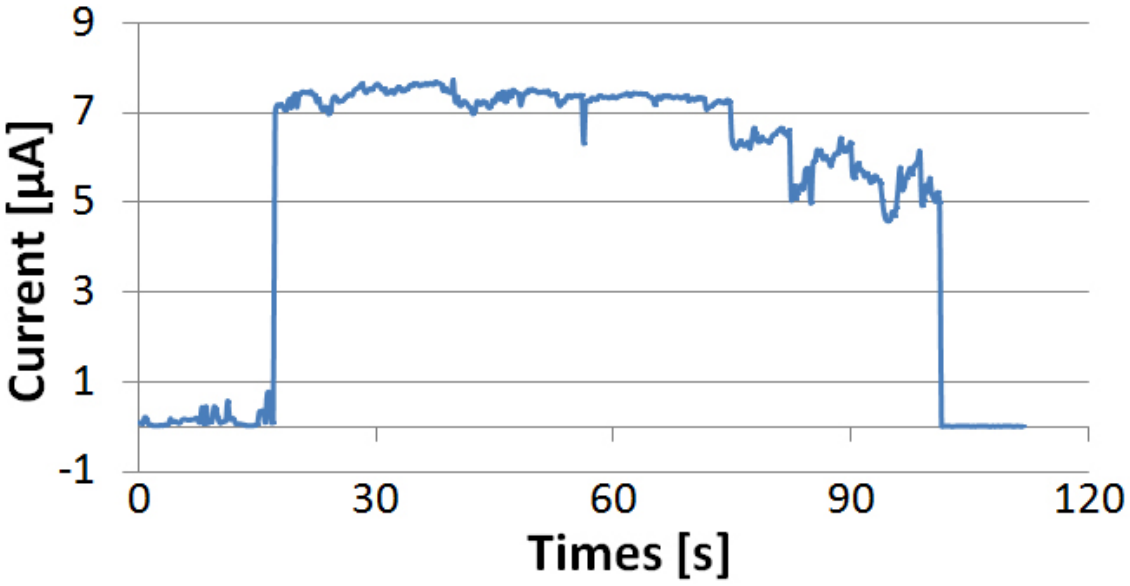

Figure 3.12: The *I-t* curve recorded by differential sliding method. During the sliding, the current value steadily decreased along the length of CNT, described precisely about the increasing of resistance.

constant, the increased resistivity will match the increased length of the CNT more closely. However, as illustrated in Figure 3.13, the measured resistance is affected by the impact of the probe during the sliding, which makes the resistance-length (*R-L*) curve failed to fit a first-order equation. In order to find the relation between the impact force ΔF and the resistance ΔR affected by it, we correlate them with:

$$\Delta R = \sigma \bullet \Delta F \tag{8}$$

and

$$\Delta F = 3\Delta EI / L^3 \tag{9}$$

where ΔE is the bending deformation of the CNT, I is the moment of inertia the CNT, and L is the length of the CNT.

Then, the relation between ΔR and ΔE can be given by:

$$\Delta R = \delta \bullet \Delta E \tag{10}$$

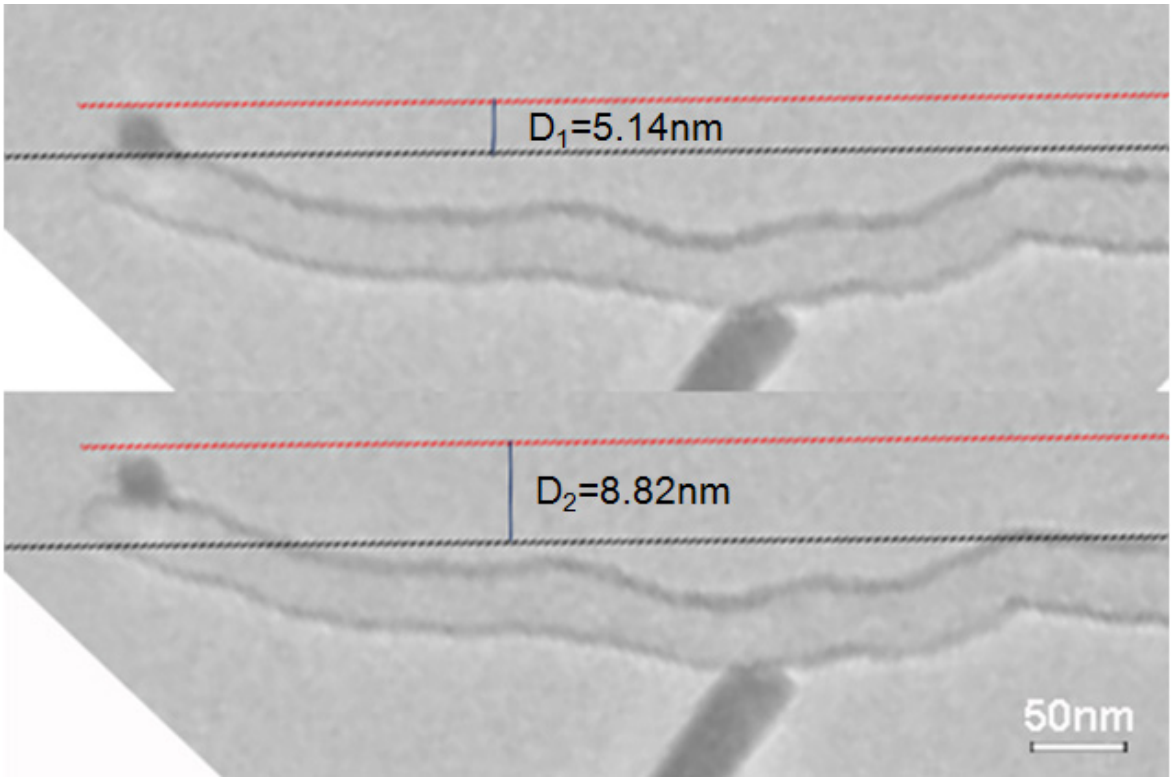

Figure 3.13: The impacting test of a CNT. The blue line is a reference line to the CNT, and the red line shows the top position of it. The distance between the tip of the CNT and the reference line before the impact is 5.14 nm. After the impact, the distance increased to 8.82 nm. Therefore, the deformation here is 3.68 nm, and the correspondent impact force is 187.8 pN. According to the change of resistance during this approach is 0.95 kΩ, then the parameter δ is calculated as 5.07 Ω/pN.

To obtain the parameter δ, we consider the situation that the probe impacted the CNT without the sliding movement. The affect of the sliding process can thus be ignored. The current is measured continuously during this approach. Therefore, the current fluctuation can be recorded. Before the impact, the distance between the tip of the CNT and the reference line is 5.14 nm (see Figure 3.12). After the impact, the distance increases to 8.82 nm. The deformation is calculated to be 3.68 nm. The corresponding impact force is 187.8 pN, and the resistance change during this approach is 0.95 kΩ. The parameter δ is then calculated to be 5.07 Ω/pN.

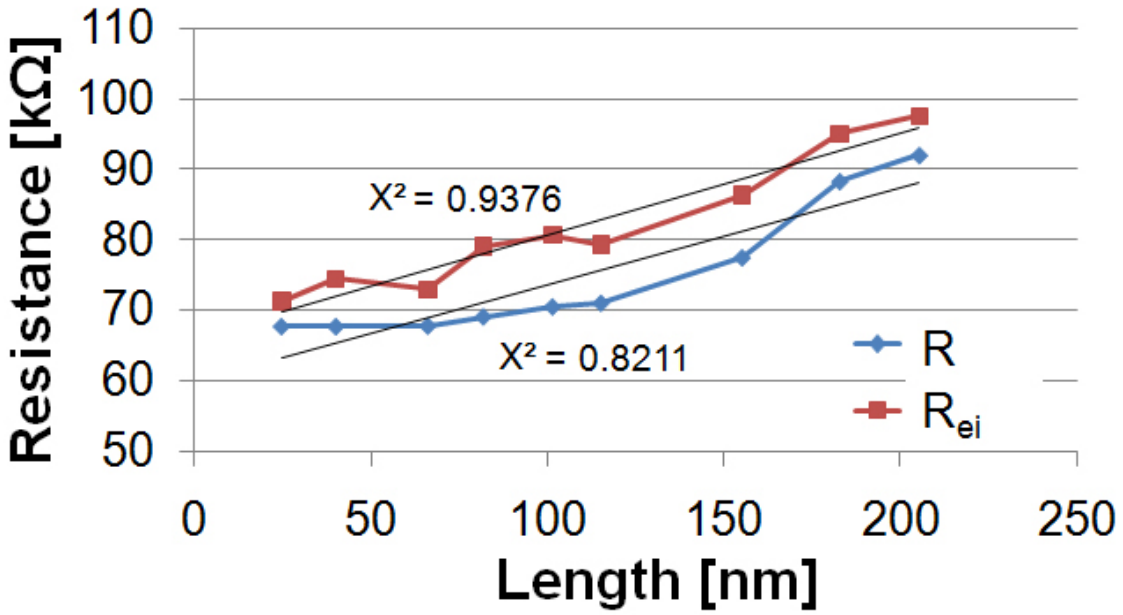

Figure 3.14: The resistance versus length curve during the sliding process. The *R-L* curve represents the resistance before the elimination of the impact force influence versus the length of CNT, which can be fitted by a one-order curve with the appropriateness of 0.8211. After the elimination of the impact force influence, the correspondent R_{ei}-*L* curve has an improved fitted appropriateness of 0.9376.

As a result, the resistance of the CNT after eliminating the influence of the impact R_{ei} can be expressed as $R_{ei} = R - \Delta R$. The R^2 of the one-order fitted curve reaches up to 0.9376, as shown in Figure 3.14, which is a significant improvement over the previous approach. The fitted first-order equation is given by:

$$R_{ei} = 0.1449L + 66.162 \tag{11}$$

Moreover, the resistivity of a single conductor is given by:

$$\rho = R / L \bullet A \tag{12}$$

The differential sliding process consists of countless small steps. Each step represents a single measurement of the nanostructure. Therefore, the resistivity of single measurement is:

$$\rho_i = \Delta R_i / \Delta L_i \bullet A_i \tag{13}$$

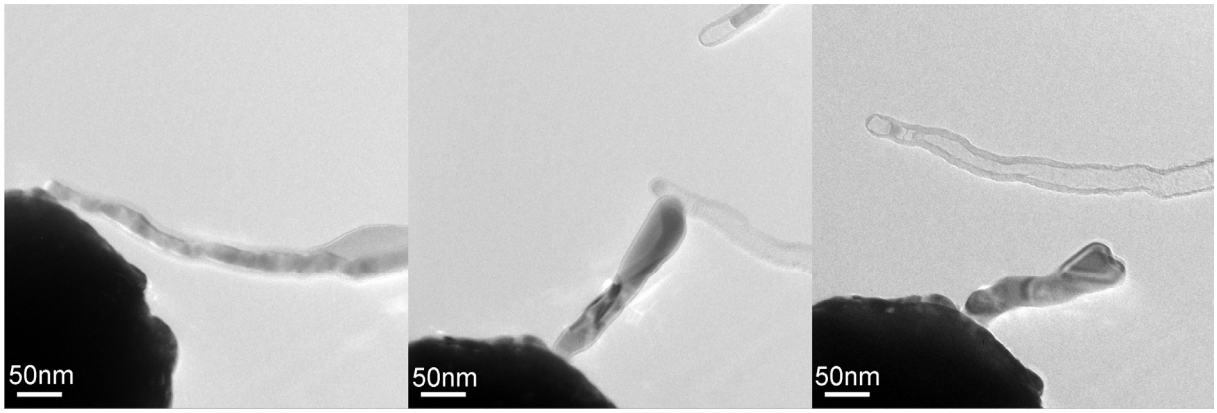

Figure 3.15: Shape adapted probe fabrication. By repeatedly attaching the CNT to the copper stick, the deposited copper tip would be reheated and reshaped to a perfectly adapted shape of the tip to the specimen.

The resistance increases gradually as the probe slides along the CNT and corresponding *RL* curve fits to a first-order function. Therefore, the $\Delta R/\Delta L$ is the same for each measurement, which can be expressed as a differential formula $dR(L)/dL$. Then, the average resistivity ρ' is given by:

$$\rho' = dR(L)/dL \bullet A' \qquad (14)$$

where A' is the average cross section area (390 nm^2) of the CNT. From equation (4), $dR(L)/dL$ is calculated to be 0.1449 kΩ/nm. The average resistivity is then obtained as 5.65×10^{-5} Ω·m. This value is comparable to the four point measurements of a supported, multi-walled carbon nanotube, where the resistivity is about 1×10^{-5} Ω·m with a cross section area of about 200 to 314 nm^2 [51].

Measuring the non-uniform nanostructure by using a soft probe differential sliding method is a good approach with the advantages of high accuracy and simplicity; however, for nanostructures with local defects or are hetero-structured, the soft probe method may not precisely reveal their electrical properties. Because the contact area changes during the soft probe sliding, the value of contact resistance is variable, which in turn influence the measured electrical

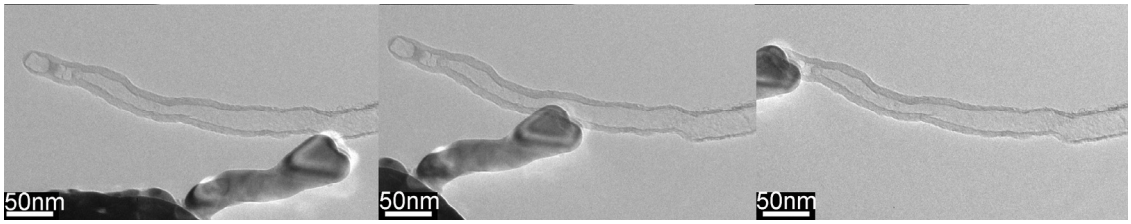

Figure 3.16: The shape adapted sliding process, which may improve the accuracy by keeping a constant contact resistance.

property. Here we propose a shape-adapted probe sliding method, which is significant useful for keeping a constant contact area between the probe and the specimen. As shown in Figure 3.15, by using the EMBD technique, the metal inside a CNT would flow out against the specimen. It is possible to reheat and reshape a deposited metal by repeatedly attaching the CNT to the metal stick [39]. Subsequently, a perfectly adapted shape of the tip to the specimen can be fabricated after the copper has cooled down. The adapted probe sliding method is a new technique for characterization the electrical transport properties of irregular shaped nanostructures. By combinaning of the adapted probe tip and the soft probe differential sliding method, the stick-slip motion can be avoided and the contact force and area are under control, as shown in Figure 3.16. This approach will be possible to keep a constant contact resistance between the sliding probe and the specimen, hence significantly improve the measurement resolution. The feasibility and the accuracy of this method enable us to explore the detailed electrical properties of one single nanostructure in a highly efficient way.

3.4 Chapter Summary

To characterize the transport properties of individual nanostructures, we have developed several enhanced *in situ* techniques for multipoint sliding methods including multipoint continuous sliding, flexible probes, and specimen-shape adapting based on nanorobotic manipulation inside

a TEM. Using a copper-nanowire-tipped probe, we illustrated that a flexible probe facilitates the contact force control. Adapting the shape of the tip is essential for keeping a constant contact area between the probe and the specimen. This was implemented by using a copper tip with a shape resembling the profile of the specimen. The tip was prepared by flowing copper from a copper-filled nanotube against the specimen. By controlling the contact force and area, it becomes possible to keep a constant contact resistance between the sliding probe and the specimen, hence significantly improving the measurement resolution. Sliding probe methods are *in situ* techniques characterized by higher resolution and simplicity in setup compared with conventional two- and four-terminal methods, respectively. Furthermore, they are superior for local property characterization, which is of particular interest for hetero-structured nanomaterials and defects detection.

CHAPTER 4

SPHERE-ON-PILLAR OPTICAL NANO-ANTENNA

After studied the application of NFP in sliding probe characterization, the controlled fabrication of metal nanospheres on nanotube tips for optical antennas is investigated experimentally, which opens a ground for the nanorobotic end-effectors in the advanced characterization. Resembling soap bubble blowing using a straw, the fabrication process is based on nanofluidic mass delivery at the attogram scale using metal-filled carbon nanotubes (m@CNTs). Two methods have been investigated including electron-beam-induced bubbling (EBIB) and electromigration-based bubbling (EMBB). EBIB involves the bombardment of an m@CNT with a high energy electron beam of a TEM, with which the encapsulated metal is melted and flowed out from the nanotube, generating a metallic particle on a nanotube tip. In the case that the encapsulated materials inside the CNT have a higher melting point than that of the beam energy can reach, EMBB, the simplified version of the NFP that without the mass reservoir is an optional process to apply. Experiments show that, under a low bias (2.0 - 2.5V), nanoparticles can be formed on the nanotube tips. The final shape and crystalline of the nanoparticles are determined by the cooling rate. Instant cooling occurs with a relatively large heat sink and causes the instant shaping of the solid deposit, which is typically similar to the shape of the molten state. With a smaller heat sink as a probe, it is possible to keep the deposit in a molten state. Instant cooling by separating the deposit from the probe can result in a perfect sphere. Surface and volume plasmons characterized with electron energy loss spectroscopy (EELS) prove that resonance occurs between a pair of the as-fabricated sphere on the tip structures. Such spheres on pillars can serve as nano-optical antennas and will enable devices such as scanning near-field optical microscope (SNOM)

probes, scanning anodes for field emitters, and single molecule detectors, which can find applications in bio-sensing, molecular detection, and high-resolution optical microscopy.

4.1 Introduction of the Metal-Filled Carbon Nanotube-Based Sphere-on-Pillar Optical Nano-Antenna

Spherical nanostructures on pillars (tubes or wires) can function as optical antennas [52-56] for apertureless scanning near-field optical microscopy (SNOM) [57, 58], laser trapping [59, 60], or single molecule detection [61, 62] in nanophotonic systems and scanning anodes for field emitters [63] in vacuum nanoelectronic devices. A variety of techniques have been developed to fabricate metallic nanostructures on a cantilever tip or an optical fiber using inversed self-assembly grafting [64], wet-chemistry surface assembly [65], water-flow suction [66], photocatalytic deposition [67], and optical trapping [68]. However, the controlled attachment of individual nanoparticles on nanopillars has been shown to not yet feasible [69].

Metal-filled CNTs (m@CNTs) are ideal building blocks for nano-sized end-effectors due to their well-defined structures and remarkable mechanical/electrionic properties. The hollow cavities of CNTs allow a variety of metals such as Au, Ag, Cu, Sn, Fe, Co, and Ni and their alloys to be encapsulated inside the core [33, 70-73]. Mimicking soap bubbles blown from a straw, the encapsulated metal may be bubbled over the nanotube tip if they can flow out and stay/remain on the tip. Previously investigated electron-beam-induced flowing and extruding [74-76] and current-driven electromigration can be applied. However, several challenges remain due to the uniqueness of sphere-on-pillar structures, extruded materials or deposits must be spherical and stay/remain on the tube tip: (1) Previous investigations demonstrated that the

exposure of m@CNTs under a high intensity electron beam resulted in the expansion, melting and flowing of the encapsulated materials, and potential applications such as thermometers and extruders have been demonstrated [74-76]. However, a further step to flow these materials out from the nanotube onto the orifice is yet to be investigated. (2) It is know that irradiation of nanotubes can cause large pressure build-up within the nanotube cores that can plastically deform, extrude, and break solid materials [75]. The effects of the pressure on molten metal are still unclear. (3) Mass melting, flowing, evaporation, and deposition based on electromigration have been realized inside a nanotube [9], between nanotubes [77], and from a nanotube to other objects [6, 33]. These have enabled new techniques [78] such as nanorobotic spot welding [6] and devices such as archival memories [9]. However, controlling the shape of the deposits was beyond the scope of these applications.

Based on these insights, here we show fabrication processes specifically designed for delivering and depositing the encapsulated materials from m@CNTs onto their tips, with the goal of achieving controllable sizes and shapes. The processes are collectively named nanobubbling and include electron-beam-induced bubbling (EBIB) and electromigration-based bubbling (EMBB). The sizes of the spheres will be determined by mass flow rate and time, and the maximum sizes are limited by the total mass encapsulated. The final shapes of the deposits will be influenced by the cooling rate. Instant cooling will result in a shape similar to that in the molten status, whereas a slower cooling rate will cause recrystallization. A molten sphere will become crystal if cooled instantly or a solid sphere if cools slowly, because surface tension dominates the recrystallization so that a ball with high sphericity can be formed. Hence, heat sink conditions will be key to the fine shaping of the spheres by controlling the cooling rate [39].

4.2 EBIB

Our EBIB experiments were performed in a TEM (JEOL 2200FS) with a field emission gun. The samples we used included Sn- and Cu-filled CNTs (Sn@CNTs and Cu@CNTs). The Sn@CNTs were synthesized by using catalytic deposition of acetylene using SnO_2 [76]. During the process, the catalysts were directly placed into the furnace without preheating and reduction. The diameters of Sn@CNTs ranged from 20 to 80 nm. Sn cores were single crystals with good crystallization.

The setup of the EBIB is illustrated in Figure 4.1(a). During the EBIB, the current density of the electron beam transmitted through the CNTs was adjusted by changing the focus, magnification, brightness, and incident area. The final shapes can be either spheres or particles with multiple facets, and are related to the heating and cooling processes. The size of the spheres on the tips was found to be related to the exposure time and the orifices of the nanotube. A series of time-resolved TEM images, demonstrated in Figure 4.1(b), show that the EBIB of a Sn@CNT occurred at a current density of 20 A/cm^2 with a magnification of ×300 K and an irradiation area of 1.3×10^{-14} cm^2. The accelerating voltage of the electron beam was kept at 200

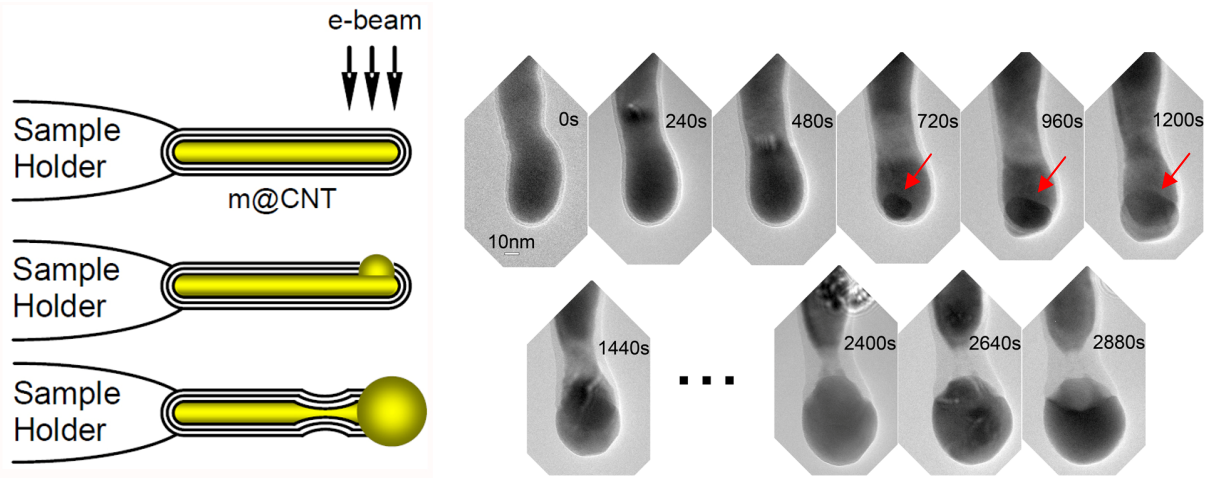

Figure 4.1: (a) The setup of EBIB, (b) Time-resolved EBIB processes.

kV in all experiments. Increasing the current density increase the local temperature due to the higher electron energy. Starting from an as-synthesized Sn@CNT, a nanosphere was formed on the tip of the CNT by exposing the electron beam. At t = 720 s (Figure 4.1(b)), the inner molten metal broke out from the nanotube. In our previous investigations, we observed that the Sn nanowire melted completely in the CNTs when the current density reached 0.4 A/cm^2, and expansion of the Sn wire occurred at the same time [76]. The much higher current density needed here (20 A/cm^2) is caused by the bubbling of the molten metal. At the beginning of the process, polyhedral nanoparticles (Figure 4.1(b), 1200 s) were formed. By increasing the temperature further, it was possible to convert polyhedral nanoparticles into spheres (Figure 4.1(b), 2880 s) [79]. We attribute the bubbling and the shape conversion to the electron irradiation and the secondary effects, including the carbon shell contraction and the surface tension of the molten metal. The encapsulated materials were melted and then squeezed out onto the tip of the nanotubes. Applying an image processing method, we analysed the mass of the

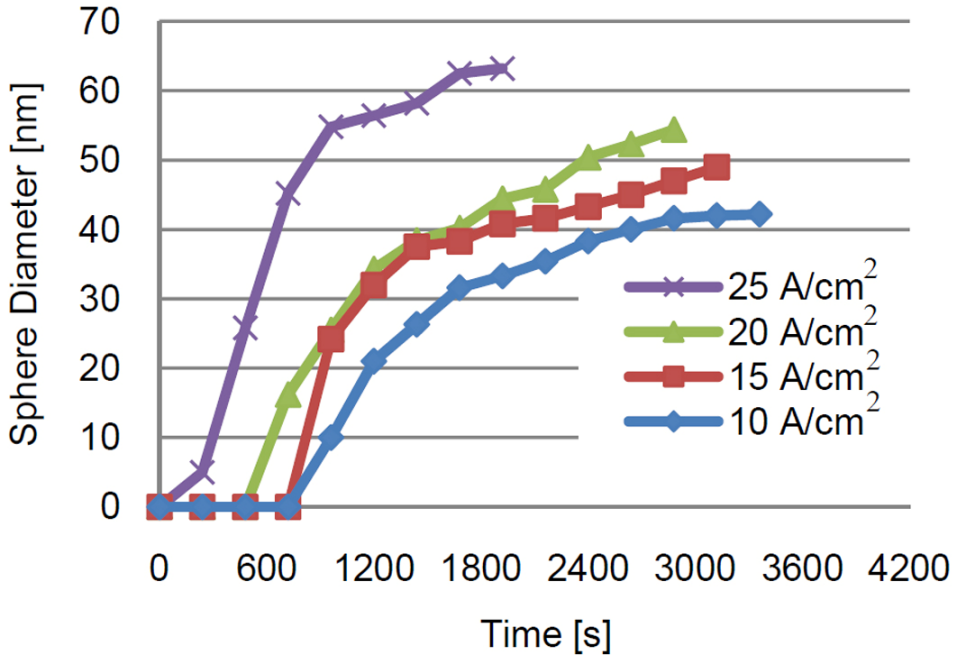

Figure 4.2: Time sequences of bubbling differed at different current densities and tube sizes.

sphere. The CNT had an external diameter of approximately 40 nm. The diameter of the final sphere was 54 nm, and the mass of the resulting sphere was 0.6 fg (femtograms) according to the density of Sn (7.31 g/cm^3).

We found that the threshold current density for sphere formation was 20 A/cm^2 at an exposure time of ~720 s. Experiments with several other CNTs showed that the threshold current density varied from 10 to 25 A/cm^2 depending on their diameters (37-40 nm). The relations between the bubbling times vs. the diameter of the sphere are depicted in Figure 4.2. The starting time of the migrating was shortened with increasing irradiation energy. The starting time decreased from 700 to 200 s for current densities from 10 to 25 A/cm^2, and bubbling time varied from 1900 to 3360 s. These variations may be related to the temperature and pressure build-up

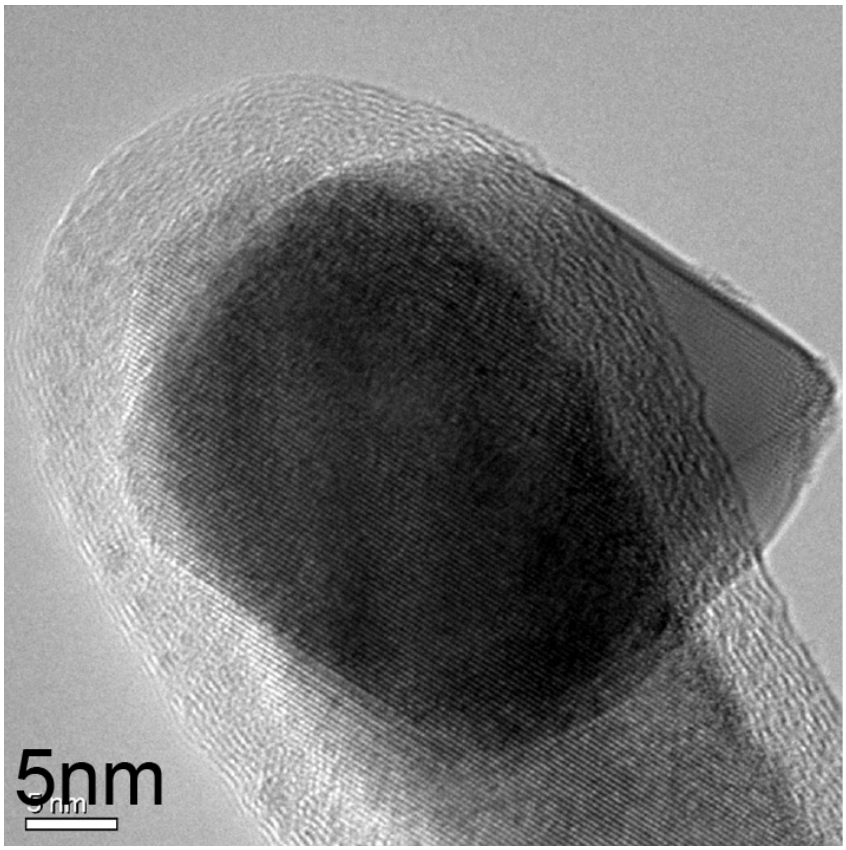

Figure 4.3: As the e-beam exposure suddenly stopped during EBIB, the squeezed-out metal recrystallized and resulted in a facet shape.

inside the CNT.

According to our experiments, the EBIB process consists of two parts, i.e., the melting of the inner metal and the shrinkage of the carbon shells. The melting was caused by the heating of the Sn by irradiation as shown in previous work [76]. The observed contraction of the carbon shells (Figure 4.1(b), 720 to 1440 s) is responsible for the extrusion out of the sphere from the nanotube shell. The contraction is caused by electron beam irradiation of CNTs, which generate a high pressure within the nanotubes that can deform and extrude the metals from them [75]. Moreover, the final shape of the nanostructure on the tip is largely dependent on whether the encapsulated materials are sufficiently melted. Sufficiently melted materials result in a perfect sphere in the molten state and that shape can be kept if cooling occurs instantly. Gradual cooling will allow the particle to recrystallize, generating a facet structure as shown in Figure 4.3. The cooling rate is mainly determined by the incident beam energy and its dissipation from the nanotubes. It is possible to remelt and reshape the sphere by injecting more thermal energy. Thus, the full process of EBIB is as follows: the ruptures of the carbon planes create defects on the carbon shells, and then the bubbling occurs at these sites. The internal pressure build-up is a result of melting, the thermal expansion of the encapsulated metal, and the shrinkage of the nanotube shells [75], which are all determined by the current density. Therefore, the rates of nanobubbling and geometry of the spheres can be controlled by adjusting the current density.

4.2 EMBB

4.2.1 EMBB on a Conductive Surface

The EBIB procedures were also applied to Cu@CNTs, but bubbling did not occur at the highest possible current density, indicating that the e-beam from the TEM cannot reach the melting point

of copper (1083°C). As an alternative method, EMBB was applied for Cu@CNTs. The setup of EMBB is depicted in Figure 4.4, which is similar to the NFP. The FM2000E STM-TEM holder mentioned above was adopted for the experiments, and was used for positioning in a millimeter-

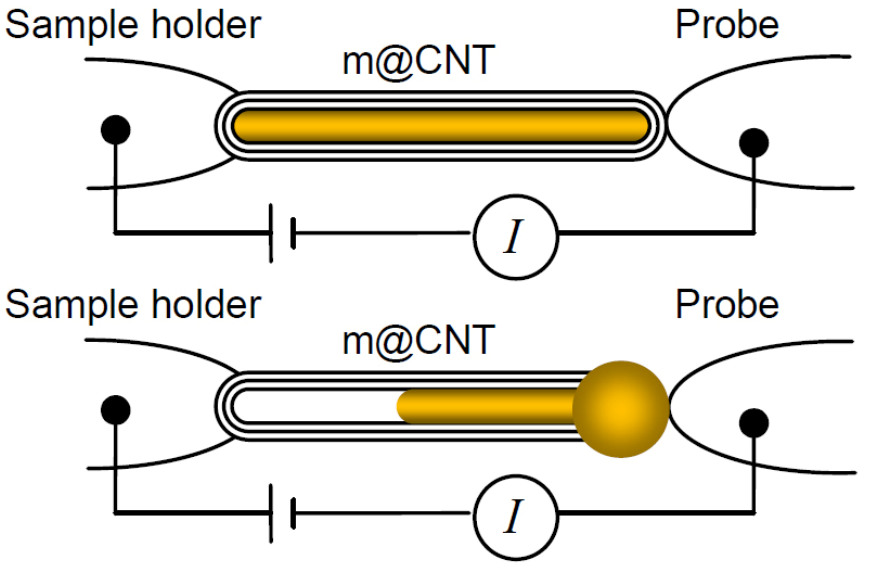

Figure 4.4: The schematic of the electromigration-based bubbling.

scale workspace with subnanometer resolution, with the STM unit actuated by a three-degree-of-freedom piezotube, making it possible to select a specific CNT. Physical contact was made between the probe and the tip of a nanotube. Applying a voltage between the probe and the sample holder establishes an electrical circuit through a CNT and injects thermal energy into the system via Joule heating. By increasing the applied voltage, the local temperature can be increased past the melting point of the copper encapsulated in a tube. Then, the encapsulated materials are delivered from the carbon shells, and nanospheres are bubbled over the CNT tips. The EMBB process is similar to nanorobotic spot welding, but the focus is on the shape and size control of the deposited spots. During the experiments, the intensity of the electron beam was kept in the range appropriate for regular imaging, which is several orders of magnitude lower than the values for EBIB.

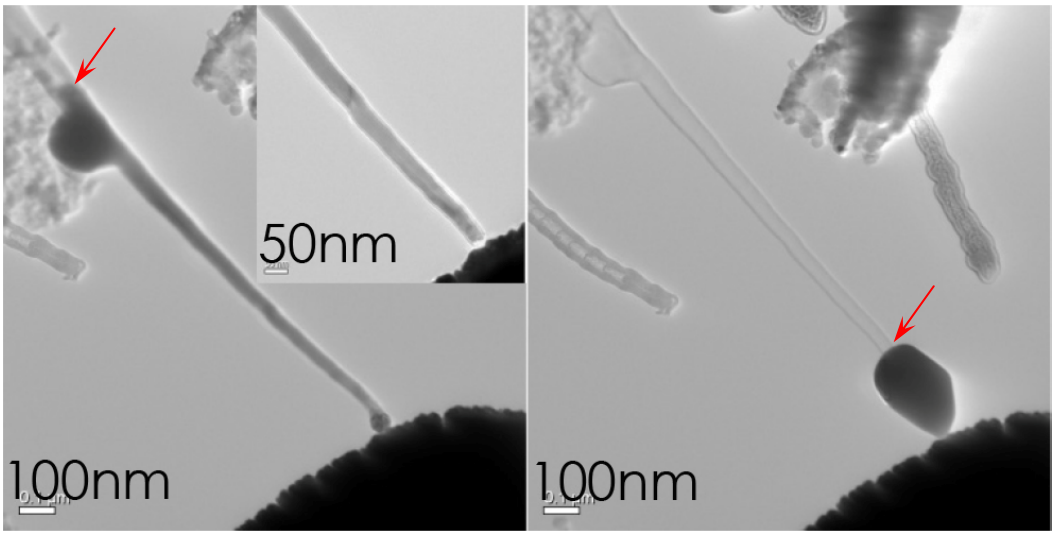

(a) (b)

Figure 4.5: A sphere on the tip formed by EMBB (a) Before the EMBB process, (b) As-formed bubble.

In the experiments, a Cu@CNT tip was first brought into contact with the STM probe, and then a bias voltage was applied to the two ends of the CNT. Figure 4.5(a) and (b) shows that with the voltage increase from 0 V in steps of 0.1 V, the inner copper core quickly flowed out to the tip of the CNT when the voltage reached the range between 2.0 V to 2.5 V. The process was recorded in a real-time video, and selected video frames of the melting process (Figure 4.6) reveal that a copper polyhedral nanoparticle was formed initially on the tip of the tube. Then, by increasing the bias further (the temperature and the driving force will be increased accordingly), a spherical particle formed on the tip of the nanotube. In this experiment, the migration of the copper started at 2.4 V and the entire process lasted about 17 s. The flow rate was found to be 82.3 nm/s according to the movement of the copper through the nanotube (Figure 4.6). The current vs. voltage (*I-V*) curves in Figure 4.7(a) were obtained before and after the copper flowed out. Comparison between the two IV curves can be found that the CNT before flowing is larger than that after the flowing occurred. The current change is a result of the exposure of the carbon

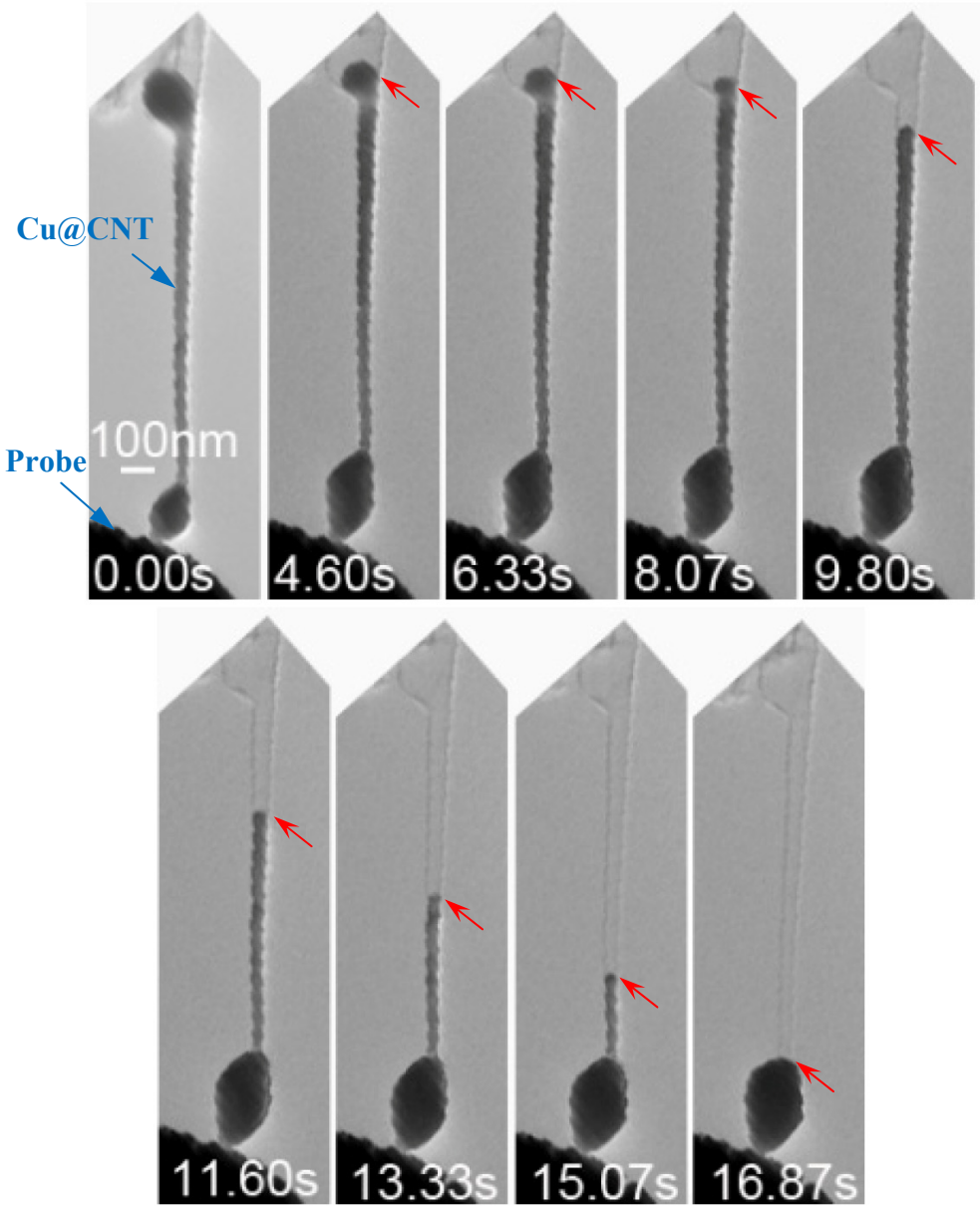

Figure 4.6: EMBB processes. The tip of Cu@CNT was physically contacted with the probe. Applying a voltage between the probe and the sample holder establishes an electrical circuit through a CNT and injects thermal energy into the system via Joule heating. By increasing the applied voltage, the local temperature can be increased past the melting point of the copper encapsulated in a tube. Then, the encapsulated materials may deliver from the carbon shells, and nanospheres are bubbled over the CNT tips in a short time (16.87 s).

shells due to the loss of the encapsulated copper, which has better conductivity than the carbon shells. The current-time (*I-t*) curve in Figure 4.7(b), simultaneously recorded by a multimeter during the copper migration, also showed that the current decreased along with the flowing time.

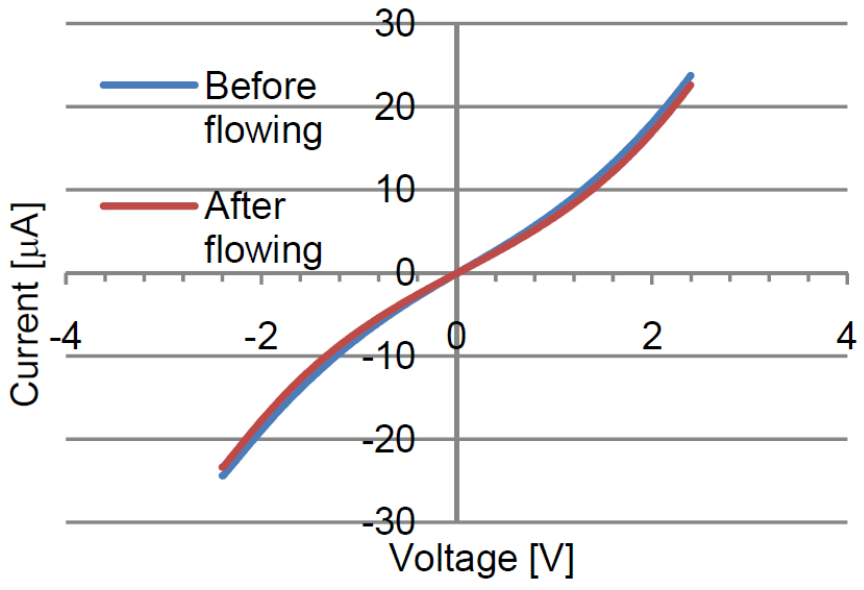

(a)

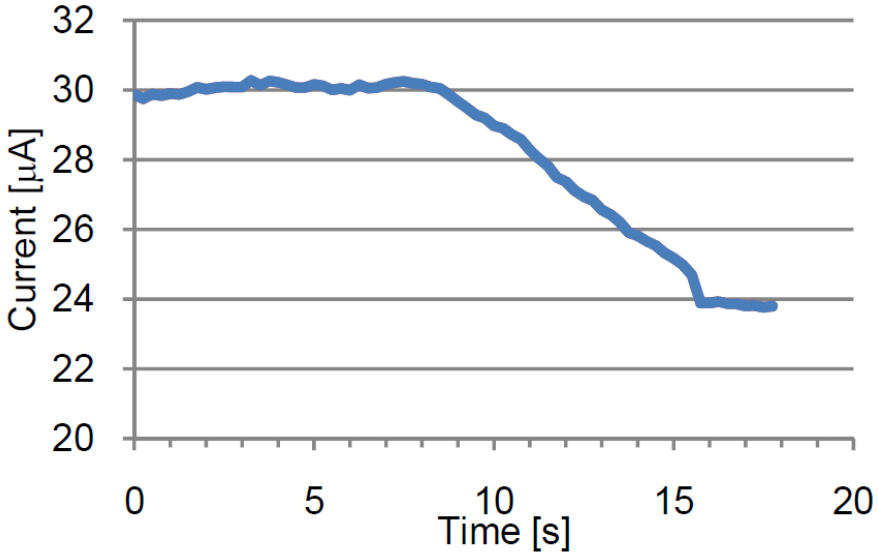

(b)

Figure 4.7: (a) I-V characterization before and after the flowing. (b) I-t characterization during EMBB.

Accordingly, the current density under the bias of 2.4 V dropped from 2.38×10^6 to 1.98×10^6 A/cm^2, causing the cooling of the deposit at the orifice. Moreover, heat dissipation increased as more copper reached the probe. As the volume of the probe (tip radius: 70 nm, root radius: 10 μm) is absolutely larger than that of the copper deposit, the probe serves as a heat sink with

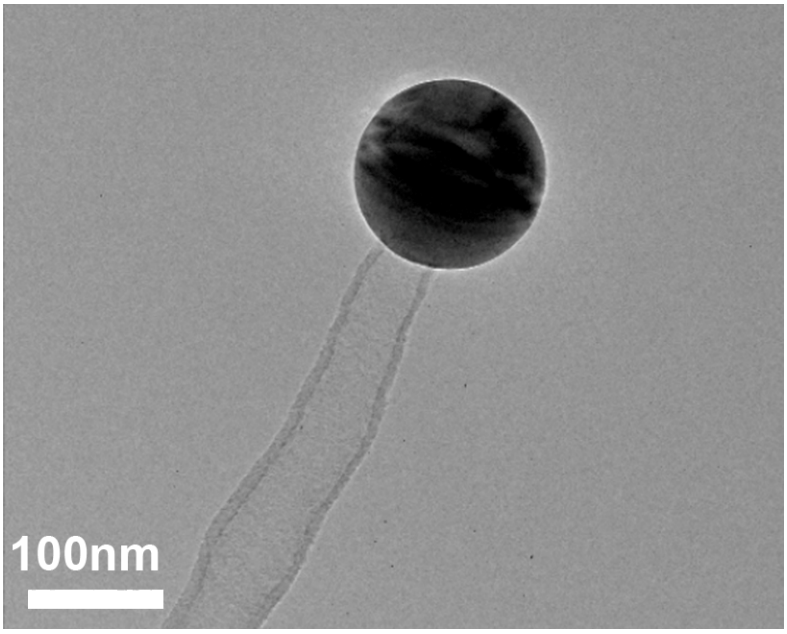

Figure 4.8: The sphere on a nanotube induced by a small probe. The small size of the probe makes it possible to keep thermal energy on the particle, which makes it remain in molten state and shape the particle into a perfect sphere. By separating the molten sphere from the probe, the spherical shape was kept.

essentially infinite capacity compared to the copper deposit. Hence, it was not possible to reheat the copper after cooling. This can also explain why the flowed out copper crystallized immediately while the bias stayed unchanged, and in most cases, without increasing the bias during the migration, polyhedral nanoparticles will form. Similar to the role of heat sinks in electric breakdown of CNTs [27, 29], the shape of the deposits is largely influenced by the thermal energy distribution and dissipation during the EMBB process. The deposit in Figure 4.5 illustrates that the large probe serves as a huge heat sink, which possesses excellent thermal conductivity to cool the particle in a short time. The reheating or reshaping is impossible due to the minimum distribution of thermal energy at the deposition site between the nanotube tip and the probe (heat sink). On the contrary, if a small probe is used, the spherical deposit can stay in molten state and appears as a sphere due to surface tension. Figure 4.8 shows that a sudden cooling by separating the deposit from the biased probe can result in a perfect sphere. The

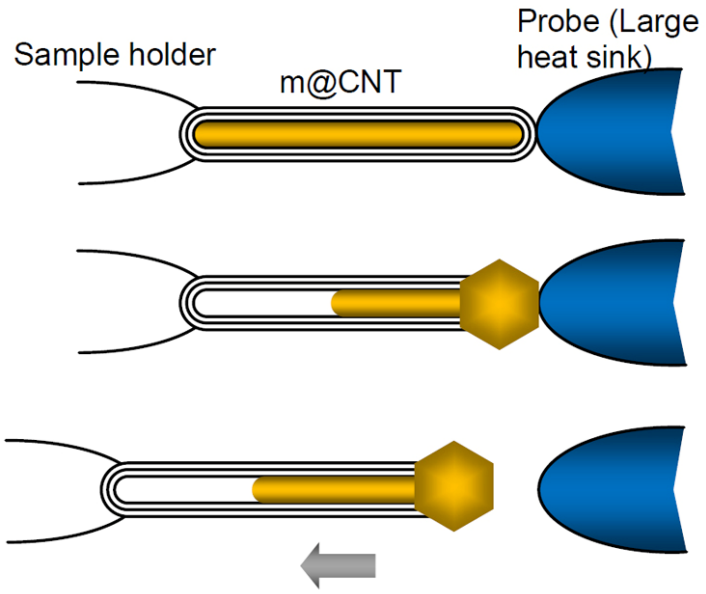

(a)

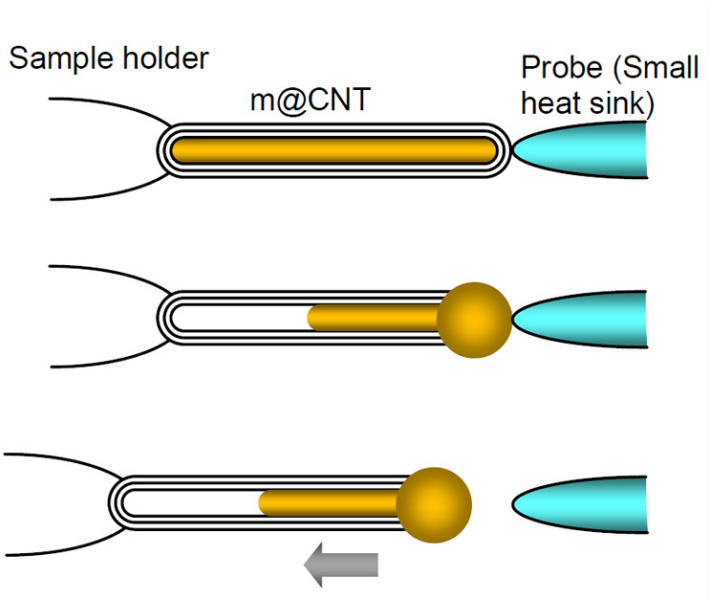

(b)

Figure 4.9: (a) The EMBB with a large probe serving as a large heat sink; (b) The EMBB with a probe serving as a small heat sink.

influences of the volumes of heat sinks are schematically illustrated in Figure 4.9(a) and (b). If a large heat sink exists, separation of the nanoparticle from the probe is not always achievable, i.e., the nanotube will be soldered onto the probe. A CNT can serve as an ideal heat sink. Due to the

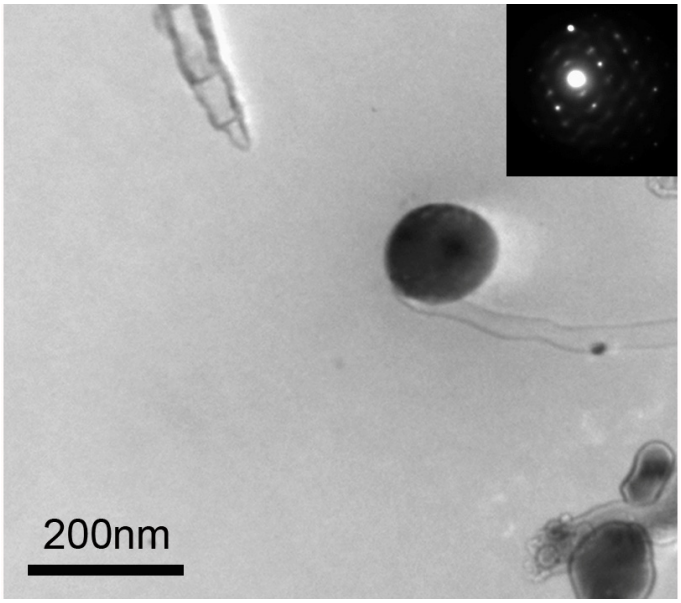

(a)

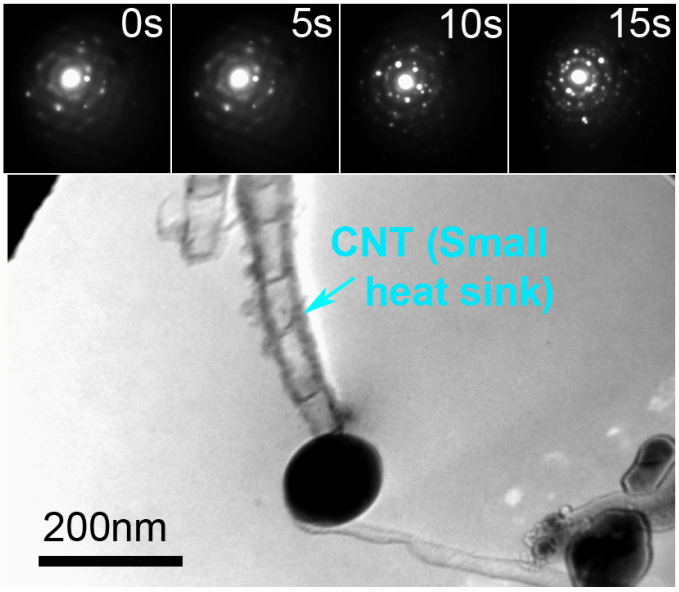

(b)

Figure 4.10: (a) The copper sphere on a nanotube induced by a CNT which served as a small heat sink. Inset illustrates that the cooledsphere shows a single crystal diffraction pattern, (b) Reheating/remelting can be achieved by placing the sphere on the tip of CNTs. Insets show the transformation of the sphere from single crystal to poly crystal, which represents the gradual melting process.

uniform size distribution to the m@CNT, the hottest spot can be positioned close to the contact point between the tips of two different CNTs where the bubble will be blown out. The probe

CNT can also be used to reheat and reshape the nanoparticles obtained either from EBIB or EMBB (with a large heat sink). An example is shown in Figure 4.10(a) and (b). A deposit was generated by EMBB under a bias of 2.4 V (Figure 4.10(a)). The apparent shape of the deposit was spherical and the selected area electron diffraction (SAED) shows that the crystalline level was high although a perfect SAED pattern was unattainable due to the orientation of TEM holder. Reattaching the CNT tip to the sphere and increasing the bias from 1.0 V in steps of 0.2 V, melting occurred again as the voltage reached 2.0 V. The particle started to melt and the diffraction pattern gradually changed (Figure 4.10(b), inset). In the beginning of melting (0 s), the diffraction pattern showed a highly crystallized phase. And then, as the heat temperature was increased accordingly, the crystal phase gradually transformed into a more polycrystalline phases at 5, 10, and 15 s.

4.2.2 EMBB on a Non-Conductive Surface

Application of EMBB to a non-conductive surface was implemented by using the architecture shown in Figure 4.11(b). The difference in architecture from the conventional one as shown in Figure 4.11(a) is that electromigration will not occur in the entire tube. The tip of the nanotube transfer thermal energy so that the encapsulated materials will be passively pushed out by the materials behind them.

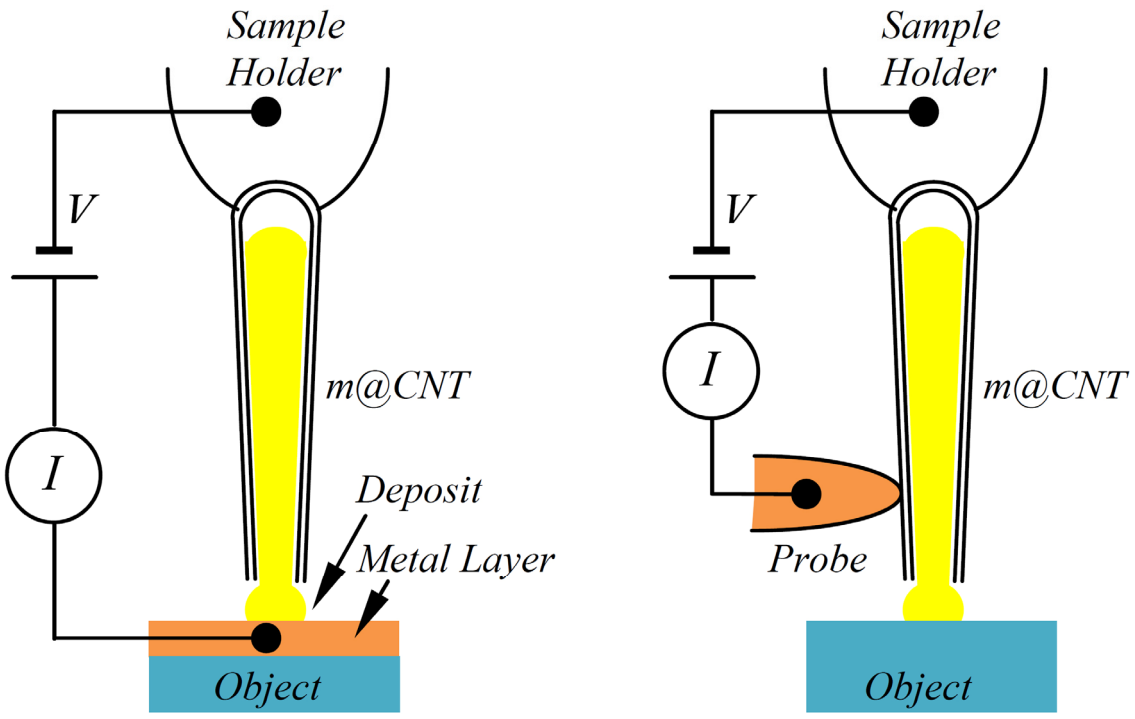

(a) (b)

Figure 4.11: (a) A metal layer on the object surface is necessary to form the electrical circuit for EMBB. (b) By using a probe attached to the side wall of the m@CNT, the surface of the object can made either conductive or insulating.

Applying a voltage between the probe and the sample holder establishes an electrical circuit through the m@CNT and injects thermal energy into the system via Joule heating. By increasing the applied voltage, the local temperature can be increased past the melting point of the copper encapsulated in the tube. Then, the encapsulated materials may separate from the carbon shells, and nanospheres are bubbled out of the CNT tips.

TEM images in Figure 4.12(a) demonstrate EMBB process using the configuration diagramed in Figure 4.11(b). The dark area is the probe tip of the manipulator. The initial mass inside the CNT is estimated to be 5.7 fg at 0 s based on high-resolution TEM images. At 663 s, 4.4 fg (77.2%) was deposited while the remaining mass evaporated and/or diffused onto the surface of the probe. At 0 s, there was an empty section close to the tip of the CNT, which was filled at 420 s, showing that the flow started inside the CNT. The extra sphere at the CNT tip was

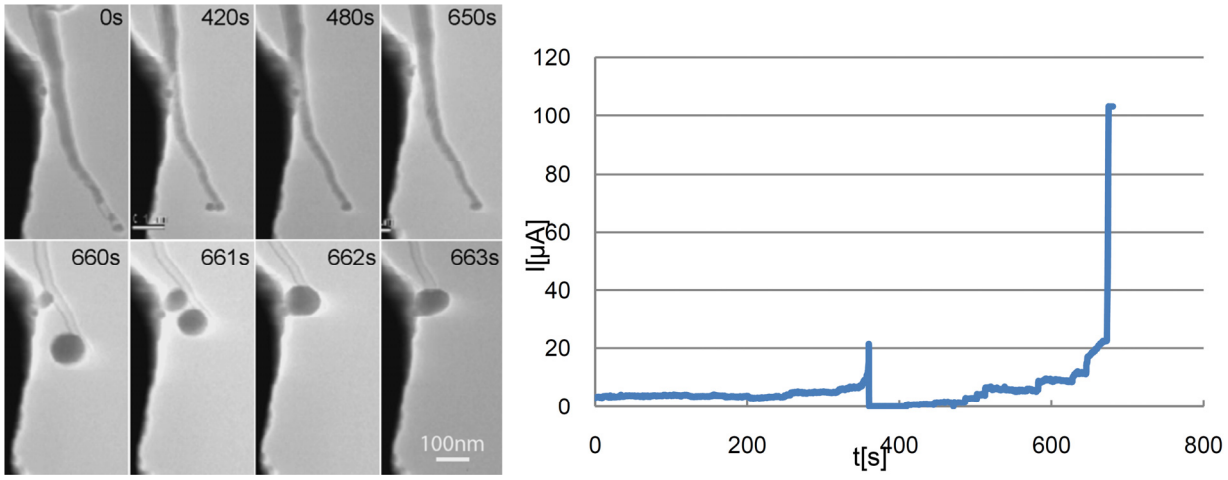

(a) (b)

Figure 4.12: (a) TEM images recorded the EMBB using the configuration shown in Figure 2.2.11(b). The initial mass inside the CNT is estimated to be 5.7 fg at 0 s. At 663 s, 4.4 fg (77.2%) has deposited while the rest mass evaporated and/or diffused onto the surface of the probe. It can be seen that at 0 s, there was an empty section close to the tip of the CNT, which was filled up at 420 s; showing that the flow started inside the CNT. The extra sphere at the CNT tip was a result of that. The fact that the transport direction was pointing to the CNT tip confirmed that the electromigration is responsible for this flow. Then, at 480 s, the volume of the sphere at the CNT tip decreased as a result of evaporation. There was no obvious change occurred till the moment at 650 s. At 660 s, within 3 seconds, the CNT was drained off and a large sphere formed on the CNT tip. Because the distance between the deposit and the probe is small and the contact between the probe and the CNT was not firm, the CNT slide back and the deposit dropped onto the probe, (b) The current-time curve recorded during the whole process. The peak at 360 s represent that the contact resistance between the probe and the CNT improved, which was caused by relative slipping of the probe and the CNT. Before and after that moment, no obvious changes of the current have been observed. During the same period, no remarkable mass flow has occurred according to the video. When the flow started at 660 s, an abrupt inflation of the current has been monitored, in the meantime, the CNT was drained off and a large spherical deposit (diameter: 37.5 nm) appeared at the CNT tip.

a result of this continuity. The fact that the transport direction was toward CNT tip confirmed that electromigration was responsible for this flow. Then, at 480 s, the volume of the sphere at the CNT tip decreased as a result of evaporation. No obvious change occurred till the moment at 650 s. At 660 s, within 3 s, the CNT was drained and a large sphere formed on the CNT tip. Because the distance between the deposit and the probe was small and the contact between the probe and the CNT was not firm, the CNT slid (slide is present, slid is past tense) back and the

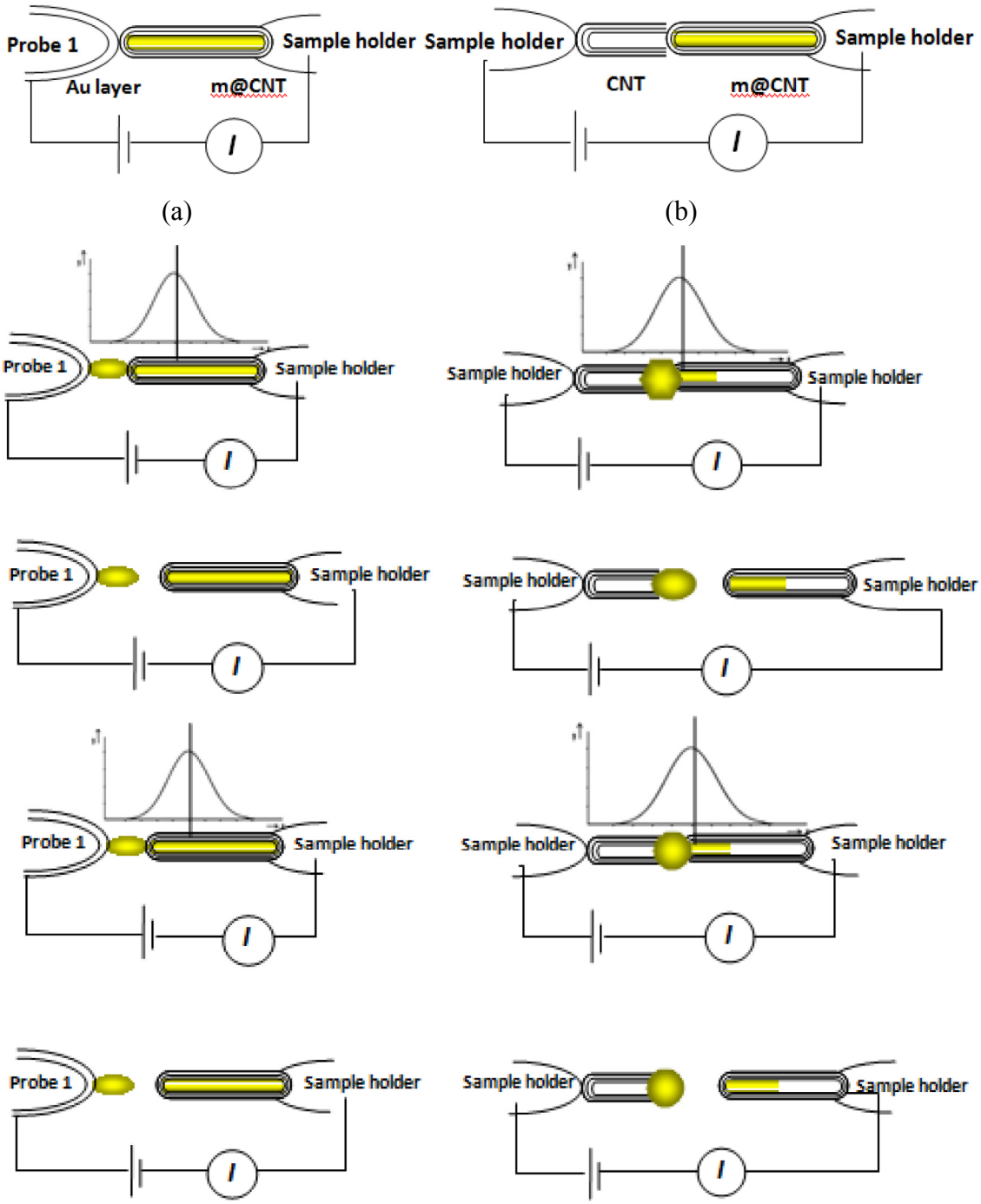

Figure 4.13: (a) The experiment setup for the EMBB on the surface with excellent electric and thermal conductivity, (b) The experiment setup for the EMBB on the surface with resistive surface, (c) The processes for the EMBB against a conductive surface (an Au-coated W-tip), (d) The processes for the EMBB against a resistive surface (an empty CNT).

deposit dropped onto the probe. Figure 4.12(b) shows the current-time curve recorded during the whole process. The peak at 360 s represents that the contact resistance between the probe and the CNT improved, which was caused by slipping of the probe relative to the CNT. Before and after that moment, no obvious changes in the current were observed. During the same period, no obvilus mass flow occurred. When the flow started at 660 s, an abrupt inflation of the current was recorded, while the CNT was drained off and a large spherical deposit (diameter: 37.5 nm) appeared at the CNT tip.

4.3 Shaping the Deposit using the Heat Sink Effect

In order to reveal the factors that determine the geometry of the EMBD deposits, experiments were performed with two setups: (1) the Cu@CNT was positioned against an excellent conductor, and (2) the Cu@CNT was positioned against a resistive surface. Here we used a tungsten probe (length: 10 μm, tip radius: 100 nm) coated by a gold thin film (21 nm thick) for (1), and an empty CNT for (2). The setups for (1) and (2) are shown schematically in Figure 4.13(a) and (b), and the processes are shown in Figure 4.13(c) and (d). Qualitative thermal energy distribution is attached to some panels in Figure 4.13(c) and (d). As illustrated in Figure 4.13(a) and (c), when the Cu@CNT contacts the probe, the heat sinks are located at the interface between the CNT and the probe, where the temperature is the lowest because the larger thermal energy capacitance of the probe than the CNT. Reattaching the Cu@CNT to the deposit once the deposition is complete, the shape of the deposit cannot be changed. In the setup 2, by replacing the probe with an empty CNT, the deposit location will have a higher temperature when the Cu@CNT reattaches to the empty CNT. The deposit will then, be reheated and its shape can be changed.

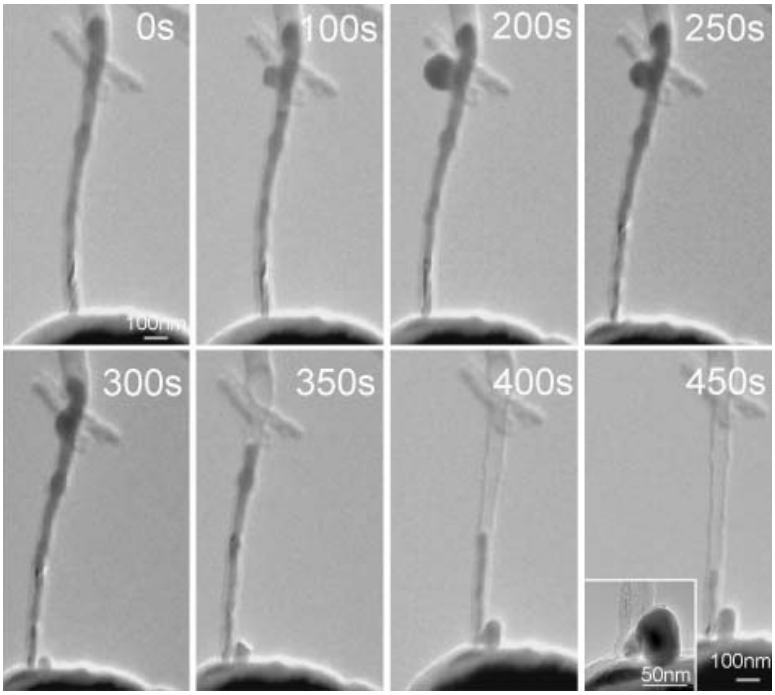

(a)

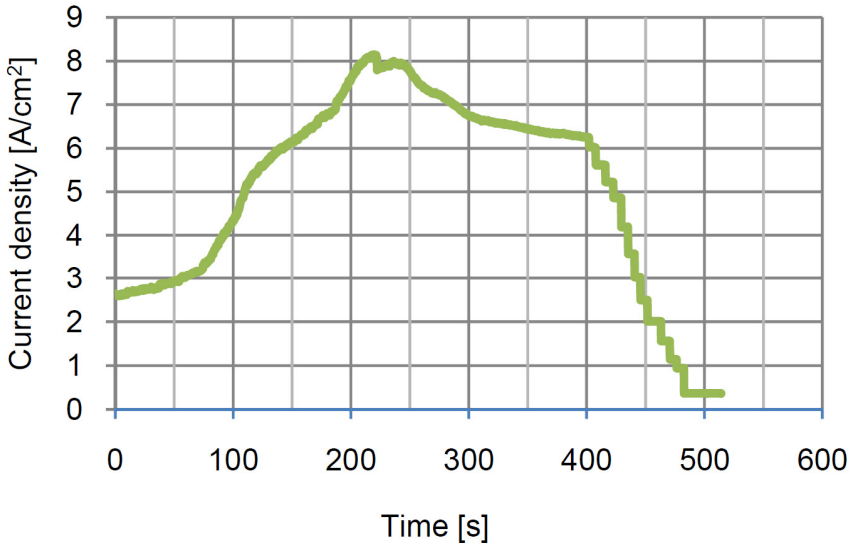

(b)

Figure 4.14: (a) TEM images (frames of a video) of EMBB against a thermal conductive surface; (b) Current density vs. time curve of the EMBB process.

This experiment was designed to confirm that it is impossible to reshape the deposit by EMBB as shown in Figure 4.13(a). But that it can be reshaped by the EMBD as shown in Figure

4.14(a). By increasing the bias from 0 V in steps of 0.1 V, the inner copper core flowed out tof the CNT tip when the voltage reached 2.0 V.

The current density vs. time curves were obtained during the reshaping process, as shown in Figure 4.14(b). An obvious current density drop from a peak of about 8.1×10^6 A/cm^2 occurred at 210 s as the migration began, which we attribute to increased resistance of the tube due to the exposure of the carbon shells, and to the draining of the encapsulated copper, which has better conductivity than carbon [6]. The deposit shape was formed instantly due to the excellent thermal conductivity of the probe, which cools the deposit in a short time. Reheating of the cooled deposit was not possible because the volume of the probe (tip radius: 120 nm, root radius: 10 μm) is larger than that of the copper deposit. The probe serves as a heat sink with essentially infinite capacity compared with the copper deposit. As a result, the EMBD experiment on a surface with excellent thermal conductivity showed that, although the deposition of copper from the nanotube occurred rapidly, cooling the deposit is also instantaneous due to the probe heat sink. Therefore, only if the probe is small enough, then the reheating or reshaping of the deposit is possible.

The same EMBB procedure was applied to a single CNT. Figure 4.15(a) to (c) shows the process of mass delivery to the interconnection of the tips and the shape control of the deposit, and Figure 4.15(d) illustrates the as-fabricated SOP nanostructure. The process was recorded

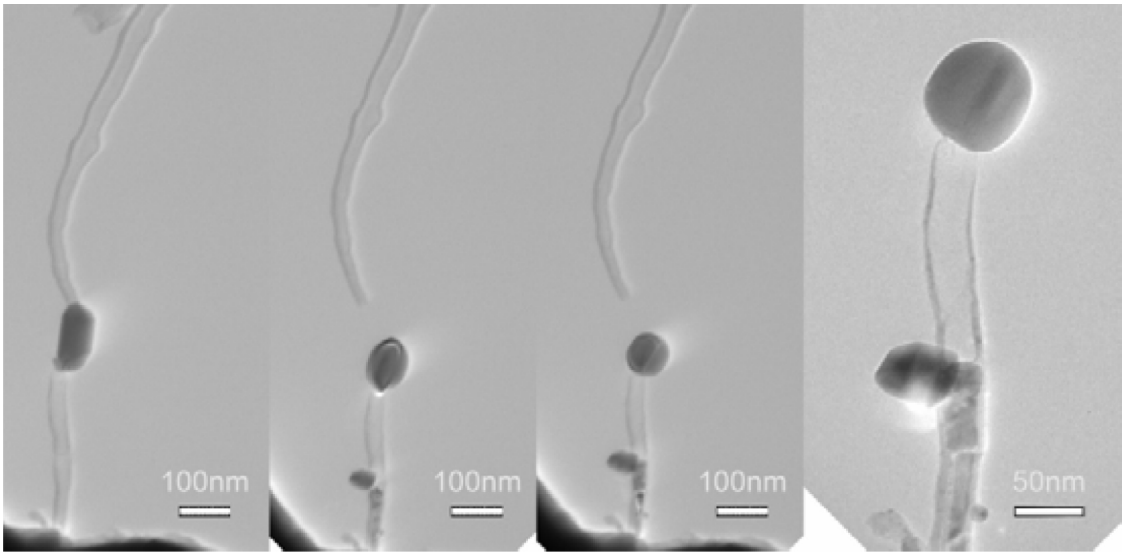

(a) (b) (c) (d)

Figure 4.15: EMBB processes on a thermally/electrically resistive object. (a) Metal flows out from a copper-filled CNT, (b) A spherical deposit on the tip of a CNT by EMBB, (c) EMBB shape control process, (d) Modified nanostructure on the tip.

by real-time video, and the main procedures can be divided into two parts: the EMBB process apply to CNT as shown in Figure 4.16, and the shape control of the deposit is shown in Figure 4.17. In this experiment, the EMBB started at 2.05 V, and the entire process continued for about 191 s. The mass flow rate was found to be 3.27 nm/s according to the changing length of the inner copper core. The extrusion of copper reveals that a copper polyhedral nanoparticle initially formed on the tip of the tube. As shown in the first panel of Figure 4.13, the middle point of the nanotube is the hottest spot. So, we positioned the polyhedral deposit close to the contact point of two CNTs, which is close to the hottest position of the system. Therefore, the deposited metal will remain in the molten state and the shape of polyhedral deposit can be changed.

The shape control of deposit was shown in Figure 4.17. The sphere formed by the above processes cooled when the two tips separated, and was then reheated by reconnecting the two nanotubes. As a result, reshaping of the deposit was achieved by attaching

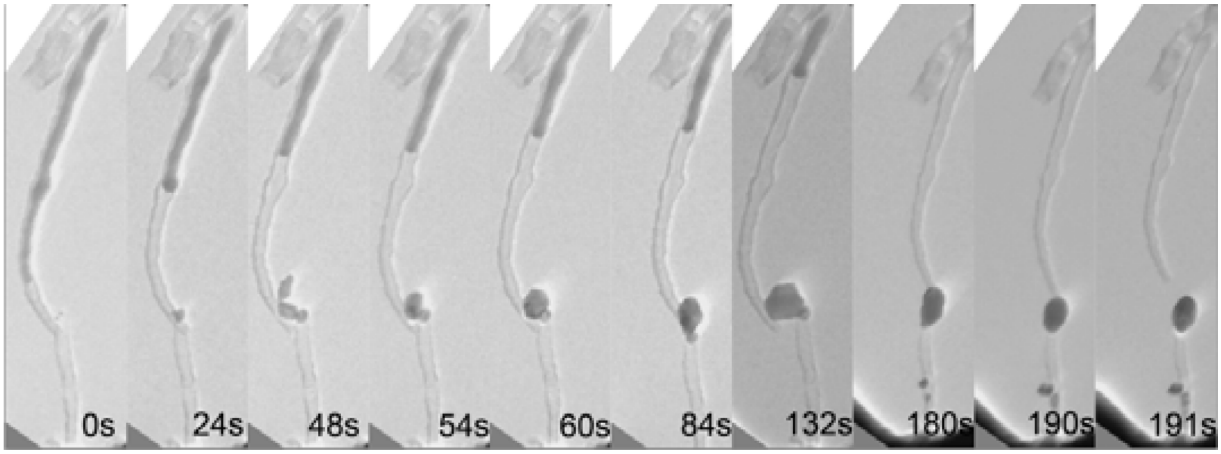

(a)

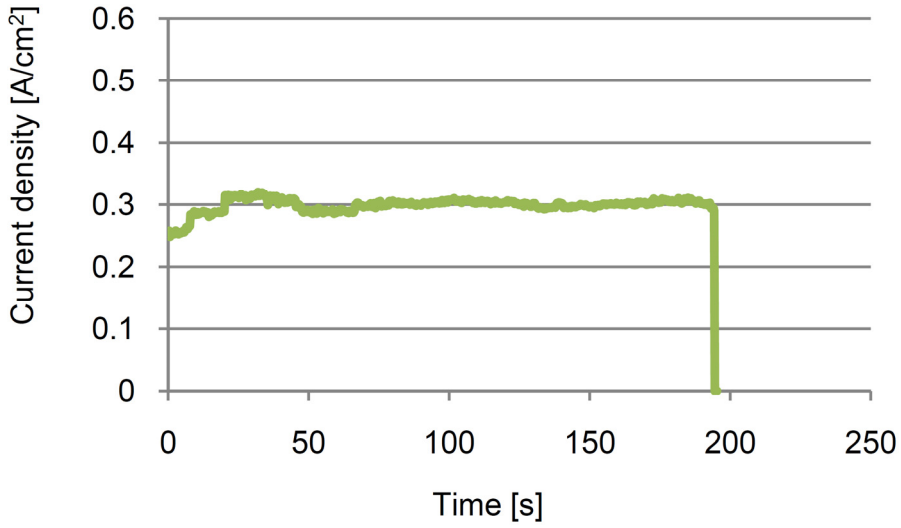

(b)

Figure 4.16: (a) EMBB process recorded by video, (b) Current density vs. time curves for EMBB.

connecting the tube to the deposit. From the current density vs. time curves depicted in Figure 4.16(b) and Figure 4.17(b), we can see that the thermal energy need to reshape the deposit is lower during the deposition process, and the current density stay in a steady value ranging from 0.25×10^6 A/cm^2 to 0.35×10^6 A/cm^2 until the separation of the two tubes. During the reshaping of the deposits, the current density was about 0.45×10^6 A/cm^2 when the two nanotubes were in contact, which is higher than that for the EMBB process due to the higher resistivity of the empty

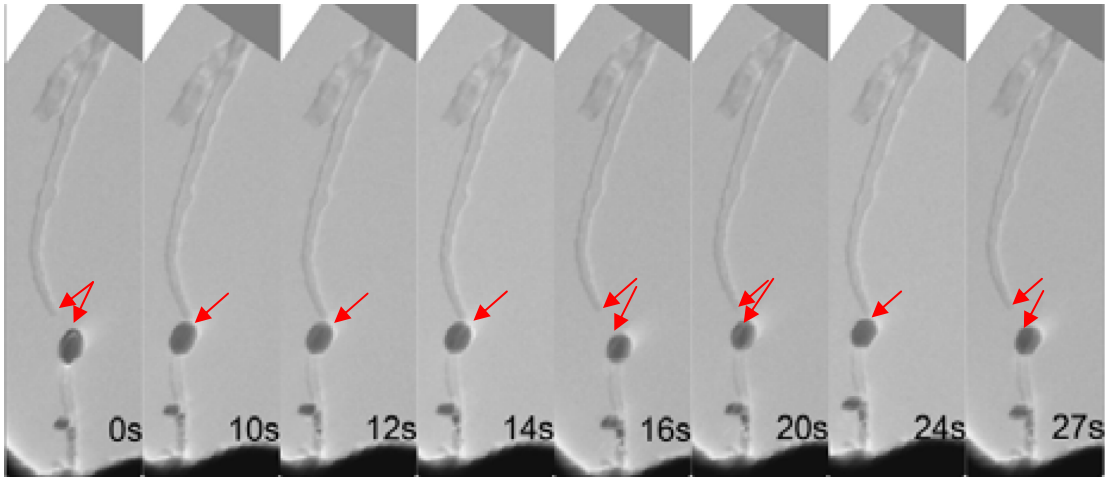

(a)

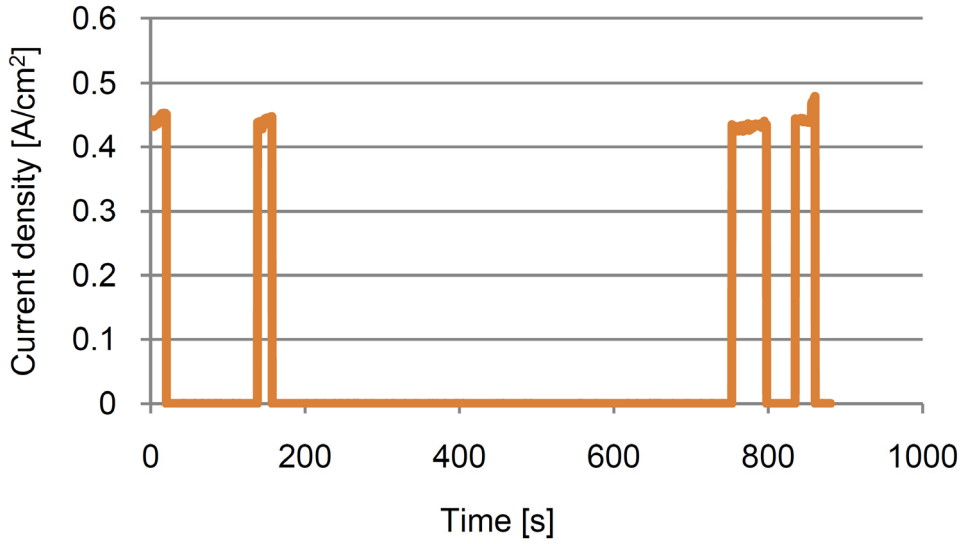

(b)

Figure 4.17: (a) Shape control process recorded by video, (b) Current density vs. time curves for shape control.

nanotubes. The cooled nanostructures will be reheated and melted under a higher current density.

We experimentally investigated several key techniques for extending the capability of EMBB including deposition against a non-conductive surface, shape control of the as-deposited nanostructure, and continuous mass feeding. By attaching a conductive probe to the sidewall of the CNT, mass flow was achieved regardless of the conductivity of the object surface. Experiments have shown the influence of heat sinks on the geometries of the deposits from

EMBB. By modulating the relative position between the deposit and the heat sinks using two CNTs, it was possible to reshape the deposits. We observed that the copper inside the neighbor CNTs adjacent to injector can be sucked into the injector, which indicates that continuous feeding is feasible. Although the mechanism is not well understood yet, electromigration and atom-by-atom penetration may be responsible for this phenomenon. As a general-purpose nanofabrication process, EMBB will enable a variety of applications such as nanorobotic arc welding and assembly, direct-writing nanoelectrodes, and nanoscale metallurgy.

4.4 In situ Optical Antenna Experiment

As proposed in our previous numerical studies, a pair of such sphere on the pillar nanostructures can function as optical antennas, as shown in Figure 4.18 [54]. In the numerical investigation, a

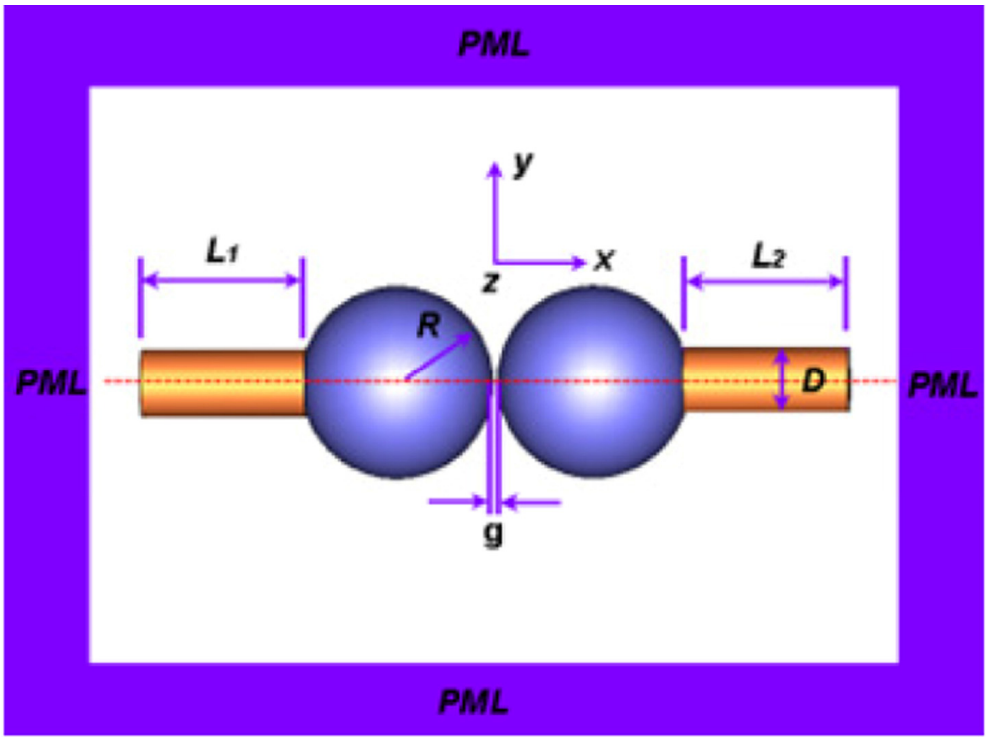

Figure 4.18: A model of a sphere-on-pillar optical nano-antenna.

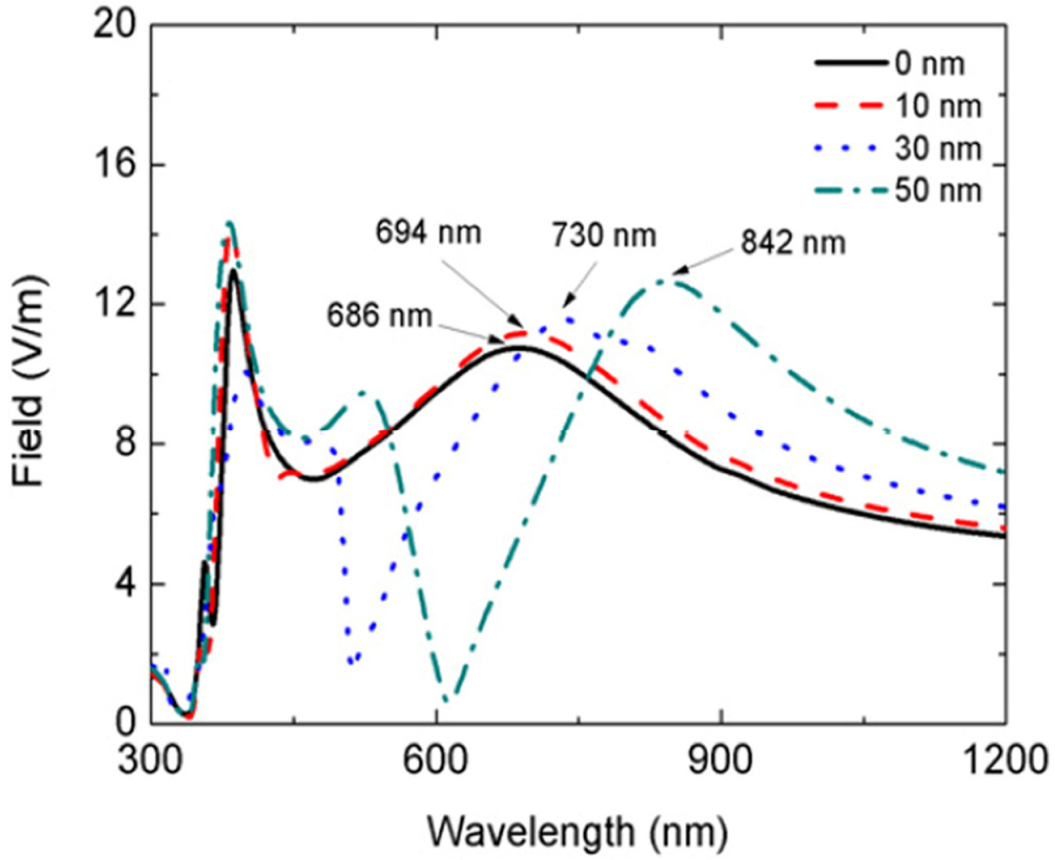

Figure 4.19: Electric field strength in the center of the gap as a function of the wavelength for various CNT lengths. Some of the resonant wavelengths for the paired structures are indicated with corresponding arrows.

metallic sphere that is attached at the near end of the nanotube was mirrored accordingly to form a paired nanostructure ($L_1 = L_2$) with a feed gap. The feed gap g was initially selected to be 20 nm. The resulting computed spectral responses of the electric field in the center of the gap (antenna feed) is shown in Figure 4.19 for different nanotube lengths [54]. It is known that for plasmonic structures the surface plasmon (SP) resonances strongly depend on the shape and size of the structure as well as the losses of the materials [80]. To justify that the as-fabricated sphere-on-pillar pairs can function as optical antennas, experiments were perofrmed using the STM-TEM holder in the TEM column. As shown in Figure 4.20, two nanotubes are positioned close and spheres are blown out from them using EBIB. Then, the two spheres were

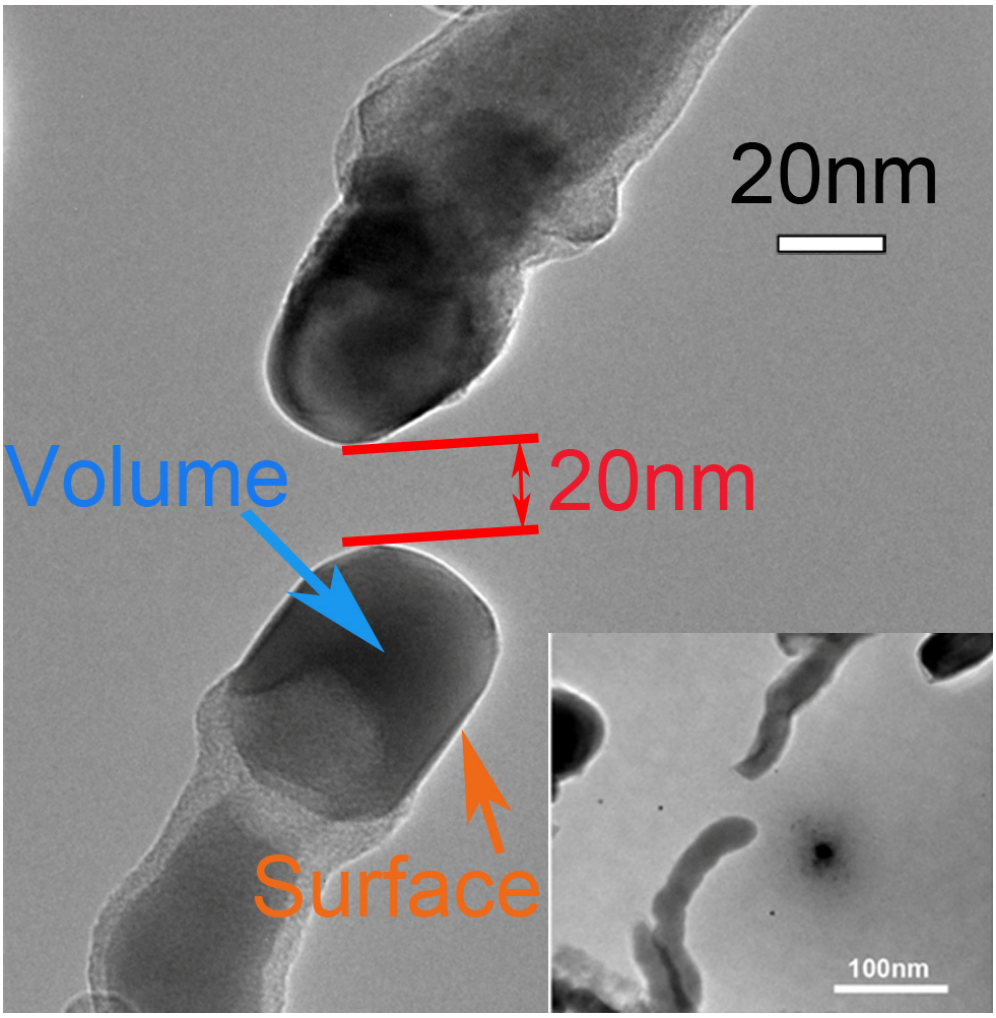

Figure 4.20: A pair of sphere-on-tip nanostructures fabricated by EBIB. Inset shows a pair of m@CNTs positioned together before EBIB is performed.

moved until thefeed gap was 20 nm. Electron energy loss spectroscopy (EELS) was applied for in situ characterization of the resonance performance. The output counts vs. excitation energy (in eV) curves are drawn in Figure 4.21. The volume plasmon (VP) appeared at around 11 eV when the electron probe was placed at the center of the sphere. As the electron probe was placed close to the surface of a sphere, the surface plasmon peak became dominant around 6 eV as shown in Figure 4.21. These energy values correspond to the equivalent photons with a wavelength of 113 nm and 226 nm. It is evident that the surface plasmon has a lower energy and thus a longer wavelength, indicating that resonance did occur.

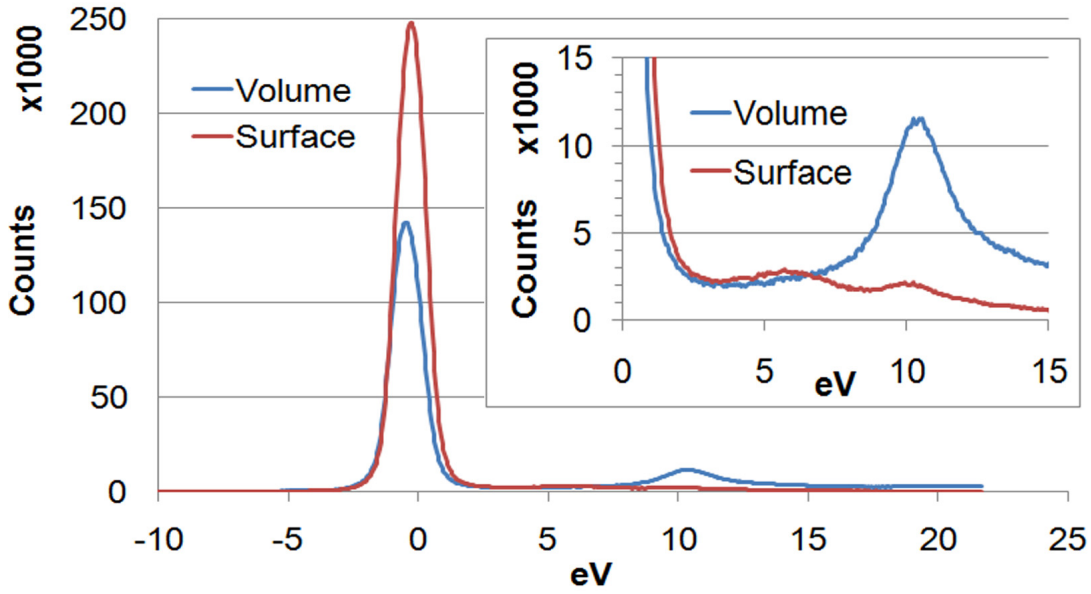

Figure 4.21: EELS excitation on the volume center and the surface of a sphere (Refer to Figure 2.1.20 for the positions that the electron beam focused on). The inset shows the eV peak at a magnification of 10x at 10 eV.

4.5 Chapter Summary

In summary, we have proposed EBIB and EMBB for the controlled fabrication of sphere-on - pillar optical nanoantennas. Melting and bubbling of tin from nanotube shells were realized at a current density of 10 to 25 A/cm^2. Bubbling started after the Sn@CNTs had been exposed to the electron beam for 1900 to 3360 s, depending on their sizes. Melting of the encapsulated tin is the result of the carbon displacement threshold energy reached by the beam irradiation, which is also the reason for the destruction of the carbon shell. The beam irradiation caused internal pressure buildup attributable to the melting and thermal expansion of the encapsulated materials and the shrinkage of the nanotube shells, which finally pushed out the molten metal bubbles. EBIB is a simple procedure, because it does not require contact between the nanotube and electrode, which is especially suitable for materials with a low melting point. For the materials with a high melting point, EMBB is the method to use. By applying a bias voltage as low as 2.0 - 2.5 V,

bubbling was realized from Cu@CNTs. The Cu@CNT in the experiment had a 40-nm diameter, and the extrusion continued for 17 s at a flow rate of 82.3 nm/s. The bias threshold for the extrusion was 2.4 V. Due to the contact between the CNT tip and the counter electrode, new challenges arose. The heat dissipation may cause immediate cooling and re-crystallization of the deposits during the draining of the CNT. Therefore, another nanotube was used in the experiment as a thermally resistive surface to keep the molten deposit spherical. By suddenly separating the deposit and the probe nanotube, the shape can be maintained. This process can also be used for remelting and reshaping as-fabricated particles on nanotubes from EBIB and EMBB with a large heat sink. The volume and surface plasmon resonances were tested using EELS and proved that resonance did occur in this structure. Experimentally, this can be achieved by EBIB and EMBB more readily than near-field optical methods.

Sphere-on-tip architectures add a new design to the family of optical nanoantennas. With a combination of the proposed fabrication processes for directed growth of m@CNT arrays, batch fabrication of such devices is possible. Single devices can already be used as SNOM probes, single molecule detectors, and solar cell antennas to enhance their energy conversion. Furthermore, photonic crystals based on sphere-on-pillar arrays can be obtained. CNTs have a melting point (3000K in vacuum) higher than almost any known materials except tungsten; therefore, the process can be universally applied to all materials important for nanophotonics.

CHAPTER 5

TUNNELING NANOSENSOR

5.1 Introduction of the Nanowire-Based Tunneling Nanosensor

Tunneling is a novel quantum effect that has been intensively explored theoretically and experimentally [81-89]. Tunneling occurs in a narrow gap that contributes to the small potential barrier, and a tunneling current happens within a very short period, the strength of which is exponentially determined by thin-film width. Due to its quick response and the intensified current value (compared with the applied bias and the thin-film width), the tunneling effect demonstrates important applications in several modern electronic devices, *e.g.* tunnel diode [90-92], quantum dot [93, 94], and scanning tunneling microscope (STM) [88, 89]. Although having many promising potentials, the tunneling effect still contains defects in realizing them. For example, though the mathematical relation between the current and the tip-sample distance (*I/d*) was clearly indicated by former researchers [95], during the operation, nanoscale alignment involved in operation of these instruments is always a considerable technical problem. Likewise, the detailed information of the tunneling barrier is still deficient within these approaches [96, 97]. To make matters worse, very few emphases has been laid on the design of an alignment-free tunneling nanodevice.

Here we proposed a practical tunneling model in which the tunneling current with different barriers heights were initiated and tailored to their quantum properties, and most importantly, the calibration of the device is necessary. Our design characterized by a built-in alignment-free nanojunction in a series of concentric nanowire, and its width could be adjusted by the buckling. Besides using it to figure out the empirical I/δ relations, we could also take advantage of it as a

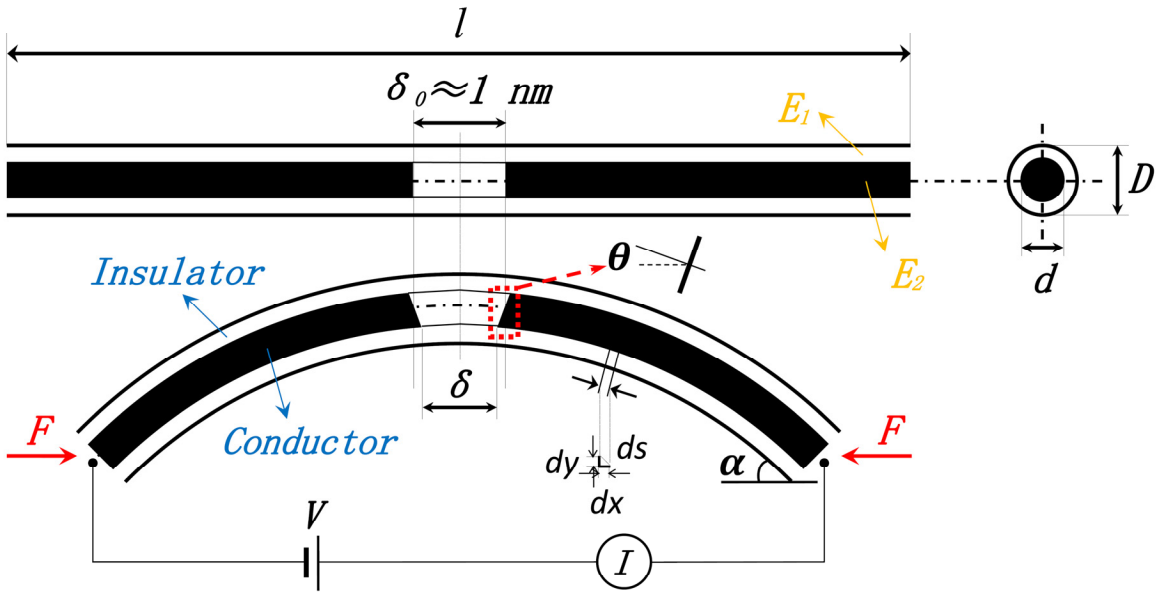

Figure 5.1: Proposed structure and the decrease in separation as the nanowire subjected to external buckling force. E_1 and E_2 are the Young's modulus of the insulating and metallic regions respectively; δ_0 is the initial separation between the metallic regions; δ is the separation between the lower edges, θ is the angle of rotation of the plane of the metallic region and α is the terminal deflection angle under the action of force; D and d are the outer and inner diameters of the core-shell structure.

force/displacement nanosensor. In implementing this model, a concentrical CuO-Cu nanostructure was developed. In the following article, we will first introduce the model, and then address the prototyped device, as well as the *in situ* characterization of it.

5.2 Modeling

Figure 5.1 shows the schematic of the device, two conductive nanowires are placed in a row and wrapped concentrically by an insulating nanotube, where the area between these two nanowires is engineered to be vacuum and the distance is limited to sub-nanometer range, thus forming a self-aligned nanoconstriction [85, 86]. A dc bias can be applied to the two ends of both nanowires with electrical properties taking simultaneously. As the uniaxial loads are applied to the compound concentric nanocylinder from the two ends, the column will remain equilibrium

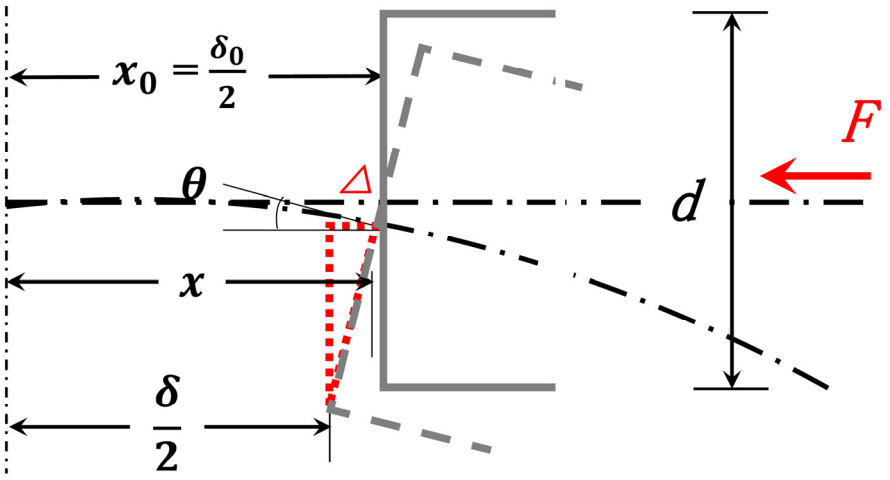

Figure 5.2: An expanded schematic for the geometric analysis to obtain relation between separation and angle of rotation.

when the load is smaller than critical load F_{cr} [98], and the elastic deformation along the nanowire will cause the decrease of the inter-nanowire separation. Furthermore, under a force stronger than or equal to the critical one, the column will ultimately buckles and the inner conductive nanowires are deflected accordingly. As shown in the red box of Figure 5.1 and the detailed schematic in Figure 5.2, because the cross-section of the embedded nanowires are twisted accordingly when the compound nanocylinder is bent or released, the distance between these two sharp edges is then shrank or expended via the change of external force/strain. Due to the thin-walled cylinder segment in the inter-nanowire separation area, the elastic deformation may be joined covalently with the buckling effect, causing rippling deformation or even wavelike distortion [99-103]. The buckle modeling of such proposed architecture is performed by applying the Temoshenko model while the compression effects are comprised.

In the model, the critical force F_{cr}, also known as the Euler force, is defined as the axial force that is sufficient to keep the column slightly bent, which can be expressed as [104]:

$$F_{cr} = \left(\frac{\pi}{l}\right)^2 (EI)_c \,, \tag{15}$$

where

$$(EI)_c = E_1 I_1 + E_2 I_2 = \frac{\pi E_1 (D^4 - d^4)}{64} + \frac{\pi E_2 d^4}{64},$$

L is the chord length of the buckled beam, E_1/E_2 is the Young's modulus of the external/inner nanowire, and D/d is the diameters of the external/inner nanowire. In Figure 5.1, ds represents the differential length of the beam, then the expression of the length of the deformed beam can be given by [105]:

$$l = \int_0^l ds = \int_0^\alpha \sqrt{\frac{(EI)_c}{2F}} \frac{d\theta}{\sqrt{cos\theta - cos\alpha}}, \tag{16}$$

where θ is the angle at the differential segment ds, α is the angle at the terminal of the beam, and F is the magnitude of the buckling force. If we define $k^* = \sqrt{\frac{F}{(EI)_c}}$ and $K(p) = \int_0^{\frac{\pi}{2}} \frac{d\Phi}{\sqrt{1-p^2 sin^2\Phi}}$ ($p = \sin\frac{\alpha}{2}$, $\Phi = sin^{-1}\left(\frac{\sin\frac{\theta}{2}}{p}\right)$, and α defines θ changing from $0 \rightarrow \alpha$) that symbolizes the variation of the terminal angle α, then the equation (16) can be reduced as:

$$l = \frac{K(p)}{k^*}. \tag{17}$$

In order to determine the curve of the deformed beams, the coordinates of a differential segment on the deformed axis are given by:

$$dx_i = ds\, cos\theta \tag{18}$$

and

$$dy_i = ds\, sin\theta, \tag{19}$$

therefore:

$$x_i = \int_0^\theta ds\, cos\theta = \int_0^\theta \frac{cos\theta d\theta}{\sqrt{2}k^* \sqrt{cos\theta - cos\alpha}}$$

$$= \frac{1}{k^*}\left[\int_0^\Phi \left(2\sqrt{1 - p^2 sin^2\Phi}\right) d\Phi - \int_0^\Phi \frac{d\Phi}{\sqrt{1-p^2 sin^2\Phi}}\right]. \tag{20}$$

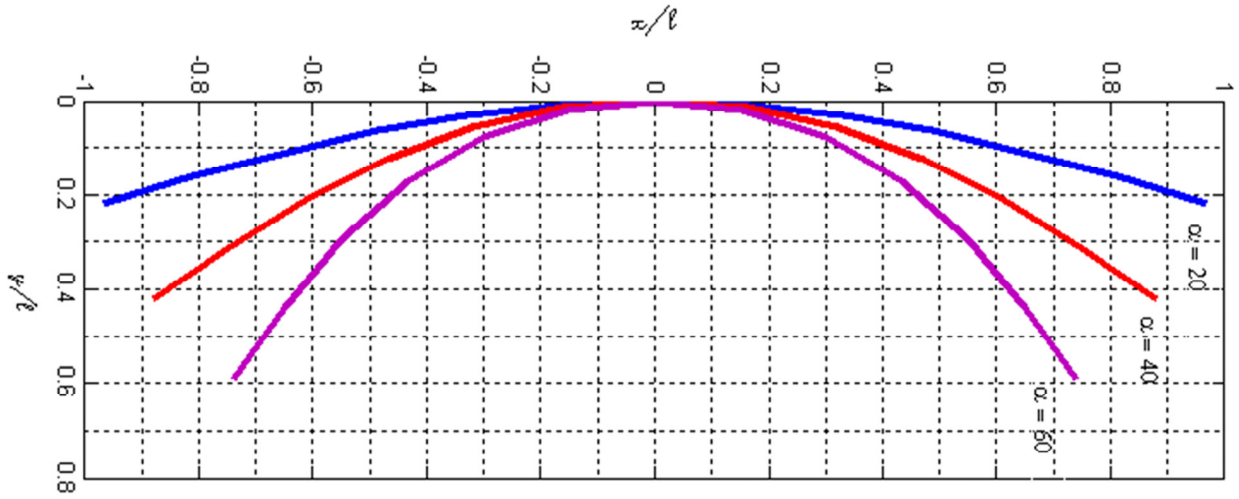

Figure 5.3: Normalized deformed axes of the nanowire corresponding to terminal angles of α = 20, 40, and 60°.

Moreover, because the incomplete elliptic integral of first kind is given by:

$$\mathrm{F}(\Phi,\mathrm{p}) = \int_0^{\Phi} \frac{\mathrm{d}\Phi}{\sqrt{1-\mathrm{p}^2\sin^2\Phi}},$$

and the incomplete elliptic integral of second kind is [106]:

$$\mathrm{E}(\Phi,\mathrm{p}) = \int_0^{\Phi} \sqrt{1-\mathrm{p}^2\sin^2\Phi}\ \mathrm{d}\Phi,$$

then equation (20) becomes:

$$x_i = \frac{l}{K(p)}[2\mathrm{E}(\Phi,\mathrm{p}) - \mathrm{F}(\Phi,\mathrm{p})], \tag{21}$$

and in the same way,

$$y_i = \frac{l}{K(p)}[2p(1-cos\Phi)]. \tag{22}$$

Here, since the parameters p, Φ, $K(p)$, $\mathrm{E}(\Phi,\mathrm{p})$ and $\mathrm{F}(\Phi,\mathrm{p})$ are all correlated to the terminal buckling angel α, the buckling curves (which are symbolized by a series of coordinated points x_i and y_i) can be plotted according to different values of α. Figure 5.3 shows the normalized deformed axes $(\frac{x_i}{l}, \frac{y_i}{l})$ corresponding to the terminal angles of α = 20, 40, and 60°.

The buckling of the nanowire will induce the deflection of embedded particles, which in turn modulates the inter-nanowire separation and address a tunable tunneling barrier. Figure 5.2 illustrates that the spacing δ is given by:

$$\delta = 2x_i - dsin\theta \ , \tag{23}$$

where x_i is the coordinate of the point of interest on the deformed axis corresponding to the terminal angle α_i, and the $sin\theta$ here can be defined as:

$$sin\theta = 2\sin\left(\frac{\theta}{2}\right) cos\left(\frac{\theta}{2}\right), \tag{24}$$

here,

$$\sin\left(\frac{\theta}{2}\right) = p\ sin\Phi \tag{25}$$

and

$$sin\Phi = sn(u), \tag{26}$$

where $sn(u)$ is a Jacobi elliptic function, and $u = K(p)\left(\frac{x_0}{l}\right)$.

Here the nominal strain ε is defined as $\Delta l/l$, which is given by:

$$\varepsilon = \frac{\Delta l}{l} = 2 \cdot \left[1 - \frac{\mathrm{E}(\Phi,\mathrm{p})}{\mathrm{F}(\Phi,\mathrm{p})}\right]. \tag{27}$$

As we substitute Equations (21) and (24-27) into Equation (23), the relation between separation δ and strain ε is found as

$$\delta = \frac{l\,\mathrm{F}(\Phi,\mathrm{p})}{K(p)}(1-\varepsilon) - 2\ d\ p\ sn\left[K(p)\ \left(\frac{x_0}{l}\right)\right]\sqrt{1 - p^2 sn^2\left[K(p)\ \left(\frac{x_0}{l}\right)\right]}. \tag{28}$$

Figure 5.4 shows the strain-gap separation characterizations obtained from nanowires with initial width δ_0 = 0.8 nm. The curve illustrates a separation decrease tendency corresponding to the increase of strain, which confirms that the gap width can be modulated by simple buckling. Since gap geometry caused by a specific strain is distinguishable, in principle each gap is electrically unique at different strain status. The conductible nanorods in the nanotube form the

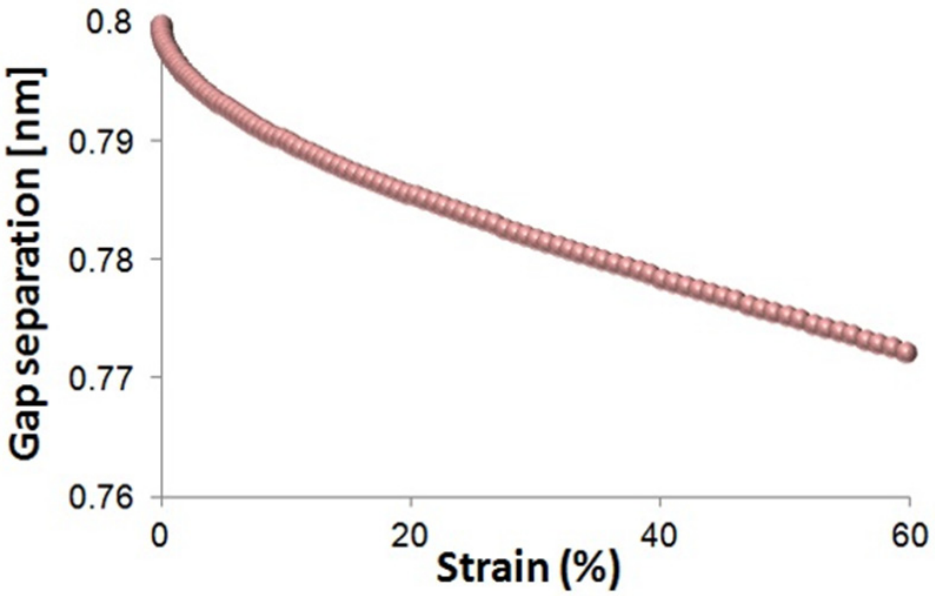

Figure 5.4: Strain-gap separation characterization obtained from nanowire with different initial width of 0.8 nm.

alignment-free electrodes to the gap junction, facilitating the electrical characterizations of the device when it is in various band structures.

The model we designed has a similar schematic as that of an STM, since both of them have conductive electrodes that approach in a sub-nanometer range. But our design has an advantage over STM in terms of the alignment between the two electrodes: the tunneling gap width could be switched within different regimes to realize tunneling behavior just by buckling the wire. Since all of the regimes are within the sub-nanometer range, and the schematic forms a unique MIM architecture, the electron tunneling effect could be addressed [85, 86, 95]. As we apply the MIM tunneling model here, the approximate expression of the tunneling current density is given by

$$J = \frac{e}{2\pi\bar{h}\delta^2}\left[\bar{\Phi}_B e^{-\frac{\sqrt{8m}}{\bar{h}}\delta\sqrt{\bar{\Phi}_B}} - (\bar{\Phi}_B + eV)e^{-\frac{\sqrt{8m}}{\bar{h}}\delta\sqrt{\bar{\Phi}_B+eV}}\right], \quad (29)$$

where m is the mass of the electron, $\bar{h}$ is the *Plank constant*, V is the voltage applied between the two electrodes, and $\bar{\Phi}_B$ is the average barrier height between the two electrodes. Figure 5.5

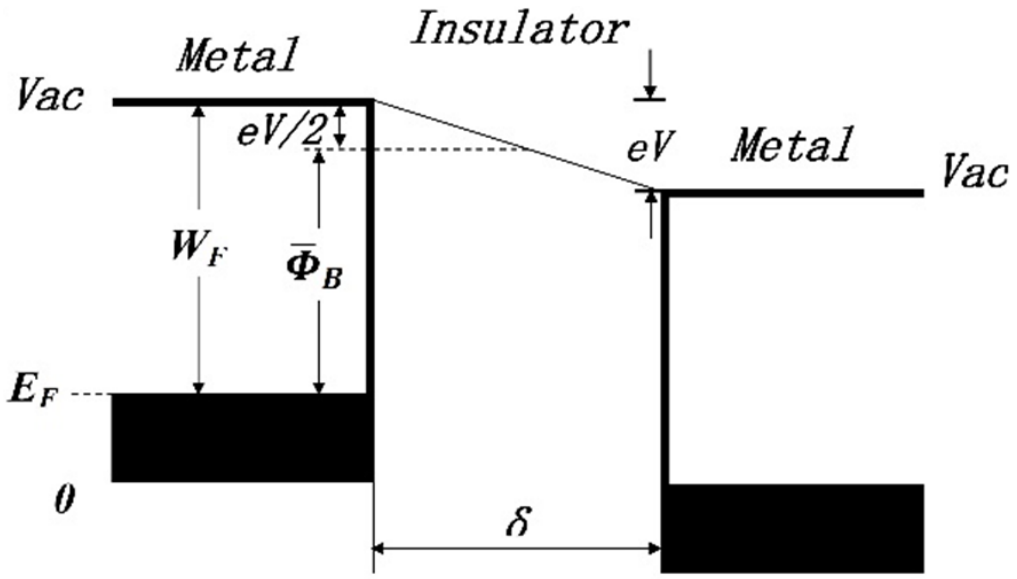

Figure 5.5: Potential profile of the metal-insulator-metal junction under the application of a low bias V. $\bar{\Phi}_B$ is the average barrier height. E_F and W_F are the Fermi energy and the work function of the conductive material respectively.

shows the potential profile of an MIM junction under a low bias. The average barrier height is given by: $\bar{\Phi}_B = W_F - \frac{eV}{2}$, where W_F is the work function of the inner conductive material. Substituting Equation (28) into (29) gives the tunneling current *vs.* buckling strain relation.

5.3 Simulation

The present model could directly reveal the contribution of the external/inner-wire diameter (D/d), initial gap separation (δ_0), bias voltage (V), and the material work function (W_F) to the tunneling current. Figure 5.5(a) indicates the influence of the concentric geometry. The diameter of the nanowire is D = 20 nm and the diameter of the nested nanorods increases from 1 to 19 nm during the buckling simulation. Meanwhile, the other factors are restricted as: E_1 = 457 GPa, E_2 = 100 GPa, V = 2.5 V, l = 400 nm (based on Timoshenko model, the length/diameter ratio should be larger than 10:1), W_F = 4.4 eV (due to the lack of the work function of the Ni_6Si_2B, we use the

work function of Ni_6Si_2 instead [107]), and δ_0 = 0.8 nm. Moreover, the strain-induced tunneling current density reaches a high value at about 5×10^7 A/m^2, indicating the potential application of this tunneling device as a high resolution sensor. Figure 5.5(b) shows the influence of the initial gap separation as δ_0 ranges from 0.7 nm to 0.8 nm, here D = 20 nm, d = 10 nm, E_1 = 457 GPa, E_2 = 100 GPa, l = 400 nm, V = 2.5 V, and W_F = 4.4 eV. The simulation of the nanowire length influence is shown in Figure 5.5(c) as l ranges from 200 nm to 600 nm, here D = 20 nm, d = 10 nm, E_1 = 457 GPa, E_2 = 100 GPa, δ_0 = 0.8 nm, V = 2.5 V, and W_F = 4.4 eV. Among these geometry influences, it is found that the contribution of the initial gap distance change to the tunneling is more prominent than the other two geometric changes. Figure 5.5(d) illustrates that when the initial gap distance decreased from 0.8 to 0.7 nm, the peak of the current density would exponentially increase from 0.15×10^8 to 2.5×10^8 A/m^2. In addition to the geometric effects including the change of concentric nanorod diameter, initial gap separation, and the nanowire length, the external bias would also affect the tunneling response at different strain statuses. As we extended the simulation to characterize the effect of the work function of the core material, we noted that the tunneling current density exponentially increased according to the decrease of the work function (from 5 to 4 eV) as shown in Figure 5.5(d), which indicates that the selection of conductive core materials is also an important factor to achieve an intensive tunneling current.

Our simulation results have demonstrated the initiation of the tunneling current by the proposed concentric nanostructure. Figures 5.6(a)-(d) summarize the influence of the nanorod diameter, gap separation, nanowire length, applied bias, and the work function on the tunneling current. The simulation results indicate the exponential correspondence of the tunneling current to the geometric or electrical properties changes. Among them, the change of the initial gap

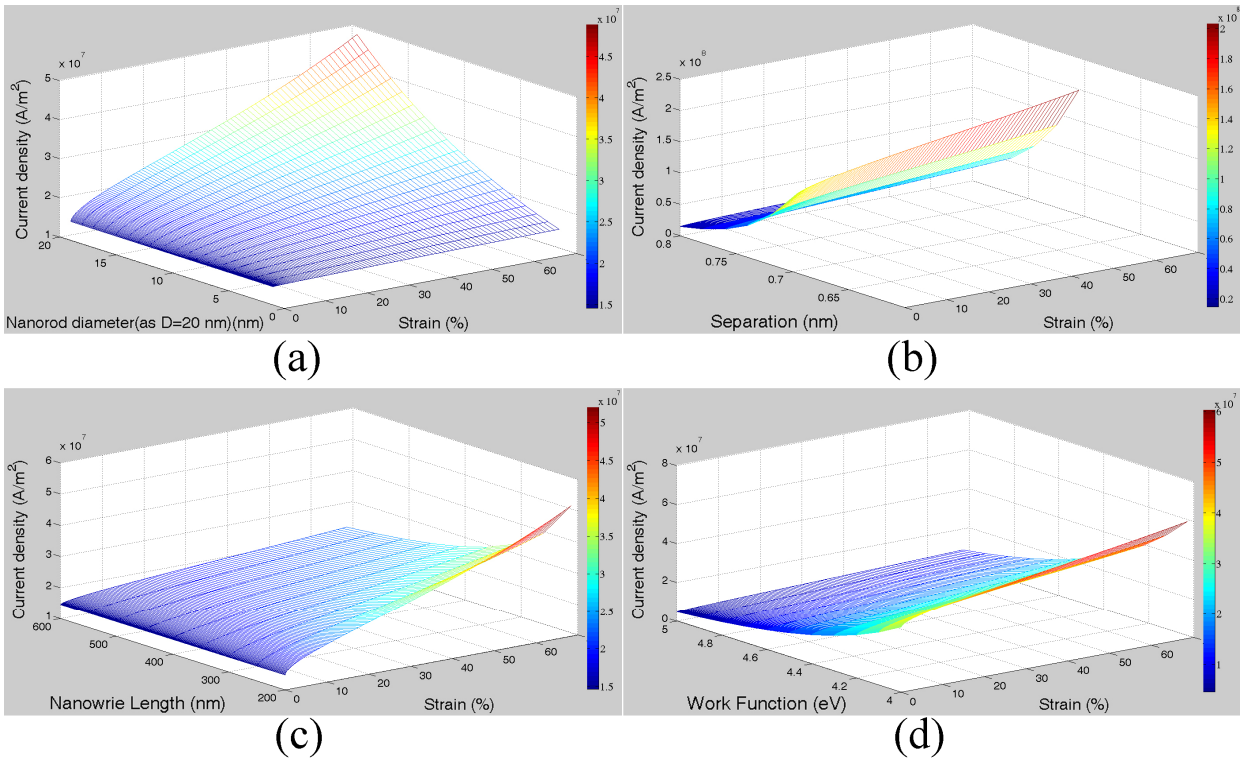

Figure 5.6: (a) Influence of nanorod diameter d on tunneling current density. D = 20 nm and d ranges from 1 to 19 nm. (b), Influence of initial separation δ_0 on tunneling current density. δ_0 ranges from 0.7 to 0.8 nm. (c), Influence of nanowire length l on tunneling current density. l ranges from 200 to 600 nm. (d), Influence of work function W_F on tunneling current density. W_F ranges from 4 to 5 eV.

separation and the work function of the core materials show a remarkable influence to the tunneling. Therefore, to achieve a better tunneling response, the concentric nanowire should consist of nanorods with a smaller gap separation made of highly conductive materials.

5.4 B_4C Peapod Nanowire-Based Tunneling Nanosensor

5.4.1 Introduction of the B_4C Peapod Nanowire

Boron carbide (B_4C) peapod nanostructures were synthesized in a horizontal alumina tube furnace (id: 41 mm, length: 1200 mm). 35 wt% boron, 18 wt% boron oxide, 2 wt% silicon powders, 35 wt% plant fiber based activate carbon and 10 wt% nickel boride nanoparticles were

mixed, ground, and loaded into a quartz tube (id: 12 mm, length: 150 mm), which was then inserted into the center of the alumina tube furnace and heated at 1160^{o}C for 3 h with a continuous flow of argon at 700 sccm (standard cubic centimeter). After cooling down, the as-prepared samples were characterized by SEM (Hitachi S4800), XRD, TEM (JEOL JEM 2010F and FEI Tecnai G2 F30) equipped with a parallel EELS detector and an EDX detector.

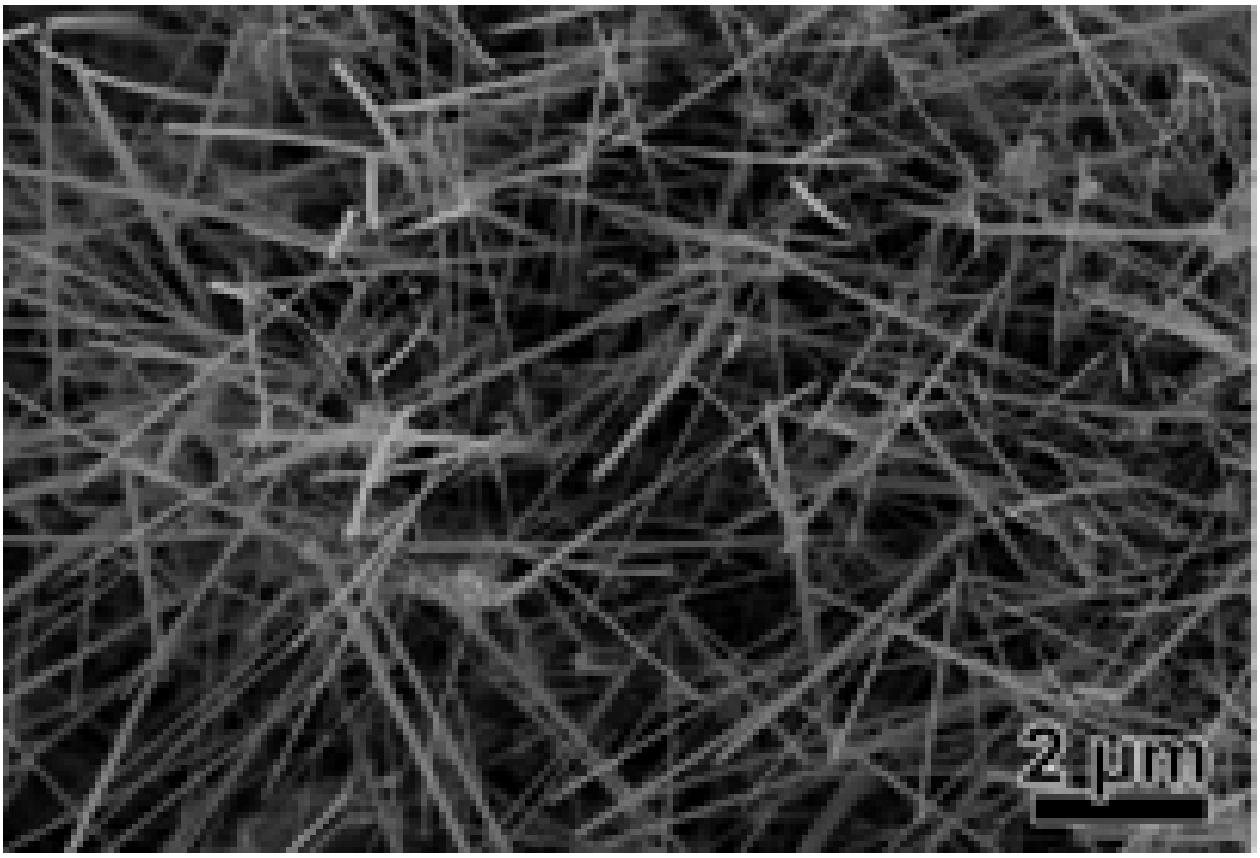

Figure 5.7: SEM image of the as-synthesized sample.

5.4.2 Elemental Detection of the B_4C Peapod Nanowire

A representative scanning electron microscopy (SEM) image of the as-synthesized product in in Figure 5.7 indicates an abundance of straight nanowires. Different from the normal boron carbide nanowires[108-112], there are discrete nanorods embedded in the individual nanowires,

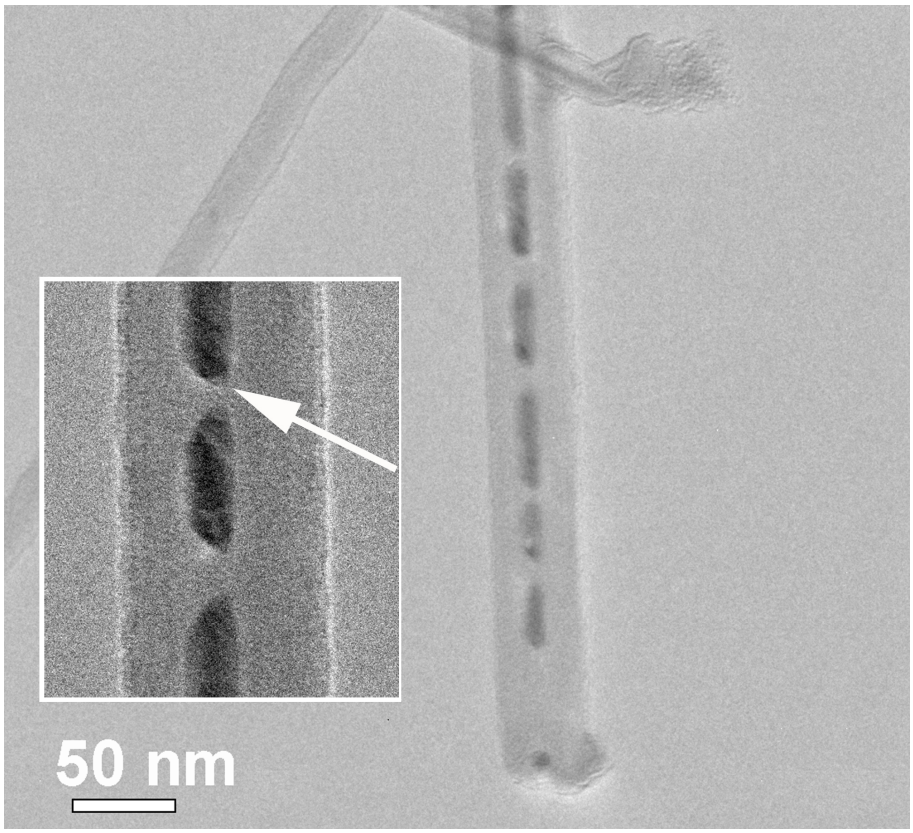

Figure 5.8: TEM image of the nanowires. Discrete nanorods with the unique cavity structures can be seen in the nanowire, as shown in the close-up view in the inset.

as shown in the high resolution TEM (HRTEM) image in Figure 5.8. Similar hybrid peapod structures have also been observed in the nanowires of Au-in-Ga_2O_3[113], fullerenes-in-CNTs[114], and Au-in-SiO_2[115]. As indicated by the arrows in the inset of Figure 5.8, the TEM image reveals that there are cavity structures between two adjacent nanorods. The nanowire terminates at the catalyst particle (Figure 5.9(a) and (b)) containing Ni (Figure 5.9(e)) and Si (Figure 5.9(f)). In Figure 5.9, the respective element distribution maps reveal that B and C are rich in the stem of nanowire and the embedded nanorods have similar components to the catalyst particle. X-ray diffraction (XRD) spectrometry in Figure 5.10 confirms that rhombohedral B_4C (JCPDF No. 35-0798) is the dominant phase. The peaks at 43.1^o and 45.3^o can be indexed as (111) and (210) of nickel silicon boride Ni_6Si_2B (JCPDF No. 65-1991) with a hexagonal

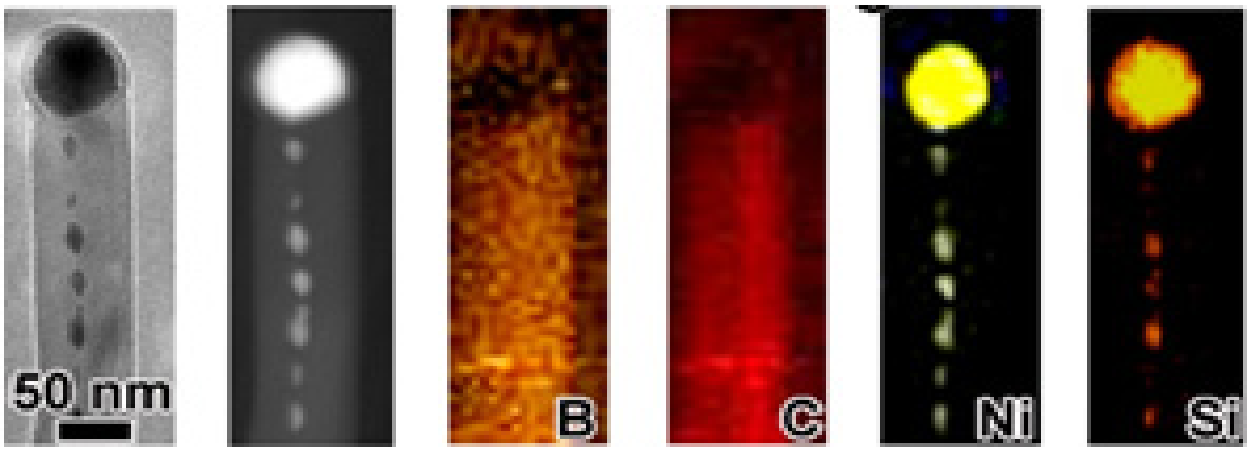

(b) (c) (d) (e) (f)

Figure 5.9: (a) TEM image of a single nanowire with a catalyst particle on the tip. (b) The corresponding scanning transmission electron microscope (STEM) image of (a). (c)-(f) Respective element distribution maps of B, C, Ni and Si.

structure of Fe_2P-type (space group P-62m, No. 189), which is an electrically conductive ternary compound[116]. The elemental mapping and XRD results jointly suggest that both the catalyst particles and the embedded nanorods are conductive Ni_6Si_2B phase. Two distinct absorption features at 188 and 284 eV in the electron energy loss spectrum (EELS) (see the inset in Figure 5.10) correspond to the known B-k and C-k edges, respectively, indicating that the nanowire stem is B_4C. The high resolution TEM (HRTEM) images in Figure 5.11(a)(b)(c) and the corresponding fast Fourier transform (FFT) diffraction pattern (insets in Figure 5.11(b)) jointly reveal that the B_4C nanowire stem is single crystalline. Figure 5.11(c) shows the close-up view and the corresponding FFT pattern (the inset) of the lower part of Figure 5.11(a), validating that the embedded nanorods are Ni_6Si_2B. Since the Ni-Si-B system has a eutectic point lower than 1000^oC[117], the Ni_6Si_2B nanorods must be in a molten or quasi-liquid state during the growth of the B_4C nanowire at 1160^oC. Moreover, B_4C has a low coefficient of thermal expansion ($4\text{-}8\times10^{-6o}C^{-1}$) and a high melting point (2350^oC). Therefore, upon solidification the embedded

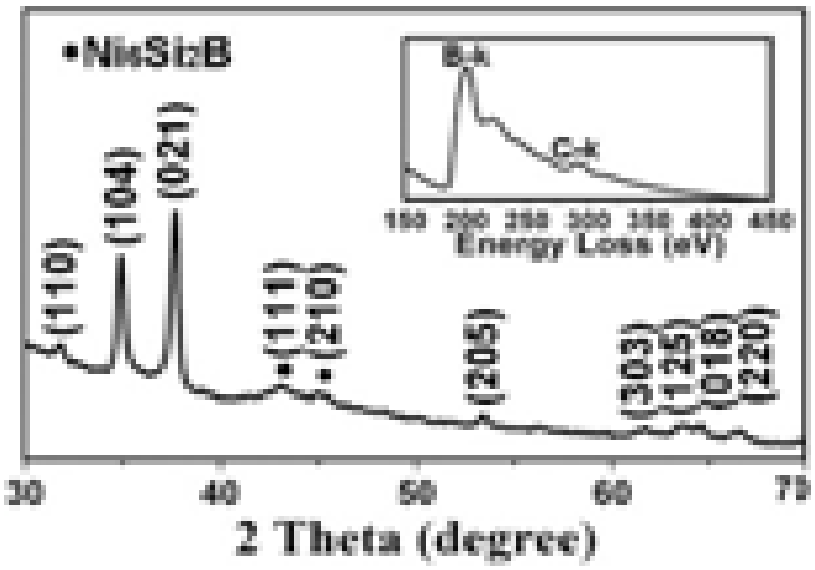

Figure 5.10: XRD pattern of the B_4C peapod nanostructures. The inset is a representative EELS spectrum taken from the nanostructure.

Ni_6Si_2B nanorods shrink more than the B_4C nanowires, forming the unique cavity structures (hollow spaces between the embedded nanorods), as observed with TEM (Figure 5.8).

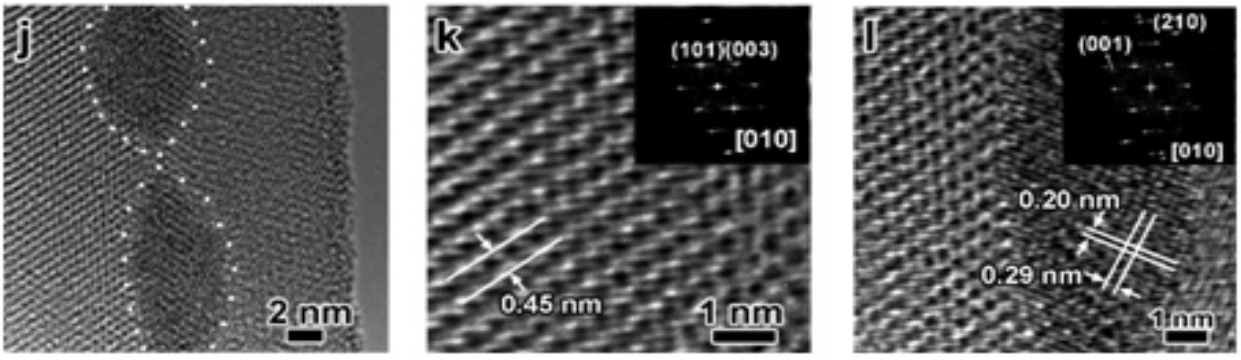

(a) (b) (c)

Figure 5.11: (a) A representative HRTEM image of the B_4C peapod nanostructure. (b) The close-up view and the corresponding FFT pattern (the inset) of (a). The electron beam irradiation direction is along [010] of B_4C. (c), The close-up view and the corresponding FFT pattern (the inset) of (a), showing that the embedded nanorods are Ni_6Si_2B.

5.4.3 *In situ* Buckling of the B_4C Peapod Nanowire

To obtain detailed electrical, mechanical, and electromechanical properties, individual B_4C peapod nanostructures were buckled *in situ* for electromechanical characterization inside a TEM. The experiment setup is demonstrated in Figure 5.12. A STM built in a TEM serves as a nanomanipulator (Figure 5.12(a)) [6]. As shown in Figure 5.12(b), the nanowire bundle was attached to a 0.35 mm thick Au wire using silver paint, and the wire was held in the probe holder.

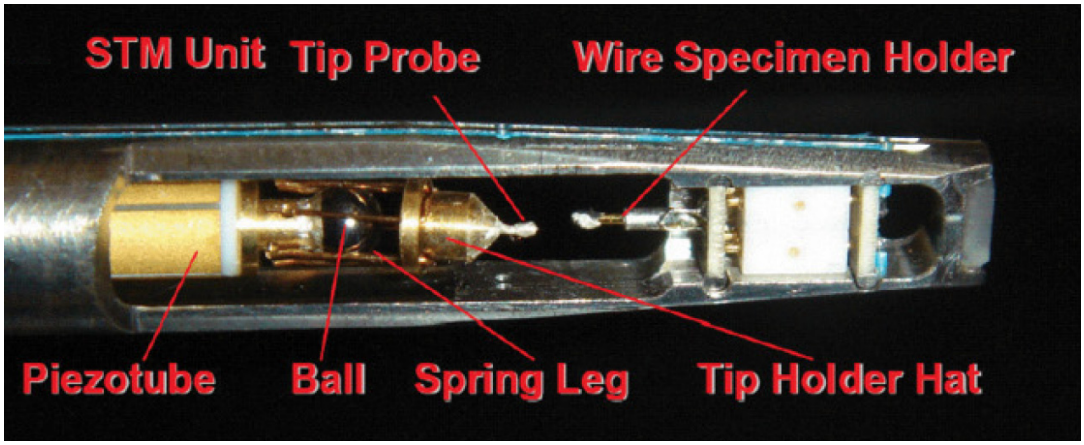

(a)

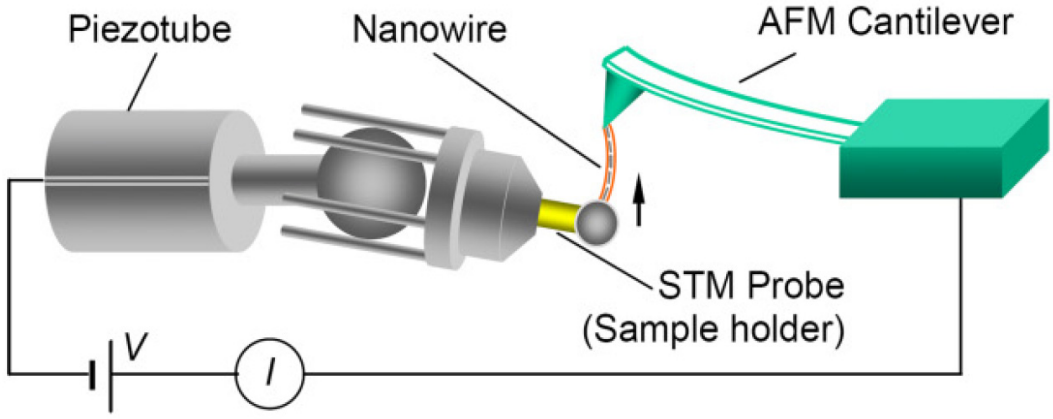

(b)

Figure 5.12: In situ buckling and electromechanical characterization of a B_4C peapod nanostructure inside a TEM. (a) An STM built in a TEM holder serves as a nanomanipulator. (b) Experimental setup. A conductive AFM cantilever was installed on the specimen holder using a 0.35 mm thick Au wire and was used to characterize the nanowires and measure the force applied on the nanowire.

A conductive AFM cantilever (Mikromasch, CSC38/Ti-Pt) was installed on the specimen holder with a 0.35 mm thick Au wire and used to characterize the nanowires and measure the force applied on the nanowire simultaneously. The representative buckling process was recorded with TEM images (Figure 5.13), which include the bending process (Figure 5.13(a)-(f)) and the releasing one (Figure 5.13(g)-(l)). Surprisingly, the nanowire can be bent to a sharp angle (70^{o}) with no apparent cracking or degradation for a strain up to 40.5%. It is well known that bulk B_4C is brittle in nature, but at the nanometer-scale, B_4C peapod nanostructures appear ductile. Both the nanowires and the embedded nickel silicon boride nanorods were elastically deformed under multiple high-load bending steps without a brittle failure or obvious residual deformation (Figure 5.13(a)-(f)).

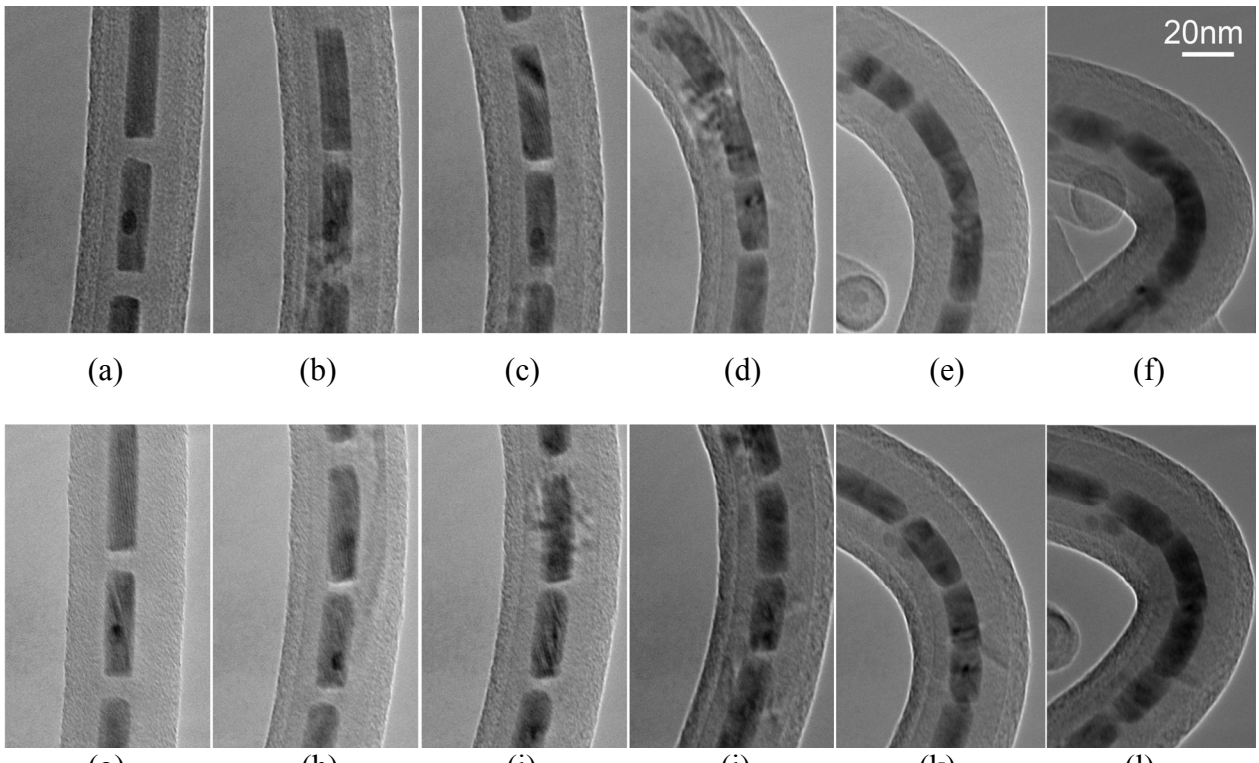

Figure 5.13: The buckling process recorded by TEM images: stressing (a)-(f), releasing (g)-(l).

As the B_4C peapod nanostructure deforms, the separation between the encapsulated nanorods decreases. Based on the detailed geometry analysis of a peapod nanostructure as shown in Figure 5.14, the chord length of the nanostructure becomes $L = L_0 - \Delta L$ when an external force F is subjected. The strain ε is defined as a function of length change of ΔL over the original

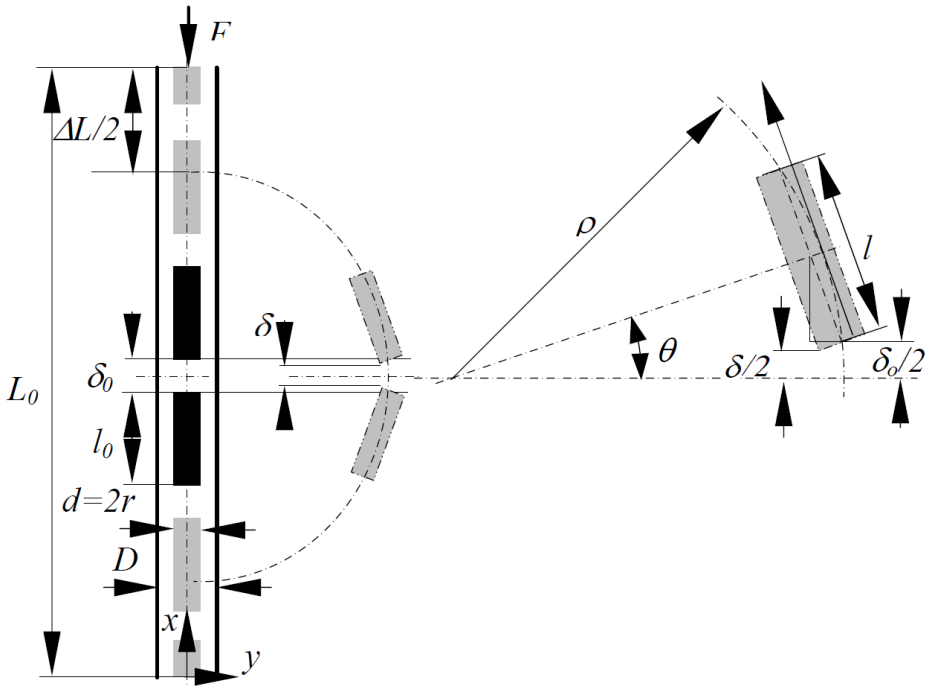

Figure 5.14: Schematic drawing of the nanowire before and after buckling.

length L_0 under the approximation of homogeneous strain: $\varepsilon = \Delta L/L_0$, and the inter-nanorod separation change is expressed as $s = (\delta_0 - \delta)/\delta_0$, where δ and δ_0 are the separation and its initial value, respectively. According to the *in situ* real-time images of the buckling process (Figure 5.13(a)-(f)), the strain *vs.* inter-nanorod separation change can be depicted in Figure 5.15, where points "a"-"f" indicate the cases shown in the corresponding individual image in the buckling process (Figure 5.13(a)-(f)). The relation between the strain and the inter-nanorod separation is depicted in Figure 5.16. Three intervals "*I*", "*II*", and "*III*" are identified to

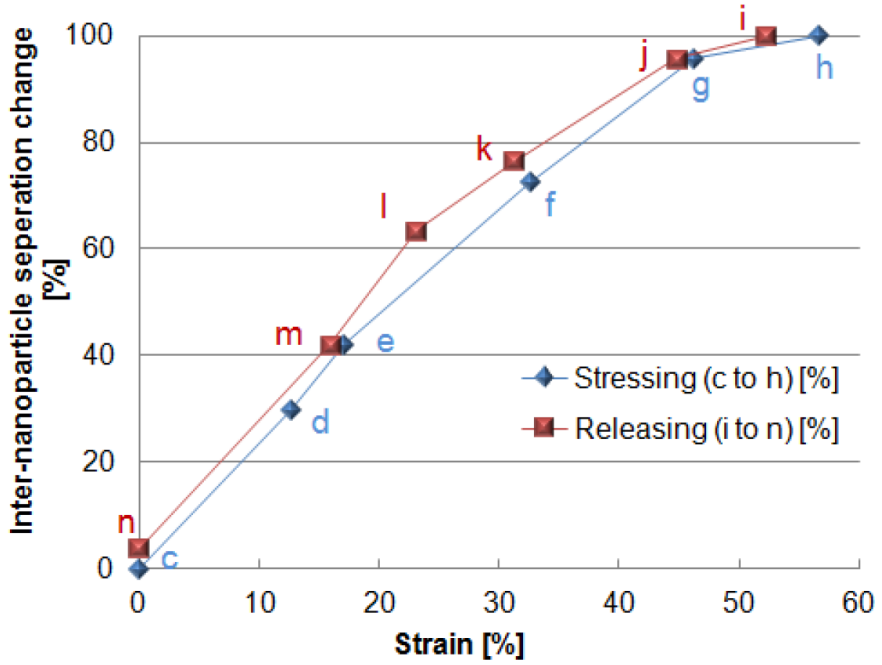

Figure 5.15: Relation between strain and the change of the inter-nanorod separation.

represent the regimes in which the inter-nanorod separation is larger than approximately 1 nm, between 1 and 0 nm, and 0 nm, respectively.

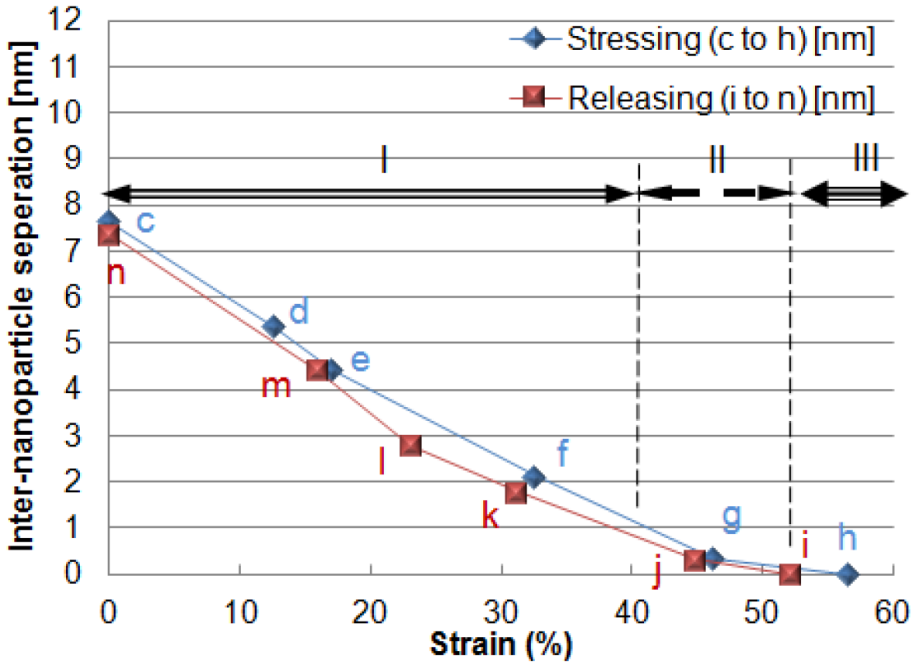

Figure 5.16: Relation between the strain and the inter-nanorod separation.

On a practical level, the controlled inter-nanorod separation allows us to effectively couple the electrical property variation with external force/strain change. More importantly, this technique provides insights into the electronic transport properties of the peapod nanostructures and creates unprecedented opportunities for inter-segment-based sensing. By adjusting the stress on the two ends of the nanowire, the distance between the two neighboring nanorods can be regulated in different regimes (regions *I, II,* and *III*). Then the nanowire will acquire different

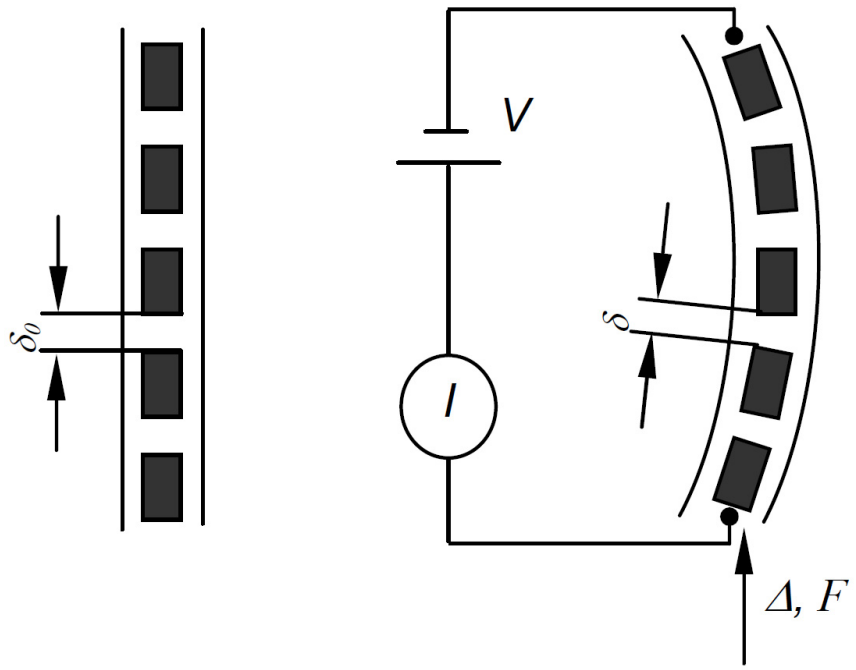

Figure 5.17: Schematic drawing of a position/force sensor based on an encapsulated B_4C peapod nanostructure.

electronic structures respectively, thus modulating its transport properties. The conductivity change of the nanowire was also recorded using a nanoampere meter during the buckling process (Figure 5.17).

5.4.4 Force/Displacement Sensing using B_4C Peapod Nanowire

According to Figure 5.18, *I-V* properties show positive piezoresistivity of the nanowire, i.e., as the nanowire undergoes stress, the current increases at a constant bias (140 V). Since the inter-nanorod separation here falls into the part of region *II* that is close to the region *I*, the tunneling effect does not dominate the current performance but rather the conventional piezoresistive effect. The nominal gauge factors for buckling stress was defined as $G = \frac{\Delta R/R}{\Delta L/L}$, where $\Delta R/R$ and $\Delta L/L$ are the changes in resistance and the length of the nanowire, respectively. Note that $\Delta L/L$ is introduced as a nominal strain due to the readiness for the detection of ΔL and its comparison with the deflection of AFM cantilever.

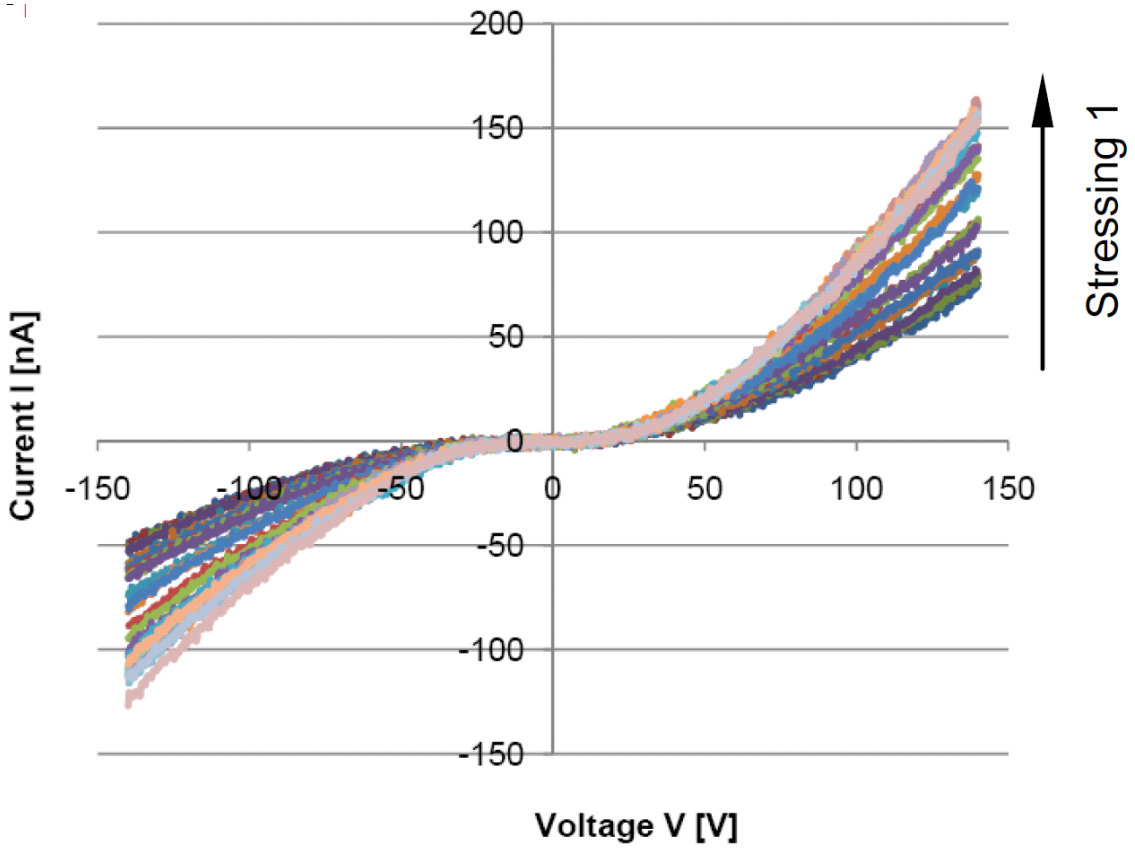

Figure 5.18: *I-V* properties show the positive piezoresistivity of the nanowire, i.e., as the nanowire undergoes stress, current increases under a constant bias (140 V).

The nominal gauge factors were determined for small deformation ($\Delta L/L < 5\%$) based on the slopes of the curves shown in Figure 5.19: G = 8.1 at 140 V and 7.9 at -140 V, respectively. The average value was 8.0, as shown in Figure 5.20. This value is ideal for position sensing applications. As the end of the nanowire on the STM probe was moved toward the AFM cantilever, its position was read out from the STM controller using either the current or the resistance monitored with a multimeter. Applied bias V are shown in Figure 5.20(a) and (b), using the average of the absolute values of current I at biases 140 and -140 V. Then, the position δ can be measured as δ = -64.6I - 8064.0 (I_0 = 124.8 nA), where I is expressed in nA and δ is given in nm. With the resistance as the input, δ = 5636.0R - 7162.5 (R_0 = 1.3 GΩ), where R is in GΩ scale.

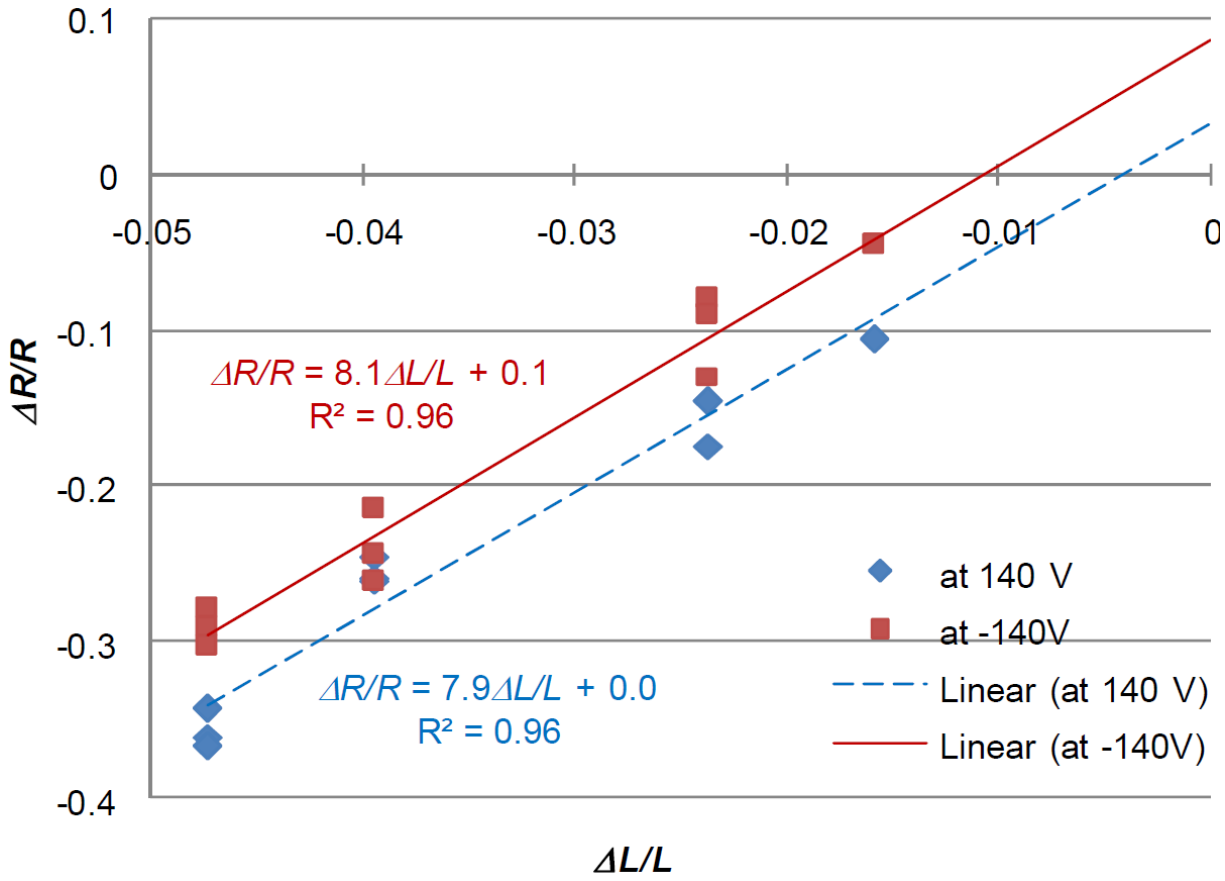

Figure 5.19: $\Delta L/L$-$\Delta R/R$ curves show that the average nominal gauge factor is 8.0.

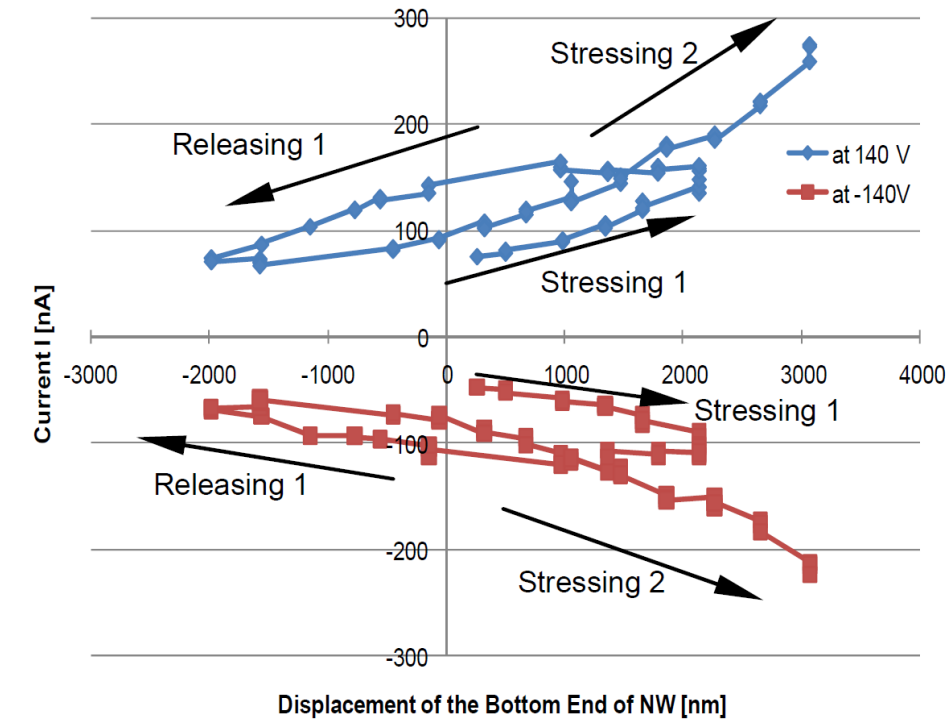

(a)

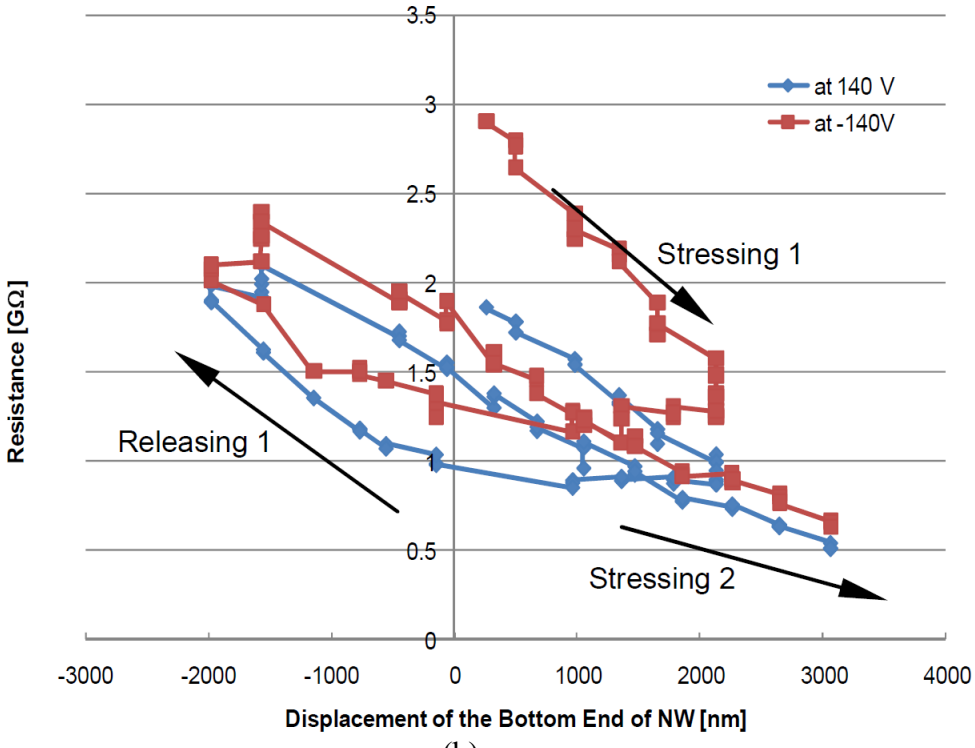

(b)

Figure 5.20: Position sensing using a nanowire. The end of the nanowire on the STM probe was moved toward the AFM cantilever, whereas the position was determined from the STM controller. The curves show the variations in the current and resistance with changes in position.

Similarly, the nanowire can be used to sense forces (Figure 5.21). The force is calibrated using an AFM cantilever by monitoring its deflection and can be determined through either current or resistance. The curves show the first eight points for the process of "Stressing 2". Using the average of the absolute values of current I at biases 140 and -140 V, the force can be read out as $F = 6.4I - 393.0$, ($I_0 = 61.3$ nA) here F is in nN scale. With the resistance as the input, $F = -392.3R + 834.4$ ($R_0 = 2.1$ GΩ).

Since the B_4C peapod nanostructure shows a piezoresistive transport characteristic as the inter-nanorod separation falls into region I (in Figure 5.13 a and f, the average inter-nanorod gap is 7.7 nm) and it is generally known that the band structure change contributes to the piezoresistive effect in common NEMS[118-121], an important question arises: Does the piezoresistive effect also originate from the band structure change? To answer this question, comparative experiments were performed on individual B_4C nanowires without having embedded nickel silicon boride nanorods. The homogenous B_4C nanowires exhibit higher resistance than the peapod nanostructures and no piezoresistive effect was observed. It is well known that nickel silicon boride is a good electrical conductor and B_4C has a relatively high resistance, indicating that the peapod B_4C nanostructure can function as a Coulomb blockade (CB)[122, 123] chain. The B_4C thin-walls, partnering together with the cavity between two adjacent conductive nanorods, act as tunneling junctions along the nanowire, forming a unique metal-insulator-metal (MIM) structure. Theoretical and experimental studies [124, 125] on the electrical transport characteristics of nanojunction systems reveal that the tunneling effect exclusively depends on the inter-nanorod separation. Hence, the change in inter-nanorod separation can alter the tunneling transport configuration, which in turn affects the tunneling current. The piezoresistive effect dominates the tunneling effect in a junction with large

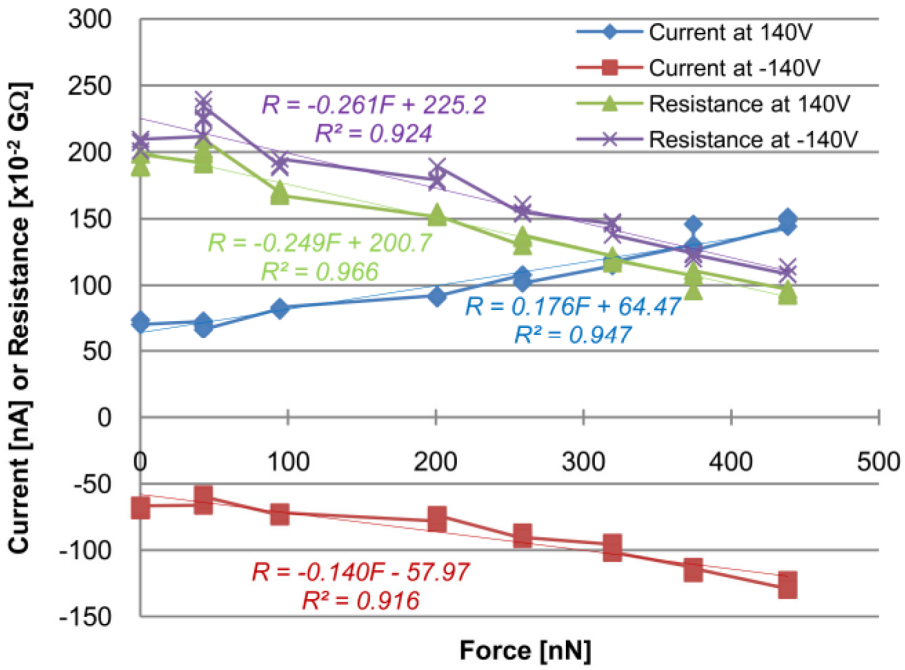

Figure 5.21: Force sensing using a nanowire. The force is calibrated using an AFM cantilever by monitoring its deflection and can be determined through either the current or the resistance. The curves show the first eight points for the process of "Stressing 2".

separation, for instance, in region *I*, where the tunneling current remains low. The linear increase in current during buckling as a result of piezoresistive effect implies its potential for sensing position/strain change.

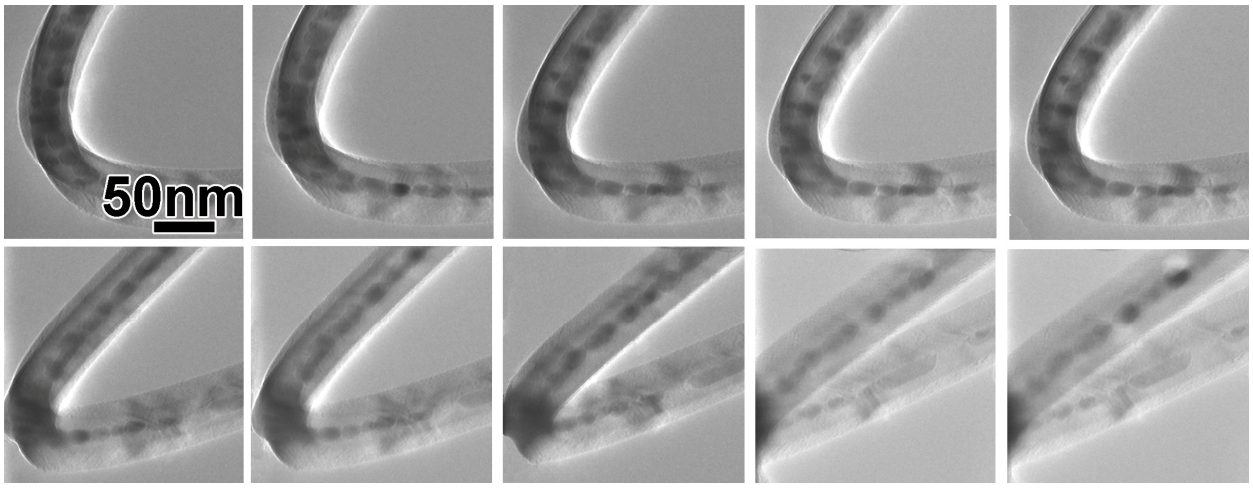

Figure 5.22: Force/displacement sensing with inter-nanorod tunneling effect in a B_4C peapod nanostructure. The stressing process recorded with TEM images.

As the bending strain increases, the inter-nanorod separation δ decreases down to a few angstroms (in region *II*) (Figure 5.22). In this region, the inter-nanorod tunneling is accordingly enhanced and starts to dominate the conductivity until the strain forces the separated nanorods into region *III*. The current density j_t changes exponentially with the inter-nanorod separation[124], $j_t \sim e^{-\delta}$. If the initial separation δ_0 is in the sub-nanometer range, the tunneling can also occur at low strain (Figure 5.23). Such an exponential increase can further amplify the strain-induced resistance change, providing an extremely high sensitivity to the position/force change. Here we demonstrate the transition from the piezoresistive electron transport to the tunneling electron transport due to the increased strain (Figure 5.24). A linear current increase is illustrated at the low-stress stage under an external bias voltage of 25 V, and the current-strain (I-ε) curve was fitted by the equation $I = 0.0741\varepsilon - 0.8626$ (Figure 5.24). Along with the increase in stress, the separation enters region *II*, the current jumps abruptly and increases with a quasi-exponential trend to the external force, and the conductivity is at least two-orders-of-magnitude higher than that in the low-stress stage. This abrupt increase doubtlessly suggested the beginning of inter-nanorod tunneling (Figure 5.22). The I-ε curve in the high strain region is fitted by an

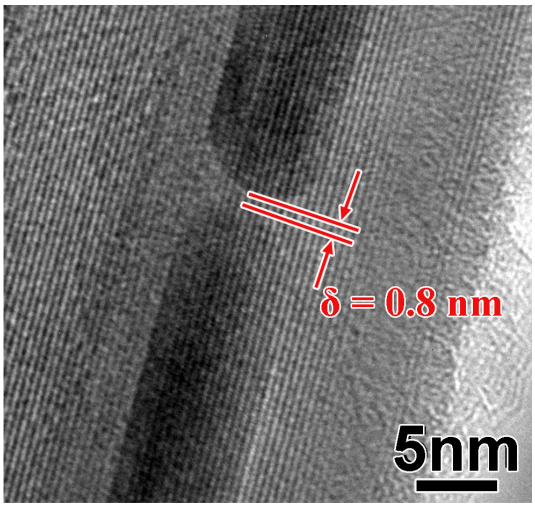

Figure 5.23: A HRTEM image shows that the inter-nanorod separation δ under the external stress can be smaller than 1 nm, which is appropriate for tunneling.

exponential curve: $I = 1E\text{-}04e^{0.121\varepsilon}$ (Figure 5.24). To further prove the reproducibility of the tunneling effect in peapod B_4C nanostructures, we have characterized the relations between the strain and current with different inter-nanorod gap distances (Figure 5.25). All curves show the quasi-exponential trend under an external bias voltage of 25 V. The sensitivity of the nanowire to the strain or the inter-nanorod gap distance change depends on the initial gap distance δ_0. The tunneling effect in the nanorod embedded nanowire configuration enables the capability and robustness of simple, highly sensitive displacement, force and strain sensing.

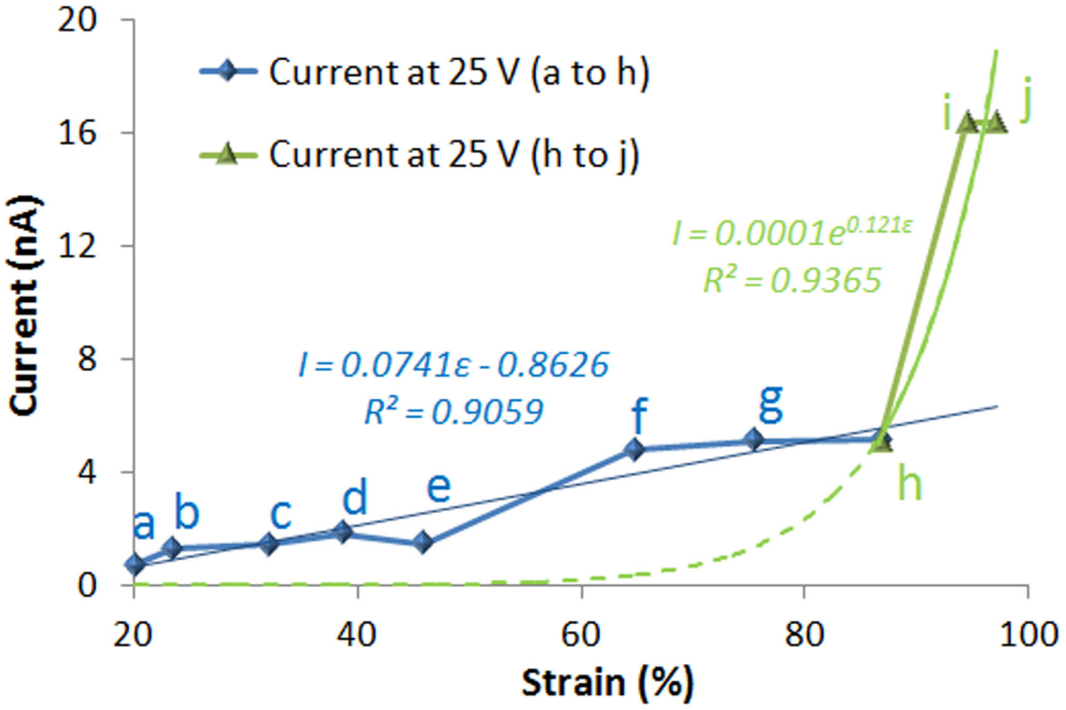

Figure 5.24: The relation between the current and the strain of the nanowire. The inter-nanorod current increases with the increase of external force at different rates under an external bias voltage of 25 V. At the low-stress stage, the current increases approximately linearly to the external force, and the strain-current curve is fitted by $I = 0.0741\varepsilon - 0.8626$. However, starting from the point h on, the current jumps abruptly and increases with a quasi-exponential trend to the external force. This abrupt increase and the quasi-exponential trend strongly suggest that inter-nanorod tunneling occurred. In this case, the current force curve in the high strain region (point h-j) fits well with an exponential curve well: $I = 1E\text{-}04e^{0.121\varepsilon}$.

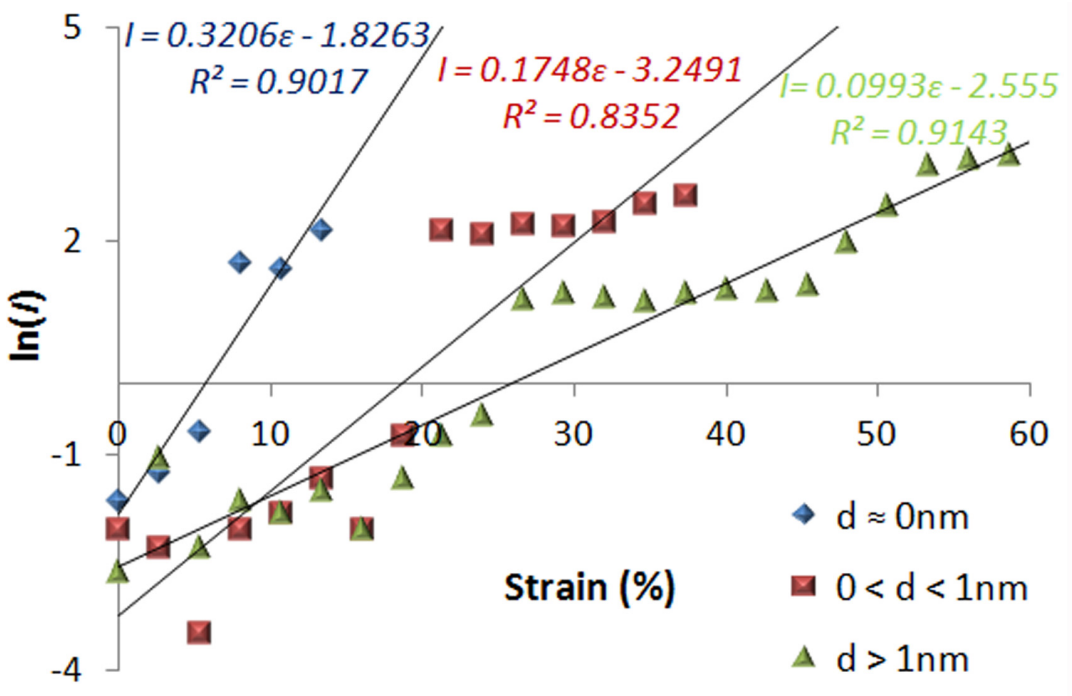

Figure 5.25: Relations between the strain and the natural logarithm value of current in the B_4C nanostructures with different inter-nanorod gap distances. All curves fit with the linear trends, thus show the quasi-exponential relations.

5.4.5 Summary

In summary, we have demonstrated the internal electron tunneling enabled electromechanical coupling in a new type of B_4C nanowire with a unique peapod structure. The peapod B_4C nanowires exhibited elastically recoverable deformation after multiple high-strain bending cycles without an apparent brittle failure or obvious residual deformation. From the measurements, we have also determined the Young's modulus of peapod B_4C nanostructures, which is an important parameter of these unique building-blocks for practical applications. The tunneling effect from the neighboring nanorods in the peapod nanostructure enables simultaneous position and force sensing at the pico-nanometer and pico-Newton levels. These findings lay a constitutive foundation for developing nanowire-based tunneling picoscopes, picosensors, and smart

nanocomposites, opening up the possibility of discovering new phenomena in a wide range of fields, such as measuring the adhesion forces of cells on extracellular matrix substrates or shear forces in microfluidic applications.

5.5 Chapter Summary

In summary, we proposed an alignment-free tunable tunneling barrier architecture and physically realized this nanostructure via peapod nanowire. The Temoshenko model has been employed to illustrate the dynamics of the tunneling gap width that alternated by the strain force, and we used MIM tunneling model to simulate the tunneling current variation that was induced by the gap width change, thus achieving a synthetic buckling-tunneling model. The internal electron tunneling enabled electromechanical coupling in a new type of B_4C nanowire with a unique peapod structure were also demonstrated. The peapod B_4C nanowires exhibited elastically recoverable deformation after multiple high-strain bending cycles without an apparent brittle failure or obvious residual deformation. From the measurements, we have also determined the Young's modulus of peapod B_4C nanostructures, which is an important parameter of these unique building-blocks for practical applications. The tunneling effect from the neighboring nanorods in the peapod nanostructure enables simultaneous position and force sensing at the pico-nanometer and pico-Newton levels. These findings lay a constitutive foundation for developing nanowire-based tunneling picoscopes, picosensors, and smart nanocomposites, opening up the possibility of discovering new phenomena in a wide range of fields, such as measuring the adhesion forces of cells on extracellular matrix substrates or shear forces in microfluidic applications.

CHAPTER 6

COPPER-OXIDE NANOWIRE-BASED MEMRISTOR

We report the nanorobotic *in situ* forming and characterization of memristors based on individual copper oxide nanowires (CuO NWs) and their potential applications as nanosensors with memory function (memristic sensors or "memsensors"). A series of *in situ* techniques for the experimental investigations of memristors are developed including nanorobotic manipulation, electro-beam-based forming, and electron energy loss spectroscopy (EELS) enabled correlation of transport properties and dopants distribution. All experimental investigations are performed inside a transmission electron microscope (TEM). The initial CuO NW memristors are formed by localized electron-beam irradiation to generate oxygen vacancies as dopants. Current-voltage properties show distinctive hysteresis characteristics of memristors. The mechanism of such memristic behaviors is explained with an oxygen vacancy migration model. The presence and migration of the oxygen vacancies is identified with EELS. Investigations also reveal that the memristic behavior can be influenced by the deformation of the nanowire, showing that the nanowire memristor can serve as a deformation/force memorable sensor. The CuO NW-based memristors will enrich the binary transition oxide family but hold a simpler and more compact design than the conventional thin-film version. With these advantages, the CuO NW-based memristors will not only facilitate their applications in nanoelectronics but play a unique role in micro-/nano-electromechanical systems (MEMS/NEMS) as well.

6.1 Introduction of the Memristor

The first experimental demonstration of a memristor (short for "memory resistor") in 2008 has stimulated fast expanding interests in nanoelectronics due to its unique circuit properties such as current-voltage hysteresis and time-dependent resistance [126-140]. Metal oxides, such as TiO_2, Nb_2O_5, NiO, and ZnO are the most common raw materials for the fabrication of memristive devices due to their resistive transition behaviors [141, 142]. Conventional metal oxide-based memristors take a thin-film design [127-134]. The thin-film structured memristors have great advantages such as low-energy electroforming and high switching speed [139, 143]. Therefore, it is the natural choice for the next generation non-volatile random memory (NVRM). However, the large energy/time consumption during the device fabrication may limit their applications in other areas [144-146].

On the other hand, as a new fundamental element for electronics, a memristor may also open new possibilities in micro-/nanoelectromechanical systems (MEMS/NEMS), providing an additional transduction mechanism to piezoresistivity/piezoelectricity, magnetoresistivity, and capacitance [146]. Any stimuli such as mechanical deformation/force, chemicals, or bio-samples that influenced the formation/reformation of a memristor will leave a historical record in it, which can be detected afterwards, resulting in a "memsensor" with a passive sensing fashion. While a variety of new possibilities are still under development, we need to tackle the challenges on the feasible ways to construct a functional memristive device from the raw material, as well as the memristive switching mechanisms based on *in situ* investigations. Previous investigations are typically *ex situ*: the transport properties have been investigated before and after the switching occurred but unable to correlate to the structural changes during the forming and switching of the memristors [130-134, 138-140, 144]. This is partly due to the setup of the thin-

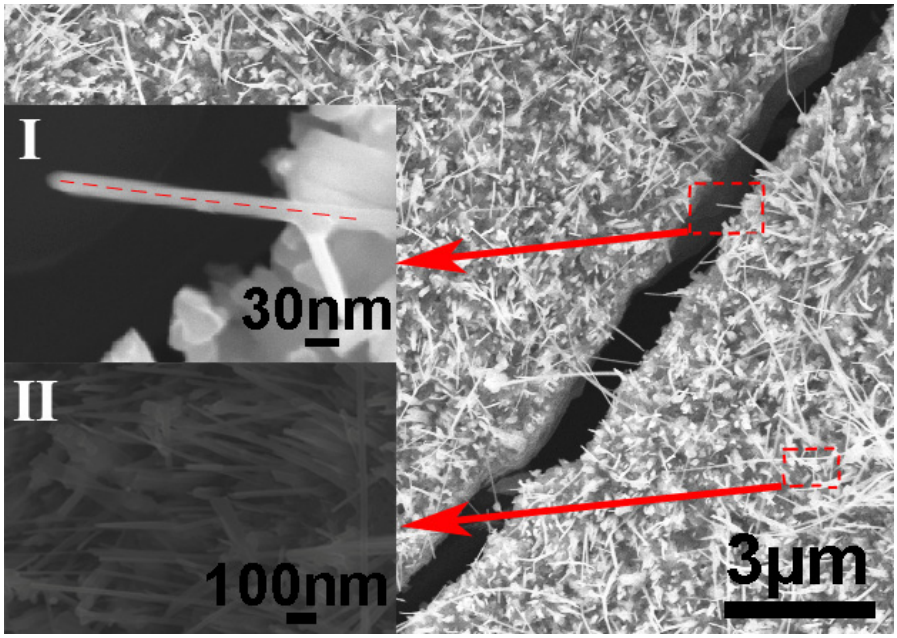

(a)

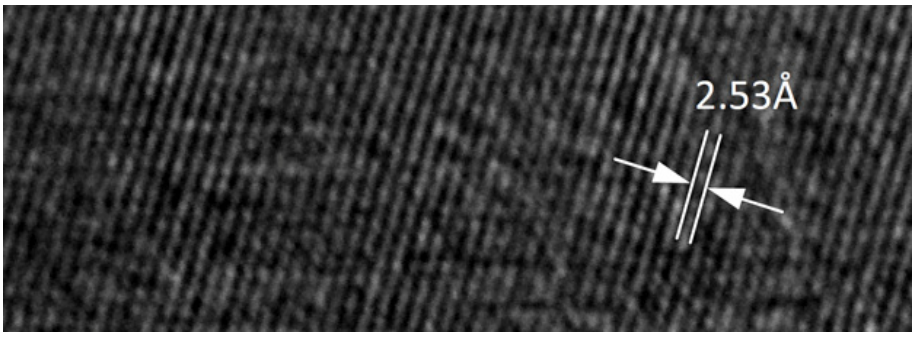

(b)

Figure 6.1: The fabrication of CuO NW (a) The non-flaking nanowire arrays were grown on the surface of the copper substrate after 2-hour incubation in a box oven at 500℃. Inset I shows the detailed image of a single nanowire. Inset II shows that as-fabricated nanowires are distributed in the substrate at a high density of about 4~6 wires per 100 square nanometer. (b) HRTEM image indicates an inter-planar spacing of 2.53 Å of the nanowire.

film based memristor where active metal oxide regions are buried under the metal electrode contact and *in situ* investigations are difficult to perform. Furthermore, the thin-film based two-dimensional memristor has limited the flexibility to be extended to other forms of nano-electronic devices.

In this report we propose an one dimensional metal-oxide nanowire based memristor with an *in situ* approach inside a transmission electron microscope (TEM), using electron beam irradiation, nanomanipulation and electron energy loss spectroscopy (EELS) for its formation, characterization and applications. This enables us to correlate the transient transport properties with the structures of individual nanowires. In the following, we will first describe the realization and characterization of this nanowire-based memristor device, and then address its mechanism as well as its applications.

6.2 Fabrication and Characterization of the Copper-Oxide Nanowire-Based Memristor

The raw materials used for this experiment are as-grown CuO NWs. The synthesis of the nanowires begins with a copper foil [147]. As shown in Figure 6.1(a), after 2-hour incubation in a box oven at 500℃, the non-flaking nanowire arrays were grown on the surface of the copper substrate. The diameters of the nanowires ranged from 30 to 50 nm. The inset I of Figure 6.1(a) shows the detailed image of a single nanowire. The inset II of Figure 6.1(a) also shows that as-fabricated nanowires are distributed in the substrate at a high density of about 4~6 wires per 100 square nanometers.

If we assume each individual wire can be built into a memory cell, the estimated order of the memory density can reach about 100~120 Gbit/in^2. Furthermore, the high resolution TEM (HRTEM) image in Figure 6.1(b) indicates an inter-planar spacing of 2.53 Å, which indicates high purity of the as-synthesized CuO NW [148]. Figure 6.2(a) demonstrates that a single wire was picked up onto a probe using a nanorobotic manipulator installed inside a scanning electron microscope (SEM) and then it was fixed in place by using focused-ion-beam chemical vapor deposition (FIB-CVD) (Figure 6.2(b)). The nanowire-attached probe acted as a sample holder

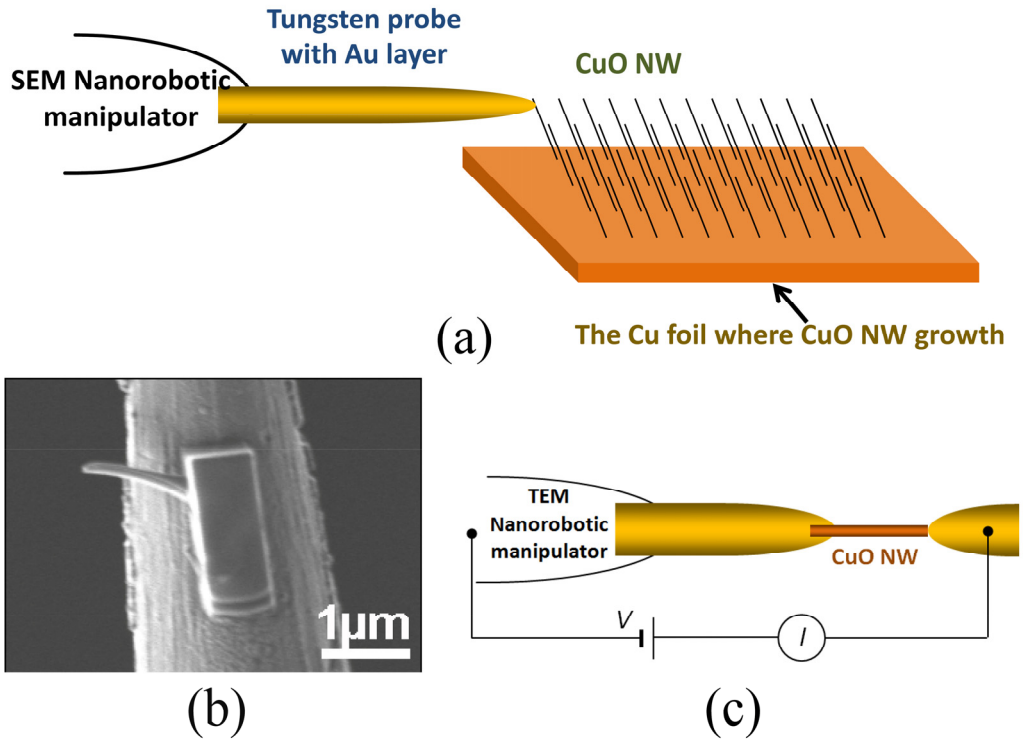

Figure 6.2: (a) A single wire was picked up by a probe using a nanorobotic manipulator installed inside a scanning electron microscope (SEM), (b) The selected nanowire was fixed on the probe by using focused-ion-beam chemical vapor deposition (FIB-CVD), (c) The setup for the electrical characterization of a single CuO NW.

and was transferred into the TEM for characterization. A scanning tunneling microscope (STM) holder installed inside the TEM served as a nanomanipulator for the investigation. As shown in Figure 6.2(c), the nanowire was connected to another probe driven by the nanomanipulator from the other end, and electrical properties of this individual nanowire were measured simultaneously. However, due to the insulate nature of the CuO NW, the measured results in the raw nanowire show an electrically insulating behavior that was expressed as a noise signal; therefore, a *forming* process is required to actuate raw nanowires into memristors and enable them with the characteristic memristive switching behaviors [139, 143, 149].

A number of memristor *forming* processes have been developed by previous researchers [139, 142, 143, 145]. Among them, electroforming processes [143, 145] and physical forming

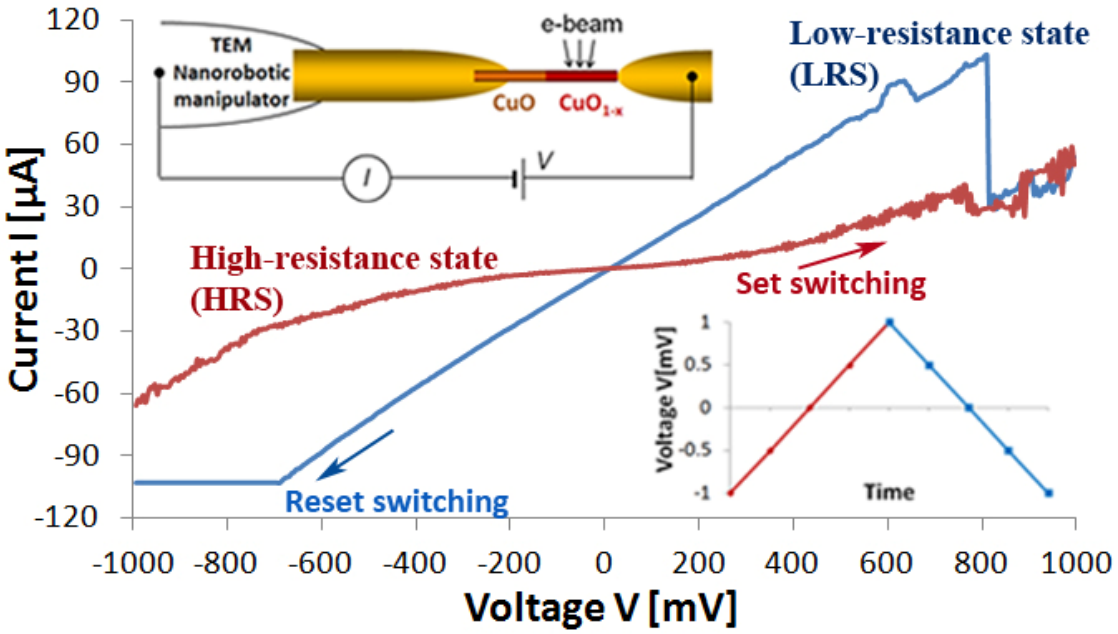

Figure 6.3: E-beam-based forming. The schematic of the e-beam-based and the insulator behavior of the original CuO NW was changed to memristive switching character during forming process.

processes [139, 142] were most commonly used. However, the electroforming are unsuitable for the nanowire-based memristor device since the overheat will cause a hard breakdown in the center of the CuO NW due to its cylindrical structure. Likewise, the physical forming is always carried out for several hours of annealing in a furnace and the inert gas should be injected at the same time, which is an energy/time consuming work. Furthermore, this process cannot be easily carried out *in situ*. For these reasons, we developed a novel *forming* method for the cylinder shaped memristors, and its setup is illustrated in the inset of Figure 6.3. By focusing the TEM electron beam on a part of the CuO NW, high energy electrons bombard the nanowire and expel oxygen atoms from the irradiated area in oxide materials [150]. Therefore, the CuO NW will be "de-oxidized" locally. The irradiation current density was adjusted by changing the focus, the magnification, the brightness and the incident area. This process was achieved at a current density of 20 A/cm^2 after 200 s of irradiation at an area of 1.3×10^{-14} cm^2. The accelerating

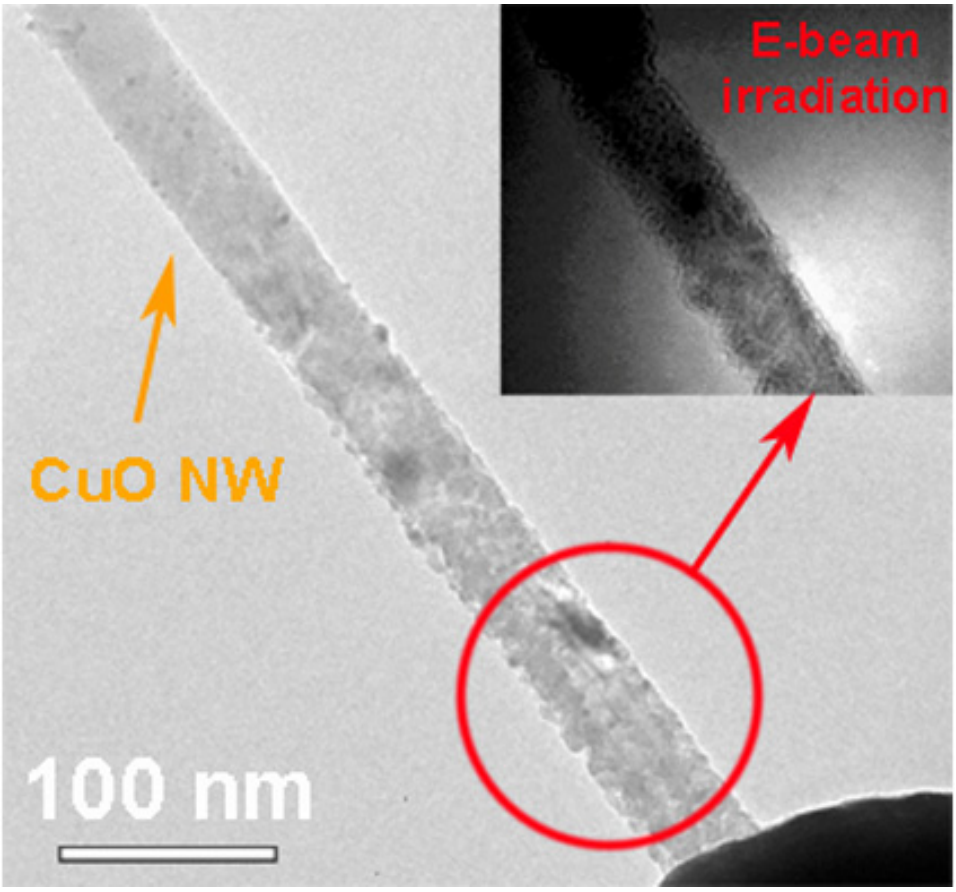

Figure 6.4: The gradual forming process of the CuO NW demonstrated by using TEM.

voltage of the electron beam was kept at 200 kV in all experiments. The completion of the *forming*, which induces CuO oxide to the memristive material, can be identified *in situ* by electrical measurement or microscopy analysis. Since the dynamic resistivity is the key character of memristive devices, the hysteresis *I-V* curve in Figure 6.3 symbolizes the *formation* of a memristor device. The high resolution TEM (HRTEM) image in Figure 6.4 demonstrates the gradual forming process of the CuO NW with a distinct difference between the metalized segment and the pristine part. The irradiated area tends to become amorphous and can be easily seen from the image.

The hysteresis *I-V* curve in Figure 6.3 shows that there are two distinctive reversible "off" and "on" states in the memristor device. The off state corresponds to the high-resistance state

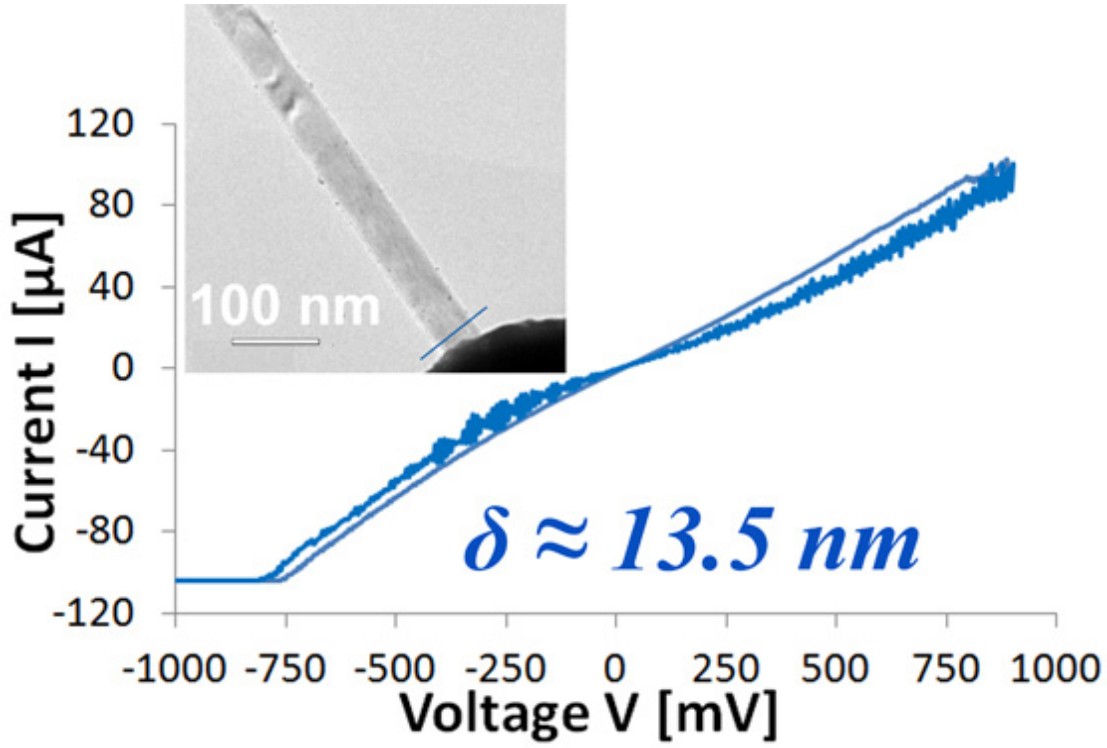

Figure 6.5: The resistive switching behavior as δ = 13.5 nm.

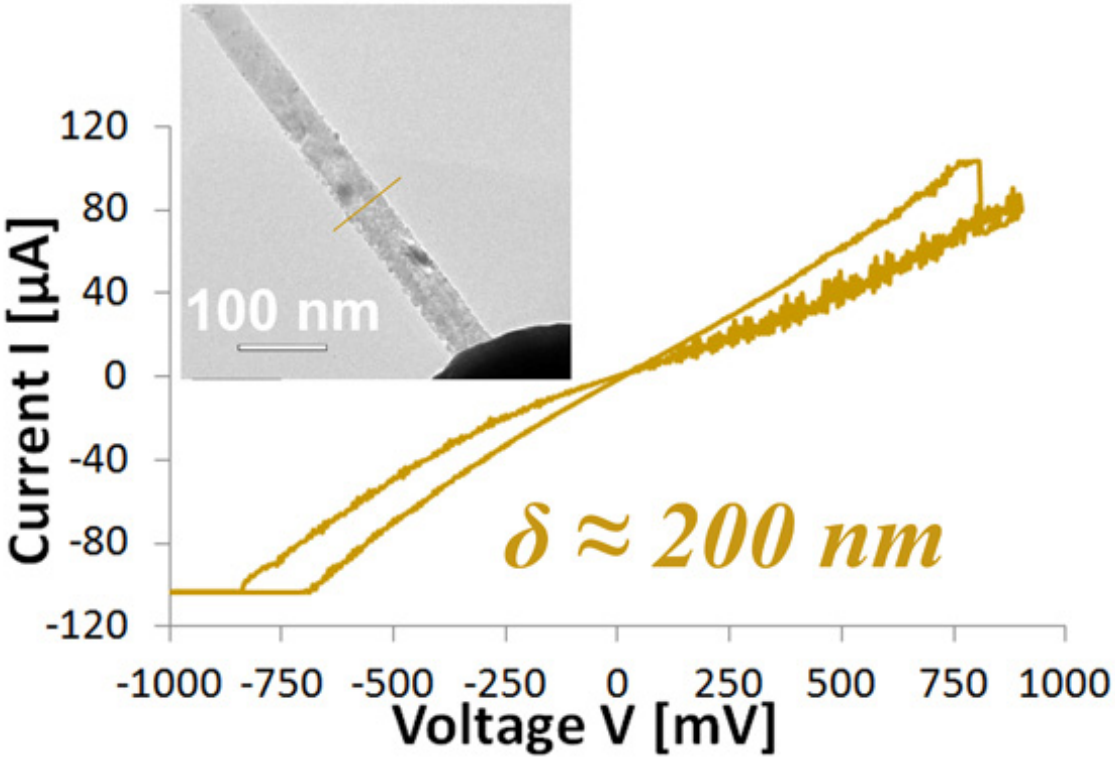

Figure 6.6: The resistive switching behavior as δ = 200 nm.

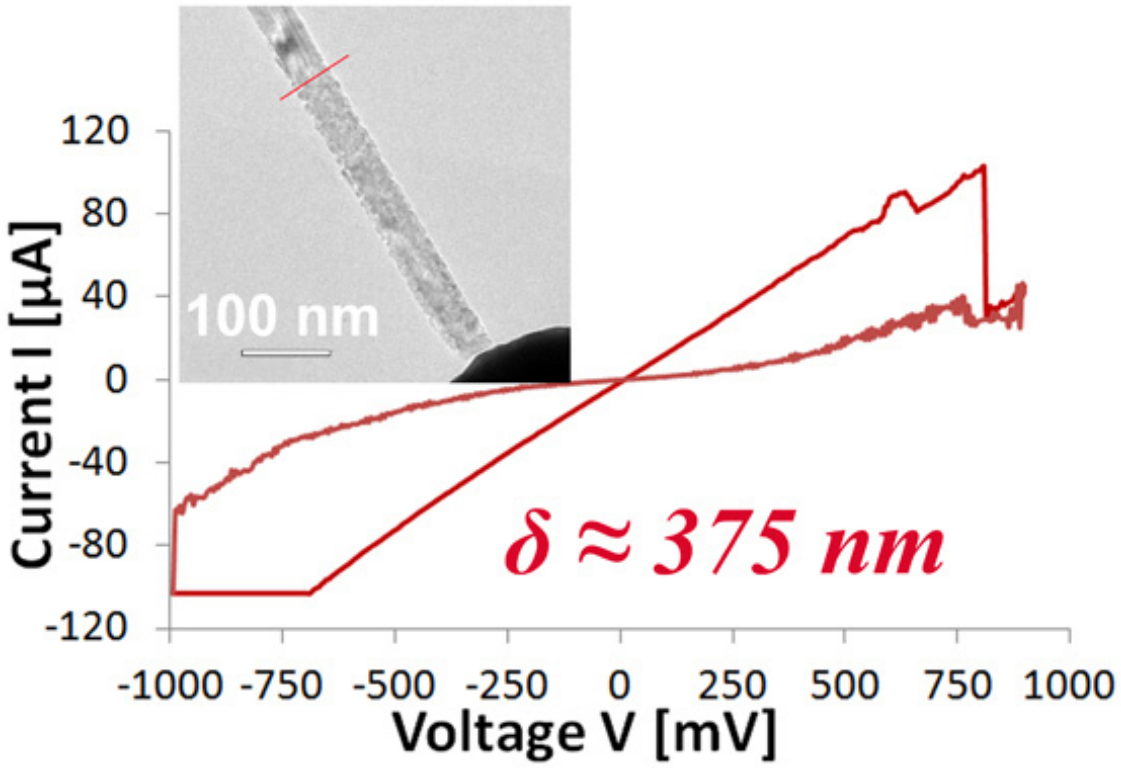

Figure 6.7: The resistive switching behavior as δ = 375 nm.

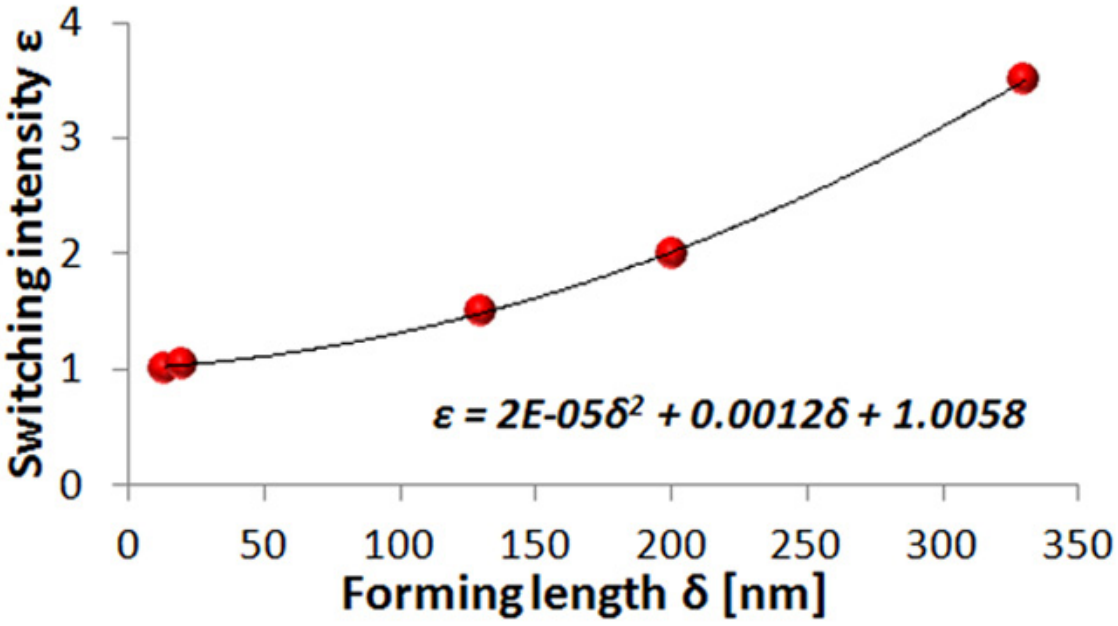

Figure 6.8: The relation between the switching intensity ε and the forming length δ is: $\varepsilon = 0.0008\,\delta^2 + 0.0082\,\delta + 1.0036$.

(HRS) and the on state corresponds to the low-resistance state (LRS). Therefore their resistances are defined as R_{off} and R_{on}, respectively. As the applied voltage increases from 0 to the threshold voltage $V_{th} \approx 800\ mV$, the device switches from the off state to the on state, known as a "set" process. After decreasing the voltage and then reversing the direction to the reverse threshold voltage, the device went through a "reset" process change from on to off state. At any given voltages, the resistance can be either R_{off} or R_{on}, depended on whether in memory of the previous applied positive or negative threshold voltage. Furthermore, we can define the magnitude of the switching by ε, the highest value of R_{off}/R_{on} in a hysteresis dual-curve. For various length δ of the irradiated area, as a function of ε, represents the dynamic *I-V* characteristics are shown in Figure 6.5 to 6.7. It is noted that only a small area (e.g. 13.5 nm) of irradiation will be enough to induce visible memristive switching behavior. On the other hand, such behaviors may only be visible if the device is at nanometer scale. With larger portion of forming the memristor will have potentially larger ε, i.e., a higher switching intensity, as shown in Figure 6.8. However the threshold voltage V_{th} remains the same. This dynamic provides insight into the switching mechanism of CuO NW-based memristive devices.

6.3 Mechanism Analysis of the Memristive Switch

There are several theories explaining the mechanism of the memristor behavior [126, 142]. The CuO NW memristor is believed to function due to the conduction through oxygen vacancies. To verify this, it is critical to investigate the oxygen vacancy presence and migration *in situ*. Previous investigations on oxygen vacancy are mainly concentrated on detecting the structural or direct stoichiometry changes [151, 152]. In this work we instead choose to detect the presense of Cu^{1+} (transit from Cu^{2+}), which is a direct result of the oxygen vacancies. The electron energy

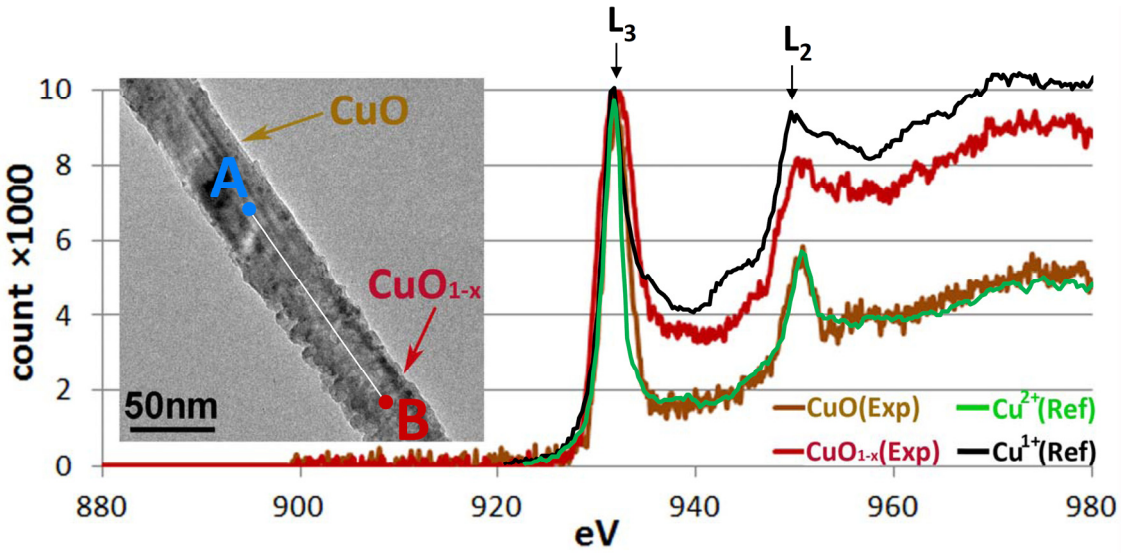

Figure 6.9: The characterization of the deoxidized segment. The Cu $L_{2,3}$ edge spectra of the nanowire at point B before and after the electron irradiation, with standard Cu^{2+} and Cu^{1+} spectra superimposed as references. Before the irradiation, the Cu spectrum is coincided with Cu^{2+} very well, proving its 100% CuO composition. The spectrum after the e-beam irradiation shows an intermediate state between the Cu^{2+} and the Cu^{1+}. We termed the state as CuO_{1-x} (a mixture of Cu_2O and CuO).

loss spectroscopy (EELS) is a multi-functional spectroscopy technique that is sensitive in measuring atomic composition, chemical bonding, surface properties, conduction band electronic properties and especially the change of valence state [153]. Since such methods can readily distinguish Cu^{2+} and Cu^{1+} and it is more sensitive to low concentration of oxygen vacancies and less depend on sample crystalinity due to damage by electron irradiation [154]. The physical/chemical property changes that are responsible for the memristive switching can be studied *in situ* by using EELS technique.

Figure 6.9 shows the Cu $L_{2,3}$ edge spectra at point A on the nanowire before and after the electron irradiation with the pristine unirradiated portion (CuO) and the irradiated portion (CuO_{1-x}). The standard Cu^{2+} and Cu^{1+} spectra is superimposed as references, showing the distinctive difference between the L_3/L_2 peak intensity ratio for Cu^{2+} and Cu^{1+}. The spectrum before the irradiation coincides with Cu^{2+} very well, proving its 100% CuO composition, while the

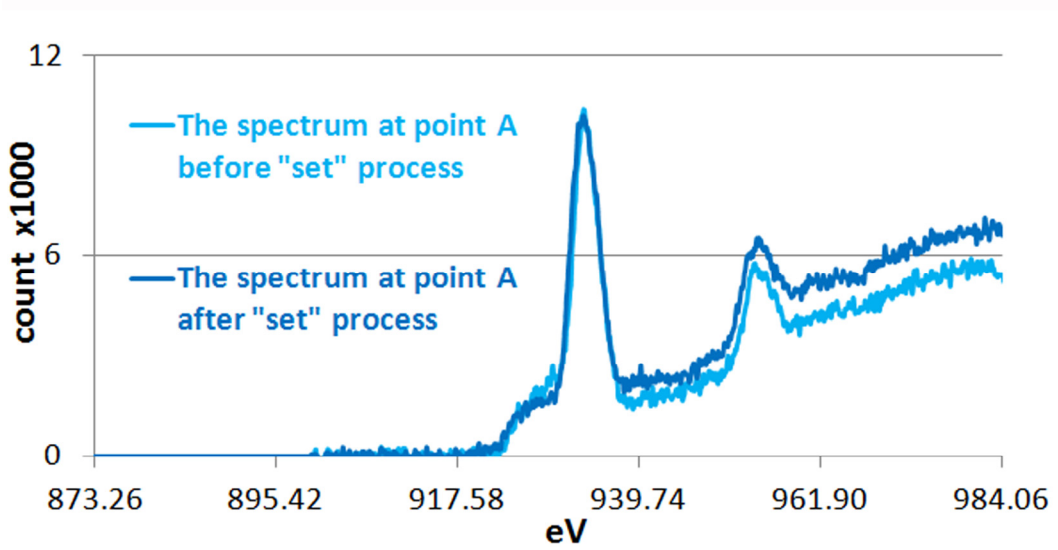

Figure 6.10: The Cu $L_{2,3}$ edge spectra of an unirradiated area at point A before and after the electron "set" process. The higher L_2 peak intensity after the "set" process indicates the presence of more Cu^{1+}, which corresponds to the increase of oxygen vacancies.

spectrum after the irradiated lies in between that of Cu^{2+} and Cu^{1+}. Therefore, the irradiated part can be represented by CuO_{1-x} which is a mixture of Cu_2O and CuO. The creation of Cu^{1+} after the irradiation proves the loss of oxygen, i.e., creation of oxygen vacancies. The amount of oxygen vacancies is qualitatively represented by the excessive L_2 peak intensity relative to that of Cu^{2+}. Figure 6.10 shows the Cu $L_{2,3}$ edge at the unirradiated CuO area (point A) before and after the memristor setting process, i.e., an applied voltage greater than V_{th}. It is clear that the spectrum after the switching voltage has a higher L_2 peak intensity than that before, indicating the presence of oxygen vacancies. Since there is no loss of overall oxygen atoms by applying a voltage, the oxygen vacancies can only be migrated from CuO_{1-x} area.

Now a complete mechanism for CuO NW-based memristors can be illustrated schematically in Figure 6.11. The initial forming process de-oxidizes CuO thus creates abundant oxygen vacancies, represented by small circles in Figure 6.11(a). However, these are localized oxygen vacancies do not conduct through the nanowire, so the nanowire will stay at a high

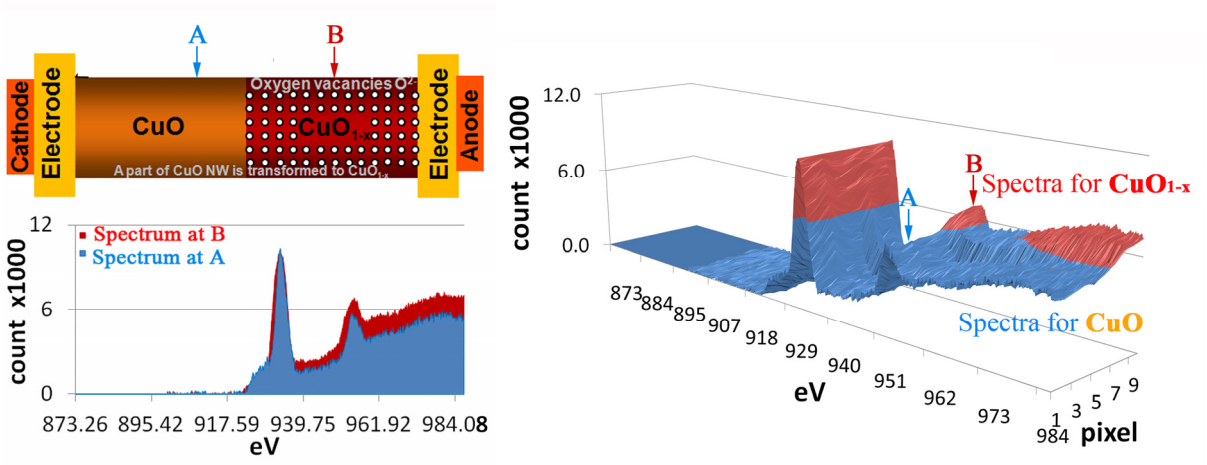

(a) (b)

Figure 6.11: (a) The model of the nanowire that after the forming process. After the forming of a part of CuO NW to CuO_{1-x}, the oxygen cations are excessive in this segment due to the loss of oxygen atoms. The spectrum at B shows an oxygen vacancies rich performance than the spectrum at point A. (b) The STEM-EEL spectra of the CuO NW after the forming process. The spectra topology represents the distinguish oxygen vacancy density difference along the nanowire.

resistivity off state. As shown in Figure 6.12, the oxygen vacancies are forced to migrate under an external bias and eventually channeling through the nanowire when the voltage reaches the threshold V_{th}. Then, the oxygen vacancies become the major charge carriers such that the nanowire switches to a low resistivity on state. Oxygen vacancies will remain as the charge carriers thus "remember" its low resistivity state. Only when a high reverse resetting threshold voltage is applied, as shown in Figure 6.13, the oxygen vacancies are forced to reversely migrate and eventually disconnect the conduction path. Then the nanowire device returns to its high resistivity off state. Again, with a bias lower than the setting voltage applied, it will remember its high resistivity state. This theory also explains very well about the relation between the switching intensity ε and the forming length δ, as well as the steady threshold voltage V_{th} in Figure 6.11(b), Figure 6.12(b), and Figure 6.13(b). The switching intensity ε is depend on the

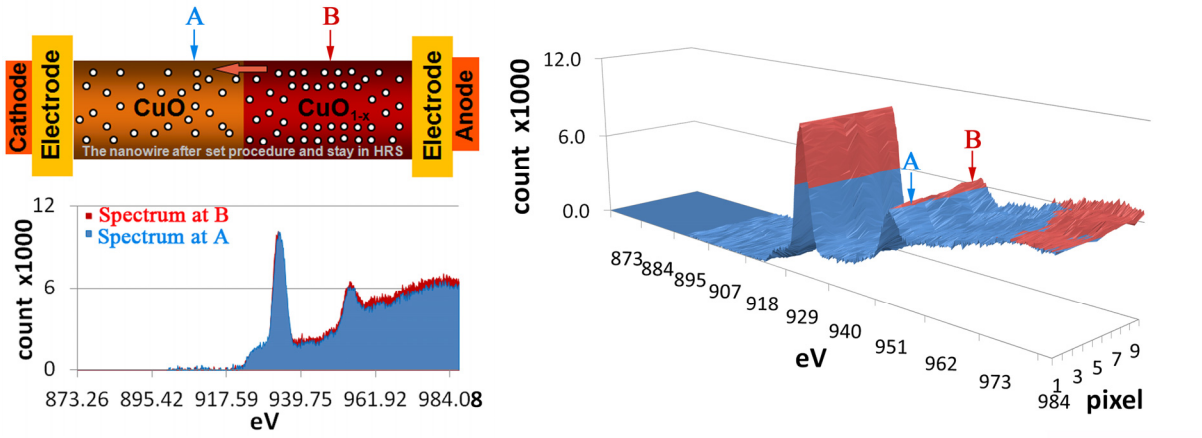

(a) (b)

Figure 6.12: (a) The model of the nanowire after the set procedure (from HRS to LRS). Set procedure: the anode is placed on the part of CuO_{1-x} and the cathode is in the CuO side. As sweeping the bias between two electrodes, the vacancies in CuO_{1-x} part are transport all through the nanowire that drives by the electric force. Meanwhile, the electrons pass through the conductive paths that explored by the cations. Therefore, the conductivity decreased. The gap between the spectrum at point A and point B is narrowed, which indicates the migration of oxygen vacancies from B to A. (b) The STEM-EEL spectra of the CuO NW after the set procedure. The spectra topology clearly indicates the migration of the oxygen vacancies from rich area (B) to the poor area (A).

amount of oxygen vacancy thus the forming length δ while the Vth is determined by minimum force needed to enable individual oxygen vacancy migration therefore it is relatively unchanged.

To verify our proposed mechanism, the scanning transmission electron microscope-based electron energy loss spectroscopy (STEM-EELS) was implemented to an individual CuO-Cu_2O nanowire. STEM is a type of TEM that the target sample is studied by scanning over a raster, which is different from the conventional TEM that focuses the electron on a narrow spot. The EELS experiment in a context of STEM allows the multi-signal detection (the energy-loss spectra and the correlated mass signal) for each probe position via scanning in a line-mode or area mode, which yields to a wealth of information in the distinguishable region of interest on the specimen, concerning atomic composition, chemical bonding structure, conduction band electronic properties, and the valence state change. Here, the EELS measurement is carried out in

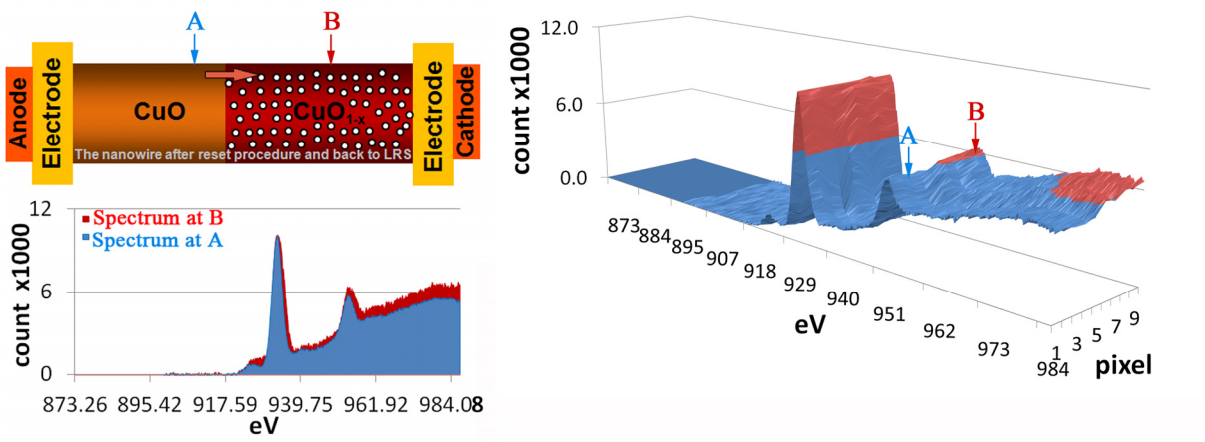

(a) (b)

Figure 6.13: (a) The model of the nanowire after the reset procedure (from LRS to HRS). To switch from LRS to HRS (reset procedure), the electric force direction was switched according to the alternate of external polar, which in turn broke the conductive path along the nanowire and makes the resistance back to the original high status. The gap between the two spectra opened again, which indicates the reversal migration of the oxygen vacancies from A to B. (b) The correspondent STEM-EEL spectra for the CuO NW after the reset switching process. The reversal of O^{2-} migration is clearly indicated.

a STEM, the EEL spectra along the nanowire can be continuously measured. A scanning oxygen EEL spectrum topology along the nanowire can be plotted, and the oxygen distributions *in situ* before and after the set process or reset process can be documented. Then, by comparing these spectrum topologies, the migration trend of the oxygen vacancies can be measured, which in turn provides a solid evidence for the migration-based switching.

As shown in the Figure 6.11(a), the STEM-EELS technique was carried out across the nanowire from point A to point B. The continuous Cu $L_{2,3}$ edge EELS profile as plotted in Figure 6.11(b), Figure 6.12(b), and Figure 6.13(b) are corresponding to each state in Figure 6.11(a), Figure 6.12(a), and Figure 6.13(a), respectively. Figure 6.11(b) represents the spectra profile from point A to B at the initial state after forming, corresponding to Figure 6.11(a). In order to give a clear visual effect, we deliberately set the color scheme so that the red color is directly correlated to the excessive L_2 peak intensity above that of Cu^{2+}. Therefore, the fact that there is

no red signal at point A area indicates that no oxygen vacancies. The excessive intensity of L_2 at point B area is represented as red color, representing the oxygen vacancy qualitatively. Moreover, as demonstrated in Figure 6.11(a), the spectrums at points A and B were also plotted. It is noted that there is a large gap between these two spectrums, indicating the oxygen vacancies density difference at these two points. However, as shown in Figure 6.12(a), the gap between these two spectrums was narrowed after the set switching process, which implies that the oxygen vacancies have changed at these two points. Furthermore, from the spectra profile in Figure 6.12(b), it is noted that there is clearly a red signal appears at L_2 peak for point A area, accompanied by a slightly reduced red signal at area B. This is a direct proof of the migration of the oxygen vacancies from B to A. After the reset switching process, the spectra profile in Figure 6.13(b) shows the disappearing of the red signal at L_2 peak in area A and the gap between the spectra in A and B in Figure 6.12(a) was opened again, indicating the reversal of oxygen vacancy migration.

6.4 Memsensor

In addition to the commonly anticipated non-volatile memory device (NVRM) application using thin-film memristors, we are far more interested in searching the possibility for new device based on nanowire memristor that has a "memory" of other physical quantities, such as mechanical deformation. We termed this type of memory devices as "memsensors".

Here we propose the application of nanowire-based memristors as displacement transducers. Figure 6.14 shows the characteristic *I-V* curves at various deformations applied to the CuO NW. We define the deformation ratio as σ, which symbolized the deformation of the nanowire when it compares to the original length. The displacement of the attached probe is

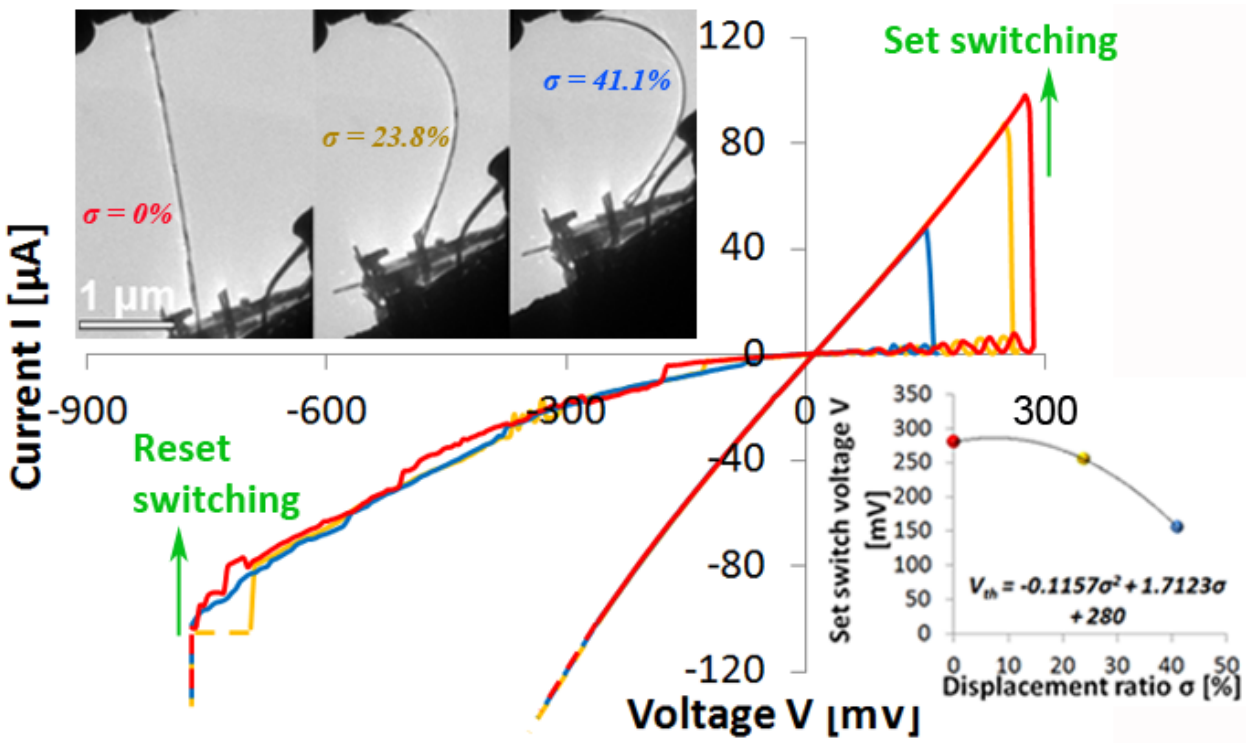

Figure 6.14: The application of CuO NW-based memristor as a displacement transducer. (a) The switching threshold voltage V_{th} was decreased according to the increasing of the deformation ratio σ. The displacement of the attached probe is measured by the deformation of the bending wire.

measured by the deformation of the bending wire. The switching threshold voltage V_{th} was decreased from 280 mV to 155 mV when the nanowire was deformed. Thus, the relations between the deformation ratio σ and the V_{th} can be given by: $V_{th} = -0.0031\sigma^2 - 2.6057\sigma + 289.42$.

This result has a profound meaning that we may have achieved a new device as we defined as "memsensor". For instance, without an external stress, when the voltage was kept at a constant intermediate value, e.g. 200 mV, the nanowire should keep its resistance since it is below the threshold voltage. By applying an external stress, it is possible to lower the memristor switching threshold voltage V_{th} below 200 mV, thus the memristor will have a transition from high resistance state to low resistance state. Also, it will remain at the low resistance state even if the stress is withdrawn. In another word, this memristor will have memory of external stress instead

of external voltage. It demonstrated the principle of memsensor which can be achieved by combining memristor properties with other sensory properties. While the detailed mechanism of CuO under a stress is not fully understood yet, and we intend to address this challenge in future investigations.

6.5 Chapter Summary

In summary, we have developed a memristor nanodevices based on an individual CuO NW. The forming process depends on irradiation-beam-induced local de-oxidization of a segment of a CuO NW. The memristivity of this device is characterized by dynamic hysteretic current-voltage curves. By using the EELS technique to investigate the switching mechanism, we have not only confirmed the creation of oxygen vacancies in CuO NWs at the forming process, but also *in situ* quantified the migration of the oxygen vacancies, which is responsible for the memristive switching in our memristor device. The nanowire-based memristor has the potential to be combined with other sensing elements to form new types of memsensor devices. One such memsensor has been demonstrated with a combination with mechanical displacement sensor. Therefore nanowire-based memristor shows great potential for designing all kinds of low-power high-throughput memory units and other functional nanodevices.

CHAPTER 7

SUMMARY AND FUTURE WORK

7.1 Summary

The low performance of conventional nano-robotic end-effectors has prevented the development of *in situ* nanotechnology. There are two major difficulties in developing the end-effectors: their nano-fabrication and their advanced characterization at the nanoscale. In this report, six types of end-effectors are introduced. During the investigation of those devices, several nanofabrication methods were developed and advanced *in situ* characterization techniques were applied to the end-effectors, which will improve the research at the nanoscale.

The nanotube fountain pen (NFP) was shown to be a reliable tool to realize the complex metallic nanostructure 3D printing. This NFP prototype uses a CNT injector attached to a reservoir and writing in a continuous mode. The experimental results established that the switching states ("ON" or "OFF") of the NFP writing were realized by drifting the copper atoms that induced by external electrical energy to overcome the energy barrier and collapsed the blocked junction (ON). The external injected energy, the bias voltage, and the current controlled the writing speed of the NFP. With the understanding of the forming process of the as-deposited nanostructures, it is possible to shape the deposit during the writingprocess. The practical applications of this technique were also studied; several 3D structures and writing methods were demonstrated.

By using the NFP technique, a super-fine nanoprobe was fabricated to characterize the transport properties of individual nanostructures. The as-fabricated nanoprobe facilitated the contact force control and the shape adapting. The probe was prepared by flowing copper from a

copper-filled nanotube against the specimen. By controlling the contact force and area, it became possible to keep a constant contact resistance between the sliding probe and the specimen, hence significantly improving the measurement resolution. Sliding probe methods are *in situ* techniques characterized by higher resolution and simplicity in setup compared with conventional two- and four-terminal methods, respectively. Furthermore, they are superior to local property characterization, which is of particular interest for hetero-structured nanomaterials and defects detection.

In the investigation of sphere-on-pillar (SOP) optical nanoantennas, electrical-beam-induced bubbling (EBIB) and electrical-migration-based bubbling (EMBB) were proposed for the controlled fabrication of sphere-on-pillar optical nanoantennas. Melting and bubbling of low melting point encapsulated materials from nanotube shells were realized at certain current densities (10 to 25 A/cm^2). For the materials with a high melting point, the simplified NFP/EMBB is the method to use. The influence of the heat sink effect on the EMBB was also investigated. The volume and surface plasmon resonances of the as-fabricated SOP architecture were tested using the EELS technique; proving that resonance did occur in this structure. Experimentally, this resonance can be achieved by SOP more readily than by near-field optical methods.

An alignment-free tunable tunneling nanosensor was developed as a force/displacement sensor at the nanoscale. The Temoshenko model was employed to illustrate the dynamics of the tunneling gap width that alternated by the strain force, and the MIM tunneling model was used to simulate the tunneling current variation that was induced by the gap width change, thus achieving a synthetic buckling-tunneling model. In materialize this tunneling model, we have demonstrated a new type of B_4C nanowire with a unique peapod structure enabled with internal

electron tunneling. The peapod B_4C nanowires exhibited elastically recoverable deformation after multiple high-strain bending cycles without an apparent brittle failure or obvious residual deformation. The tunneling effect from the neighboring nanorods in the peapod nanostructure enables simultaneous position and force sensing at the pico-nanometer and pico-Newton levels. These findings lay a constitutive foundation for developing nanowire-based tunneling picoscopes, picosensors, and smart nanocomposites, opening up the possibility of discovering new phenomena in a wide range of fields, such as measuring the adhesion forces of cells on extracellular matrix substrates or shear forces in microfluidic applications.

A memristor nanodevice was developed based on individual CuO NW. The forming process depends on irradiation-beam-induced local de-oxidation of a segment of a CuO NW. The memristivity of this device is characterized by dynamic hysteretic current-voltage curves. By using the EELS technique to investigate the switching mechanism, we not only confirmed the creation of oxygen vacancies in CuO NWs at the forming process, but also *in situ* quantified the migration of the oxygen vacancies, which is responsible for the memristive switching in our memristor device. The nanowire-based memristor also shows potential application as a memsensor.

7.2 Future Works

More work is needed to develop the CuO NW-based memsensor as a reliable tool for sensing the external influence. The necessity and value of further investigation are clear: first, the batch fabrication of the CuO NW array is relatively simple; second, the feasibility of the e-beam-based forming method applied to a single nanowire was demonstrated, the applications of which provides an easy way to assemble memristor arrays.

In future works, we will further investigate the response performance of the memsensor to the external variable. Three aspects of work are most important:

1. Repeat the electrical property characterizations of the nanowire at different strain status and confirm the sensing mechanism;

2. To investigate the CuO NW-based memsensor as a reliable sensor, we should study the "zero setting" of such device.

3. Investigate sensing response of this sensor to the other variables, such as the temperature, the applied voltage, and the gas environment.

BIBLIOGRAPHY

BIBLIOGRAPHY

[1] R. P. Feynman, There's plenty of room at the bottom. *Engineering and Science,* 23(5):22-36, 1960.

[2] S. Martel, O. Felfoul, J. B. Mathieu, A. Chanu, S. Tamaz, M. Mohammadi, M. Mankiewicz, and N. Tabatabaei, Mri-based medical nanorobotic platform for the control of magnetic nanoparticles and flagellated bacteria for target interventions in human capillaries. *International Journal of Robotics Research,* 28(9):1169-1182, Sep 2009.

[3] R. A. Freitas, *Nanomedicine, volume i: Basic capabilities*: Landes Bioscience Georgetown, TX, 1999.

[4] M. Ohtsu and H. Hori, *Near-field nano-optics: From basic principles to nano-fabrication and nano-photonics*: Plenum Publishing Corporation, 1999.

[5] O. Benson, Assembly of hybrid photonic architectures from nanophotonic constituents. *Nature,* 480(7376):193-199, Dec 2011.

[6] L. X. Dong, X. Y. Tao, L. Zhang, X. B. Zhang, and B. J. Nelson, Nanorobotic spot welding: Controlled metal deposition with attogram precision from copper-filled carbon nanotubes. *Nano Letters,* 7(1):58-63, Jan 2007.

[7] L. X. Dong, X. Y. Tao, M. Hamdi, L. Zhang, X. B. Zhang, A. Ferreira, and B. J. Nelson, Nanotube fluidic junctions: Internanotube attogram mass transport through walls. *Nano Letters,* 9(1):210-214, Jan 2009.

[8] J. A. Weldon, B. Aleman, A. Sussman, W. Gannett, and A. K. Zettl, Sustained mechanical self-oscillations in carbon nanotubes. *Nano Letters,* 10(5):1728-1733, May 2010.

[9] G. E. Begtrup, W. Gannett, T. D. Yuzvinsky, V. H. Crespi, and A. Zettl, Nanoscale reversible mass transport for archival memory. *Nano Letters,* 9(5):1835-1838, 2009.

[10] Y. H. Gao, Y. Bando, Z. W. Liu, D. Golberg, and H. Nakanishi, Temperature measurement using a gallium-filled carbon nanotube nanothermometer. *Applied Physics Letters,* 83(14):2913-2915, Oct 2003.

[11] A. Kochan, Rapid prototyping gains speed, volume and precision. *Assembly Automation,* 20(4):295-299, 2000 2000.

[12] C. B. Williams, J. K. Cochran, and D. W. Rosen, Additive manufacturing of metallic cellular materials via three-dimensional printing. *International Journal of Advanced Manufacturing Technology,* 53(1-4):231-239, Mar 2011.

[13] M. S. Kim, W. S. Chu, Y. M. Kim, A. P. G. Avila, and S. H. Ahn, Direct metal printing of 3d electrical circuit using rapid prototyping. *International Journal of Precision Engineering and Manufacturing,* 10(5):147-150, Dec 2009.

[14] S. H. Ko, J. Chung, N. Hotz, K. H. Nam, and C. P. Grigoropoulos, Metal nanoparticle direct inkjet printing for low-temperature 3d micro metal structure fabrication. *Journal of Micromechanics and Microengineering,* 20(12):Dec 2010.

[15] S. S. Gill and M. Kaplas, Comparative study of 3d printing technologies for rapid casting of aluminium alloy. *Materials and Manufacturing Processes,* 24(12):1405-1411, 2009.

[16] V. Sanchez-Romaguera, M. B. Madec, and S. G. Yeates, Inkjet printing of 3d metal-insulator-metal crossovers. *Reactive & Functional Polymers,* 68(6):1052-1058, Jun 2008.

[17] K. E. Drexler, Nanotechnology - the past and the future. *Science,* 255(5042):268-269, Jan 1992.

[18] R. D. Heidenre, L. F. Thompson, E. D. Feit, and C. M. Melliars, Fundamental aspects of electron-beam lithography .1. Depth-dose response of polymeric electron-beam resists. *Journal of Applied Physics,* 44(9):4039-4047, 1973.

[19] L. F. Thompson, E. D. Feit, C. M. Melliars, and R. D. Heidenre, Fundamental aspects of electron-beam lithography .2. Low-voltage exposure of negative resists. *Journal of Applied Physics,* 44(9):4048-4051, 1973.

[20] H. J. Dai, N. Franklin, and J. Han, Exploiting the properties of carbon nanotubes for nanolithography. *Applied Physics Letters,* 73(11):1508-1510, Sep 1998.

[21] N. Anscombe, Direct laser writing. *Nature Photonics,* 4(1):22-23, Jan 2010.

[22] R. D. Piner, J. Zhu, F. Xu, S. H. Hong, and C. A. Mirkin, "Dip-pen" nanolithography. *Science,* 283(5402):661-663, Jan 1999.

[23] H. W. P. Koops, J. Kretz, M. Rudolph, and M. Weber, Constructive 3-dimensional lithography with electron-beam-induced deposition for quantum effect devices. *Journal of Vacuum Science & Technology B,* 11(6):2386-2389, Nov-Dec 1993.

[24] S. Matsui, T. Kaito, J. Fujita, M. Komuro, K. Kanda, and Y. Haruyama, Three-dimensional nanostructure fabrication by focused-ion-beam chemical vapor deposition. *Journal of Vacuum Science & Technology B,* 18(6):3181-3184, 2000.

[25] Z. Fan, X. Y. Tao, X. D. Cui, X. D. Fan, X. B. Zhang, and L. X. Dong. Electromigration-based deposition enabled by nanorobotic manipulation inside a transmission electron microscope. In *2011 IEEE International Conference on Robotics and Automation (ICRA 2011)*, *2011 IEEE*, pages 2686-2691, 2011.

[26] F. W. Huo, Z. J. Zheng, G. F. Zheng, L. R. Giam, H. Zhang, and C. A. Mirkin, Polymer pen lithography. *Science,* 321(5896):1658-1660, Sep 2008.

[27] X. Y. Huang, Z. Y. Zhang, Y. Liu, and L. M. Peng, Analytical analysis of heat conduction in a suspended one-dimensional object. *Applied Physics Letters,* 95(14):Oct 2009.

[28] P. C. Collins, M. S. Arnold, and P. Avouris, Engineering carbon nanotubes and nanotube circuits using electrical breakdown. *Science,* 292(5517):706-709, Apr 2001.

[29] J. Y. Huang, S. Chen, S. H. Jo, Z. Wang, D. X. Han, G. Chen, M. S. Dresselhaus, and Z. F. Ren, Atomic-scale imaging of wall-by-wall breakdown and concurrent transport measurements in multiwall carbon nanotubes. *Physical Review Letters,* 94(23):Jun 2005.

[30] L. X. Dong, X. Y. Tao, L. Zhang, X. Zhang, and B. Nelson, Plumbing the depths of the nanometer scale. *Nanotechnology Magazine, IEEE,* 4(1):13-22, Mar 2010.

[31] J. P. Dekker and A. Lodder, Calculated electromigration wind force in face-centered-cubic and body-centered-cubic metals. *Journal of Applied Physics,* 84(4):1958-1962, 1998.

[32] J. P. Dekker, A. Lodder, and J. van Ek, Theory for the electromigration wind force in dilute alloys. *Physical Review B,* 56(19):12167-12177, Nov 1997.

[33] K. Svensson, H. Olin, and E. Olsson, Nanopipettes for metal transport. *Physical Review Letters,* 93(14):Oct 2004.

[34] S. Heinze, N. P. Wang, and J. Tersoff, Electromigration forces on ions in carbon nanotubes. *Physical Review Letters,* 95(18):Oct 2005.

[35] B. C. Regan, S. Aloni, R. O. Ritchie, U. Dahmen, and A. Zettl, Carbon nanotubes as nanoscale mass conveyors. *Nature,* 428(6986):924-927, Apr 2004.

[36] A. Barreiro, R. Rurali, E. R. Hernandez, J. Moser, T. Pichler, L. Forro, and A. Bachtold, Subnanometer motion of cargoes driven by thermal gradients along carbon nanotubes. *Science,* 320(5877):775-778, May 2008.

[37] J. O. Zhao, J. Q. Huang, F. Wei, and J. Zhu, Mass transportation mechanism in electric-biased carbon nanotubes. *Nano Letters,* 10(11):4309-4315, Mar 2010.

[38] P. G. Collins, M. Hersam, M. Arnold, R. Martel, and P. Avouris, Current saturation and electrical breakdown in multiwalled carbon nanotubes. *Physical Review Letters,* 86(14):Apr 2001.

[39] Z. Fan, X. Y. Tao, X. D. Cui, X. D. Fan, X. B. Zhang, and L. X. Dong. Shaping the nanostructures from electromigration-based deposition. In *Proc. of the 2010 IEEE Nanotechnology Materials and Devices Conference (IEEE-NMDC2010)*, *2010 IEEE*, pages 22-25, 2010.

[40] Z. F. Liu, Z. Y. Shen, T. Zhu, S. F. Hou, L. Z. Ying, Z. J. Shi, and Z. N. Gu, Organizing single-walled carbon nanotubes on gold using a wet chemical self-assembling technique. *Langmuir,* 16(8):3569-3573, Apr 2000.

[41] B. Q. Wei, R. Vajtai, Y. Jung, J. Ward, R. Zhang, G. Ramanath, and P. M. Ajayan, Organized assembly of carbon nanotubes - cunning refinements help to customize the architecture of nanotube structures. *Nature,* 416(6880):495-496, Apr 2002.

[42] T. W. Ebbesen, H. J. Lezec, H. Hiura, J. W. Bennett, H. F. Ghaemi, and T. Thio, Electrical conductivity of individual carbon nanotubes. *Nature,* 382(6586):54-56, Jul 1996.

[43] H. J. Dai, E. W. Wong, and C. M. Lieber, Probing electrical transport in nanomaterials: Conductivity of individual carbon nanotubes. *Science,* 272(5261):523-526, Apr 1996.

[44] L. X. Dong, A. Subramanian, and B. J. Nelson, Carbon nanotubes for nanorobotics. *Nano Today,* 2(6):12-21, Dec 2007.

[45] S. J. Tans, M. H. Devoret, H. J. Dai, A. Thess, R. E. Smalley, L. J. Geerligs, and C. Dekker, Individual single-wall carbon nanotubes as quantum wires. *Nature,* 386(6624):474-477, 1997.

[46] B. Gao, Y. F. Chen, M. S. Fuhrer, D. C. Glattli, and A. Bachtold, Four-point resistance of individual single-wall carbon nanotubes. *Physical Review Letters,* 95(19):Nov 2005.

[47] S. Yoshimoto, Y. Murata, K. Kubo, K. Tomita, K. Motoyoshi, T. Kimura, H. Okino, R. Hobara, I. Matsuda, S. Honda, M. Katayama, and S. Hasegawa, Four-point probe resistance measurements using ptlr-coated carbon nanotube tips. *Nano Letters,* 7(4):956-959, Apr 2007.

[48] R. Lin, M. Bammerlin, O. Hansen, R. R. Schlittler, and P. Boggild, Micro-four-point-probe characterization of nanowires fabricated using the nanostencil technique. *Nanotechnology,* 15(9):1363-1367, Sep 2004.

[49] Z. Fan, X. Tao, Y. Li, Y. Yang, J. Du, W. Zhang, H. Huang, Y. Gan, X. Li, and L. Dong. *In situ* electrical property characterization of individual nanostructures using a sliding probe inside a transmission electron microscope. In *Proc. of the 2010 IEEE Nanotechnology Materials and Devices Conference (IEEE-NMDC2010)*, *2010*, pages 149-152, 2010.

[50] J. R. Cooper and R. L. Hansler, Variation of electrical resistivity of cubic tantalum carbide with composition. *Journal of Chemical Physics,* 39(1):248-&, 1963.

[51] C. Schonenberger, A. Bachtold, C. Strunk, J. P. Salvetat, and L. Forro, Interference and interaction in multi-wall carbon nanotubes. *Applied Physics A-Materials Science & Processing,* 69(3):283-295, 1999.

[52] L. Novotny, Nano-optics - optical antennas tuned to pitch. *Nature,* 455(7215):887, Oct 2008.

[53] P. Muhlschlegel, H. J. Eisler, O. J. F. Martin, B. Hecht, and D. W. Pohl, Resonant optical antennas. *Science,* 308(5728):1607-9, Jun 2005.

[54] X. D. Cui, L. X. Dong, W. H. Zhang, W. Wu, Y. Tang, and D. Erni, Numerical investigations of a multi-walled carbon nanotube-based multi-segmented optical antenna. *Applied Physics B: Lasers and Optics,* 101(3):601-609, Nov. 2010.

[55] A. M. Kern and O. J. F. Martin, Excitation and reemission of molecules near realistic plasmonic nanostructures. *Nano Letters,* 11(2):482-7, Feb 2011.

[56] P. Bharadwaj and L. Novotny, Robustness of quantum dot power-law blinking. *Nano Letters,* 11(5):2137-41, May 2011.

[57] T. Kalkbrenner, U. Hakanson, A. Schadle, S. Burger, C. Henkel, and V. Sandoghdar, Optical microscopy via spectral modifications of a nanoantenna. *Physical Review Letters,* 95(20):Nov 2005.

[58] M. Fleischer, A. Weber-Bargioni, M. V. P. Altoe, A. M. Schwartzberg, P. J. Schuck, S. Cabrini, and D. P. Kern, Gold nanocone near-field scanning optical microscopy probes. *Acs Nano,* 5(4):2570-9, Apr 2011.

[59] M. Righini, P. Ghenuche, S. Cherukulappurath, V. Myroshnychenko, F. J. G. de Abajo, and R. Quidant, Nano-optical trapping of rayleigh particles and escherichia coli bacteria with resonant optical antennas. *Nano Letters,* 9(10):3387-91, Oct 2009.

[60] M. L. Juan, M. Righini, and R. Quidant, Plasmon nano-optical tweezers. *Nature Photonics,* 5(6):349-56, Jun 2011.

[61] P. Anger, P. Bharadwaj, and L. Novotny, Enhancement and quenching of single-molecule fluorescence. *Physical Review Letters,* 96(11):Mar 2006.

[62] C. Hoppener and L. Novotny, Antenna-based optical imaging of single ca2+ transmembrane proteins in liquids. *Nano Letters,* 8(2):642-6, Feb 2008.

[63] L. X. Dong, A. Subramanian, D. Hugentobler, B. J. Nelson, and Y. Sun, Nano encoders based on vertical arrays of individual carbon nanotubes. *Advanced Robotics,* 20(11):1281–1301, Nov. 2006.

[64] O. Sqalli, M. P. Bernal, P. Hoffmann, and F. Marquis-Weible, Improved tip performance for scanning near-field optical microscopy by the attachment of a single gold nanoparticle. *Applied Physics Letters,* 76(15):2134-2136, Apr 2000.

[65] I. U. Vakarelski and K. Higashitani, Single-nanoparticle-terminated tips for scanning probe microscopy. *Langmuir,* 22(7):2931-4, Mar 2006.

[66] Y. Kawata, S. Urahama, M. Murakami, and F. Iwata, The use of capillary force for fabricating probe tips for scattering-type near-field scanning optical microscopes. *Applied Physics Letters,* 82(10):1598-600, Mar 2003.

[67] T. Okamoto and I. Yamaguchi, Photocatalytic deposition of a gold nanoparticle onto the top of a sin cantilever tip. *Journal of Microscopy-Oxford,* 202100-103, Apr 2001.

[68] F. Pampaloni, G. Lattanzi, A. Jonas, T. Surrey, E. Frey, and E. L. Florin, Thermal fluctuations of grafted microtubules provide evidence of a length-dependent persistence length. *Proceedings of the National Academy of Sciences of the United States of America,* 103(27):10248-53, Jul 2006.

[69] Y. Gan, A review of techniques for attaching micro- and nanoparticles to a probe's tip for surface force and near-field optical measurements. *Review of Scientific Instruments,* 78(8):Aug 2007.

[70] A. Chu, J. Cook, R. J. R. Heesom, J. L. Hutchison, M. L. H. Green, and J. Sloan, Filling of carbon nanotubes with silver, gold, and gold chloride. *Chemistry of Materials,* 8(12):2751-4, Dec 1996.

[71] D. Ugarte, A. Chatelain, and W. A. de Heer, Nanocapillarity and chemistry in carbon nanotubes. *Science,* 274(5294):1897-1899, Dec 1996.

[72] X. Y. Tao, X. B. Zhang, J. P. Cheng, Z. Q. Luo, S. M. Zhou, and F. Liu, Thermal cvd synthesis of carbon nanotubes filled with single-crystalline cu nanoneedles at tips. *Diamond and Related Materials,* 15(9):1271-1275, Sep 2006.

[73] P. M. Ajayan, T. W. Ebbesen, T. Ichihashi, S. Iijima, K. Tanigaki, and H. Hiura, Opening carbon nanotubes with oxygen and implications for filling. *Nature,* 362(6420):522-5, Apr 1993.

[74] Y. H. Gao and Y. Bando, Carbon nanothermometer containing gallium - gallium's macroscopic properties are retained on a miniature scale in this nanodevice. *Nature,* 415(6872):599-600, Feb 2002.

[75] L. Sun, F. Banhart, A. V. Krasheninnikov, J. A. Rodriguez-Manzo, M. Terrones, and P. M. Ajayan, Carbon nanotubes as high-pressure cylinders and nanoextruders. *Science,* 312(5777):1199-1202, May 2006.

[76] X. Y. Tao, L. X. Dong, W. K. Zhang, X. B. Zhang, J. P. Cheng, H. Huang, and Y. P. Gan, Controllable melting and flow of β-sn in flexible amorphous carbon nanotubes. *Carbon,* 47(13):3122-3127, Nov. 2009.

[77] L. X. Dong, X. Y. Tao, M. Hamdi, L. Zhang, X. B. Zhang, A. Ferreira, and B. J. Nelson, Nanotube fluidic junctions: Inter-nanotube attogram mass transport through walls. *Nano Letters,* 9(1):210-214, Jan 2009.

[78] L. X. Dong, X. Y. Tao, L. Zhang, X. B. Zhang, and B. J. Nelson, Plumbing the depths of the nanometer scale: Attogram mass transport via nanochannels. *IEEE Nanotechnology Magazine,* 4(1):13-22, Mar. 2010.

[79] X. D. Feng, D. C. Sayle, Z. L. Wang, M. S. Paras, B. Santora, A. C. Sutorik, T. X. T. Sayle, Y. Yang, Y. Ding, X. D. Wang, and Y. S. Her, Converting ceria polyhedral nanoparticles into single-crystal nanospheres. *Science,* 312(5779):1504-8, Jun 2006.

[80] J. Rybczynski, K. Kempa, Y. Wang, Z. F. Ren, J. B. Carlson, B. R. Kimball, and G. Benham, Visible light diffraction studies on periodically aligned arrays of carbon nanotubes: Experimental and theoretical comparison. *Applied Physics Letters,* 88(20):May 2006.

[81] A. O. Caldeira and A. J. Leggett, Quantum tunnelling in a dissipative system. *Annals of Physics,* 149(2):374-456, 1983.

[82] M. H. Devoret, D. Esteve, H. Grabert, G. L. Ingold, H. Pothier, and C. Urbina, On the observability of coulomb blockade and single-electron tunneling. *Ultramicroscopy,* 4222-32, Jul 1992.

[83] D. Gatteschi and R. Sessoli, Quantum tunneling of magnetization and related phenomena in molecular materials. *Angewandte Chemie-International Edition,* 42(3):268-297, 2003.

[84] L. Thomas, F. Lionti, R. Ballou, D. Gatteschi, R. Sessoli, and B. Barbara, Macroscopic quantum tunnelling of magnetization in a single crystal of nanomagnets. *Nature,* 383(6596):145-147, Sep 1996.

[85] S. E. Kubatkin, A. V. Danilov, A. L. Bogdanov, H. Olin, and T. Claeson, Coulomb blockade effects at room temperature in thin-film nanoconstrictions fabricated by a novel technique. *Applied Physics Letters,* 73(24):3604-3606, Dec 1998.

[86] D. L. Klein, P. L. McEuen, J. E. B. Katari, R. Roth, and A. P. Alivisatos, An approach to electrical studies of single nanocrystals. *Applied Physics Letters,* 68(18):2574-2576, Apr 1996.

[87] M. A. Kastner, The single-electron transistor. *Reviews of Modern Physics,* 64(3):849-858, Jul 1992.

[88] D. M. Eigler and E. K. Schweizer, Position single atoms with a scanning tunneling microscope. *Nature,* 344(6266):524-526, Apr 1990.

[89] J. Tersoff and D. R. Hamann, Theory of the scanning tunneling microscope. *Physical Review B,* 31(2):805-813, 1985.

[90] E. R. Brown, J. R. Soderstrom, C. D. Parker, L. J. Mahoney, K. M. Molvar, and T. C. McGill, Oscillations up to 712 ghz in inas/alsb resonant-tunneling diodes. *Applied Physics Letters,* 58(20):2291-2293, May 1991.

[91] N. C. Kluksdahl, A. M. Kriman, D. K. Ferry, and C. Ringhofer, Self-consistent study of the resonant-tunneling diode. *Physical Review B,* 39(11):7720-7735, Apr 1989.

[92] J. M. Seminario, A. G. Zacarias, and J. M. Tour, Theoretical study of a molecular resonant tunneling diode. *Journal of the American Chemical Society,* 122(13):3015-3020, Apr 2000.

[93] A. P. Alivisatos, Semiconductor clusters, nanocrystals, and quantum dots. *Science,* 271(5251):933-937, Feb 1996.

[94] D. Loss and D. P. DiVincenzo, Quantum computation with quantum dots. *Physical Review A,* 57(1):120-126, Jan 1998.

[95] J. G. Simmons, Generalized formula for electric tunnel effect between similiar electrodes separated by a thin insulating film. *Journal of Applied Physics,* 34(6):1793-1803, 1963.

[96] L. Olesen, M. Brandbyge, M. R. Sorensen, K. W. Jacobsen, E. Laegsgaard, I. Stensgaard, and F. Besenbacher, Apparent barrier height in scanning tunneling microscopy revisited. *Physical Review Letters,* 76(9):1485-1488, Feb 1996.

[97] G. Binnig, H. Rohrer, C. Gerber, and E. Weibel, Tunneling through a controllable vacuum gap. *Applied Physics Letters,* 40(2):178-180, 1982.

[98] M. Riaz, O. Nur, M. Willander, and P. Klason, Buckling of zno nanowires under uniaxial compression. *Applied Physics Letters,* 92(10):Mar 2008.

[99] A. Pantano, M. C. Boyce, and D. M. Parks, Mechanics of axial compression of single and multi-wall carbon nanotubes. *Journal of Engineering Materials and Technology-Transactions of the Asme,* 126(3):279-284, Jul 2004.

[100] A. Pantano, D. M. Parks, and M. C. Boyce, Mechanics of deformation of single- and multi-wall carbon nanotubes. *Journal of the Mechanics and Physics of Solids,* 52(4):789-821, Apr 2004.

[101] C. Q. Ru, Axially compressed buckling of a doublewalled carbon nanotube embedded in an elastic medium. *Journal of the Mechanics and Physics of Solids,* 49(6):1265-1279, Jun 2001.

[102] O. Lourie, D. M. Cox, and H. D. Wagner, Buckling and collapse of embedded carbon nanotubes. *Physical Review Letters,* 81(8):1638-1641, Aug 1998.

[103] H. Shima, Buckling of carbon nanotubes: A state of the art review. *Materials,* 5(1):47-84, Jan 2012.

[104] S. P. Timoshenko and J. M. Gere, *Theory of elastic stability*, 2nd ed. New York: Tata McGraw-Hill Education, 1961.

[105] L. D. Landau, E. Lifshitz, J. Sykes, W. Reid, and E. H. Dill, *Theory of elasticity: Vol. 5 of course of theoretical physics* vol. 5. Pergamon, Oxford, 1959.

[106] T. F. Lemczyk and M. M. Yovanovich, Efficient evaluation of incomplete elliptic integrals and functions. *Computers & Mathematics with Applications,* 16(9):747-757, 1988.

[107] N. Biswas, J. Gurganus, and V. Misra, Work function tuning of nickel silicide by co-sputtering nickel and silicon. *Applied Physics Letters,* 87(17):Oct 2005.

[108] X. Y. Tao, Y. P. Li, J. Du, Y. Xia, Y. C. Yang, H. Huang, Y. P. Gan, W. K. Zhang, and X. D. Li, A generic bamboo-based carbothermal method for preparing carbide (sic, b_4c, tic, tac, nbc, $ti_xnb_{1-x}c$, and $ta_xnb_{1-x}c$) nanowires. *Journal of Materials Chemistry,* 21(25):9095-9102, 2011.

[109] X. Y. Tao, L. X. Dong, X. N. Wang, W. K. Zhang, B. J. Nelson, and X. D. Li, B_4c-nanowires/carbon-microfiber hybrid structures and composites from cotton t-shirts. *Advanced Materials,* 22(18):2055-2059, May 2010.

[110] D. T. Welna, J. D. Bender, X. L. Wei, L. G. Sneddon, and H. R. Allcock, Preparation of boron-carbide/carbon nanofibers from a poly(norbornenyldecaborane) single-source precursor via electrostatic spinning. *Advanced Materials,* 17(7):859-862, Apr 2005.

[111] R. Ma and Y. Bando, Investigation on the growth of boron carbide nanowires. *Chemistry of Materials,* 14(10):4403-4407, Oct 2002.

[112] H. J. Dai, E. W. Wong, Y. Z. Lu, S. S. Fan, and C. M. Lieber, Synthesis and characterization of carbide nanorods. *Nature,* 375(6534):769-772, Jun 1995.

[113] P. H. Chen, C. H. Hsieh, S. Y. Chen, C. H. Wu, Y. J. Wu, L. J. Chou, and L. J. Chen, Direct observation of au/ga_2o_3 peapodded nanowires and their plasmonic behaviors. *Nano Letters,* 10(9):3267-3271, Sep 2010.

[114] P. Utko, R. Ferone, I. V. Krive, R. I. Shekhter, M. Jonson, M. Monthioux, L. Noe, and J. Nygard, Nanoelectromechanical coupling in fullerene peapods probed by resonant electrical transport experiments. *Nature Communications,* 137, Jul 2010.

[115] M. S. Hu, H. L. Chen, C. H. Shen, L. S. Hong, B. R. Huang, K. H. Chen, and L. C. Chen, Photosensitive gold-nanoparticle-embedded dielectric nanowires. *Nature Materials,* 5(2):102-106, Feb 2006.

[116] C. Colinet and J. C. Tedenac, Investigation of structural, electronic and thermodynamic properties of ni_6si_2b and ni_6ge_2b compounds with the fe_2p-type structure. *Intermetallics,* 2473-78, May 2012.

[117] T. Tokunaga, K. Nishio, and M. Hasebe, Thermodynamic study of phase equilibria in the ni-si-b system. *Journal of Phase Equilibria,* 22(3):291-299, Jun 2001.

[118] J. Zhou, Y. D. Gu, P. Fei, W. J. Mai, Y. F. Gao, R. S. Yang, G. Bao, and Z. L. Wang, Flexible piezotronic strain sensor. *Nano Letters,* 8(9):3035-3040, Sep 2008.

[119] C. Stampfer, A. Jungen, R. Linderman, D. Obergfell, S. Roth, and C. Hierold, Nano-electromechanical displacement sensing based on single-walled carbon nanotubes. *Nano Letters,* 6(7):1449-1453, Jul 2006.

[120] R. R. He and P. D. Yang, Giant piezoresistance effect in silicon nanowires. *Nature Nanotechnology,* 1(1):42-46, Oct 2006.

[121] A. R. Hall, M. R. Falvo, R. Superfine, and S. Washburn, Electromechanical response of single-walled carbon nanotubes to torsional strain in a self-contained device. *Nature Nanotechnology,* 2(7):413-416, Jul 2007.

[122] J. Park, A. N. Pasupathy, J. I. Goldsmith, C. Chang, Y. Yaish, J. R. Petta, M. Rinkoski, J. P. Sethna, H. D. Abruna, P. L. McEuen, and D. C. Ralph, Coulomb blockade and the kondo effect in single-atom transistors. *Nature,* 417(6890):722-725, Jun 2002.

[123] C. Livermore, C. H. Crouch, R. M. Westervelt, K. L. Campman, and A. C. Gossard, The coulomb blockade in coupled quantum dots. *Science,* 274(5291):1332-1335, Nov 1996.

[124] J. G. Simmons, Generalized formula for electric tunnel effect between similar electrodes separated by a thin insulating film *Journal of Applied Physics,* 34(6):1793-1803, 1963.

[125] G. Binning, H. Rohrer, C. Gerber, and E. Weibel, Surface studies by scanning tunneling microscopy. *Physical Review Letters,* 49(1):57-61, 1982.

[126] D. B. Strukov, G. S. Snider, D. R. Stewart, and R. S. Williams, The missing memristor found. *Nature,* 453(7191):80-83, May 2008.

[127] T. Driscoll, H. T. Kim, B. G. Chae, M. Di Ventra, and D. N. Basov, Phase-transition driven memristive system. *Applied Physics Letters,* 95(4):Jul 2009.

[128] S. H. Jo, T. Chang, I. Ebong, B. B. Bhadviya, P. Mazumder, and W. Lu, Nanoscale memristor device as synapse in neuromorphic systems. *Nano Letters,* 10(4):1297-1301, Apr 2010.

[129] S. H. Jo, K. H. Kim, and W. Lu, Programmable resistance switching in nanoscale two-terminal devices. *Nano Letters,* 9(1):496-500, Jan 2009.

[130] K. M. Kim, G. H. Kim, S. J. Song, J. Y. Seok, M. H. Lee, J. H. Yoon, and C. S. Hwang, Electrically configurable electroforming and bipolar resistive switching in pt/tio_2/pt structures. *Nanotechnology,* 21(30):Jul 2010.

[131] Y. V. Pershin and M. Di Ventra, Experimental demonstration of associative memory with memristive neural networks. *Neural Networks,* 23(7):881-886, Sep 2010.

[132] F. Miao, J. P. Strachan, J. J. Yang, M. X. Zhang, I. Goldfarb, A. C. Torrezan, P. Eschbach, R. D. Kelley, G. Medeiros-Ribeiro, and R. S. Williams, Anatomy of a nanoscale conduction channel reveals the mechanism of a high-performance memristor. *Advanced Materials,* 23(47):5633-5640, Dec 2011.

[133] Q. Liu, S. B. Long, H. B. Lv, W. Wang, J. B. Niu, Z. L. Huo, J. N. Chen, and M. Liu, Controllable growth of nanoscale conductive filaments in solid-electrolyte-based reram by using a metal nanocrystal covered bottom electrode. *Acs Nano,* 4(10):6162-6168, Oct 2010.

[134] M. J. Lee, C. B. Lee, D. Lee, S. R. Lee, M. Chang, J. H. Hur, Y. B. Kim, C. J. Kim, D. H. Seo, S. Seo, U. I. Chung, I. K. Yoo, and K. Kim, A fast, high-endurance and scalable non-volatile memory device made from asymmetric ta_2o_{5-x}/tao_{2-x} bilayer structures. *Nature Materials,* 10(8):625-630, Aug 2011.

[135] B. Muthuswamy, Implementing memristor based chaotic circuits. *International Journal of Bifurcation and Chaos,* 20(5):1335-1350, May 2010.

[136] Q. F. Xia, W. Robinett, M. W. Cumbie, N. Banerjee, T. J. Cardinali, J. J. Yang, W. Wu, X. M. Li, W. M. Tong, D. B. Strukov, G. S. Snider, G. Medeiros-Ribeiro, and R. S. Williams, Memristor-cmos hybrid integrated circuits for reconfigurable logic. *Nano Letters,* 9(10):3640-3645, Oct 2009.

[137] J. J. Yang, J. Borghetti, D. Murphy, D. R. Stewart, and R. S. Williams, A family of electronically reconfiguiable nanodevices. *Advanced Materials,* 21(37):3754-3758, Oct 2009.

[138] J. J. Yang, F. Miao, M. D. Pickett, D. A. A. Ohlberg, D. R. Stewart, C. N. Lau, and R. S. Williams, The mechanism of electroforming of metal oxide memristive switches. *Nanotechnology,* 20(21):May 2009.

[139] J. J. Yang, M. D. Pickett, X. M. Li, D. A. A. Ohlberg, D. R. Stewart, and R. S. Williams, Memristive switching mechanism for metal/oxide/metal nanodevices. *Nature Nanotechnology,* 3(7):429-433, Jul 2008.

[140] Y. C. Yang, P. Gao, S. Gaba, T. Chang, X. Q. Pan, and W. Lu, Observation of conducting filament growth in nanoscale resistive memories. *Nature Communications,* 3Mar 2012.

[141] B. J. Choi, D. S. Jeong, S. K. Kim, C. Rohde, S. Choi, J. H. Oh, H. J. Kim, C. S. Hwang, K. Szot, R. Waser, B. Reichenberg, and S. Tiedke, Resistive switching mechanism of tio_2 thin films grown by atomic-layer deposition. *Journal of Applied Physics,* 98(3):Aug 2005.

[142] D. S. Jeong, H. Schroeder, and R. Waser, Coexistence of bipolar and unipolar resistive switching behaviors in a pt/tio_2/pt stack. *Electrochemical and Solid State Letters,* 10(8):51-53, Mar 2007.

[143] D. S. Jeong, H. Schroeder, U. Breuer, and R. Waser, Characteristic electroforming behavior in pt/tio_2/pt resistive switching cells depending on atmosphere. *Journal of Applied Physics,* 104(12):Dec 2008.

[144] D. H. Kwon, K. M. Kim, J. H. Jang, J. M. Jeon, M. H. Lee, G. H. Kim, X. S. Li, G. S. Park, B. Lee, S. Han, M. Kim, and C. S. Hwang, Atomic structure of conducting nanofilaments in tio_2 resistive switching memory. *Nature Nanotechnology,* 5(2):148-153, Feb 2010.

[145] R. Waser and M. Aono, Nanoionics-based resistive switching memories. *Nature Materials,* 6(11):833-840, Nov 2007.

[146] W. Z. Wu and Z. L. Wang, Piezotronic nanowire-based resistive switches as programmable electromechanical memories. *Nano Letters,* 11(7):2779-2785, Jul 2011.

[147] F. Mumm and P. Sikorski, Oxidative fabrication of patterned, large, non-flaking cuo nanowire arrays. *Nanotechnology,* 22(10):Mar 2011.

[148] X. C. Jiang, T. Herricks, and Y. N. Xia, Cuo nanowires can be synthesized by heating copper substrates in air. *Nano Letters,* 2(12):1333-1338, Dec 2002.

[149] D.-H. Kwon, K. M. Kim, J. H. Jang, J. M. Jeon, M. H. Lee, G. H. Kim, X.-S. Li, G.-S. Park, B. Lee, S. Han, M. Kim, and C. S. Hwang, Atomic structure of conducting nanofilaments in tio_2 resistive switching memory. *Nature Nanotechnology,* 5(2):148-153, Feb 2010.

[150] L. A. Bursill and A. C. McLaren, Transmission electron microscope study of natural radiation damage in zircon ($zrsio_4$). *Physica Status Solidi,* 13(2):331-343, 1966.

[151] Z. L. Liao, P. Gao, X. D. Bai, D. M. Chen, and J. D. Zhang, Evidence for electric-field-driven migration and diffusion of oxygen vacancies in pr0.7ca0.3mno3. *Journal of Applied Physics,* 111(11):Jun 2012.

[152] Y. M. Kim, J. He, M. D. Biegalski, H. Ambaye, V. Lauter, H. M. Christen, S. T. Pantelides, S. J. Pennycook, S. V. Kalinin, and A. Y. Borisevich, Probing oxygen vacancy concentration and homogeneity in solid-oxide fuel-cell cathode materials on the subunit-cell level. *Nature Materials,* 11(10):888-894, Oct 2012.

[153] R. F. Egerton, *Electron energy-loss spectroscopy in the electron microscope*, 3rd ed. New York: Springer, 2011.

[154] R. D. Leapman, L. A. Grunes, and P. L. Fejes, Study of the l_{23} edges in the 3d transition-metals and their oxides by electron-energy-loss spectroscopy with comparisons to theory. *Physical Review B,* 26(2):614-635, 1982.